Alma Mater Studiorum – Università di Bologna

DOTTORATO DI RICERCA IN

ASTROFISICA

Ciclo XXX

Settore Concorsuale: 02/C1

Settore Scientifico Disciplinare: FIS/05

A Multi-Conjugate Adaptive Optics view of Bulge Globular Clusters

Presentata da: Sara Saracino

Coordinatore Dottorato

Chiar.mo Prof. F. R. Ferraro

Supervisore

Chiar.mo Prof. F. R. Ferraro

Co-Relatori

Chiar.ma Prof.ssa B. Lanzoni
Dr. E. Dalessandro
Dr.ssa L. Origlia

Esame finale anno 2018

Sommario

Il Bulge è una delle componenti più massive della nostra Galassia ed è composta principalmente da stelle molto vecchie e di alta metallicità. Comprendere la sua struttura e le proprietà della sua popolazione stellare è di grande importanza per tutti i modelli teorici che tentano di descrivere come si è formata ed evoluta nel tempo la Via Lattea e, più in generale, quali sono i processi fisici che regolano la formazione dei bulge e delle galassie sferoidali. Tuttavia molte cose restano ancora da capire sulla formazione e l'evoluzione di questo sistema, principalmente a causa di limiti osservativi. Il bulge è infatti una delle regioni più inaccessibili della nostra Galassia per via di nubi di polvere lungo la linea di vista che assorbono quasi completamente la radiazione a lunghezze d'onda ottiche.

Gli ammassi globulari del Bulge sono degli importanti strumenti per vincolare le proprietà di questo sistema, poichè presentano la stessa cinematica e composizione chimica delle stelle del bulge. Sfortunatamente questi sistemi sono ad oggi ancora poco studiati poichè sono stati esclusi in modo sistematico da numerose campagne osservative a causa della loro forte estinzione.

Lo scopo di questa Tesi è quello di contribuire a colmare questa mancanza, attraverso lo studio delle popolazioni stellari e dei parametri strutturali di ammassi globulari del bulge, grazie a strumenti ad alta risoluzione di ultima generazione. Per raggiungere questo obiettivo abbiamo sfruttato il sistema di ottica adattiva multiconiugata GeMS che lavora in sincrono con la camera infrarossa GSAOI, al telescopio Gemini Sud in Cile.

Il nostro lavoro ha dimostrato che le prestazioni fotometriche ed astrometriche di GeMS+GSAOI sono ideali per lo studio di questi sistemi stellari. In particolare ci siamo occupati di analizzare in dettaglio due casi estremi. Il primo è Liller 1, che è uno degli ammassi globulari più oscurati e quindi meno studiati della nostra Galassia. Questo sistema stellare è perfetto per verificare le prestazioni di un sistema di ottica adattiva su un telescopio da 8 metri. Il secondo è NGC 6624. Questo ammasso è stato ampiamente studiato in letteratura grazie al telescopio spaziale Hubble, permettono quindi un confronto accurato ed una quantitativa valutazione delle performance di GeMS+GSAOI. Grazie a questi dati abbiamo eseguito una caratterizzazione dettagliata del sistema soffermandoci sul *modeling* della *Point Spread Function* e sull'analisi delle variazioni di *Strehl Ratio* ed *Encircled Energy distribution* nel campo di vista. Abbiamo inoltre derivato la prima soluzione analitica per correggere le distorsioni

geometriche della camera. Sfruttando l'eccellente qualità e l'inedita profondità delle immagini di NGC 6624, combinate ad osservazioni infrarosse ottenute dallo spazio per 47 Tucanae, abbiamo poi studiato in dettaglio l'affidabilità ed i limiti del "*knee* della sequenza principale" come strumento per derivare l'età assoluta degli ammassi globulari da diagrammi infrarossi. Questo lavoro ha messo in evidenza quali sono i miglioramenti possibili nel prossimo futuro in questo campo grazie a strumenti come *E-ELT (European Extremely Large Telescope)* e *JWST (James Webb Space Telescope)* e alcune nuove sfide per lo sviluppo di modelli teorici di stelle di piccola massa.

Abstract

The Galactic bulge represents one of the most massive stellar components of the Galaxy, mainly made of very old and metal-rich stars. Understanding its structure and the properties of its stellar population is therefore key to describe how the Milky Way, as well as any galaxy spheroid, formed and evolved with cosmic time. However, many open issues still remain about the formation and evolution of this system, mainly due to observational limitations. In fact, because of the presence of thick clouds of dust along the line of sight that almost totally absorb the optical light, the bulge is one of the most inaccessible region of the Galaxy.

Bulge globular clusters are useful tools to constrain the properties of this system, as they share the same kinematics and chemical composition with bulge field stars. However, these systems have been widely excluded from large surveys due to the huge extinction, and they remain in many cases only poorly known so far.

The aim of this Thesis is to contribute to fill this gap by studying the stellar populations and structural parameters of bulge globular clusters by means of state-of-the-art high resolution near-infrared instruments. Indeed, to this aim we exploited the capabilities offered by the Multi-Conjugate Adaptive Optics system GeMS combined with the GSAOI imager at the Gemini South Telescope, in Chile.

The photometric and astrometric performance of GeMS+GSAOI have been proven to be ideal to study such stellar systems. We mainly focused on two extreme cases. The first is Liller 1, which is one of the most obscured and therefore least studied systems in the Galaxy. This target is ideal to probe the benefit of using an Adaptive Optics system on an 8 meter telescope. The second is NGC 6624. This cluster has been extensively studied in the literature with the Hubble Space Telescope (HST) and therefore allows a detailed comparison and assessment of the GeMS+GSAOI performance. Based on these data we performed an in-depth characterization of the instruments in terms of Point Spread Function modeling, Strehl Ratio and Encircled Energy distribution variations within the field of view. We have also derived the first analytic solution to correct the geometric distortions of this system. Taking advantage of the exquisite quality and depth of the NGC 6624 images, in combination with deep HST infrared observations of 47 Tucanae, we performed a detailed analysis aimed at probing the reliability and the limits of the so-called "main sequence knee" as a tool to derive accurate absolute ages in near-infrared color-magnitude diagrams of globular clusters. This work puts important constraints to the future improvements achievable

in this field with E-ELT (European Extremely Large Telescope) and JWST (James Webb Space Telescope) observations, and it provides new challenges for models of low-mass stars.

Contents

List of abbreviations **1**

Thesis outline **3**

1 The Galactic Bulge and its globular cluster system **5**
1.1 Introduction 5
1.2 Interstellar extinction 6
1.3 The Galactic bulge - a global view 6
1.4 The Bulge GC system 19

2 Multi-Conjugate Adaptive Optics **25**
2.1 Introduction 25
2.2 The AO technique 28
2.3 The first AO systems 31
2.4 Laser Guide Stars 32
2.5 The MCAO era 34
2.6 GeMS at Gemini South Telescope 37

3 GeMS/GSAOI photometric and astrometric performance in dense stellar fields **41**
3.1 Introduction 41
3.2 Dataset and observing conditions 44
3.3 Overall performance 45
3.4 GeMS/GSAOI astrometric performance 54
3.5 Conclusions 61

4 GEMINI/GeMS observations unveil the structure of the heavily obscured globular cluster Liller 1 **67**
4.1 Introduction 68
4.2 Observations and data analysis 69
4.3 Results 73
4.4 Summary and conclusions 84

5 Ultra-deep GEMINI near-infrared observations of the bulge globular cluster NGC 6624 **87**
5.1 Introduction 88
5.2 Observations and data analysis 88
5.3 Near-Infrared Color-Magnitude diagrams of NGC 6624 92
5.4 Absolute age determination 92
5.5 The Luminosity and Mass Function of NGC 6624 100
5.6 Summary & Conclusions 105
5.7 Appendix 107

6 On the use of the main sequence knee to measure absolute globular cluster ages **111**
6.1 Introduction 112
6.2 A knee or a saddle? 114
6.3 Observational data - 47 Tucanae and NGC 6624 120
6.4 Absolute GC ages derived from the MS-saddle 126
6.5 Summary and Conclusions 128

Conclusions and Future Perspectives **133**

Bibliography **137**

List of Figures

1.1 **(a):** Extinction map of the Galactic bulge for the entire region covered by the VVV survey. A_{K_s} values are computed from Cardelli et al. (1989) and values higher than 1.5 mag are saturated in the color scale shown in the right side. **(b):** Extinction map for the inner $\sim 4^{\circ}$ region around the Galactic plane. In this plot the color scale reaches 3.5 mag to take account for highly obscured regions very close to the Galactic center. . 7
1.2 The Galactic bar and the boxy/peanut shape as seen from the North Galactic Pole. Figure from Wegg and Gerhard (2013), reproduced by Zoccali and Valenti (2016). 9
1.3 Shape and orientation of the main bar as it appears if the Galaxy is seen face-on. The near side of the bar is at positive Galactic longitude. The clockwise rotation of the bar is also marked (Figure from Rich (2013)). 10
1.4 *Upper panel:* Spatial distribution of RR Lyrae stars in the Galactic bulge area of the VVV survey, from Dékány et al. (2013). The black rectangle is the region for which the mean distance of RR Lyrae and RC stars are compared in the lower panel. *Lower panel:* The projected mean distances of RR Lyrae is shown in black filled circles, while for RC stars as red open circles. The different trend is evident and the spheroidal structure is highlighted through iso-density contours for the projected distance distribution of the RR Lyrae sample. 11
1.5 **(a):** Statistical disk decontamination of a field at the edge of the bar, from Valenti et al. (2013). **(b):** Proper-motion disk decontamination of a bulge inner region, from Clarkson et al. (2008). 12
1.6 The metallicity of the microlensed dwarfs of the bulge as a function of their ages, from Bensby et al. (2017). The information about [α/Fe] is presented as a color code at the right side of the plot. 13
1.7 Metallicity distribution of RGB and RC stars in the bulge from Zoccali et al. (2008) and Lecureur et al. (2007) from high resolution spectra. Figure from Minniti and Zoccali (2008). 14
1.8 Map of the mean values of the metallicity distribution for the Galactic bulge covered by the VVV survey using the Cardelli et al. (1989) extinction law, from Gonzalez et al. (2013). 15

1.9 Oxygen and magnesium over iron ratios as measured from high dispersion spectra of bulge K giants (Zoccali et al., 2008; Lecureur et al., 2007). Green circles with error bars are bulge stars, compared with thick (blue triangles) and thin (orange squares) disk stars. Figure from Minniti and Zoccali (2008). 16
1.10 Milky Way bulge and halo position in the Binney (1978) diagram adapted from Minniti (1996) and Kormendy and Kennicutt (2004). Figure from (Minniti and Zoccali, 2008). 17
1.11 Radial velocity *(upper panel)* and velocity dispersion *(lower panel)* vs. Galactic longitude trends for the bulge fields studied in the BRAVA survey. Different colors indicate different Galactic latitudes. The typical features of cylindrical rotation are evident in both cases. Figure from Kunder et al. (2012). 18
1.12 Rotation *(left panel)* and dispersion *(right panel)* profiles as a function of Galactic latitude from the study of Ness and Freeman (2012) with ARGOS and of Ness et al. (2016) with APOGEE. The results are similar to BRAVA but span twice the range in latitude. 19
1.13 Radial velocity *(upper panel)* and radial velocity dispersion *(lower panel)* surface in the longitude-latitude plane constructed from the measured rotation profiles at negative latitudes from the GIBS survey by Zoccali et al. (2014). 20
1.14 Spatial distribution of bulge GCs with respect to the Galactic center (blue-filled circle). Well known bulge GCs are shown as red-filled triangles while VVV clusters and candidates as green open circles. Figure from Bica et al. (2016). 21
1.15 [α/Fe] vs [Fe/H] for bulge GCs (red triangles), compared with field stars (green circles) analyzed by Lecureur et al. (2007), Barbuy et al. (2015) and Gonzalez et al. (2011). Magenta circles are microlensed bulge dwarfs by Bensby et al. (2013). Figure from Bica et al. (2016). . . 22

2.1 Illustrative comparison of the angular resolution of a telescope with a short (left) and long exposure image (middle) in the presence of atmospheric turbulence. At the right a diffraction-limited image shows the presence of two point sources that were below the resolution allowed by the seeing. 26
2.2 Schematic showing the definition of the Fried parameter r_0, and how it relates to coherence time, $\tau_0 = t_2 - t_1$, and isoplanatic angle, θ_0. . . . 27
2.3 Explanation of the AO operating scheme. 30
2.4 Schematic view of a Shack-Hartmann wavefront sensor. 31
2.5 The sky coverage as a function of wavelength and distance from a reference star, for different galactic latitudes. 32
2.6 Schematic showing the different types of LGSs available for AO, and the cone effect. 33

2.7 Schematic view of an LTAO. Credits: ESO/Marchetti. 35
2.8 The principle of MCAO. Several WFS' and DM's are combined in order to "optimize" the adaptive correction in a larger FOV. Credits: ESO/Marchetti. 36
2.9 The Star Oriented mode (left) and the Layer Oriented mode (right) of an MCAO. Credits: ESO/Marchetti. 37
2.10 The deepest K-band image ever obtained for Terzan 5, with MAD at the ESO/VLT. It demonstrates how uniform and sharp can be the images realized with MCAO systems. Credits: ESO/Ferraro. 38
2.11 A schematic view of the MCAO system GeMS mounted at the Gemini South Telescope. 39
2.12 An example of LGS spots constellations for GeMS at Gemini. 39

3.1 The seeing disc of a star superposed on the theoretical diffraction pattern. The SR is the ratio of the peak intensities of the two profiles. . 42
3.2 Average FWHM, SR and EE values with varying the seeing at 500 nm at the zenith. Left panels: measurements in the K_s band, right panels: measurements in the J band. Triangles refer to measurements of stars in NGC 6624, circles and squares refer to measurements of stars in Liller 1 observed in two different nights, respectively (see Table 3.1). . 47
3.3 Same as in Figure 3.2, but for seeing at 500nm at the observing airmass. 48
3.4 Dispersion around the average FWHM, SR and EE values with varying the seeing at 500 nm at the zenith. Left panels: measurements in the K_s band, right panels: measurements in the J band. Triangles refer to measurements of stars in NGC 6624, circles and squares refer to measurements of stars in Liller 1 as observed in two different nights, respectively (see Table 3.1). 49
3.5 Same as in Figure 3.4, but for seeing at 500 nm at the observing airmass. 50
3.6 FWHM (left panels), SR (middle panels) and EE (right panels) maps for three K_s band images of Liller 1 acquired under different seeing conditions. The triangle indicates the guide star asterism. The quoted seeing values are at the zenith and at 500 nm. Color coding from magenta (worst) to red (best) is a performance indicator. 51
3.7 FWHM (left panels), SR (middle panels) and EE (right panels) maps for three J band images of Liller 1 acquired under different seeing conditions. The triangle indicates the guide star asterism. The quoted seeing values are at the zenith and at 500 nm. Color coding from magenta (worst) to red (best) is a performance indicator. 52
3.8 Dispersion around the average FWHM, SR and EE values as a function of the corresponding average values for the GeMS/GSAOI J (open circles) and K_s (filled circles) images, and the ACS/HST F606W (hexagon) and F814W (pentagon) ones. 54

3.9 FWHM (left panels), SR (middle panels) and EE (right panels) maps for three NGC 6624 images in the K_s (top panels), J (middle panels) and F814W (bottom panels) filters, respectively. The triangle indicates the guide star asterism for the GSAOI ground-based images. The central, white area in the HST maps was excluded due to the prohibitive crowding, while the black square indicates the GeMS/GSAOI FOV. . . 55
3.10 $V, V-I$ (left panel) and $K_s, J-K_s$ (right panel) CMDs of the stars in common between the *master catalog* and the GeMS/GSAOI catalog of NGC 6624 by Saracino et al. (2016). 57
3.11 Geometric distortion map of the four chips of GSAOI camera, in the K_s filter. Residual vectors are magnified by a factor of 10. For each chip, we also show individual residuals as function of x and y axes. Units are in GSAOI pixels. 62
3.12 As in Figure 3.11, but for the J band. 63
3.13 Residual map of the four chips of GSAOI camera, in the K_s filter, after the GD correction. Residual vectors are magnified by a factor of 5000. . 64
3.14 As in Figure 3.13, but for the J band. 65

4.1 False-color image of Liller 1 obtained by combining GEMINI observations in the NIR J and K_s bands. North is up, east is on the right. The FOV is 85″ × 85″. The bluish stars are hot field objects. 70
4.2 Distribution of the photometric errors of the GEMINI data set as a function of J and K_s magnitudes (upper and lower panel, respectively). 71
4.3 Distributions of the (SOFI - GeMS) magnitudes as a function of the SOFI color $(J-K_s)$. Stars at a distance larger than 30″ from the cluster center and with 2.8 < (SOFI K_s - GeMS K_s) < 3.6 and 2.6 < (SOFI J - GeMS J) < 3.6 respectively, are shown in figure. The solid lines instead represent the median values obtained by applying an iterative σ-clipping procedure. Finally we obtain (SOFI K_s - GeMS K_s) = 3.299 and (SOFI J - GeMS J) = 3.146. 72
4.4 NIR differential reddening-corrected CMD of Liller 1 obtained from the GEMINI observations discussed in the chapter. The main evolutionary sequences of the cluster are well visible down to the MS-TO point. On the blue side of the CMD, for $(J-K_s) < 1.5$, the blue plume defined by the Galactic field MS is also distinguishable. The photometric errors for each bin of K_s magnitudes are shown on the right side of the panel. 74
4.5 NIR CMDs of Liller 1 as obtained from the VVV data. In the *left panel* only stars external to the GEMINI FOV and located at distances smaller than r_t from $C_{\rm grav}$ are shown. In the *right panel* only stars located at $r_t < r < 500''$. 75

4.6 Luminosity function of the RC and the brightest portion of the RGB in Liller 1 (upper panel) and in the reference cluster NGC 6553 shifted by $\delta K = 1.9$ (lower panel). The two dashed vertical lines mark the location of the RC and the RGB bump. 76
4.7 Differential reddening-corrected $(K_s, J - K_s)$ CMD of Liller 1 with the best-fit `BaSTI` isochrone of 12 Gyr superimposed (orange line). Isochrones of 11 and 13 Gyrs are overplotted as red and yellow lines, respectively. They represent the 1 Gyr uncertainty on the absolute age estimate. 77
4.8 The NIR CMD of Liller 1 has been divided in three different components: *i)* the RGB of the cluster (black box); *ii)* the MS of the disk (blue box) and *iii)* the intermediate sequence (red box). 78
4.9 Cumulative radial distributions of the stars selected in the three boxes of Figure 4.8. The radial extension of the intermediate sequence (red line) seems to be compatible with the radial extension of the cluster itself (black line). 79
4.10 The radial distribution ($\alpha - \alpha_c$ vs $\delta - \delta_c$) of the stars in Liller 1 (back dots). The stars in the intermediate sequence are plotted in red. They are uniformly distributed, with a higher concentration around the cluster center. Blue dots instead represent field stars, which randomly populate the FOV. 79
4.11 Star density profile of Liller 1, obtained from resolved star counts in the combined data set. Empty circles represent the observed profile, while solid ones are obtained after subtraction of the Galactic field density (marked with the dotted line). The best-fit single-mass King model is shown as a solid line and the corresponding structural parameters are labeled in the figure. The lower panel shows the residuals between the observations and the fitted profile at each radial coordinate. 81
4.12 SB profiles of Liller 1 in the K_s and J bands (top and bottom panels, respectively), obtained from the 2MASS data set. Empty circles represent the observed profile, while solid ones are obtained after background subtraction (marked with a dotted line). In both panels, the solid line corresponds to the best-fit King model shown in Figure 4.11. 82

5.1 Two-color image of NGC 6624 obtained by combining GEMINI observations in the NIR J and K_s bands. North is up, east is on the left. The FOV is $93'' \times 93''$. 89
5.2 A zoom-in of a central region ($10'' \times 10''$) of the cluster as seen by ACS/HRC (F435W filter) on board HST (Dalessandro et al., 2014, *left*) and by GSAOI+GeMS in the K_s band (this work, *right*). The spatial resolution of GEMINI in the NIR turns out to be comparable to that of HST in the optical. 90

5.3 Photometric calibration plots for the GEMINI catalog of NGC 6624 in the K_s and J bands. Only bright stars (black points) have been used to determine the calibration zero points. The median values, estimated by using a $2\sigma-$rejection, are shown in the figure. 91
5.4 Plot of the sharpness as a function of the K_s magnitude. The black points are the stars lying within 6σ from the red line, which represents the 2σ-clipped median value in sharpness. This selection criterion is applied to all the detected stars in order to remove spurious objects and stars with large photometric errors. 93
5.5 $(K_s, J-K_s)$ and $(J, J-K_s)$ CMDs of NGC 6624 obtained from the GEMINI observations discussed in the section 5.2. All the main evolutionary sequences of the cluster are well visible, from the RGB, HB, MS-TO down to the MS-knee. These NIR diagrams turn out to be comparable to the HST optical ones, both in depth and in photometric accuracy. The photometric errors for each bin of K_s and J magnitudes are shown on the right side of the panels. 94
5.6 $(K_s, J-K_s)$ and $(J, J-K_s)$ CMDs of NGC 6624 CMDs with overplotted a set of `BaSTI` (Pietrinferni et al., 2004) isochrones with ages ranging from 10.5 Gyr up to 13.5 Gyr, in steps of 0.5 Gyr (see labels). 96
5.7 *Left panel:* zoomed MS-TO region of the $(K_s, J-K_s)$ CMD, with the selected set of `BaSTI` isochrones (with different ages) overplotted. *Right panel:* χ^2 parameter as a function of isochrone ages considered in the *Left Panel*. A well defined minimum identifies the best-fit isochrone (with t_{age} = 12.0 Gyr). 97
5.8 The same as in Figure 5.6 but for `DSED` isochrones (Dotter et al., 2007). . 97
5.9 The same as in Figure 5.7 but for `DSED` isochrones. 98
5.10 The same as in Figure 5.6 but for `VR` isochrones (VandenBerg et al., 2014). 98
5.11 The same as in Figure 5.7 but for `VR` isochrones. 99
5.12 Age estimates of NGC 6624 determined in previous studies, compared to that obtained in this work (red point). The acronyms shown in the figure are so defined: **MW06**[1] & **MW06**[2] (Meissner and Weiss, 2006), **SW02** (Salaris and Weiss, 2002), **Van13** (VandenBerg et al., 2013), **Roe14** (Roediger et al., 2014), **Dot10** (Dotter et al., 2010) and **Hea00** (Heasley et al., 2000). 101
5.13 Simulated (*left* panel) and observed (*right* panel) $(K_s, J-K_s)$ CMD of NGC 6624, for all the stars that survived the selection: -0.2 $\leq$ sharpness $\leq$ 0.2. As clearly visible, the two CMDs turn out to be fully comparable, especially in the MS region (at $K_s > 16$). The red line in the left panel represents the MRL of NGC 6624 in the $(K_s, J-K_s)$ CMD. 103
5.14 Photometric completeness (Γ) as a function of the K_s magnitude for the GEMINI catalog of NGC 6624 in three different radial bins (see labels). 104

5.15 NGC 6624 completeness-corrected and field-decontaminated MS-LFs in the K_s band obtained from the GEMINI catalog in three different radial bins. The LF corresponding to the innermost radial bin is used as reference to normalize those at larger radii at the brightest bin. . . . 105
5.16 MFs derived by using a BaSTI isochrone with [Fe/H] = -0.60 and t_{age} = 12.0 Gyr (see Section 4.1). Radial bins, symbols and colors are the same as in Figure 5.15. . . . 106
5.17 *Left panel*: K_s image of a region of (2.5″ × 2.5″) of NGC 6624, centered on the position of ComStar1, marked with a red circle, as observed by the GeMS/GSAOI system. *Right panel*: The same, but for the J band. . 108
5.18 *Left panel*: K_s image of a region of (2.5″ × 2.5″) of NGC 6624, centered on the position of StarB, marked with a blue circle, as observed by the GeMS/GSAOI system. This star has the same magnitude as ComStar1 and is adopted for a comparison. *Right panel*: The same, but in the J band. . . . 108
5.19 *Top panels*: Positions in the $(K_s, J - K_s)$ and $(J, J - K_s)$ CMDs of ComStar1 and StarB are highlighted with a red circle and a blue triangle, respectively. *Bottom panels*: The red circles represent the light curve of ComStar1 folded with the estimated orbital period $P_{orb} \approx 98$ min (Dalessandro et al., 2014). The black line is a sinusoidal function of amplitude ≈ 0.2. For comparison the blue triangles show the light curve of StarB, that has the same average K_s magnitude of ComStar1 but does not show any evidence of flux modulation (dashed black line). 109

6.1 Location of the MS-TO (black triangle), MS-knee (red circle) and MS-saddle (blue square) along a 12 Gyr old isochrone extracted from the family of VandenBerg et al. (2014). The MS-knee is here defined as the reddest point along the MS MRL. The MS-saddle is the point where the MS MRL changes shape, from convex to concave, and thus shows the minimum curvature. A dashed line tangential to the isochrone is shown at the MS-saddle point to better illustrate the morphological meaning of this point. . . . 115
6.2 Location of the MS-knee (red circle) and MS-saddle (blue square) marked along the same isochrone plotted in Figure 6.1, but here shown in CMDs with three different color baselines: from left to right, $(K_s, J - K_s)$, $(K_s, I - K_s)$, and $(K_s, V - K_s)$. The MS-knee only occurs in the pure NIR-CMD. The MS-saddle, instead, can be defined in all the considered diagrams. . . . 116

6.3 Location of the MS-TO (triangles), MS-knee (circles) and MS-saddle (squares) marked along 12 Gyr old isochrones from three different sets of theoretical models: BaSTI (red), DSED (purple) and VR (green) in the (K_s, $J - K_s$, *left panel*) and ($F110W$, $F110W - F160W$, *right panel*) filter combinations. The three models predict different locations of the MS-knee, while they agree on the color-magnitude position of the MS-saddle. This clearly illustrates that the two features are different. . 117

6.4 The same as in Figure 6.3 but in the ($L - T_{eff}$) plane. At the MS-knee level, the three models start to be different even in the theoretical plane, suggesting that not only bolometric corrections but also input physics for low-mass stars can be responsible of the mismatch among the models. 118

6.5 *Upper panel*– Dependence of the MS-saddle K_s-band magnitude on cluster age for the three different sets of adopted isochrones (BaSTI, DSED and VR in red, purple and green, respectively). Ages vary from 9.5 to 13.5 Gyr in steps of 0.5 Gyr. At fixed chemical composition, the MS-saddle K-band magnitude is independent of age and shows small difference in all the considered models. *Lower panel* – The same as in the upper panel, but for the MS-knee. In this case, different models predict significantly different values of the K-band magnitude of the MS-saddle. 119

6.6 *Left panel* – ($F110W$, $F110W - F160W$) CMD of 47 Tucanae from HST observations. *Right panel* – (K_s, $J - K_s$) CMD of NGC 6624 from deep observations acquired with a ground-based adaptive optics system. . . 121

6.7 Histograms of the MS-saddle K-band magnitude measured in the (K_s, $J - K_s$), (K_s, $I - K_s$), and (K_s, $V - K_s$) CMDs (upper, central and bottom rows, respectively), for NGC 6624. Multiple measures of this value have been obtained in each case because the MS MRL has been determined with different methods (see Section 6.3.1): Method 1 or static bins (left column, providing 41 MRLs and 41 measures of the MS-saddle magnitude), Method 2 or dynamic bins (central column, 9 measures) and Method 3 or Polynomial fit (right column, 11 measures). 124

6.8 Location of the MS-TO (black triangle) and MS-saddle (blue square) in the three CMDs available for NGC 6624. The horizontal black dashed line marks the MS-TO level, the horizontal dashed blue lines flag the two extreme values of the MS-saddle, which vary by 0.2 mag. 125

6.9 Predicted relation between age (in Gyr) and the parameter $\Delta_{\rm TO}^{\rm saddle}$ obtained from BaSTI, DSED and VR isochrones of varying metallicity (see also Table 6.2): the dashed lines are the theoretical relations computed at the metallicity of 47 Tucanae ([Fe/H] = -0.77, from Correnti et al. (2016) and references therein); the dark gray regions surrounding each dashed line mark the variation induced by changes of ± 0.1 dex in the adopted metallicity. The solid line and gray region in each panel mark the observed value and uncertainty of the $\Delta_{\rm TO}^{\rm saddle}$ parameter measured in the ($F110W$, $F110W - F160W$) CMD of 47 Tucanae. 128

6.10 The same as in Figure 6.8 but for NGC 6624. In this case the theoretical relations and the observed values have been determined in the three available CMDs (see labels): (K_s, $J - K_s$), (K_s, $I - K_s$), and (K_s, $V - K_s$). 129

List of Tables

3.1 Dataset properties. 44
3.2 Selected tip-tilt guide stars. 45
3.3 Coefficients of the third-order polynomial for each chip, representing the final GD solution for the K_s filter. 59
3.4 Coefficients of the third-order polynomial for each chip, representing the final GD solution for the J filter. 60

4.1 New parameters for Liller 1. 83

5.1 MRL of NGC 6624 in the $(K_s, J - K_s)$ CMD. 102

6.1 MS-TO and MS-saddle magnitudes, and their difference Δ_{TO}^{saddle} in the $F110W$ (for 47 Tucanae) and in the K_s band (for NGC 6624). The listed values are the average of the 41 measures determined by adopting the *static bin* and the *geometric* approaches (see Sect. 3.1). 125
6.2 Analytic relations between age (t, in Gyr), Δ_{TO}^{saddle} and metallicity derived from the three adopted families of stellar models and the color combinations available in our observational datasets of 47 Tucanae and NGC 6624. 127
6.3 Absolute ages of 47 Tucanae and NGC 6624 estimated from the measured values of Δ_{TO}^{saddle} and for the three adopted families of stellar models (BsSTI, DSED, VR; see text). 128

List of abbreviations

ACS	Advanced Camera for Surveys
AGB	Asinthotic Giant Branch
AO	Adaptive Optics
BSS	Blue Straggler Star
BW	Baade's Window
CMD	Color Magnitude Diagram
CV	Cataclismic Variable
DM	Deformable Mirror
EE	Encircled Energy
ELT	Extremely Large Telescope
ESO	European Southern Observatory
FOV	Field Of View
FWHM	Full With at Half Maximum
GC	Globular Cluster
GD	Geometric Distortions
GeMS	Gemini Multi-conjugate adaptive optics System
GSAOI	Gemini South Adaptive Optics Imager
HB	Horizontal Branch
HST	Hubble Space Telescope
IMF	Initial Mass Function
JWST	James Webb Space Telescope
LF	Luminosity Function
LGS	Laser Guide Star
LMXB	Low-Mass X-ray Binary
LTAO	Laser Tomography Adaptive Optics
MAD	Multi-Conjugate Adaptive Optics Demonstrator
MCAO	Multi-Conjugate Adaptive Optics
MF	Mass Function
MRL	Mean Ridge Line
MS	Main Sequence
MSP	Millisecond Pulsar
NIR	Near-Infrared
NGS	Natural Guide Star
NTT	New Technology Telescope
PSF	Point Spread Function
RC	Red Clump
RGB	Red Giant Branch
RTC	Real Time Computer
SB	Surface Brightness

SCAO	Single Conjugate Adaptive Optics
SGB	Sub-Giant Branch
SNe	Supernovae
SNIa	Type Ia Supernovae
SR	Strehl Ratio
SSP	Simple Stellar Population
TO	Turn - Off
VLT	Very Large Telescope
VVV	Vista Variable in the Via lactea
WFC	Wide Field Camera
WFS	Wavefront Sensor
2MASS	Two Micron All Sky Survey

Thesis outline

Thanks to the exceptional capabilities of the near-infrared (NIR) high resolution Gemini South Adaptive Optics Imager (GSAOI), in tandem with the Gemini Multi-conjugate Adaptive Optics system (GeMS) on the 8.1 m Gemini South Telescope, we started an observational campaign of a sample of globular clusters (GC) orbiting the Galactic bulge (Liller 1, NGC 6624, Terzan 6, NGC 6440 and NGC 6569; Proposal ID: 091.D-0562; PI: D. Geisler) with the aim of understanding their properties in terms of stellar population content, age and structure. These objects are all metal-rich ([Fe/H]>-0.6), and relatively massive ($M_v > -7$). Some of these targets have been investigated by very shallow and low-resolution observations reaching only a couple of magnitudes below the cluster red clump (Davidge, 2000; Ortolani et al., 2001, 2007; Valenti et al., 2007, 2010).
This thesis is mainly focused on the results obtained for Liller 1 and NGC 6624, which represent two ideal test cases. A high obscured cluster (Liller 1) and a very well-studied one (NGC 6624) in order to test the global GeMS+GSAOI performance.

The Thesis outline is presented in the following:

- In Chapter 1 a general overview of our current understanding of the Galactic bulge in terms of morphology, age, metal content and kinematics is provided along with a description of the bulge GC system.

- In Chapter 2 a description of the state-of-the-art of Adaptive Optics (AO) systems is presented, and their importance for bulge GC observations is highlighted.

- In Chapter 3 we focus on the analysis of the GeMS+GSAOI performance, from a photometric and astrometric (e.g. geometric distortions) point of view, based on the data acquired for Liller 1 and NGC 6624 (Dalessandro et al., 2016).

- A detailed description of the highly obscured cluster Liller 1 is presented in Chapter 4. We sample for the first time the main-sequence turn-off (MS-TO) of the cluster and we discuss its main structural properties (Saracino et al., 2015).

- Chapter 5 is focused on NGC 6624. We present the deepest and highest-precision color-magnitude diagram (CMD) from the ground obtained so far for this system, we estimate its age via the isochrone fitting technique and we finally

analyze its luminosity and mass functions down to masses of about 0.4 $M_{\odot}$ (Saracino et al., 2016).

- In Chapter 6 we discuss the reliability and accuracy of different age estimate indicators in NIR CMDs. For this application we make use of the highest-quality ground-based and HST CMDs available at the moment (Saracino et al., 2017 submitted).
- Finally we draw our conclusions with particular attention to the future perspectives of this work in the context of the systematic study of the Galactic bulge.

CHAPTER 1

The Galactic Bulge and its globular cluster system

1.1 Introduction

The Milky Way is the only galaxy where we can resolve and accurately measure individual stars at all evolutionary phases from the very center to the outskirts. Over the years, ever-growing details about the physical, chemical and kinematic properties of its stellar populations have been provided, taking advantage of the new observational facilities both from the ground and the space and state-of-the-art theoretical models. In recent years, Gaia and the ongoing (e.g. VVV, PTF, OGLE, WISE, UKIDS) ground-based surveys, complemented with massive spectroscopic campaigns (e.g. Gaia-ESO (European Southern Observatory), GALAH, APOGEE, WEAVE[1]) are providing comprehensive spectro-photometric and astrometric information, proper motions and radial velocities, metallicities and detailed chemical abundances for huge samples of Galactic stars in the Milky Way halo, disk and bulge. This information, together will provide a detailed description of the Milky Way structure and formation processes.

However, not all the regions of our Galaxy are known with the same degree of accuracy. In particular the very central regions, where the inner bulge and disk are located, are still poorly explored, mostly because of the huge extinction along that line of sight. There, observations are mostly possible only at infrared (IR) and longer wavelengths.

[1] *VVV* - Vista Variables in the Via Lactea; *PTF* - Palomar Transient Factory; *OGLE* - Optical Gravitational Lensing Experiment; *WISE* - Wide-field Infrared Survey Explorer; *UKIDSS* - UKIRT Infrared Deep Sky Survey; *GALAH* - Galactic Archeology with Hermes; *APOGEE* - APO Galactic Evolution Experiment; *WEAVE* - William Herschel Telescope Enhanced Area Velocity Explorer

1.2 Interstellar extinction

The presence of thick and patchy clouds of dust in the Galactic plane hampered deep and accurate observations of the stellar populations towards the Galaxy center for many years.
First wide-field maps of the interstellar extinction have been published by Burstein and Heiles (1982), then superseded by the Schlegel maps (Schlegel et al., 1998). Based on IRAS and DIRBE experiments, the latter were unfortunately unreliable for regions within $|b| = 6°$. Schultheis et al. (1999) provided a high resolution (2′) map of the inner regions of the Galactic bulge ($|b| \leq 2°$) by using red giant branch (RGB) stars from the NIR photometric survey DENIS while Marshall et al. (2006) provided a full three-dimensional (3D) extinction map of the bulge comparing the Two Micron All Sky Survey (2MASS; Cutri et al. 2003) photometry to the Besançon model. The first high resolution and homogeneous extinction map covering all the inner Galactic regions have been produced by Gonzalez et al. (2012) using an ideal dataset from the Vista Variables in the Via Lactea (VVV) survey[2]. Red Clump (RC) stars were used as standard candles to measure the shift in color and magnitude as a function of direction. The extinction maps by Gonzalez et al. (2012) are presented in Figure 1.1. The *upper panel* shows the entire region covered by the VVV survey while the *lower panel* the inner $\sim 4°$ region around the Galactic plane. These maps clearly demonstrate that the most extinct regions of the Galactic bulge, where A_{K_s} >3.5 mag (E(B-V)>10 mag), are located very close to the Galactic plane ($-1° \leq b \leq 1°$). These results have been further confirmed by Schultheis et al. (2014), with data coming from the NIR spectroscopic survey APOGEE.

1.3 The Galactic bulge - a global view

The Galactic bulge is the Milky Way region located within a radius of about 3 kpc from the Galactic center. This region is one of the most inaccessible of our Galaxy because of the huge extinction. Only the outer bulge at negative latitudes $b < -4°$ has a moderate obscuration (E(B-V)<0.5 mag).
The Galactic bulge contains about 1/5 of the total stellar mass of the Milky Way and about ten times the mass of the halo. Recent studies suggest for the bulge a mass ranging from $6 \times 10^9 M_\odot$ (Robin et al., 2012) to $2 \times 10^{10} M_\odot$ (Valenti et al., 2016, see also Portail et al., 2017).
Because of its relatively low and uniform extinction, the first and most studied region of the Galactic bulge has been the Baade's Window (BW, e.g. Baade, 1951; Arp, 1965; Blanco et al., 1984), located at $l, b = 0.9°, -3.9°$ and centered on the metal-poor GC NGC 6522. Indeed, the first chemical abundances of bulge stars and first age estimates have been obtained in this region. Based on these results it has been shown that the bulk population of the bulge is old and has a metallicity peaked around solar

[2]The VVV is an ESO public NIR variability survey of the Milky Way bulge covering ∼109 point sources within an area of 520 squared degrees. Minniti et al., 2010; Catelan et al., 2011

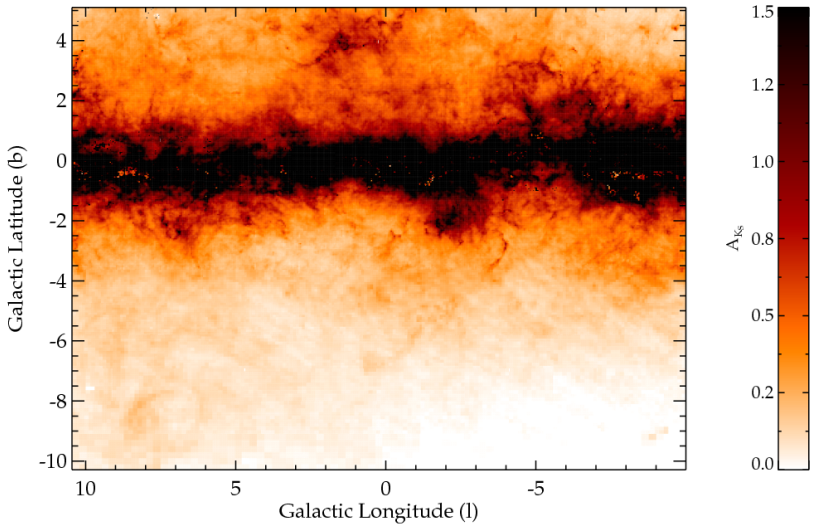

(a)

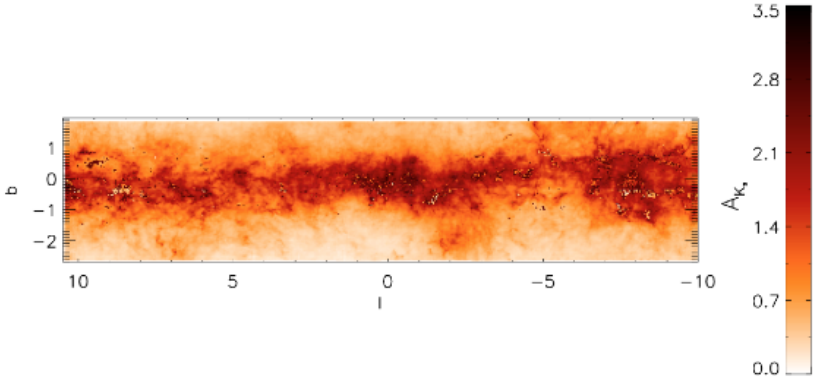

(b)

Figure 1.1: (a): Extinction map of the Galactic bulge for the entire region covered by the VVV survey. A_{K_s} values are computed from Cardelli et al. (1989) and values higher than 1.5 mag are saturated in the color scale shown in the right side. **(b):** Extinction map for the inner $\sim 4^\circ$ region around the Galactic plane. In this plot the color scale reaches 3.5 mag to take account for highly obscured regions very close to the Galactic center.

with [α/Fe] enhancement (e.g. Rich, 1988, 1990; McWilliam and Rich, 1994; Rich and Origlia, 2005; Fulbright et al., 2006, 2007; Alves-Brito et al., 2010; Hill et al., 2011). The first estimate of the bulge age with HST has been obtained for the two GCs in the BW (NGC 6553 and NGC 6528), and first proper motions of bulge stars with HST have been also measured there and in the nearby Sagittarius I field (Kuijken and Rich, 2002; Clarkson et al., 2008; Clarkson et al., 2011), providing evidence of old ages and rotation.

1.3.1 Morphology & Structure

The first insights into the Galactic bulge morphology come from the Cosmic Background Experiment (COBE) and Diffuse Infrared Background Experiment (DIRBE) (Boggess, 1992; Hauser et al., 1998; Smith et al., 2004). These experiments provided first evidences of a global boxy/peanut structure for the Milky Way bulge (e.g. Weiland et al., 1994). This finding has been interpreted as a signature of an edge-on bar with the near side in the first quadrant and the major axis at an angle $\theta = 20^\circ \pm 10^\circ$ (Dwek et al., 1995) with respect the Sun-Galactic center line of sight.
More recent analysis focused on the bulge morphology have been based on RC stars density and distribution. The absolute magnitudes of these stars seem to have a small dependence on age and metallicity, so they represent a powerful tool for deriving distances towards the bulge (i.e. Salaris and Girardi (2002)). The presence of a split in magnitude between RC stars located in different fields along the projected minor axis ($l = 0^\circ$), at latitudes $|b| > 5^\circ$ was discovered by Zoccali (2010) and McWilliam and Zoccali (2010) and further confirmed by Nataf et al. (2010) using the OGLE-II photometry. McWilliam and Zoccali (2010) interpreted the evidence for the bright and faint RC as a consequence of having two over-densities of stars located at different distances, i.e. the two southern arms of an X-shaped structure both crossing the line of sights.
Subsequent studies (e.g. Saito et al., 2011; Robin et al., 2012; Ness and Freeman, 2012; Vásquez et al., 2013, and references therein) confirmed this finding and recently Wegg and Gerhard (2013) provided a comprehensive modeling of the distribution of RC stars observed in the VVV survey (see Figure 1.2).
The bulge main bar turns out to have a 3.1-3.5 kpc diameter, an axial ratio of 1:0.4:0.3 and an inclination angle of about 27° with respect to the Sun-Galactic center line of sight. A sketch of the main bar structure as it would appear if the Galaxy would be seen face-on is shown in Figure 1.3.

The possible presence of an inner (nuclear) bar has been also suggested (e.g. Rodriguez-Fernandez and Combes, 2008) in order to explain the evidence of a clear change in the orientation of the main bar in the central regions, observed as a tilt in the RC distribution slope at small latitudes (see Gonzalez et al., 2011 and references therein). This possibility has been largely excluded in recent studies (Martinez-Valpuesta and Gerhard, 2011 and Valenti et al. (2016)) where the tilt in the RC distribution slope has been interpreted as an effect of the higher star formation density in the very central regions, with respect to the external ones.
An additional longer bar has been extensively debated in the literature (e.g. Garzón and López-Corredoira, 2014 and references therein). Model observations of barred galaxies strongly argue that the apparent long bar is only an artifact due to the interaction of the outer part of the main bar with the adjacent spiral arm near the plane. This interaction finally produces leading ends that apparently move with a larger position angle (45°, Romero-Gómez et al., 2011; Athanassoula, 2012; Webb and Vesperini, 2016). Wegg et al. (2015) instead provided a global view of the Milky Way bulge and

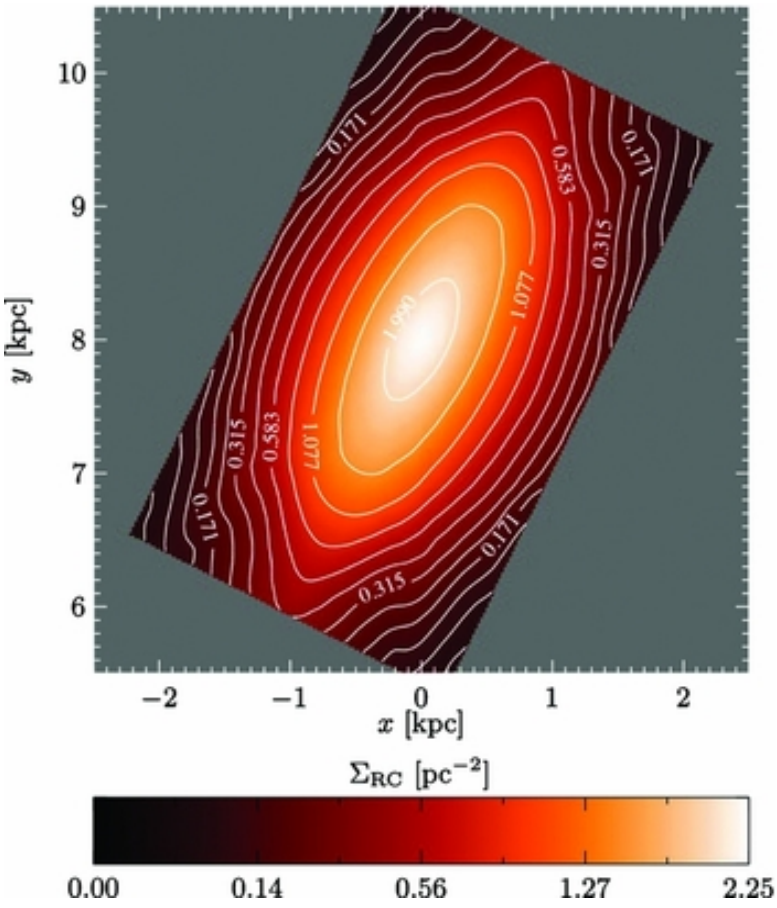

Figure 1.2: The Galactic bar and the boxy/peanut shape as seen from the North Galactic Pole. Figure from Wegg and Gerhard (2013), reproduced by Zoccali and Valenti (2016).

long bar by using RC stars as distance and density tracers. They found an orientation angle for the long bar quite consistent with that of the triaxial bulge, concluding that they cannot be considered two different structures.

Another interesting debate is related to the possible presence of an old, metal-poor spheroidal component in the Milky Way bulge. In this respect, RR-Lyrae stars are powerful tracers of such a possible stellar population. Recent studies performed by Dékány et al. (2013) have shown that bulge RR-Lyrae stars follow a remarkably different spatial distribution (more spheroidal and centrally concentrated) compared to RC stars. Figure 1.4 shows a comparison of the projected mean distances obtained from RR-Lyrae stars *(upper panel)* and those from the mean magnitude distribution of RC stars (*lower panel)*.

Pietrukowicz et al. (2015) instead found a slightly different result by analyzing the RR-Lyrae stars detected by the OGLE survey towards the Galactic bulge. Their spatial distribution in fact has an ellipsoidal shape with a major axis located in the Galactic plane and an inclination angle of $20^\circ \pm 3^\circ$ to the Sun-Galactic center line of sight.

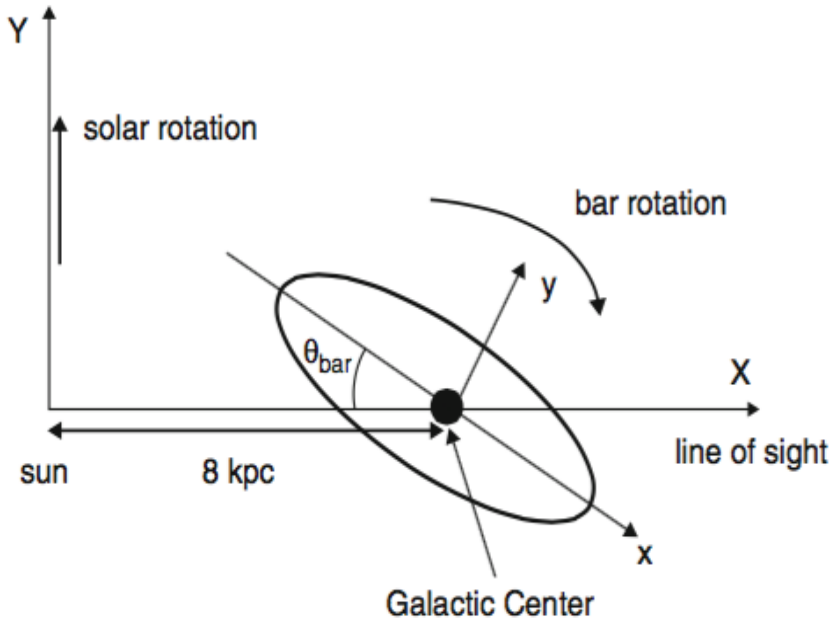

Figure 1.3: Shape and orientation of the main bar as it appears if the Galaxy is seen face-on. The near side of the bar is at positive Galactic longitude. The clockwise rotation of the bar is also marked (Figure from Rich (2013)).

1.3.2 Age

A key ingredient to reconstruct the Galactic bulge formation and evolution history is the age distribution of its stellar populations. Unfortunately, age derivations of the Galactic bulge have been strongly limited by the severe dust extinction and strong field contamination by disk stars.

Holtzman et al. (1993) reported the first Hubble Space Telescope (HST) photometry of the bulge towards the BW, going several magnitudes fainter than previous ground-based photometric studies. However, the effect of differential reddening and the uncertainties related to the distance did not allow the derivation of an absolute age estimate. An important breakthrough was made by Ortolani et al. (1995), who adopted a differential method, based on the position of RC stars in the luminosity function. Thanks to the very small dependence of the RC on age and metallicity, the authors were able to match its position in the luminosity function to that of the reference old GC NGC 6528, finding a remarkable agreement between the relative positions of their MS-TOs. Their result represent the first, robust evidence that the Milky Way bulge stellar population is predominantly old. A confirmation also came from Feltzing and Gilmore (2000) and Kuijken and Rich (2002), who were able to discriminate between bulge stars and foreground disk stars using proper motion studies. Subsequent observations of field decontaminated bulge samples confirmed old ages for the bulge stellar populations (e.g. Zoccali et al., 2003; Clarkson et al.,

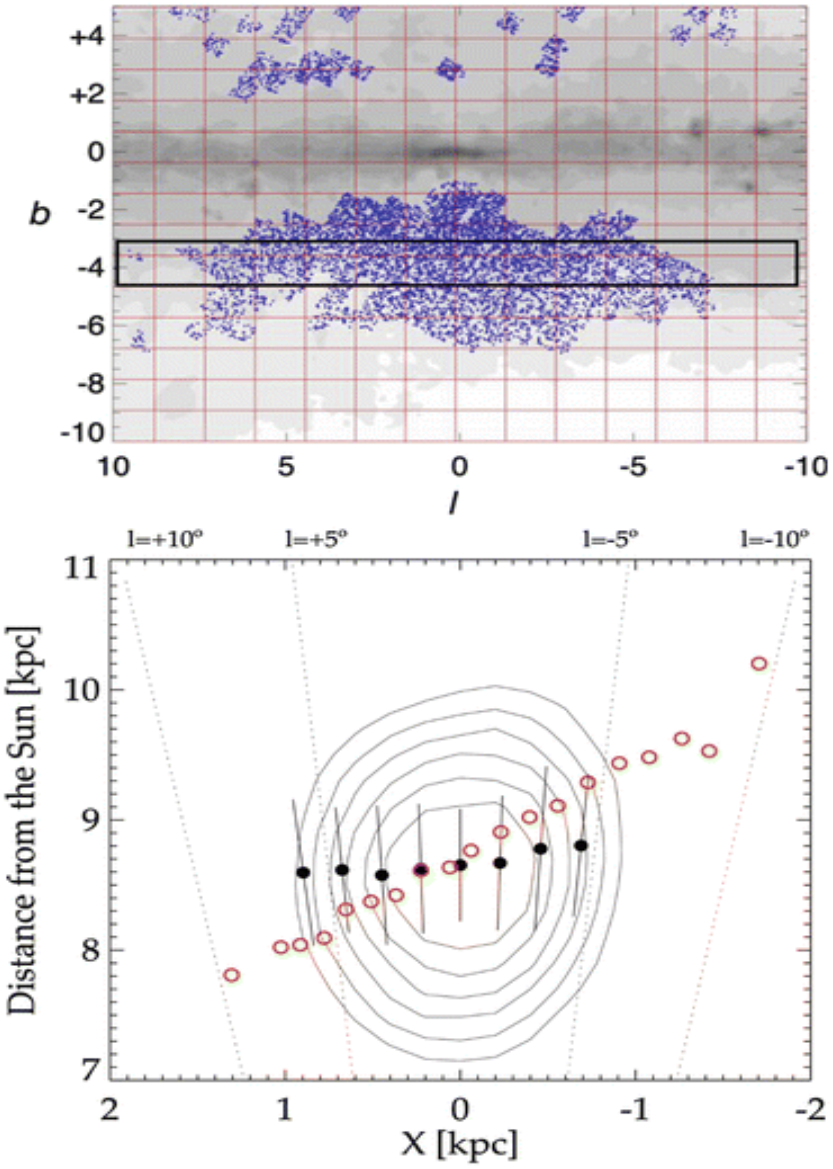

Figure 1.4: *Upper panel:* Spatial distribution of RR Lyrae stars in the Galactic bulge area of the VVV survey, from Dékány et al. (2013). The black rectangle is the region for which the mean distance of RR Lyrae and RC stars are compared in the lower panel. *Lower panel:* The projected mean distances of RR Lyrae is shown in black filled circles, while for RC stars as red open circles. The different trend is evident and the spheroidal structure is highlighted through iso-density contours for the projected distance distribution of the RR Lyrae sample.

2011; Valenti et al., 2013).

Although the bulk of the bulge is old, some pieces of evidence have been found supporting the presence of some younger stellar populations. Clarkson et al. (2011) posed an upper limit of about 3.5% to the fraction of bulge stars possibly younger than 5 Gyr, while Bensby et al. (2013), Bensby (2015), and Bensby et al. (2017) found a significant fraction of relatively young stars (at [Fe/H] $>$ 0 more than 35% are

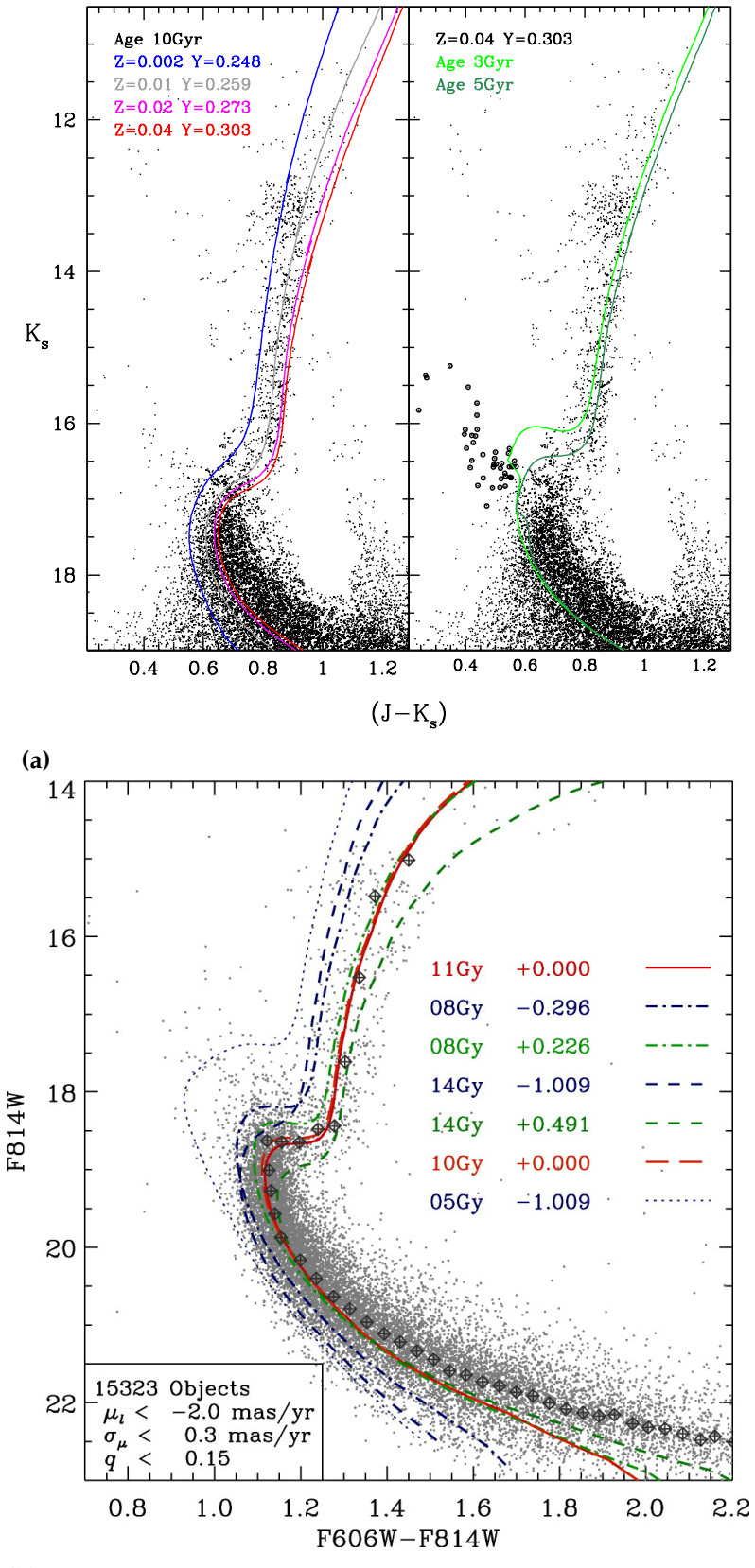

Figure 1.5: (a): Statistical disk decontamination of a field at the edge of the bar, from Valenti et al. (2013). **(b):** Proper-motion disk decontamination of a bulge inner region, from Clarkson et al. (2008).

younger than 8 Gyr), based on microlensing events of dwarfs. The age distribution of these stars is presented in Figure 1.6. In this regards, a recent study of Haywood et al. (2016) points out that a stellar population predominantly old (11 Gyr or older) and a metallicity distribution compatible with that of Baade's Window should present a spread in the TO color that is significantly wider than that observed, thus opening the case of a younger bulge. Systematic, multi-epoch observations of the MS-TO region in different bulge fields are definitely needed to derive accurate ages for their stellar populations and better constrain the overall fraction of younger stars.

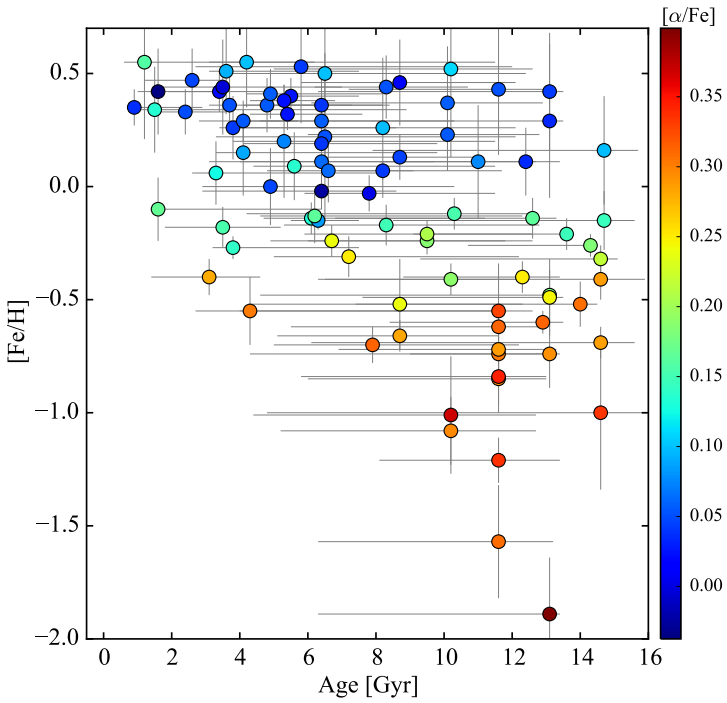

Figure 1.6: The metallicity of the microlensed dwarfs of the bulge as a function of their ages, from Bensby et al. (2017). The information about $[\alpha/\mathrm{Fe}]$ is presented as a color code at the right side of the plot.

1.3.3 Chemical composition

With the advent of the new millennium, the Galactic bulge has been spectroscopically surveyed in a systematic way by using high and low resolution spectrographs both in optical and IR bands. For instance, high resolution echelle spectroscopy provided detailed chemical abundances for a few hundreds bulge giants. In particular, optical spectroscopy allowed the measurements of stars in the BW and some other outer bulge fields, while IR spectroscopy allowed to get chemical abundances and radial velocities of stars in the inner few hundreds pc and in a number of heavily reddened GCs. On the other hand, efficient multi-object spectrographs working at low-medium resolution allowed to perform more massive surveys of the bulge stellar populations, and to obtain radial velocities and some chemical abundances for thousands stars.

Most of the surveys made use of optical spectroscopy and sampled outer bulge fields mostly at negative latitudes, while the few IR surveys allowed to sample a number of fields much closer to the Galactic plane.

Metallicity distribution

Spectroscopic surveys of the BW and some outer bulge fields at negative latitudes between b=-4° and b=-12° (e.g. Lecureur et al., 2007; Zoccali et al., 2008; Gonzalez et al., 2011; Ness et al., 2013a; Johnson et al., 2014, and references therein) found broad metallicity distributions (see Figure 1.7), with [Fe/H] values ranging from -1 to 0.4 with a broad peak around solar. Some works found this metallicity distribution to be multi-modal, with a significance consisting of 100 stars per field or more (Hill et al., 2011; Ness et al., 2013a; Rojas-Arriagada et al., 2014; Gonzalez et al., 2015), with two main components peaking at sub-solar ([Fe/H] $\sim$ -0.3 dex) and super-solar ([Fe/H] $\sim$ +0.3 dex) metallicity. These surveys also revealed the presence of negative, vertical gradients, likely due to the changing contribution of different populations, with the most metal-rich stars being located closer to the plane (see Ness et al., 2016). Gonzalez et al. (2013) constructed a photometric metallicity map based on the 2MASS and VVV surveys for almost the entire bulge region where the metallicity gradient is quite evident. It is shown in Figure 1.8,
Such gradient may flatten in the innermost hundreds pc (Ramírez et al., 2000; Rich et al., 2012).

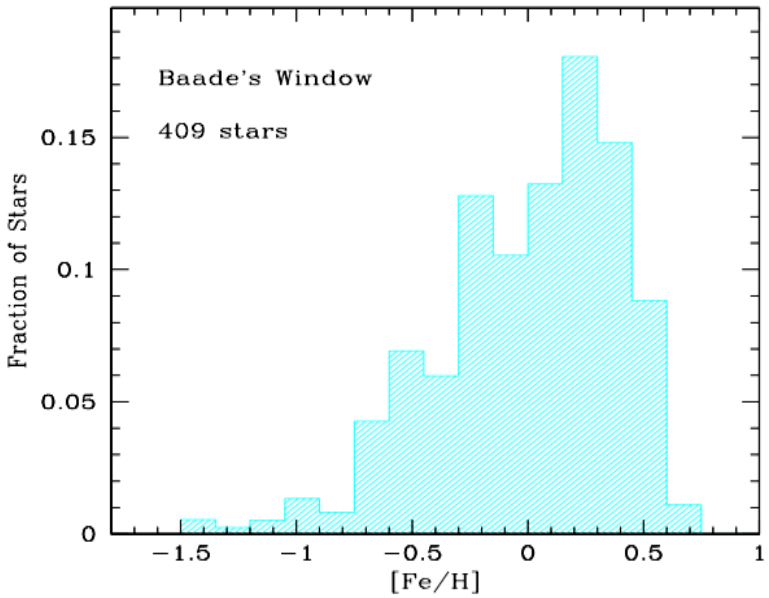

Figure 1.7: Metallicity distribution of RGB and RC stars in the bulge from Zoccali et al. (2008) and Lecureur et al. (2007) from high resolution spectra. Figure from Minniti and Zoccali (2008).

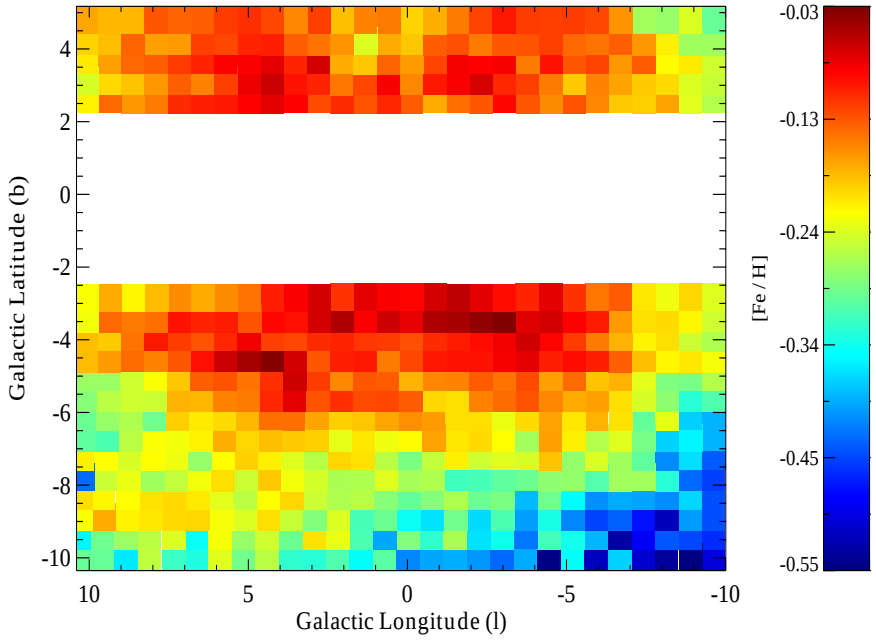

Figure 1.8: Map of the mean values of the metallicity distribution for the Galactic bulge covered by the VVV survey using the Cardelli et al. (1989) extinction law, from Gonzalez et al. (2013).

The α-elements abundance

The α-elements abundance of bulge stars with [Fe/H]<-0.3 have been found to be enhanced with respect to iron by [α/Fe]$\sim$+0.3 dex, while more metal-rich stars at [Fe/H]>-0.3 show a lower [α/Fe], reaching solar-scaled values for super-solar metallicities. In Figure 1.9 this behavior is presented in terms of two different α-elements ([O/Fe] and [Mg/Fe]) vs [Fe/H] as observed by Lecureur et al. (2007) and Zoccali et al. (2008). Similar plots have been obtained in subsequent surveys (e.g. Rich et al., 2012; Johnson et al., 2014; Schultheis et al., 2017).

All the surveys generally agree that bulge stars with [Fe/H]<0 dex are α-enhanced and probably formed from a gas mainly enriched by core collapse supernovae (SNe) on very short timescales and with a quite high star formation rate, while stars with super-solar metallicity and less α-enhanced probably formed from a gas further polluted by supernovae Ia (SNIa). However, some differences in trends (e.g. slopes, position of the knee at which the [α/Fe] abundance ratio start to decrease etc.) and spreads among different surveys are present and still need to be fully understood. Some similarities but also some differences have been found in the [α/Fe] distribution of bulge and thin/thick disk stars. Indeed disk can well fit the lower envelope of the bulge distribution (e.g. Di Matteo, 2016), but a significant fraction of bulge stars have [α/Fe] in excess of disk values.

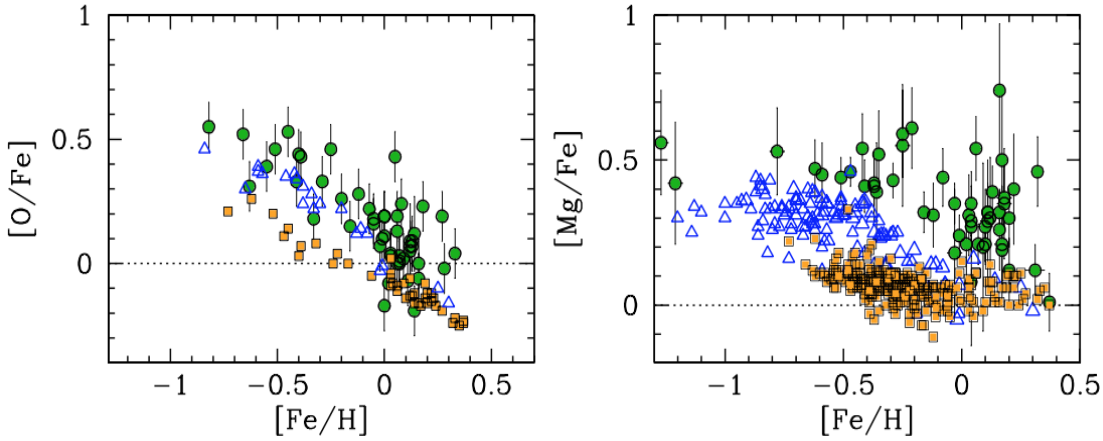

Figure 1.9: Oxygen and magnesium over iron ratios as measured from high dispersion spectra of bulge K giants (Zoccali et al., 2008; Lecureur et al., 2007). Green circles with error bars are bulge stars, compared with thick (blue triangles) and thin (orange squares) disk stars. Figure from Minniti and Zoccali (2008).

1.3.4 Kinematics

The first efforts to characterize the kinematics of bulge stars have been made in the 90's by measuring radial velocities of bulge K giant stars (Frogel and Whitford, 1987; Rich, 1988, 1990; Terndrup et al., 1995; Minniti, 1996; Sadler et al., 1996; Tiede and Terndrup, 1997). Several authors found that the bulge is rotating with a peak rotation of about 75 km/s and it has a large velocity dispersion that decreases with Galactocentric distance. In particular the bulge kinematics appears to be intermediate between a purely rotating system (as the Galactic disk) and a hotter system supported by velocity dispersion (as the Galactic halo). This is quite evident in the updated version of the so-called V_{max}/σ Binney (1978) diagram, adapted from Minniti (1996) and Kormendy and Kennicutt (2004) where the Galactic bulge has $V_{max}/\sigma = 0.65$ (Minniti and Zoccali, 2008) (see Figure 1.10).

A broad view of the bulge kinematics has been recently obtained thanks to dedicated spectroscopic surveys like BRAVA (Bulge Radial Velocity Assay), ARGOS, GIBS and APOGEE. BRAVA measured radial velocities for 4500 M giants located between $-10^\circ < l < 10^\circ$ and $-8^\circ < b < -4^\circ$, finding that the bulge follows a cylindrical rotation (see Figure 1.11, see also Howard et al., 2008, 2009; Kunder et al., 2012). This is a characteristic feature of boxy/peanut bulges originating from secularly evolved bars. Based on these results and using N-body simulations, Shen et al. (2010) demonstrated that the fraction of the bulge component in a non-barred configuration should be smaller than the 8%.

These findings have been later confirmed by ARGOS and APOGEE (Freeman et al., 2013; Ness et al., 2013a, 2016) and GIBS (Zoccali et al., 2014), as reported in figures 1.12 and 1.13, respectively. In some cases, by using both radial velocities and proper

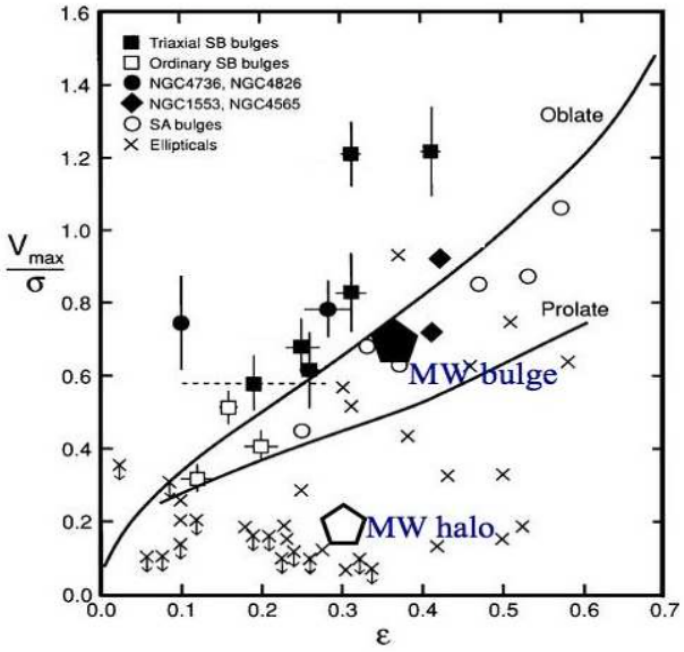

Figure 1.10: Milky Way bulge and halo position in the Binney (1978) diagram adapted from Minniti (1996) and Kormendy and Kennicutt (2004). Figure from (Minniti and Zoccali, 2008).

motions it has been possible to derive the so-called velocity ellipsoid (3D information), thus to built the orbits of different stars. This approach demonstrated that the high metallicity stars ([Fe/H]>-0.25) have a larger vertex deviations of the velocity ellipsoid than their metal-poor ([Fe/H]<-0.25) counterpart (e.g. Babusiaux et al., 2010). The authors also associated the more metal-rich stars to a barred population (moving closer to the galactic plane) while the metal-poor ones to a spheroidal component. This interpretation is well in agreement with recent results by Ness et al. (2013b) and Vásquez et al. (2013), who have shown that metal-rich stars trace the split RC in the luminosity function due to the boxy/peanuts shape, while the metal-poor ones do not share the same split in magnitude.

All these evidences suggest that the Galactic bulge stellar populations are quite complex in terms of structure, age, kinematics and metal content. Also for the overall bulge formation and evolution different scenarios have been proposed and still debated in the literature. [1.] *Merger-driven bulge scenarios* suggested that the bulge formed violently and quickly from the merger of clumps due to the fragmentation of a gaseous proto-disk in the early phases of the evolution of the Galaxy (e.g. Abadi et al., 2003; Immeli et al., 2004; Carollo et al., 2007; Elmegreen, 1999; Elmegreen et al., 2008; Elmegreen, 2009). [2.] *Secular evolution scenario* suggested that dynamical instabilities of the disk form the bar, which undergoes vertical buckling. The bar buckling is then responsible for the boxy/peanut/X shape (Combes and Sanders, 1981; Raha et al., 1991; Norman et al., 1996; Athanassoula, 2005; Shen et al., 2010; Saha et al., 2012). Recent works suggest to consider again the possibility that the Galactic stellar disc

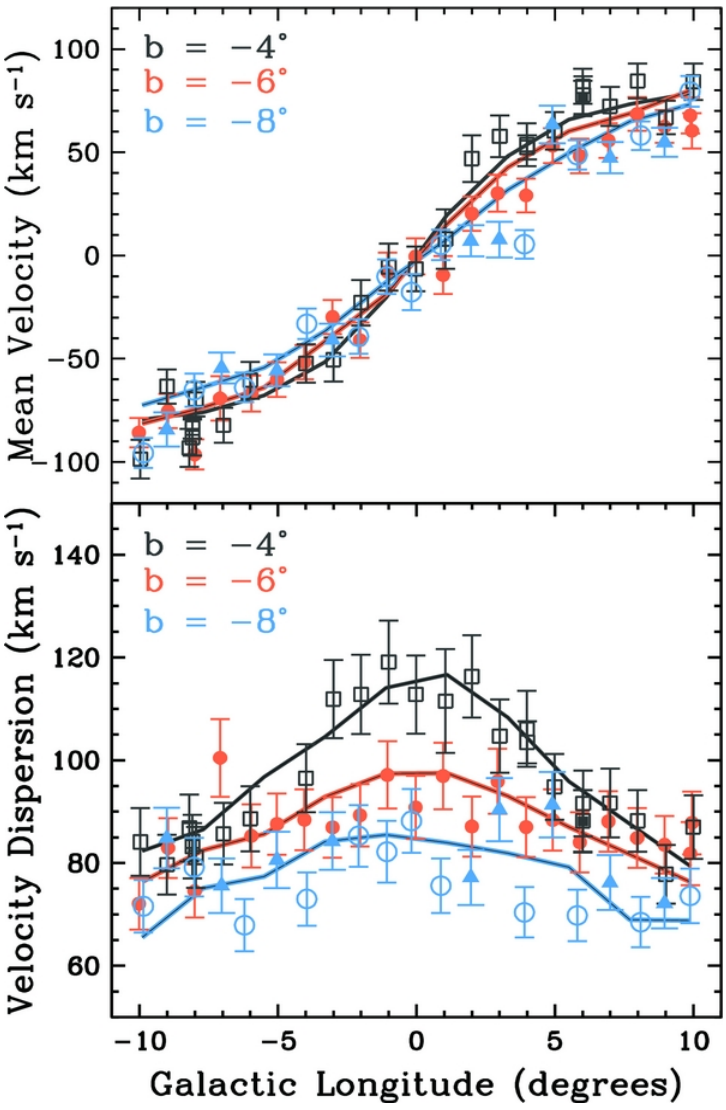

Figure 1.11: Radial velocity *(upper panel)* and velocity dispersion *(lower panel)* vs. Galactic longitude trends for the bulge fields studied in the BRAVA survey. Different colors indicate different Galactic latitudes. The typical features of cylindrical rotation are evident in both cases. Figure from Kunder et al. (2012).

may be one of the main contributors to the formation of the bulge (Fragkoudi et al., 2018; Di Matteo, 2016).

The current and near-future photometric (VVV, Gaia, JWST, LSST etc.) and spectroscopic (APOGEE, MOONS, 4MOST[3] etc.) surveys will soon provide complete samples of bulge stars for which distances, ages, 3D velocities and chemical abundances will be simultaneously available. These information coupled with state-of-the art chemo-dynamical evolutionary models should provide the necessary framework to better unveil the complexity of the bulge formation and evolution history.

[3] *LSST* - Large Synoptic Survey Telescope; *MOONS* - Multi-Object Optical and Near-infrared Spectrograph; *4MOST* - 4-meter Multi-Object Spectroscopic Telescope

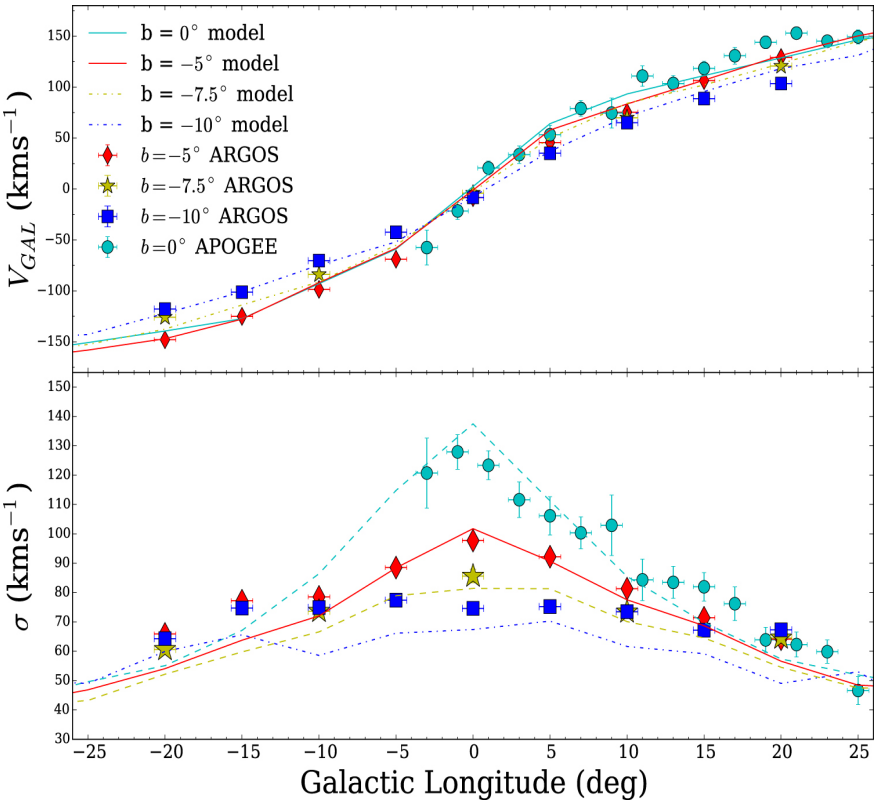

Figure 1.12: Rotation *(left panel)* and dispersion *(right panel)* profiles as a function of Galactic latitude from the study of Ness and Freeman (2012) with ARGOS and of Ness et al. (2016) with APOGEE. The results are similar to BRAVA but span twice the range in latitude.

1.4 The Bulge GC system

The Galactic bulge has its own system of GCs. GCs are among the oldest stellar systems in the Universe, they can be found in all the old components of the Galaxy (bulge, disk and halo) and are fundamental tracers of the early phases of the Galaxy formation and evolution.

The recent compilation by Bica et al. (2016) counts 43 GCs, likely bulge members according to a selection criterion based on both metallicity and distance from the Galactic center. In particular, the authors included GCs located within a distance of 5 kpc from the Galactic center and a metallicity higher than [Fe/H]>-1.5. The projected angular distribution of the selected bulge GCs is presented in Figure 1.14.

Figure 1.14 clearly shows that the very central region of the bulge, approximately $-1^\circ \leq b \leq 1^\circ$, is poorly populated by GCs but this is likely an observational bias. In fact, as already discussed in Section 1.2, the huge dust extinction towards the inner kpc of the Galaxy severely hampers the search and identification of candidate star clusters. The main properties of the bulge GC system can be summarized as follows: *i):* they are old (t ≈ 10-12 Gyr, Buonanno et al., 1998; Rosenberg et al., 1999; Stetson et al., 1999; De Angeli et al., 2005; Marín-Franch et al., 2009; VandenBerg et al., 2013);

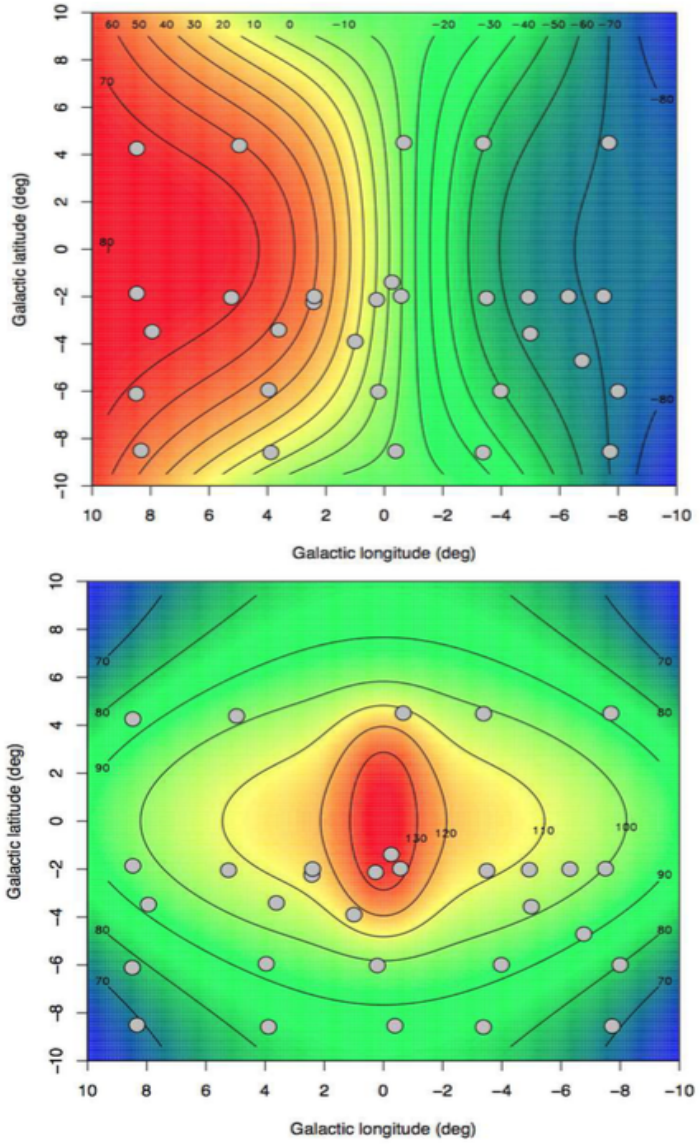

Figure 1.13: Radial velocity *(upper panel)* and radial velocity dispersion *(lower panel)* surface in the longitude-latitude plane constructed from the measured rotation profiles at negative latitudes from the GIBS survey by Zoccali et al. (2014).

ii): they show a metallicity distribution peaked at [Fe/H]=-1 and *iii):* they have [α/Fe] vs [Fe/H] values quite similar to those of bulge field stars (Bica et al., 2016, see Figure 1.15). Kinematics information are still quite sparse. Radial velocity and proper motion studies are only available for a few clusters (Zoccali et al., 2001, 2003; Dinescu et al., 1997, 1999b,a, 2003; Casetti-Dinescu et al., 2007, 2010, 2013), thus space velocities and orbits are very difficult to be extrapolated. Rossi et al. (2015, 2016) suggest that all GCs located in the inner bulge, regardless of their metallicity, are confined and possibly trapped in the bar potential.

A significant improvement of our knowledge of the bulge GCs system has been

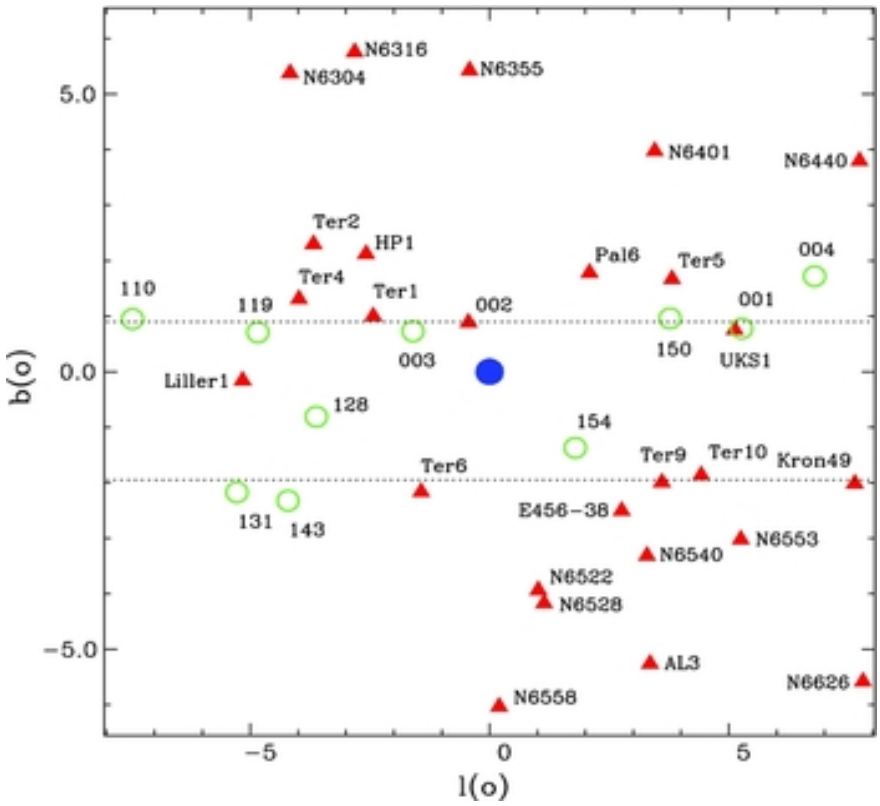

Figure 1.14: Spatial distribution of bulge GCs with respect to the Galactic center (blue-filled circle). Well known bulge GCs are shown as red-filled triangles while VVV clusters and candidates as green open circles. Figure from Bica et al. (2016).

achieved in the last years thanks to an extensive photometric campaign based on SOFI at the New Technology Telescope (NTT, Chile) (Valenti et al., 2007, 2010) and/or with HST (Ortolani et al., 2001, 2007). These works have enabled an homogeneous characterization of GCs in the bulge in terms of extinction, distance and metallicity. Very recently, new GCs candidates in the inner bulge have been discovered with VVV (Minniti et al., 2017b,a). However, for most of the bulge GCs with high reddening, precise age determinations based on the measurement of the MS-TO luminosity are still lacking, requiring very deep photometry at high spatial resolution in the optical with HST and in the NIR with HST (and JWST in the near future) and ground-based AO assisted imagers.

1.4.1 Terzan 5: a complex bulge stellar system

In the bulge GC system, a quite interesting case is represented by Terzan 5.
Terzan 5 is a bulge stellar system located at a distance of ∼2 kpc from the Galactic center and with an average color excess of E(B-V)=2.38 (Barbuy et al., 1998; Valenti et al., 2007) and quite significant differential reddening (Massari et al., 2012). For many years it has been classified as a classical GC (Terzan, 1968). More recently, NIR imaging with the Multi-coniugate Adaptive Optics Demonstrator (MAD) at the Very

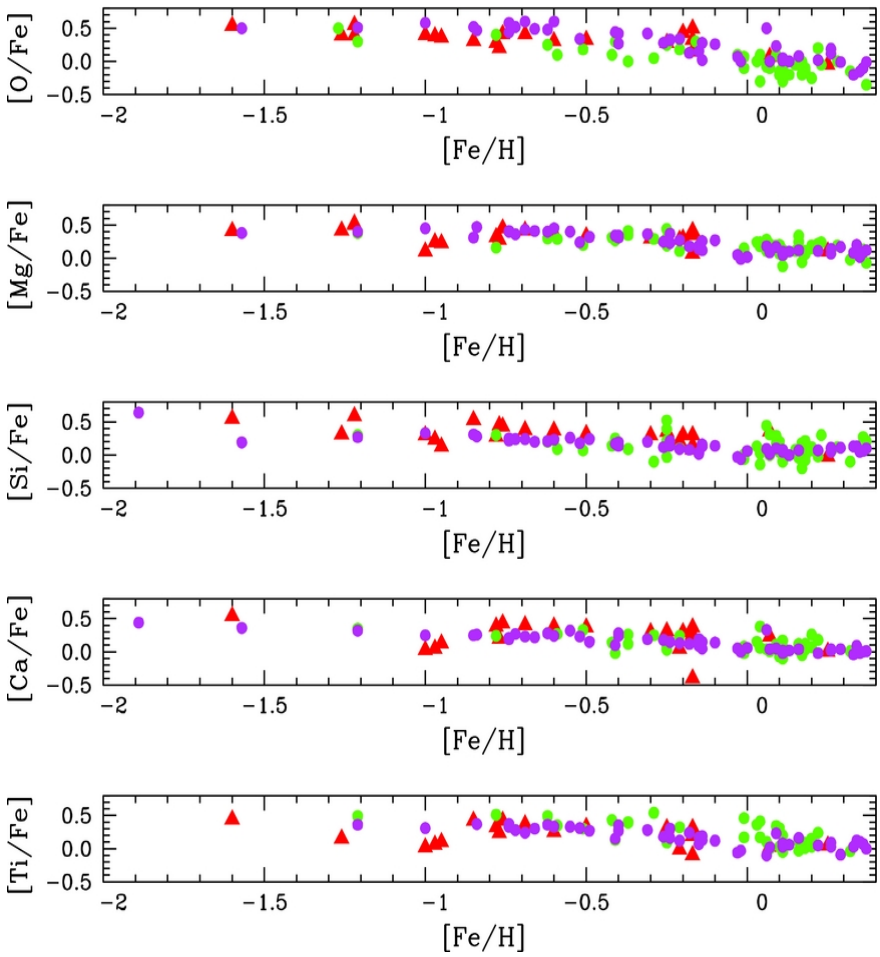

Figure 1.15: [α/Fe] vs [Fe/H] for bulge GCs (red triangles), compared with field stars (green circles) analyzed by Lecureur et al. (2007), Barbuy et al. (2015) and Gonzalez et al. (2011). Magenta circles are microlensed bulge dwarfs by Bensby et al. (2013). Figure from Bica et al. (2016).

Large Telescope (VLT) and spectroscopy with NIRSPEC at Keck revealed the presence of two distinct RCs in the CMD, that cannot be explained by differential reddening or distance effects, while they show very different iron abundances ([Fe/H]=-0.2 and +0.3 dex, respectively, Ferraro et al., 2009a). Subsequent spectroscopic studies (Origlia et al., 2011, 2013; Massari et al., 2014b,a) fully confirmed this finding and revealed an additional, minor (a few percent) stellar population of metal poor stars at [Fe/H]$\sim$-0.8 dex, bringing the overall metallicity range covered by the Terzan 5 stellar populations to $\sim$1 dex. Note that such a large iron spread has never been observed in any Galactic GC, with the only exception of ω-Centauri in the halo, now believed to be the remnant of a dwarf galaxy accreted by the Milky Way (see e.g. Bekki and Freeman, 2003; Bekki and Norris, 2006).

These studies also indicated that the sub-solar stellar populations of Terzan 5 with peaks at [Fe/H]$\sim$-0.2 and -0.8 dex are α-enhanced and they likely formed early and quickly from a gas mainly polluted by core collapse SNe. The super-solar component at [Fe/H]$\sim$+0.3 dex, which is possibly a few Gyr younger and more

centrally concentrated (Ferraro et al., 2009a; Lanzoni et al., 2010), has approximately solar [α/Fe] ratio, requiring a progenitor gas polluted by both core collapse SNe and SNIa on a longer timescale.
An intriguing scenario is emerging from these observational facts. (**1**) Terzan5 is not a genuine GC, nor it can simply be the result of the merging of two globulars; (**2**) it has experienced a complex star formation and chemical enrichment history, possibly characterized by short episodes of star formation (thus accounting for the small metallicity spread of the individual sub-populations) in a stellar system originally much more massive than today (Lanzoni et al., 2010), thus able to retain the SNe ejecta and to also explain its exceptionally large population of millisecond pulsars (MSPs). (**3**) Terzan 5 seems to have formed and evolved in deep connection with the bulge (Massari et al., 2015). Indeed, there is a striking chemical similarity between the Terzan 5 and the bulge stellar populations.
Recently, by means of HST and ground-based AO deep imaging (Ferraro et al., 2016), two distinct MS-TO points have been also detected in Terzan 5, providing the age of the two main stellar populations: 12 Gyr for the (dominant) sub-solar component and 4.5 Gyr for the component at super-solar metallicity.
All these discoveries classifies Terzan 5 as a complex stellar system of the Galactic bulge, where multiple bursts of star formation occurred, thus suggesting a quite massive progenitor of $\sim 10^7$ $M_\odot$.
Recently, it has been suggested that the giant clumps observed in high redshift galaxy bulges (see e.g. Genzel et al., 2011; Tacchella et al., 2015) could have originated by the clustering of smaller, seed clumps of typical masses of $\sim 10^7$-10^8 $M_\odot$ (see e.g. Behrendt et al., 2016), in a bottom-up scenario. In this framework, the proto-Terzan 5 could have been one of those seed clumps that did not grow and merge into the Galactic bulge, but for some unknown reasons evolved in isolation and self-enriched. This discovery triggers the search of other Terzan 5-like stellar systems in the Galactic bulge. One promising system is Liller 1, a GC located very close to the Galactic plane and characterized by a very high dust obscuration (approximately 10 mag in the V band). It has been recently observed with GeMS at the Gemini South telescope and it has been found to be as massive as Terzan 5, with the second highest stellar encounter rate (after Terzan 5; Verbunt and Hut, 1987) and with some peculiar evolutionary features not yet well understood (Saracino et al., 2015). The results of this work are part of my PhD project and will be extensively described in Chapter 4 of this thesis.

CHAPTER 2

Multi-Conjugate Adaptive Optics

2.1 Introduction

As already presented in Chapter 1, the Galactic bulge is strongly affected by severe dust extinction, which absorbs a significant fraction of light coming from its stellar content, hampering a detailed study of the systems orbiting within it, like GCs.
In fact, because of the strong extinction, the properties of bulge GCs (like age, structural parameters, etc.) are only poorly known, and some of them are not accessible at optical wavelengths. The census of the bulge GC population is still incomplete and a large number of new candidates has been found in the last years (Borissova et al., 2011, 2014; Moni Bidin et al., 2011; Minniti et al., 2011, 2017b,a) thanks to extensive IR surveys (like VVV).
One key ingredient to study the Galactic bulge and its stellar components is therefore the use of IR observations (0.9 - 2.4 μm). Indeed, in the last decades several NIR surveys have been planned to this aim. Examples are 2MASS, SOFI and the most recent VVV. In addition, since GCs are compact stellar aggregates characterized by very high central densities ($> 10^3$ stars/pc), high spatial resolution is necessary to resolve individual stars in the innermost regions of these systems.
Many efforts have been made in this direction by space facilities as the HST (Bellini et al., 2013; Brown et al., 2009; Ortolani et al., 2001, 2007) and good results have been achieved despite the main limitation of being a 2.4-meter telescope. Unfortunately, in the case of ground-based facilities the situation is very different. Even with large telescopes (as the NTT 3.6-meter at La Silla), observations are predominantly shallow and in some cases we are not able to resolve stars even in the center of the loosest GCs. The origin of such a discrepancy is the presence of the Earth's atmosphere.

2.1.1 The atmospheric turbulence

The atmosphere can be considered as a dielectric medium which absorbs, emits but also refracts radiation coming from stars. Indeed, the presence of patches of air

with different temperatures triggers the formation of local under- and over-densities inducing temporal and spatial variations of the refractive index. This is the so-called *atmospheric turbulence*. The turbulence randomly distorts, in very short timescales, the plane wavefront from distant objects, like stars. As a consequence, astronomical images becomes blurry and distorted. The term generally used to describe the impact of the atmospheric turbulence on astronomical observations is "seeing". Seeing is the main limitation, in terms of spatial resolution, for ground-based facilities. In fact, if the diffraction limit[1] of an intermediate-large size (6-8 m) telescope operating in the NIR is of about 0.1", the average seeing is about 6-8 times larger (0.6"-0.8").
The effect of the atmospheric turbulence on short and long exposure images in terms of angular resolution can be summarized as follows: If we want to observe two stars which are quite "close" in the sky by using a ground-based telescope of an intermediate size, the atmospheric turbulence moves the diffraction-limited profile of both stars around in a random fashion. If the exposure time is quite small, the image appears as a snapshot of this motion. When the exposure time increases, this motion simply smears out the image of the stars over the seeing disc. When we move to large telescopes, the seeing is not just an image motion, but a diffraction pattern of interfering wavefronts. If we make a short exposure then this interference pattern yields a semi random set of dots called speckles, each having a width of about the telescope diffraction limit. The speckles are distributed over an area the size of the seeing disc. For long exposures, light coming from both stars is equally distributed over the seeing disc, loosing all the information about their position, brightness etc.. It happens whenever two objects are below the resolution allowed by the seeing of the observing site. This effect is schematically shown in Figure 2.1.

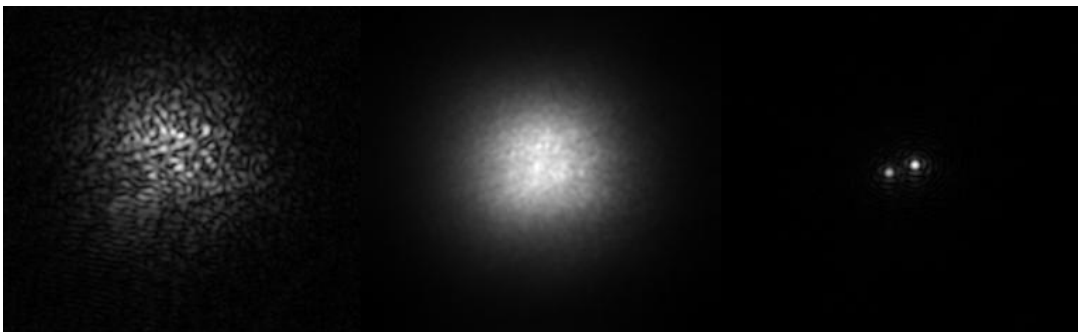

Figure 2.1: Illustrative comparison of the angular resolution of a telescope with a short (left) and long exposure image (middle) in the presence of atmospheric turbulence. At the right a diffraction-limited image shows the presence of two point sources that were below the resolution allowed by the seeing.

[1]The diffraction limit of a telescope can be roughly measured as λ/D, where λ is the observed wavelength while D is the diameter of the telescope.

2.1.2 Definitions

We introduce three main atmospheric parameters which are useful to quantify the effect of turbulence in the Earth's atmosphere on a wavefront propagating through it. The meaning of these terms is schematically presented in Figure 2.2.

The Fried Parameter r_0, defined for the first time by Fried (1965), is usually used

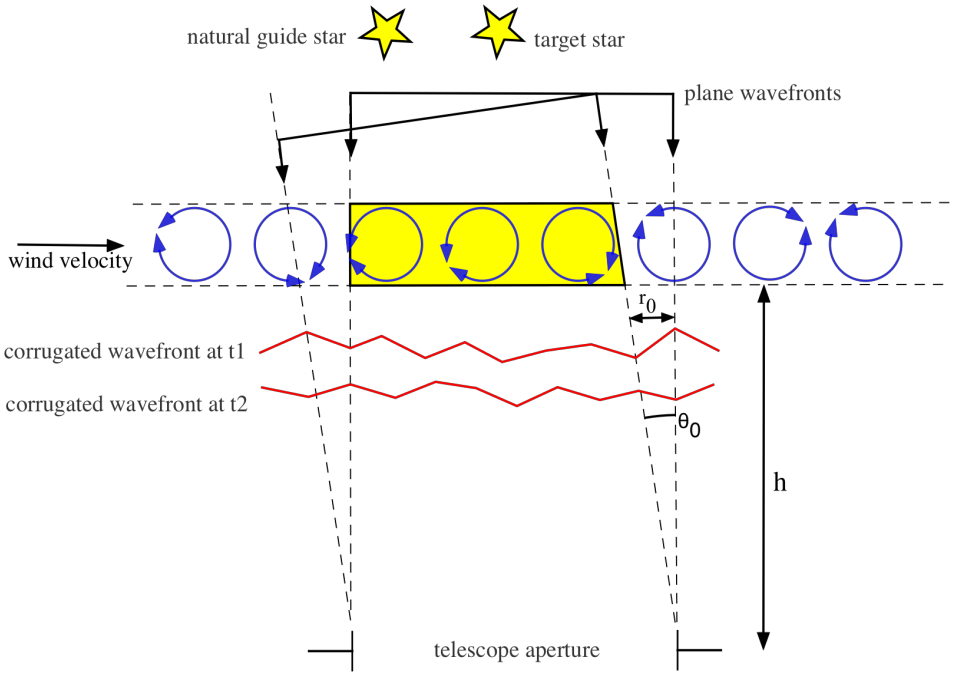

Figure 2.2: Schematic showing the definition of the Fried parameter r_0, and how it relates to coherence time, $\tau_0 = t_2 - t_1$, and isoplanatic angle, θ_0.

to describe the characteristic spatial extent of the wavefront aberrations. It can be calculated, with a complex mathematical formulation by Kolmogorov (Tatarskii, 1961), as:

$$r_0 = \left[0.423 \left(\frac{2\pi}{\lambda}\right)^2 sec\xi \int C_n^2(h)dh\right]^{-3/5} \tag{2.1}$$

where λ is the wavelength of the observation, ξ is the zenith angle while C_n^2 defines the turbulence profile. C_n^2 is the vertical distribution of the strength of refractive index variations through atmospheric turbulence as a function of height h. This term indicates the length over which the wavefront can be considered approximately planar. For simplicity, the turbulence can be visualized as a set of cells. Each cell has the same size as the Fried parameter, thus the perturbation can be considered constant in each of them. In other words, r_0 does not identify a characteristic scale of the atmospheric perturbations, but it suggests that only the perturbations of the size of the order of r_0 are relevant. By simplifying the equation 2.1, the Fried parameter

is predicted to vary with wavelength as $r_0 \approx \lambda^{6/5}$. This implies that the longer the wavelength, the larger the Fried parameter, the better the atmospheric conditions. Indeed, at a good observing site, at an optical wavelength of λ = 500 nm, r_0 has a typical value of 10 cm. In the same site, it should reach $\approx$ 70 cm at NIR wavelengths (λ = 2.5 μm).
An other parameter used to describe the atmospheric turbulence is the coherence time τ_0. The turbulence cells, which are responsible for distorting the incident wavefront, generally evolve on long timescales. In fact, the reason the wavefront changes between time t_1 and time t_2 (see Fig. 2.2) is because the wind moves the turbulent cells across the sky. The time scale on which the wavefront changes is the time taken for a turbulent cell, of size r_0, to move it's own size. Its general formula is the following:

$$\tau_0 = 0.057 \left[\lambda^{-2} sec\xi \int C_n^2(h) v_w(h)^{5/3} dh \right]^{-3/5} \tag{2.2}$$

where v_w is the wind velocity at the layer altitude h. This formula can be easily simplified as $\tau_0 = t_2 - t_1 = r_0/v$, where v is the mean velocity of the wind. At a good observing site on a typical night, if v = 10 m/s, the coherence time is τ_0 = 10 ms. A longer coherence time of about 70 ms can be obtained in the NIR bands.
The last term is the isoplanatic angle θ_0. Considering two stars, the same as in Figure 2.1, if they are sufficiently close that the light from them passes through roughly the same turbulent region, their wavefronts will be distorted exactly in the same way. The measurement of how much two stellar objects can be separated, still having their light passing through the same turbulent region, is called isoplanatic angle and it can be defined as:

$$\tau_0 = 0.057 \lambda^{6/5} \left(sec\xi \int C_n^2(h) h^{5/3} dh \right)^{-3/5} \tag{2.3}$$

by using the Kolmogorov formalism. The formula can be easily simplified as: $\theta_0 = r_0/h$ where h is the characteristic altitude of the turbulence. θ_0 is typically of few arcsec (2″) at optical wavelength, strongly increasing in the NIR where it is around 15″.
Whenever we observe two stars separated by more than θ_0 with a telescope larger than r_0 and for an exposure time greater that τ_0, the uncorrected image will have an angular dimension $\approx \lambda/r_0$, which represents the well known seeing disk (fig. 2.1, middle) that identifies the limit angular resolution for any telescope with a diameter bigger than r_0.

2.2 The AO technique

To overcome the physical limitations of ground-based observations due to the presence of the atmospheric turbulence, techniques able to correct for them are needed.

AO are the state-of-the-art of such techniques. The AO concept was first proposed in the 1950s (Babcock, 1953), but it was developed only in the late 1980s, when the first astronomical AO instrument COME-ON was tested at the 1.52 m telescope (Merkle et al., 1989; Rousset et al., 1990) of the Observatoire de Haute-Provence. In a few words, AO systems are able to sample and correct in real time the wavefront deformation due to the atmospheric turbulence, thus recovering most of the light coming from astronomical objects otherwise lost. It translates into a significant increase in spatial resolution of the astronomical images obtained with ground-based telescopes. The basic principle of AO correction is shown in Figure 2.3, where the main components are a deformable mirror (DM), a real-time computer (RTC) and a wavefront sensor (WFS) that work together to compensate the blurriness of the images. More in detail, the wavefront initially planar of an astronomical object is randomly distorted by turbulence in the Earth's atmosphere. The diverging beam beyond the focal plane of the telescope is then made parallel using a collimator and the light reflects off a DM. Using information provided by a WFS, the RTC calculates the correction to be applied to the incoming beam by means of the DM. In particular the DM modifies its shape in order to match the one of the incident wavefront, changing hundreds of times per second because of wavefront's fast variations. The reflected wavefront of the astronomical object becomes planar, thus the beam can be focalized and detected from a scientific camera. A dichroic splits the beam between two light-paths, so that the detector acquires a portion of the light (often the red component) while the WFS receives and analyzes the other one (the blue component, in many cases). It is worth to note that the wavefront is independent of wavelength, which is why it is possible to sense and correct at different wavelengths.
AO systems generally operates in closed loop since the WFS measures the residual WF after the correction of the previous cycle. This process ends only when the desired conditions (in terms of convergence and stability) are achieved. In other words, when the correction is successfully applied.
To date, AO systems preferentially work in the NIR, where the constraints on the main atmospheric parameters, especially the coherence time τ_0, are more relaxed, thus it could be easier to correct for them. In order to better understand AO systems, it is important to give some details about their main components: the WFS and the DM.

2.2.1 Wavefront sensors, RTC and deformable mirrors

The key concept of an AO system is the interplay between a WFS and a DM. The WFS has to be extremely sensitive to record and measure the spatial and temporal variations of the incident wavefront, so that the DM can correct for it in the real time. This game can be successfully played only thanks to an RTC.
There are many different designs of WFSs. The most used are the Shack-Hartmann sensor (Shack and Platt, 1971), which is schematically presented in Figure 2.4 and the

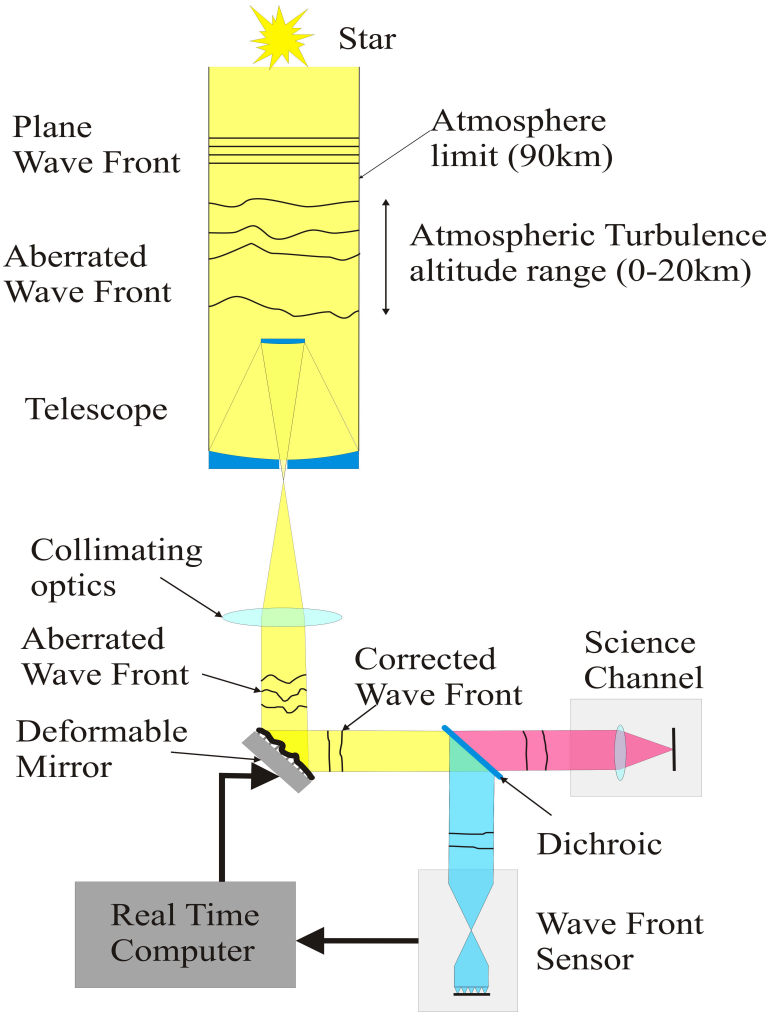

Figure 2.3: Explanation of the AO operating scheme.

curvature sensor (Roddier and Roddier, 1988).
The Shack-Hartmann sensor consists of a lenslet array through which the corrugated wavefront is incident upon. When a plane wavefront passes through the lenslet array, it produces a regular series of spots on the high speed detector in the focal plane. The relative position of these spots can be considered as a reference pattern. A corrugated wavefront instead produces irregularly spaced spots. The displacement of each spot with respect to its reference position represents a measure of the tilt of each section of the incident wavefront. This information is then used to set the tilt of each corresponding element in the segmented DM. The sizes of the lenslets, and hence the mirror segments need to be comparable to the typical values of the Fried parameter r_0 at the observing time and wavelength of interest (which in the NIR is of about 70 cm, see Section 2.1.2). For an accurate correction, it is also crucial that the delay between sensing the wavefront and adjusting the shape of the DM is smaller than the coherence time of the atmosphere τ_0. In the case that the DM consists of an array of actuators which are connected to a thin optical surface that deforms under the expansion of the actuators, the requirements set by r_0 and τ_0 reflects on the spacing

and the response time of the actuators. Unlike the Shack-Hartmann, which measures the displacement of the spots, the curvature sensor instead measures the intensity on either side of the focal plane. If a wavefront has a phase curvature, it modifies the position of the focal spot along the axis of the beam, thus by measuring the relative intensities in two places the curvature can be deduced.

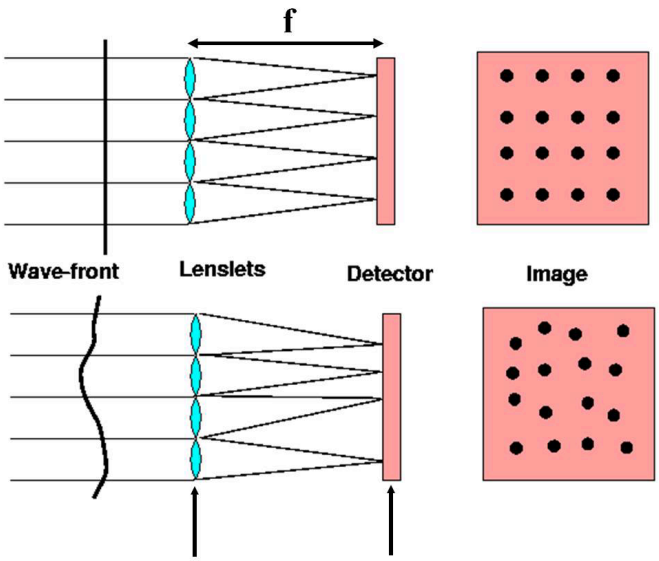

Figure 2.4: Schematic view of a Shack-Hartmann wavefront sensor.

2.3 The first AO systems

The first AO systems are the Single-Conjugated AO (SCAO). SCAO systems sample the atmospheric perturbations by using a single reference source which is adopted for wavefront sensing. The derived perturbations are than corrected by means of a single DM. When the science target is too faint or not a point-like source (e.g. a star or the nucleus of a distant Galaxy), SCAO systems adopt two different astronomical targets: one for science and the other one for WFS correction (hereafter called Natural Guide Star, NGS). The main limitation of SCAO systems is that they provide reliable corrections on very small field of views (FOV, a few arcseconds in the visible up to about 0.5-1 arcmin in the IR bands (K - 2.2 μm)) with performances decreasing as a function of the distance from the reference target. This limitation is due to the anisoplanatism effect. As described in Section 2.1.2, when two sources (here the science target and the NGS) are separated by more than θ_0, their light pass through different turbulence layers in the atmosphere, thus their wavefronts are distorted in a different way and the correction becomes inefficient. An additional limit of SCAO systems is related to the brightness needed for reference sources. In fact, for

a reasonable correction performance the NGS has to be bright enough (less than 10-12 mag in the m_R band), so that the distortions of its wavefront can be sensed at a sufficient signal-to-noise ratio in the short exposure times. This sensibly reduces the probability to find suitable guide stars close to the scientific targets. The situation is well explained in Figure 2.5 (see also the table). It shows that the sky coverage is a strong function of λ. In fact, at longer wavelengths, the sky coverage increases because the isoplanatic angle θ_0 becomes larger (from 2″ to 15″). Moreover, the probability to find a suitable guide star strongly decreases going from the Galactic plane (several tens of percent) to the Galactic Pole (a few tenths of a percent) (Ellerbroek and Tyler, 1998).

Image spectral band	R	I	J	H	K
Wavelength (for imaging)	0.65	0.85	1.22	1.65	2.2
Maximum guide star mag (at 0.63 μm)	13.1	14.0	15.2	16.3	17.3
Maximum angular distance (arcsec)	13.4	18.6	28.6	41.1	58.1

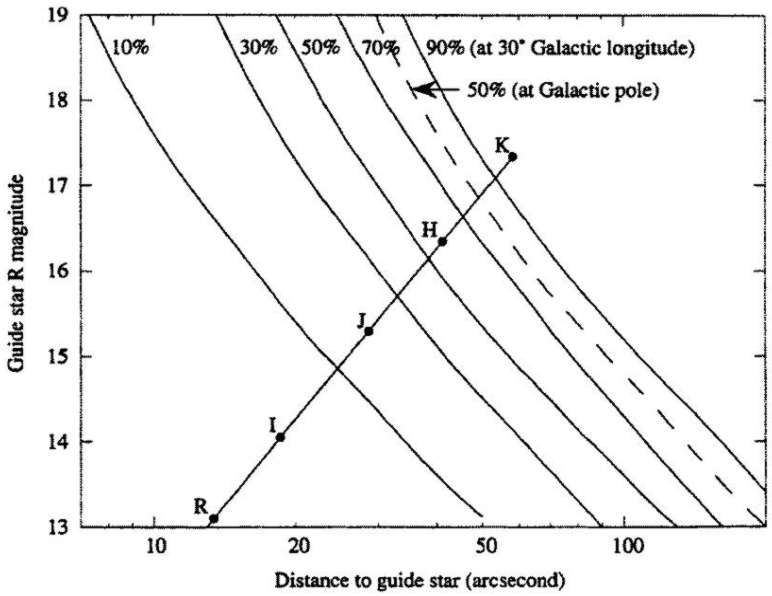

Figure 2.5: The sky coverage as a function of wavelength and distance from a reference star, for different galactic latitudes.

2.4 Laser Guide Stars

To overcome the constraints imposed by the availability of bright reference sources, the use of an artificial guide star has been introduced. The artificial star is generated close to the scientific target using a laser, and it is typically called laser guide star (LGS). This idea has been proposed for the first time by Foy and Labeyrie (1985). There are two types of LGS: the first, known as a Rayleigh beacon, uses the Rayleigh

back-scattering of light from molecules in the lower atmosphere to produce an artificial star at altitudes of approximately 20 km; the second type, defined as sodium beacon, uses the resonance fluorescence of sodium atoms in the mesosphere at an altitude of about 90 km. A schematic view of these two types is shown in Figure 2.6.
While LGSs improve the sky coverage and permit observations otherwise impossible,

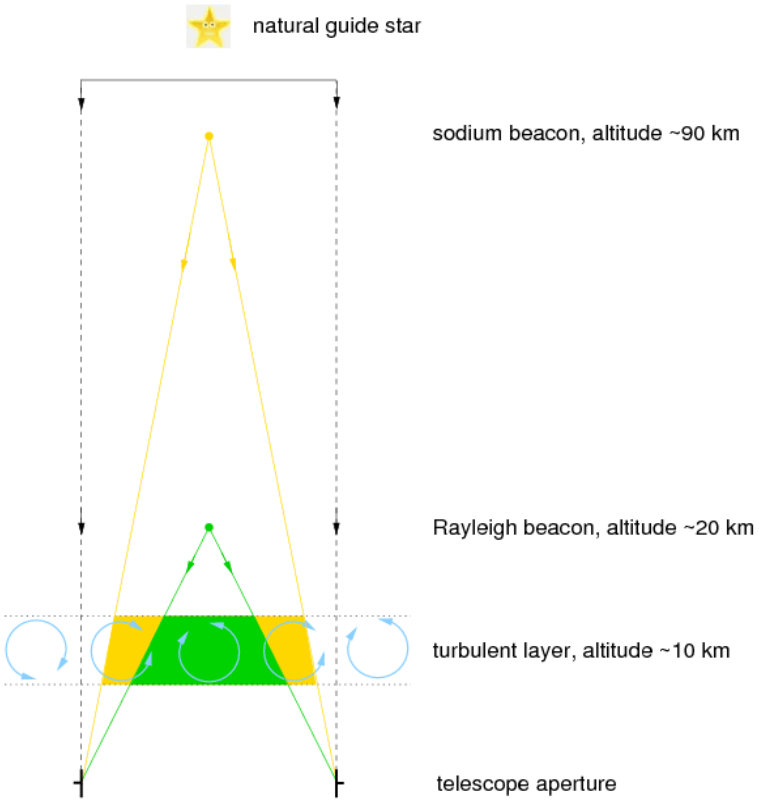

Figure 2.6: Schematic showing the different types of LGSs available for AO, and the cone effect.

they introduce additional sources of error, as the "cone effect or focus anisoplanatism", limiting their performance. Due to the finite distance between telescope and LGS, the backscattered beam does not intercept the same turbulence layer of the atmosphere as the scientific target. This effect becomes increasingly important for larger telescopes and higher turbulent layers. This effect is less severe in sodium beacon lasers as they are created at higher latitudes. In order to overcome the cone effect, measurements from several LGSs can be combined to fully reconstruct the turbulence column in the direction of the astronomical target. In this case, the separation of the LGSs can be significantly larger than the isoplanatic angle θ_0, but their beams should still overlap at the highest turbulent layer in order to prevent possible un-sampled turbulence (Fusco et al., 2010).
However, NGSs cannot be totally replaced by LGSs. In fact, the LGSs are not sensitive to the overall motion (tip and tilt) of the scientific target on the image. Laser beam is deflected by the atmosphere twice, on its way upwards and downwards,

whereas stellar beam experiences only one deflection. The upward and downward tilts compensate completely and the LGS image is stable in the telescope focal plane. As a consequence, NGSs are needed also in LGS AO systems to correct for tip-tilt effects. However in these cases, requirements related to their brightness and distance from the scientific targets are significantly relaxed, leading to a ten-fold increase in sky coverage (Ellerbroek and Tyler, 1998). However, LGS AO systems still provide corrections limited to a relatively small FOV.

2.5 The MCAO era

A significant improvement in AO systems has been achieved by the adoption of multiple LGSs. The first system with these properties is the so-called Laser Tomography AO (LTAO; presented in Figure 2.7). It uses multiple laser beacons, each one optically related to a WFS, which senses the wavefront perturbations due to a single LGS. Combined informations are used to optimize the correction within the observable region of the instrument by a single DM, associated to the ground layer. LTAO systems are able to sensibly reduce the cone effect, so that they perform at the level of a SCAO system with the difference that no bright natural star is required and the corrected FOV slightly increases.
Unlike LTAO systems which are successfully used to obtain a high correction very close to the scientific target, Ground Layer AO (GLAO) systems are instead adopted to improve the image quality in a very large FoV. A GLAO system may be used in combination with an Multi-Object AO (MOAO) system, in which multiple DMs provide independent corrections towards individual objects of interest.
This concept was further developed in the last decades. Based on the original idea of LTAO/GLAO systems, the state-of-the-art is now represented by Multi-Conjugate AO (MCAO) systems (Dicke, 1975; Beckers, 1988). The basic scheme of an MCAO system is presented in Figure 2.8. These systems have been developed in order to overcome anisoplanatism, which is the basic limitation of using a single guide star. MCAO systems in fact use multiple reference sources (NGSs) and/or different LGSs. They control different DMs, which are optically conjugated to different atmospheric layers at a different altitude. At least one of these DMs need to be conjugated to the ground layer as a significant contribution to the total turbulence is usually at this altitude. The correction is much more uniform over a significantly increased FOV (Ragazzoni et al., 2000; Rigaut et al., 2000; Ellerbroek and Cochran, 2002; Diolaiti et al., 2001).
Different types of MCAO systems are available, in particular Star Oriented or Tomographic MCAO (Foy and Labeyrie, 1985; Ragazzoni et al., 1999) and Layer Oriented MCAO (Ragazzoni et al., 2000). For classical "star oriented MCAO", the wavefront signals from several guide stars (laser or natural) are measured on separate detectors, and combined afterwards during the computation of the contribution to the turbulence originated from the different layers. The advantages of this concept is

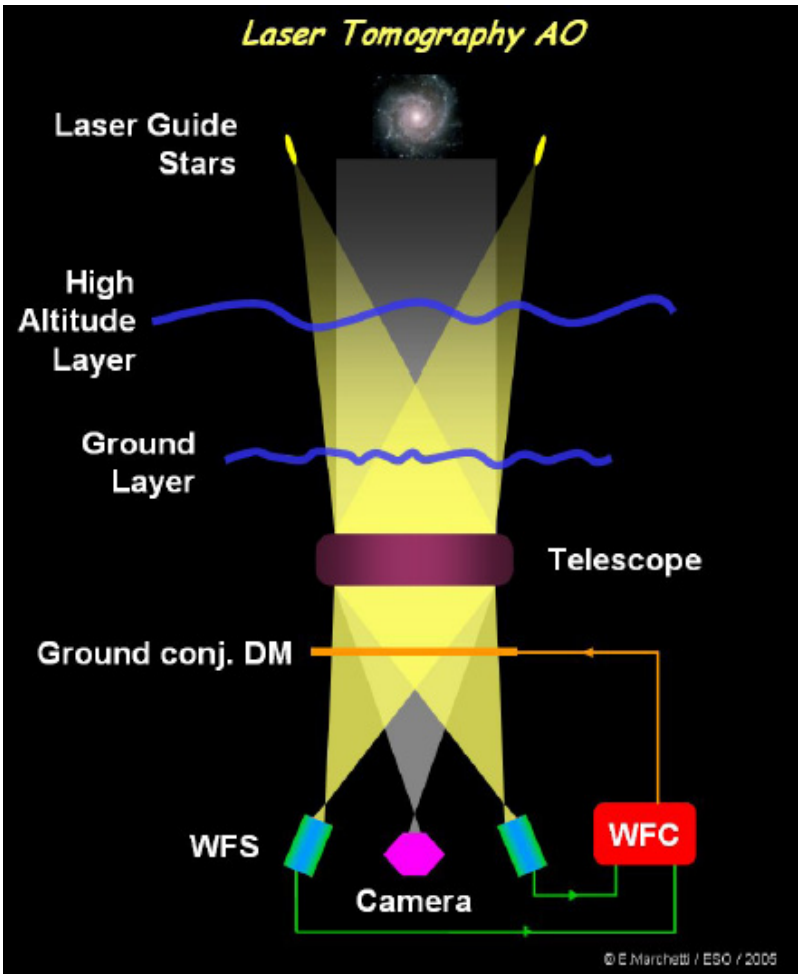

Figure 2.7: Schematic view of an LTAO. Credits: ESO/Marchetti.

that established WFS techniques can be used, and with the help of sophisticated wavefront reconstruction algorithms, an optimal performance in the direction of the science object can be achieved (Fusco et al., 1999). In the "layer oriented MCAO", each layer is separately measured by optically combining the guide star signals for that layer onto a single detector. Each detector is then corrected independently. In this way, also fainter NGSs can be used but this causes a not-uniform correction over the FOV, rather biased towards the brighter sources. A schematic view of the two approaches is shown in Figure 2.9.

The first MCAO system used for scientific observations was the MCAO Demonstrator (MAD), an MCAO prototype realized at the European Southern Observatory (ESO) and temporarily installed in 2007 at the ESO/VLT (Very Large Telescope) at Cerro Paranal (Chile - Marchetti et al., 2007, 2008). MAD used three NGSs and two DMs optically conjugated at the ground layer and at an altitude of 8.5 km in the atmosphere. This system was able to deliver a NIR resolution down to 0.1" across a 120" FOV. MAD tested the two different ways (Star Oriented and Layer Oriented) to achieve the wide-field AO correction, in order to understand which one was the best to reconstruct the corrugated wavefront of the scientific target.

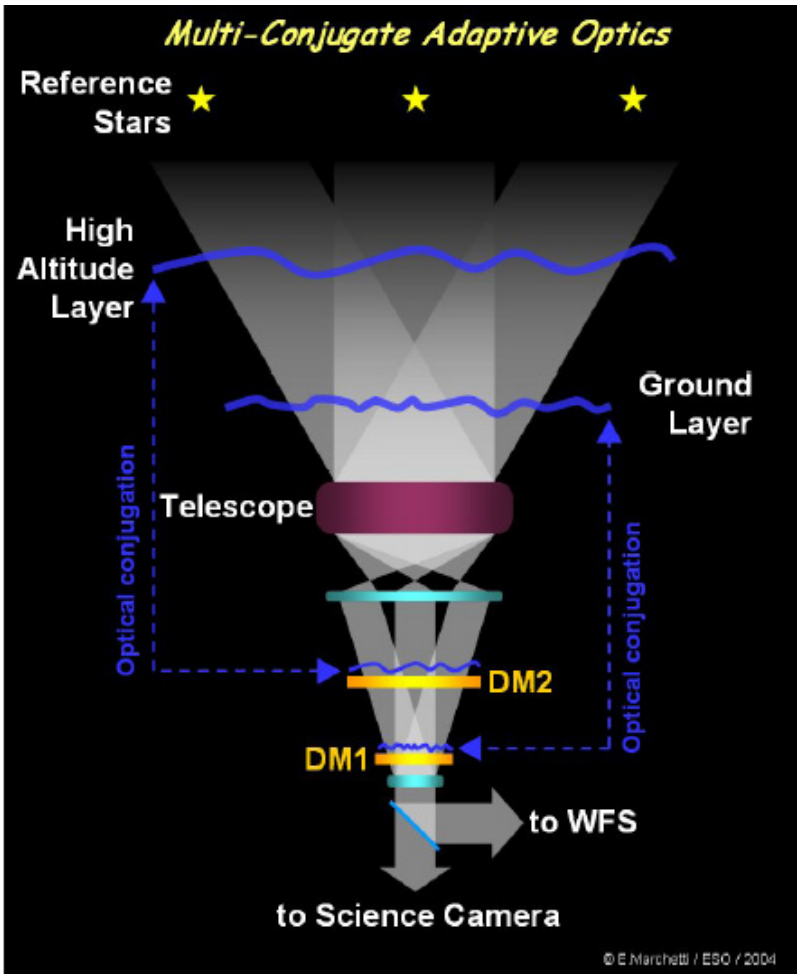

Figure 2.8: The principle of MCAO. Several WFS' and DM's are combined in order to "optimize" the adaptive correction in a larger FOV. Credits: ESO/Marchetti.

Despite the limited sky coverage, numerous interesting results have been published in many fields (Liuzzo et al., 2016; Ortolani et al., 2011; Calamida et al., 2009; Moretti et al., 2009; Gullieuszik et al., 2008; Mignani et al., 2008; Momany et al., 2008). One that demonstrates the potential of MCAO is the discovery of two stellar populations in the star cluster Terzan 5 (Ferraro et al., 2009b, as already mentioned in the previous chapter). The main limitation of MAD is that the quality and uniformity of the corrections depend on the brightness and locations of the NGSs. Better performances can be achieved by using LGSs.

The first laser MCAO system is GeMS. It was commissioned in 2011 on the 8 m Gemini South Telescope in Chile (Neichel and Rigaut, 2011) and since 2013 it operates in a star oriented mode using five LGSs and typically 3 tip-tilt stars (Rigaut et al., 2014; Neichel et al., 2014a).

The real advantage of MCAO systems is that they could achieve accurate and reliable corrections over quite large FOVs with respect to previous AO systems. Moreover, with GeMS the sky coverage becomes much higher than for SCAO, but it can be

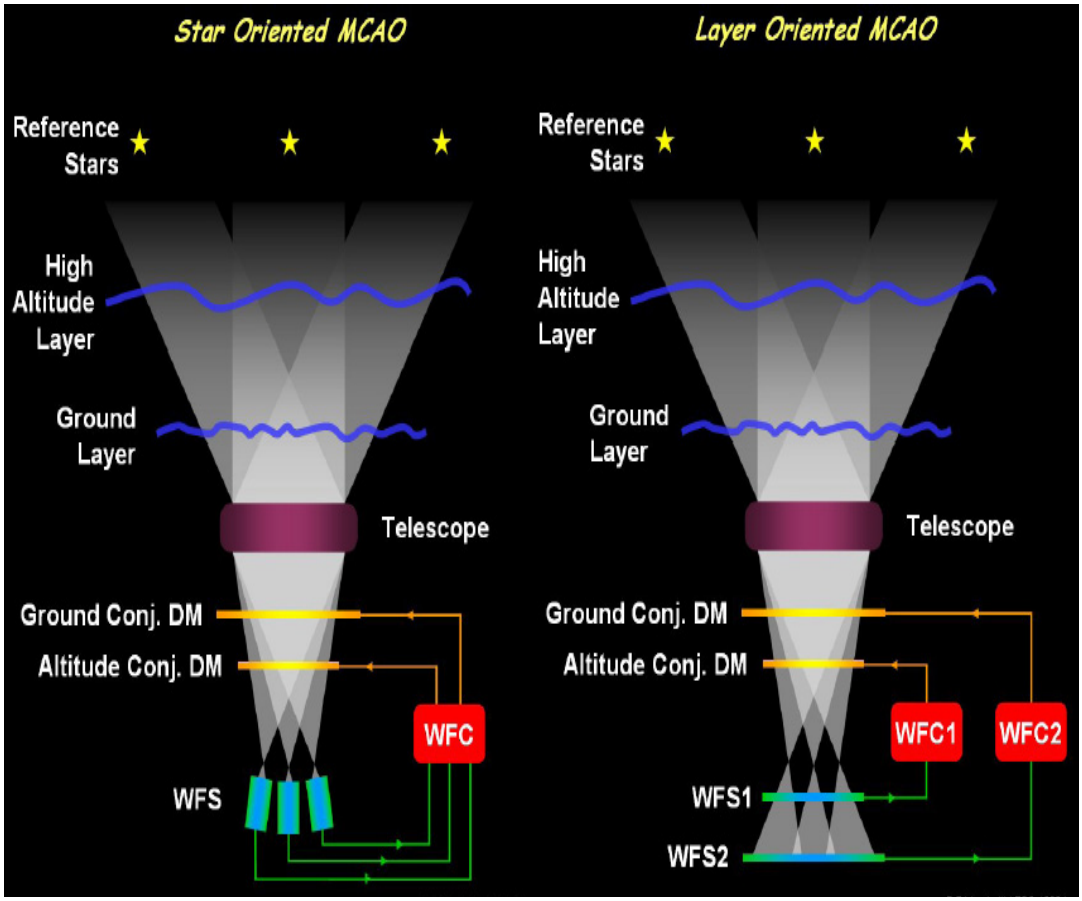

Figure 2.9: The Star Oriented mode (left) and the Layer Oriented mode (right) of an MCAO. Credits: ESO/Marchetti.

improved still further by making use of "image sharpening" at NIR wavelengths for the tip-tilt stars. The design of the Keck Next Generation AO system includes DMs specifically to correct the wavefront from the tip-tilt stars (Wizinowich et al., 2010). In the future, with the MCAO module MAORY at the European Extremely Large Telescope (EELT), tip-tilt stars can be selected within a wide region beyond the science field where there is still a substantial correction, leading a sky coverage exceeding 50 per cent at the Galactic Pole (Diolaiti et al., 2010; Herriot et al., 2010). Waiting for the significant improvements introduced by third-generation telescopes as EELT, we focus now on GeMS which is the best MCAO system available today for the astronomical community, both in terms of scientific and technical performance.

2.6 GeMS at Gemini South Telescope

The MCAO module GeMS at the Gemini South Telescope, shown in Figure 2.11, is mostly characterized by two main subsystems (Neichel et al., 2014a):

1. the Laser Guide Star Facility (LGSF) that includes a 50 W laser (D'Orgeville et al., 2002; d'Orgeville et al., 2003; Hankla et al., 2006) and an optical system

Figure 2.10: The deepest K-band image ever obtained for Terzan 5, with MAD at the ESO/VLT. It demonstrates how uniform and sharp can be the images realized with MCAO systems. Credits: ESO/Ferraro.

called Beam Transfer Optics (BTO - d'Orgeville et al., 2008) that relays the laser light, and controls the LGSs;

2. the MCAO bench, called Canopus.

In particular, the 50 W laser is split in 5 $\times$ 10 W beams to produce the 5 LGSs projected on the sky at the corners and centre of a 60 $arcsec^2$ square (see Figure 2.12).

GeMS operates in a star oriented mode so that each LGS is optically conjugated to a single WFS. The information about the wavefront distortion of the guide stars are combined afterwards and corrected by a tip-tilt mirror and two DMs conjugated to the ground layer and at an altitude of 9 km in the atmosphere. In order to compensate for the tip-tilt anisoplanatism, GeMS uses three NGSs which can be anywhere in a 120 arcsec diameter acquisition FOV and within a 1' radius from the image center. Hence, the science target can be as distant as 60" from the NGS, and because of the MCAO correction, the performance will be essentially as good as if the target would have been closer to the NGS (Neichel et al., 2014a). This is a great improvement with respect to AO systems based on a single reference star.

An important issue related to NGSs is the discrepancy between their brightness and the limiting magnitude imposed by the instruments themselves. In fact, due to alignment issues and design flaws, the current limiting magnitude achievable with GeMS is $m_R < 15.5$ and it sets the sky coverage of the system, which is quite good with respect to previous AO systems. In particular, with GeMS the probability of finding three NGSs or more is 30 per cent, while the probability to have no NGS at all is 35 per cent. Pushing the limiting magnitude to m_R = 18.5 (which should be the case

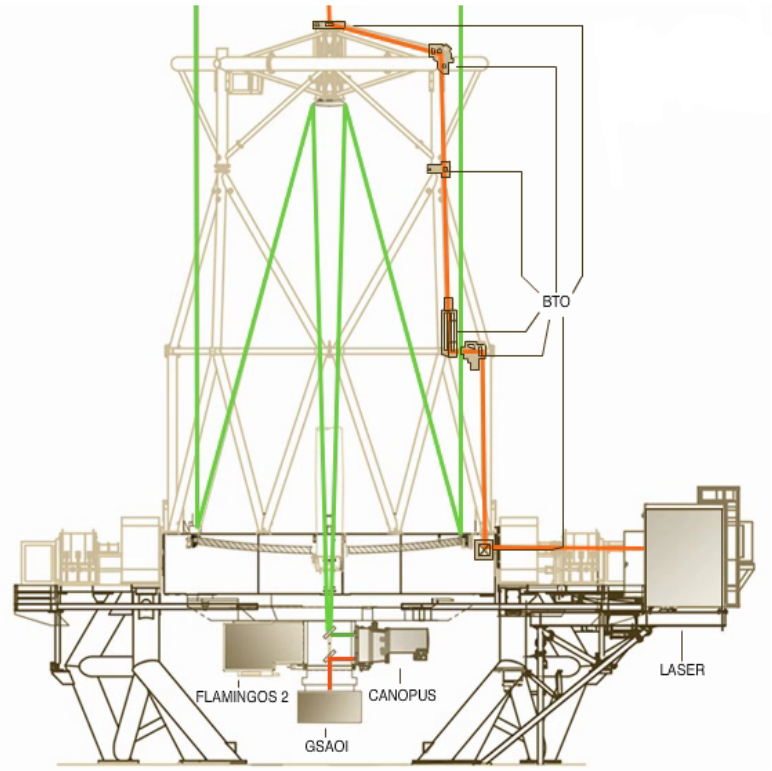

Figure 2.11: A schematic view of the MCAO system GeMS mounted at the Gemini South Telescope.

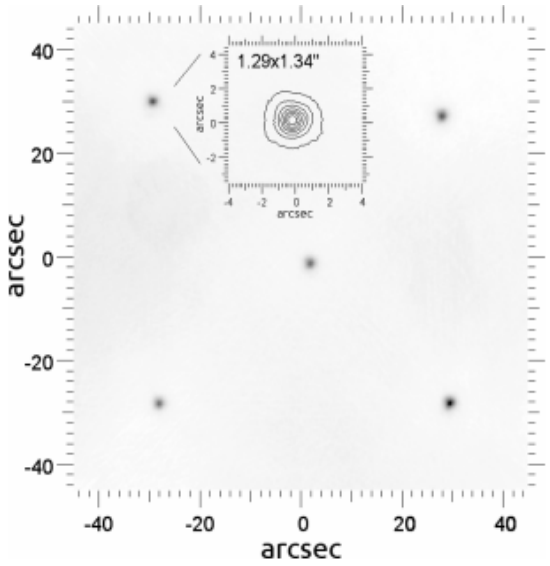

Figure 2.12: An example of LGS spots constellations for GeMS at Gemini.

after the WFS upgrade), the probability can increase to 72 per cent for three NGS, and for no NGS at all it can decrease to only 8 per cent.
The first mode of operation offered to the scientific community was to combine GeMS with the GSAOI. GSAOI is an high resolution NIR (0.9 - 2.4 μm) imager designed

to work at the diffraction limit of the 8 m telescope (McGregor et al., 2004). It uses four Hawaii-2RG 2k $\times$ 2k arrays, forming a 4k $\times$ 4k detector covering approximately 85″ $\times$ 85″ at 0.02 arcsec per pixel.

CHAPTER 3

GeMS/GSAOI photometric and astrometric performance in dense stellar fields

Based on the results published in:
Dalessandro E., Saracino S., Origlia L., Marchetti E., Ferraro F. R., Lanzoni B., Geisler D., Cohen R. E., Mauro F., Villanova S.
2016, *The Astrophysical Journal*, **833, 111**

Abstract

Ground-based imagers at 8 m class telescopes assisted by MCAO are primary facilities to obtain accurate photometry and proper motions in dense stellar fields. We observed the central region of the GCs Liller 1 and NGC 6624 with the MCAO system GeMS feeding the GSAOI imager currently available at the Gemini South telescope, under different observing conditions. We characterized the stellar PSF in terms of Full Width at Half Maximum (FWHM), Strehl Ratio (SR) and Encircled Energy (EE), over the FOV. We found that, for sub-arcsec seeing at the observed airmass, diffraction limit PSF FWHM ($\approx$ 80 mas), SR $\sim$ 40% and EE $\geq$ 50% with a dispersion around 10% over the 85″ $\times$ 85″ FOV, can be obtained in the K_s band. In the J band the best images provide FWHMs between 60 and 80 mas, SR $>$ 10% and EE $>$ 40%. For seeing at the observed airmass exceeding 1″, the performance worsen but it is still possible to perform PSF fitting photometry with 25% EE in J and 40% in K_s. We also computed the geometric distortions of GeMS/GSAOI and we obtained corrected images with an astrometric accuracy of $\sim$1 mas in a stellar field with high crowding.

3.1 Introduction

Since 2013 the MCAO system GeMS together with the GSAOI imager at the Gemini South telescope (Rigaut et al., 2012, 2014; Neichel et al., 2014b,a) is regularly offered

to the Community for observations. This is the only MCAO facility currently at work in the world. GeMS is the first sodium based multi-laser MCAO system. It uses five lasers and three tip-tilt stars to provide an efficient correction over a $\sim 1.5' \times 1.5'$ FOV. GSAOI is a NIR imager equipped with four $2k \times 2k$ detectors with 20 mas pixel size, covering $85'' \times 85''$, designed to work at the diffraction limit of an 8 m telescope.

The proper characterization of the image quality delivered by the GeMS/ GSAOI system and of the parameters that mostly contribute to set its overall efficiency is extremely important to decide the best observational strategy and to maximize the scientific output. It also provides useful information for the future generation of MCAO systems at the 20-40 m class giant telescopes currently underway.

Different parameters can be used for a general description of the performance of an instrument. In addition to the FWHM, which provides information about the delivered spatial resolution, a useful quantity widely used is the SR. The SR is defined as the ratio between the intensity at the peak of the observed seeing disc and the intensity of the theoretical Airy disk[1], as shown in Figure 3.1. SR provides crucial information about the efficiency of the AO corrections. As a complementary quantity to the SR, astronomers use the so-called EE distribution, which is defined as the fraction of the total integrated flux in an image within a given radius.

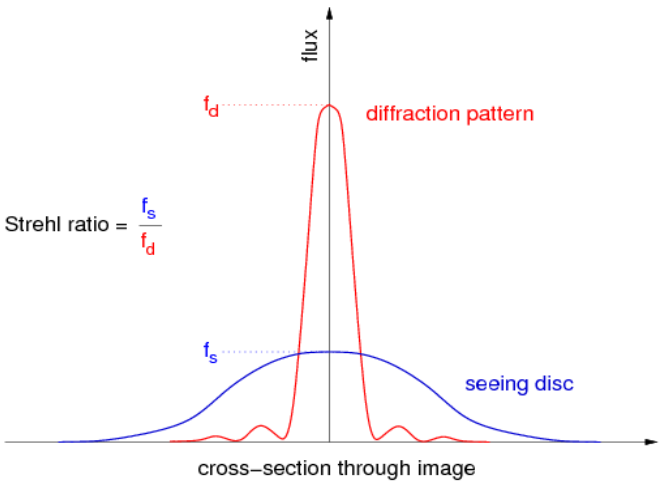

Figure 3.1: The seeing disc of a star superposed on the theoretical diffraction pattern. The SR is the ratio of the peak intensities of the two profiles.

Various authors have put significant effort on this task. In particular Neichel et al. (2014a; see also Rigaut et al. 2012, 2014 and Vidal et al. 2013) have analyzed the average performance of GeMS in terms of SR and FWHM variations for a large sample of images acquired during the Science Verification. They find that, with a median seeing of 0.73″, the average FWHM delivered by the system for the 50% of

[1]The Airy disk is a description of the best focused spot of light that a perfect lens with a circular aperture can make, limited by the diffraction of light. It is the bright central spot and its size sets the diffraction-limited resolution of a telescope

the images is 0.087″, 0.075″ and 0.095″ in the J, H and K_s bands respectively. For reference, the diffraction limited FWHM are e.g. 0.037″, 0.049″ and 0.068″ at 1.2, 1.6 and 2.2 μm, respectively. They also find that the average FWHM variation over a field of one square arcmin is $\sim$ 5% (relative r.m.s.) with the maximum variation being $\sim$ 15%. For the same images the average SR is 5% in J and 17% in K_s. More generally, the SR and FWHM can vary by a factor of 2-3 (also depending on the considered filter) for seeing variation in the range 0.5″ - 1.5″.

In addition to the natural seeing, there are other physical parameters that can affect the performance of the GeMS/GSAOI and AO systems in general. Among them, a non-negligible role is played by the NGSs brightness and asterism, the LGS photon return, turbulence speed and profile. In particular, Vidal et al. (2013) and Neichel et al. (2014b) have shown that the seasonal change of the LGS photon return can affect the delivered average FHWM and SR values by up to a factor of 2-3. On the same line, Vidal et al. (2013) illustrate a case where for the same targets, same photon return and natural seeing, the SR drops by a factor of two, most likely due to variations of the atmospheric turbulence profile (C_n^2).

These works clearly demonstrate the importance and complexity of disentangling the impact of different factors on the final performance of the AO system. By following on these first characterizations, we present here a complementary analysis with the aim of looking at the GeMS/GSAOI performance from an observer/user perspective and providing additional information to be eventually used for Phase I and Phase II preparation. To this aim, we use a sample of images acquired within a scientific proposal devoted to the study of the properties and stellar content of a sample of Galactic bulge GCs. First results from this project have been recently published by Saracino et al. (2015, 2016). They will be presented in detail in Chapter 4 and Chapter 5 of this Thesis.

In addition to the FWHM and SR average values that have been analyzed also in the literature, we examine the behavior of the EE as a function of natural seeing. This quantity is a very intuitive parameter characterizing the properties of the PSF and it can be directly compared to diffraction-limited space telescopes as well as ground-based instruments not supported by AO facilities. We also add a systematic analysis about how natural seeing impacts the uniformity of the PSF. For the first time we tentatively account for the role played by the airmass and NGS brightness and we present the first analytic solution for the geometric distortions of the GeMS/GSAOI system.

The chapter is structured as follows: in Section 3.2 we describe the dataset and data analysis; in Section 3.3 we provide a characterization of the GeMS/ GSAOI performance by using the PSF FWHM, SR and EE as figures of merit and a comparison with Hubble Space Telescope (HST) images; in Section 3.4 we analyze the geometric distortions and in Section 3.5 we draw our conclusions.

3.2 Dataset and observing conditions

By using GeMS/GSAOI we observed the central regions of two Galactic bulge GCs Liller 1 and NGC 6624, between April 2013 and May 2013 (Program ID: GS-2013A-Q-23; PI: D. Geisler). Two different sets of J and K_s images for Liller 1 and one set for NGC 6624 (see Table 3.1) have been acquired using an exposure time of 30 sec for each individual acquisition.

Table 3.1: Dataset properties.

Cluster	Date	# J-exp	# K_s-exp	<s(500nm)>	<airmass>
Liller 1	20 April 2013	3	10	1.07	1.03
Liller 1	22 May 2013	0	5	1.05	1.44
Liller 1	24 May 2013	9	0	0.75	1.018
NGC 6624	24 May 2013	13	14	0.66	1.02

Note: Average seeing values at zenith s(500nm) are in arcsec.

Each image has been sky-subtracted and flat-field corrected by using suitable master sky and dome flat frames in the J and K_s filters. We recall that each image is actually the mosaic of four chips that have been reduced and calibrated independently.

The atmospheric seeing at the zenith and at a given wavelength λ can be computed using the formula: $s(\lambda) = \lambda / R_0(\lambda)$. We used the r_0 Fried parameter at $\lambda = 500nm$ and at the zenith reported in each image header to obtain $s(500nm) = 10.31/r_0(500nm)$, where r_0 is in units of cm and the seeing in units of arcsec.

However, it is eventually useful to compute the seeing at the sky position of the target (i.e. at the observing airmass). We thus used the following formula $s(\lambda, z) = \lambda/(r_0(\lambda) \times sec(z)^{-3/5})$ to obtain $s(500nm, z) = 10.31/(r_0(500nm) \times sec(z)^{-3/5})$. Seeing can be computed at other reference wavelengths by using the scaling relation $s(\lambda)/s(500nm) = (\lambda/500)^{-0.2}$. Hereafter, we always refer to seeing at 500 nm.

It turns out that our images have been acquired under significantly different atmospheric conditions, with seeing $s(500nm)$ varying from $\sim 0.5''$ to $\sim 1.5''$. In particular, the data of NGC 6624 have been obtained with an average value of $s(500nm) \sim 0.65''$, while those for Liller 1 have been obtained under worse conditions with $s(500nm) \sim 1.00''$.

Three reference guide stars in each cluster (see Table 3.2) for the tip-tilt correction have been selected. The guide stars of NGC 6624 are likely luminous and cool cluster member giants near the tip of the RGB with fmag $\sim$ R = 13-14. The guide stars in Liller 1 are likely blue, foreground stars, with significantly fainter J, H, K_s magnitudes and similar fmag $\sim$ R band magnitudes compared to those of NGC 6624, with the exception of NGS 1, which is a couple of magnitudes fainter. Since the R band is the spectral range where the wavefront is mostly sensed, this may have some relevance in the final performance (see Section 3.3.1).

Table 3.2: Selected tip-tilt guide stars.

Star	K_s	H	J	I	V	R	$fmag$
Liller 1							
NGS 1 (2MASS J17332197-3323043)	12.799	12.715	12.958	–	–	–	15.338
NGS 2 (2MASS J17332484-3322502)	11.127	11.185	11.418	–	–	–	13.947
NGS 3 (2MASS J17332609-3323129)	11.297	11.074	11.735	–	–	–	13.577
NGC 6624							
NGS 1 (2MASS J18233752-3022018)	8.472	8.723	9.730	11.3850	13.4520	13.094	13.793
NGS 2 (2MASS J18234108-3022221)	8.987	9.202	10.100	11.6230	12.9890	13.219	13.662
NGS 3 (2MASS J18234052-3021392)	8.827	9.274	9.899	12.8800	14.1040	13.776	10.889

Note: Identification name J, H and K_s magnitudes from 2MASS; V, I from Sarajedini et al. (2007); R estimated from isochrones and $fmag$ (in the 579-642 nm spectral range) from the UCAC3 catalog.

To quantify how the LGS photon return changed during the observing nights, we use the LGS wavefront sensor photon counts reported in the header of each image. First, it is important to stress here that all the images analyzed in this chapter have been acquired mostly over two nights separated by a relatively short time interval (see Table 3.1), while the LGS photon return is expected to vary mostly seasonally (Vidal et al. 2013; Neichel et al. 2014b). Also, about half of the images of Liller 1 were obtained in the same night as those of NGC 6624 (May 24th, 2013). As expected, we find a negligible variation of the average photon counts of the LGS during the observing nights.

3.3 Overall performance

We used the IDL-based `Multi-Strehl Meter` software written by E. Marchetti (Marchetti et al., 2006) to analyze the PSF of the science images and measure their FWHM, SR and EE with variable observing conditions, in order to characterize the performance of the AO system over a range of conditions.

The first step of the analysis is the identification of the candidate star peaks. The software requires as input parameters a first-guess FWHM, the detection threshold and the size of the sub-image to search for the star peaks and to compute the local (residual) background. The first-guess FWHM has been determined by computing the average FWHM of a number of reference stars manually selected on each image. A detection threshold of 1000 ADU and a sub-image size of 60 pixels have been used. Moreover, the software requires a few additional input parameters, among them the

reference wavelength (1.25 μm and 2.15 μm for the J and K_s filters, respectively), the pixel size (20 mas), the telescope aperture (8.1 m) and the obstruction factor of the primary mirror (12.35%).

The obtained list of candidate stellar peaks for each image, suitably filtered by spurious detections, has been then cross-correlated with the photometric catalogs containing calibrated magnitudes and astrometric positions published by Saracino et al. (2015, 2016) for Liller 1 and NGC 6624 respectively, in order to deliver the final list of stars to be analyzed. Typically about 200 stars homogeneously distributed in the FOV in each image have been selected and their FWHM, SR and EE have been measured. The EE has been computed within a circular aperture of two times the measured FWHM, i.e. the typical aperture adopted in the photometric analysis[2].

We then computed average and corresponding dispersion values of the FWHM, SR and EE in each observed image and we analyzed their trend as a function of the seeing at the zenith ($s(500nm)$, see Figures 3.2 and 3.4) and at the observing airmass ($s(500nm, z)$, see Figures 3.3 and 3.5).

3.3.1 PSF average properties

As shown in the left panels of Figure 3.2, in the K_s band average FWHMs very close to the diffraction limit of 70 mas, SR of $\sim$ 40% and EE of 55% have been measured in the NGC 6624 images with sub-arcsec seeing and airmass close to one. In the Liller 1 images with seeing between 0.9″ and 1.5″, the average FWHM, SR and EE show a clear trend with the seeing but also quite a large scatter at a given seeing. For seeing at the observing airmass increasing from 0.9″ to 1.5″, FWHM increases from 85 to 140 mas, while SR drops from 30% to 12% and EE from 50% to 40%. The general observed trend, as well as the total range of values derived for NGC 6624 and Liller 1 in terms of both FWHM and SR, is consistent with what found by Vidal et al. (2013) and Neichel et al. (2014b) for K_s images. It is interesting to note that the largest average FWHM and the lowest SR and EE for a given seeing are measured in those images acquired at the largest airmass corresponding to $\sim$ 1.4. Hence, as shown in the left panels of Figure 3.3, when the FWHM, SR and EE are plotted against the seeing at the observing airmass, the scatter is reduced. These measurements and comparisons indicate that also the airmass has an impact on the delivered performance, and in this respect, it is worth noting that different observing airmasses could indeed explain some of the scatter observed in Figure 6 by Neichel et al. (2014b), where their measured FWHMs and SRs are plotted against seeing at the zenith.

Most of the J band images have been acquired at airmass close to one, hence their seeing at the observing airmass is very similar to the seeing at the zenith. As shown in the right panels of Figures 3.2 and 3.3 the average FWHMs always exceed the diffraction limit of 40 mas, even with good seeing conditions of 0.6″ and increases almost linearly with increasing the seeing. The corresponding average SR and EE

[2]The Multi-Strehl Meter software actually yields the ensquared energy within 2 times the FWHM. We then rescaled such a quantity to a circular aperture having the corresponding diameter.

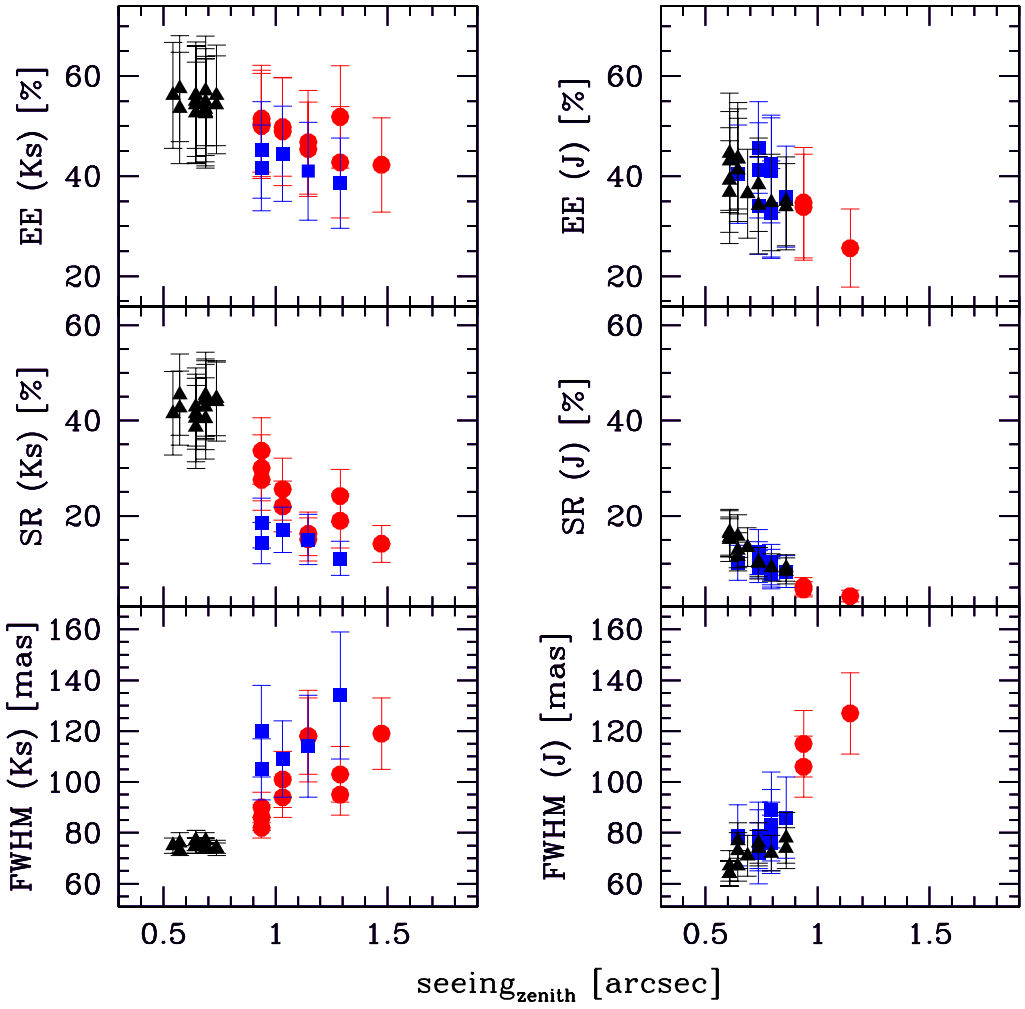

Figure 3.2: Average FWHM, SR and EE values with varying the seeing at 500 nm at the zenith. Left panels: measurements in the K_s band, right panels: measurements in the J band. Triangles refer to measurements of stars in NGC 6624, circles and squares refer to measurements of stars in Liller 1 observed in two different nights, respectively (see Table 3.1).

values decrease with increasing seeing. For seeing increasing from 0.6″ to 1.2″, FWHM increases from 70 mas to 120 mas, while SR drops from 15% to a few percent and EE from 40% to 25%. Our FWHM and SR values indicate somewhat better performance of GeMS/GSAOI in the J band with respect to the findings by Vidal et al. (2013) and Neichel et al. (2014b), likely because of the uniform and good atmospheric conditions during our observations.

A subsample of images in the J band of Liller 1 and NGC 6624 have been acquired with the same seeing, between 0.6″ and 0.9″ and can be used to check the impact of the different asterisms of the two clusters, and in particular the fact that one guide star in Liller 1 has a significantly fainter R band magnitude (see Table 3.2). On average, the Liller 1 images show a $\sim 10-15\%$ larger FWHM and smaller SR values, that

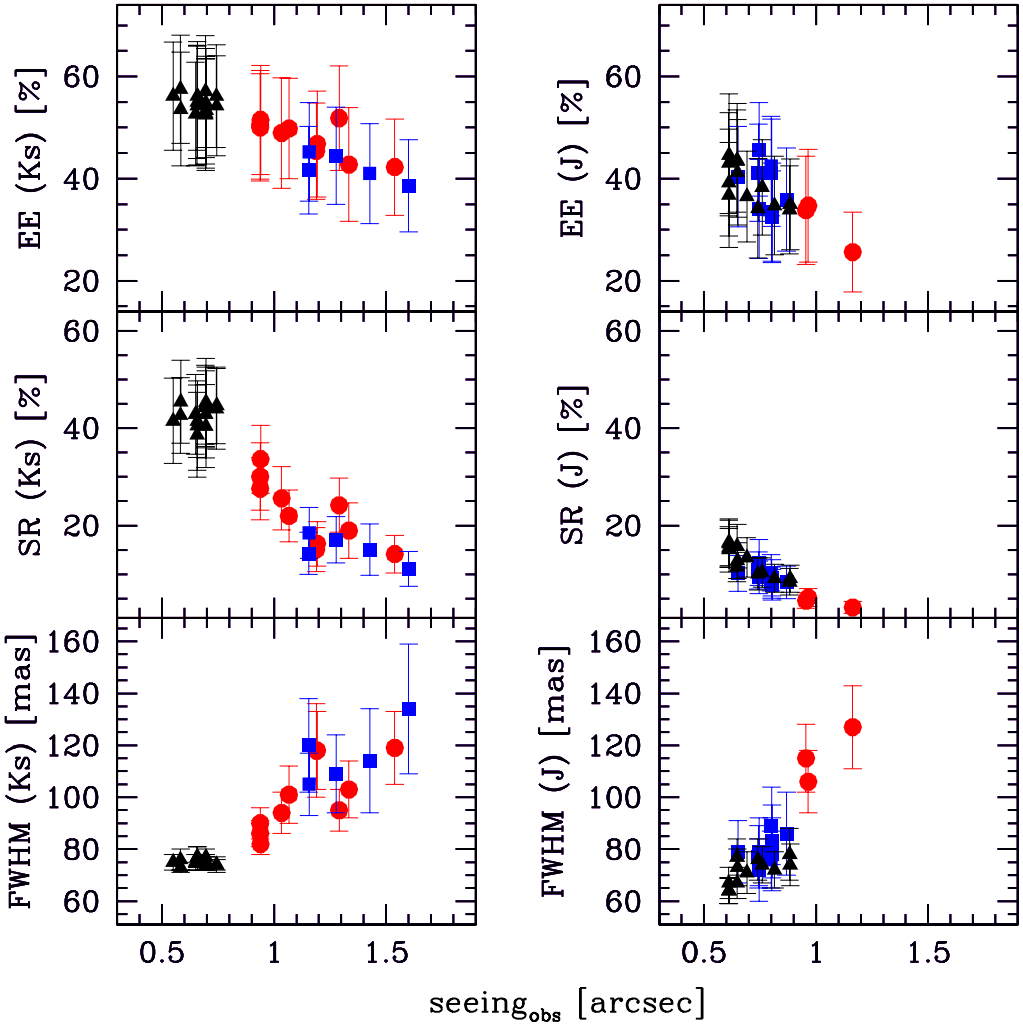

Figure 3.3: Same as in Figure 3.2, but for seeing at 500nm at the observing airmass.

could be indeed a consequence of the significantly fainter guide star.

Finally, we note that both in the K_s and J bands, the average EE values show a smoother variation with the seeing when compared to the variation of the FWHM and SR parameters. This is somewhat expected, given that the EE is computed within a variable aperture, proportional to the variable FWHM, and it indicates that the seeing primarily impacts the spatial resolution (i.e. the FWHM and the SR) and to a lower extent the photometric signal (i.e. the EE), when computed via variable PSF fitting.

3.3.2 PSF uniformity

The average values of the FWHM, SR and EE provide a measurement of the system efficiency, while their dispersion and spatial variation provides an estimate of the

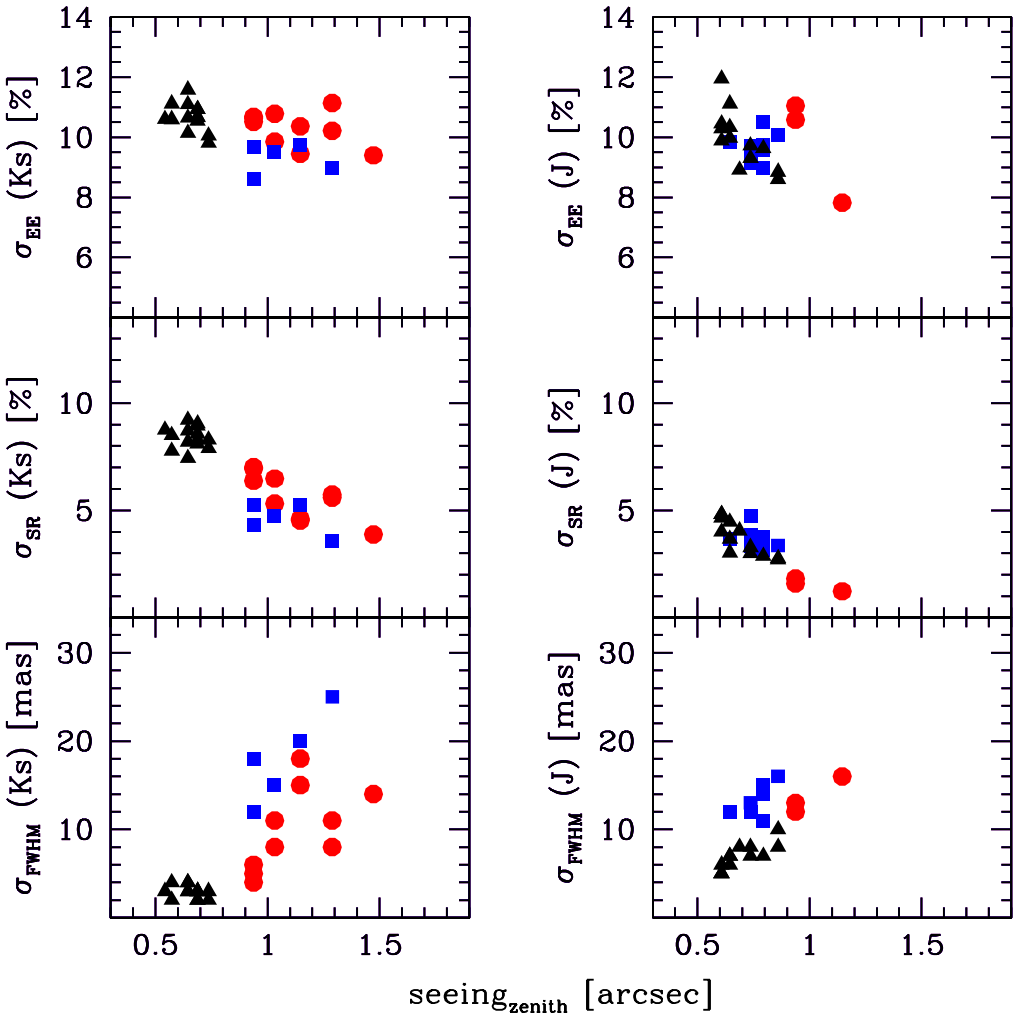

Figure 3.4: Dispersion around the average FWHM, SR and EE values with varying the seeing at 500 nm at the zenith. Left panels: measurements in the K_s band, right panels: measurements in the J band. Triangles refer to measurements of stars in NGC 6624, circles and squares refer to measurements of stars in Liller 1 as observed in two different nights, respectively (see Table 3.1).

uniformity of the PSF across the FOV. Modeling the PSF variations within the FOV is one of the major issues in the photometric analysis of crowded stellar fields in general, and especially when observed with ground-based AO-assisted imagers. Typical values of FWHM and SR variations can be found in the literature, in the following we quantify how their amplitudes vary as a function of the observing conditions.

As shown in Figures 3.4 and 3.5, the dispersion around the average FWHM increases with increasing seeing in a similar fashion as the FWHM itself. This indicates that bad seeing worsens both the spatial resolution and its uniformity over the FOV. At variance, the dispersion around the average SR and EE decreases with increasing the seeing. A more uniform SR and EE across the FOV with worsening seeing

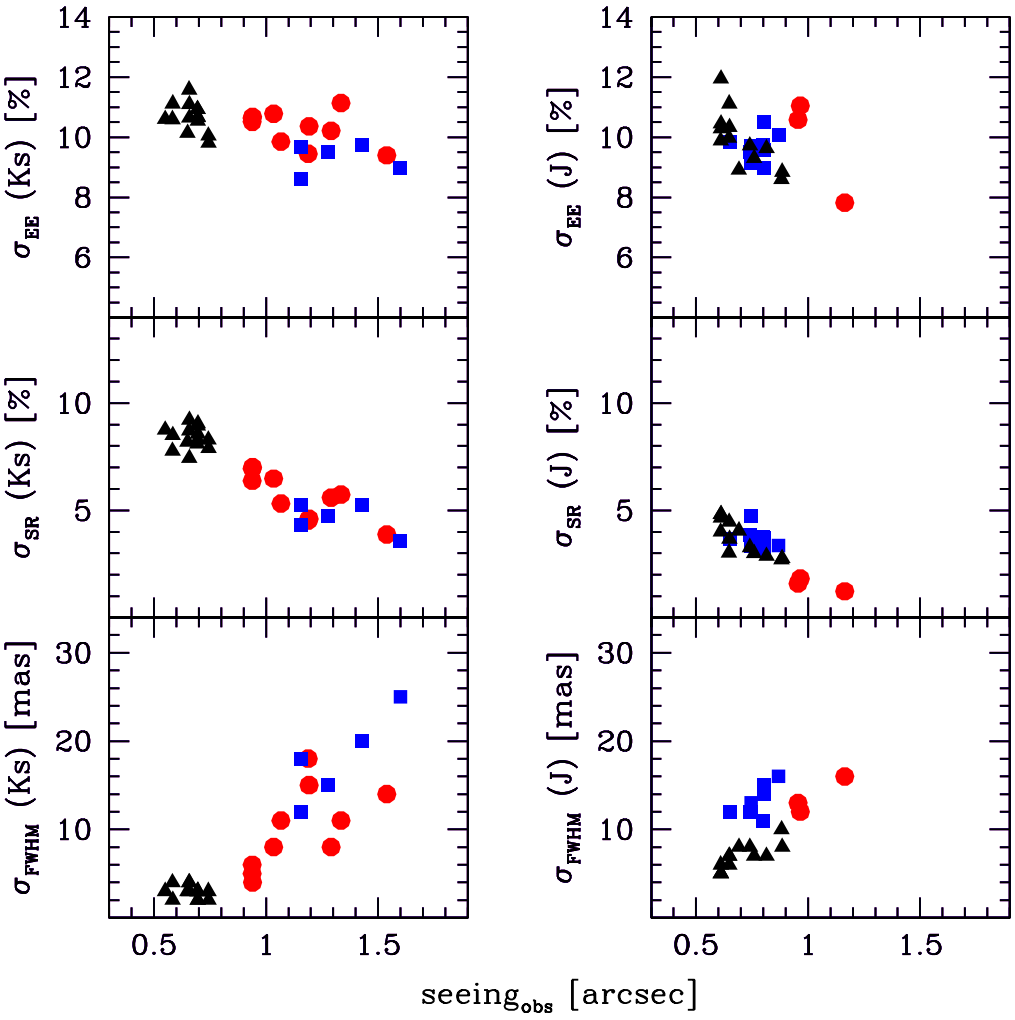

Figure 3.5: Same as in Figure 3.4, but for seeing at 500 nm at the observing airmass.

conditions is somewhat expected. Indeed, at variance with the FWHM, the SR and the EE are quantities somewhat normalized to the seeing contribution. Hence, when the seeing worsens, its contribution progressively dominates over the diffraction limit peak, and being practically constant across the FOV, provides a progressively more uniform PSF.

In order to better visualize the spatial variations of the FWHM, SR and EE, in Figures 3.6 and 3.7 we show the maps of their values for three Liller 1 images acquired under different seeing conditions in the K_s and J bands, respectively. The color coding is the same in both figures to allow a direct comparison. As expected, better performance are obtained in better seeing conditions and closer to the guide star asterism, where AO corrections are more efficient, thus yielding smaller values of FWHM and higher values of the SR and EE. It is also interesting to note that the measured counts of the five LGSs, as reported in the header of the used images,

can vary up to a factor of two, thus possibly contributing to some of the observed gradient.

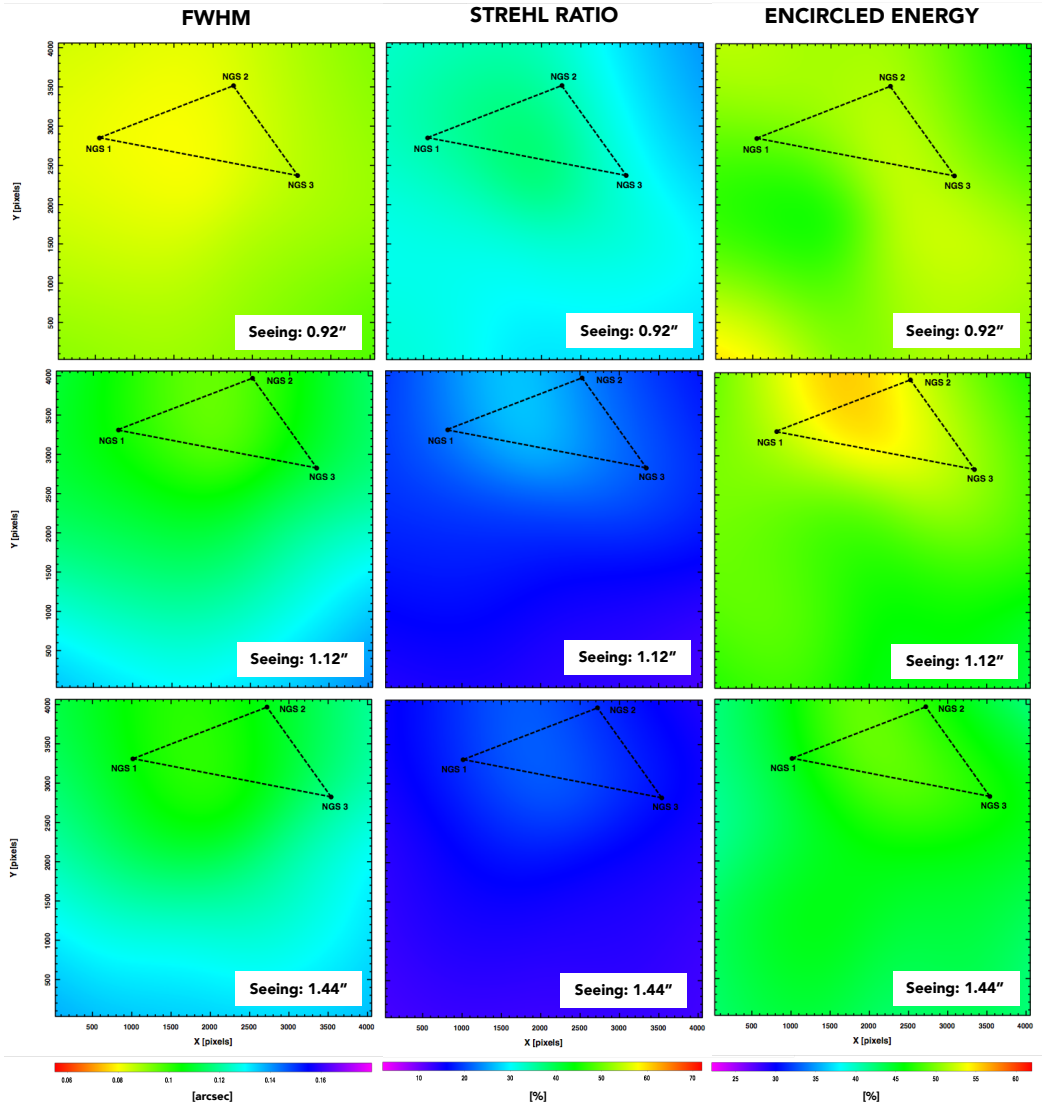

Figure 3.6: FWHM (left panels), SR (middle panels) and EE (right panels) maps for three K_s band images of Liller 1 acquired under different seeing conditions. The triangle indicates the guide star asterism. The quoted seeing values are at the zenith and at 500 nm. Color coding from magenta (worst) to red (best) is a performance indicator.

3.3.3 GeMS/GSAOI *versus* HST/ACS performance

In verifying the potentiality of ground-based MCAO-assisted imagers to obtain accurate photometry in dense stellar fields, it is very interesting to compare the performance of the GeMS/GSAOI system with those of HST. However, to perform a meaningful comparison, it is necessary to probe wavelength ranges where similar diffraction limits are expected between the two telescopes. As the primary mirror of

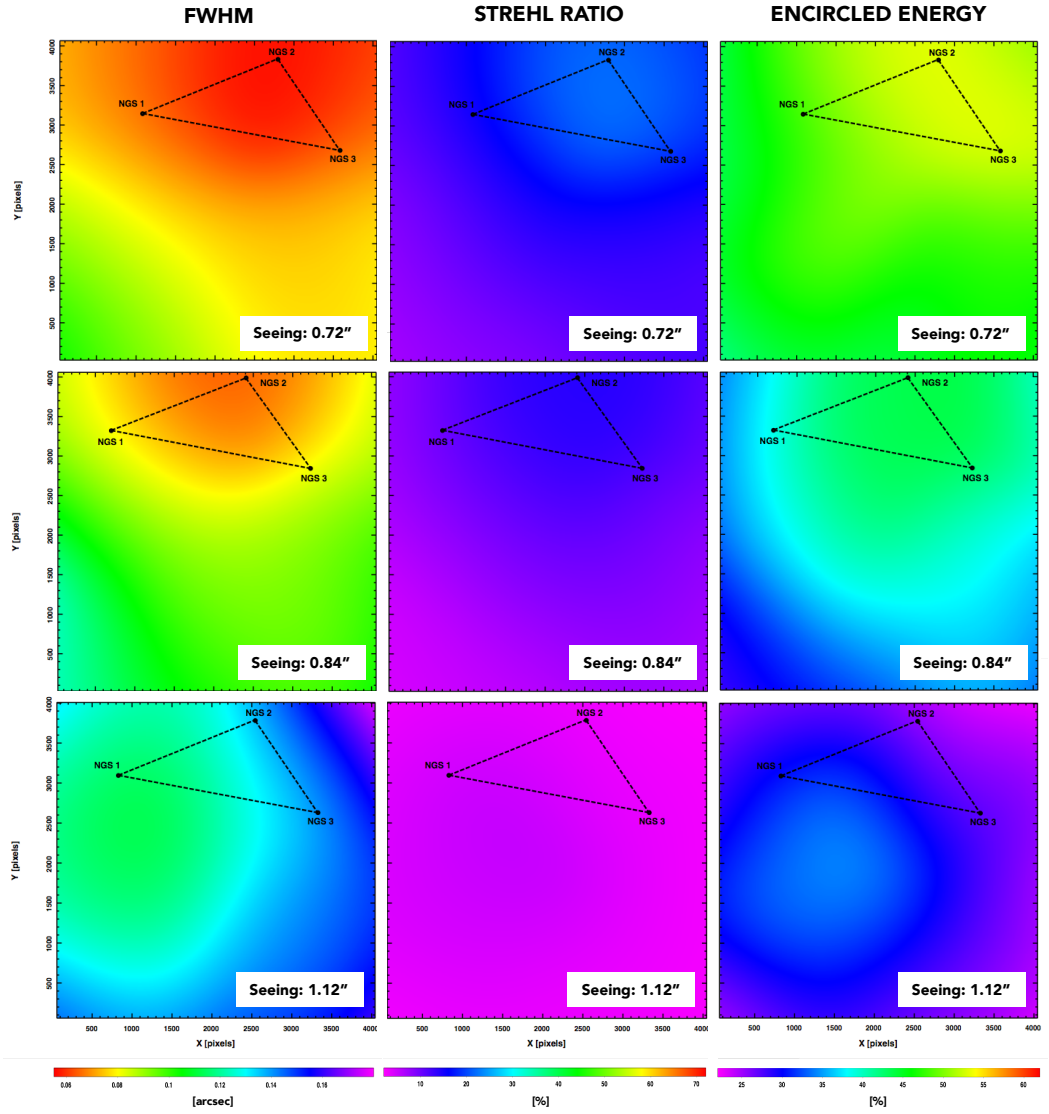

Figure 3.7: FWHM (left panels), SR (middle panels) and EE (right panels) maps for three J band images of Liller 1 acquired under different seeing conditions. The triangle indicates the guide star asterism. The quoted seeing values are at the zenith and at 500 nm. Color coding from magenta (worst) to red (best) is a performance indicator.

HST is about three times smaller ($\sim$ 2.4m) than that of the Gemini South telescope, the diffraction limit expected for Gemini J and K_s images ($0.04'' - 0.07''$), is obtained at optical wavelengths with HST.

We used two short exposures ($t_{exp} = 15$ sec) of NGC 6624 taken with Advanced Camera for Surveys/Wide Field Camera (ACS/WFC) onboard HST, in the F606W and F814W bands (Prop: 10775; PI: Sarajedini). A sample of about 200 high signal-to-noise and isolated stars have been selected to compute average FWHM, SR and EE and their dispersions around the mean, by using the same analysis as for GeMS/GSAOI images.

We obtain average values of FWHM of 82 mas and 86 mas for the F606W and F814W, respectively. While the average FWHM for the F814W is consistent with the nominal diffraction limit of HST at these wavelength ($\sim$ 85 mas), the FWHM in the F606W is significantly larger (by $\sim$ 30%) than the nominal diffraction limit ($\sim$ 63 mas), but this is somewhat expected, since at these wavelengths the limiting factor is the undersampling of the PSF. We find also that the overall variation of the FWHM along the entire ACS FOV ($\sim$ $200'' \times 200''$) is $\sim$ 8%. This value is consistent with a $\pm$10% variation estimated by using a significantly larger dataset by Anderson et al. (2006). For the same stars we estimated $SR \sim 50\%$ and $\sim 65\%$ for the F606W and F814W, respectively, and $\sigma_{SR} < 10\%$ for both filters. Moreover, we find $EE \sim 55\%$ and $\sigma_{EE} \sim 10\%$ for both filters. These latter values are consistent with those estimated by Sirianni et al. (2005; Table 3) within a comparable aperture of 2$\times$FWHM (corresponding to an equivalent circular radius between 50 and 100 mas) for white dwarf spectro-photometric standards located at the center of the two ACS/WFC chips.

In Figure 3.8 we plot the dispersion around the average FWHM, SR and EE values as a function of the corresponding average values for the GeMS/ GSAOI J and K_s images, as well as for the ACS/HST F606W and F814W ones. For sub-arcsec seeing conditions, GeMS / GSAOI delivers images with comparable or even better PSF FWHMs than ACS and also similar uniformity over the FOV (at least in the K_s band). At variance, both the SR and the EE are in most cases lower than the corresponding values of ACS, while their variation over the FOV is comparable (around 10%). Only in the best seeing conditions and in the K_s band, GeMS/GSAOI can reach EE values comparable with those delivered by HST/ACS.

In Figure 3.9 we show the FWHM, SR and EE maps for three NGC 6624 images in the K_s, J and F814W filters, respectively. The color coding is the same of Figures 3.6 and 3.7 for a direct comparison. As in the case of Liller 1, GeMS/GSAOI delivers better performance (i.e. smaller FWHM and higher SR and EE) in the surrounding of the guide star asterism. HST-ACS provides very uniform FWHMs over the entire FOV. SR and EE improve smoothly with increasing the radial distance from the center, as expected since crowding decreases. The stars in the very central region of the cluster (white circular area in the bottom panels of Figure 3.9) were not used to sample the PSF FWHM, SR and EE in the HST images, because measurements are quite uncertain due to the prohibitive crowding. However, it was possible to measure them in the GeMS/GSAOI near infrared images (the sampled FOV is indicated as a black square in Figure 3.9), since in that case crowding by resolved stars is less severe than in the HST images, due to a combination of a slightly higher spatial resolution and a lower sensitivity to faint stars, which only contribute in the form of unresolved stellar background.

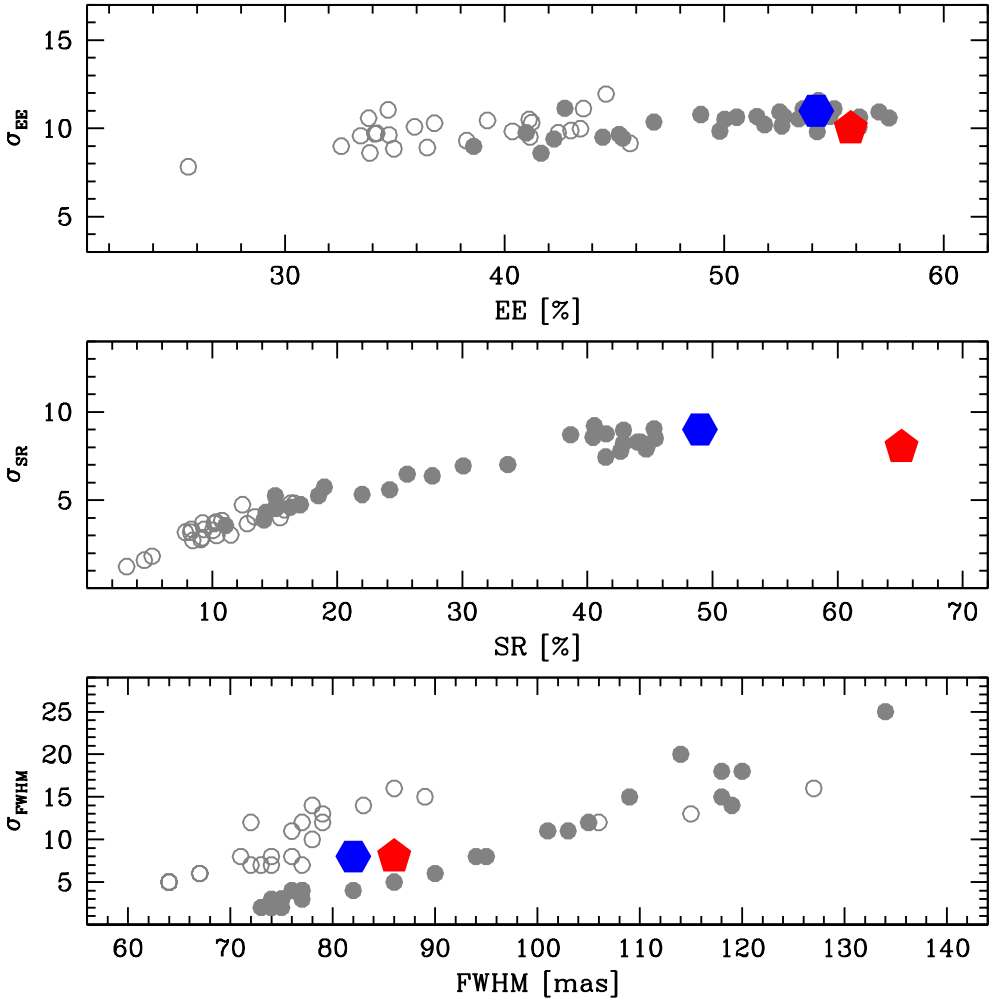

Figure 3.8: Dispersion around the average FWHM, SR and EE values as a function of the corresponding average values for the GeMS/GSAOI J (open circles) and K_s (filled circles) images, and the ACS/HST F606W (hexagon) and F814W (pentagon) ones.

3.4 GeMS/GSAOI astrometric performance

High-precision astrometry is crucial for many science cases in modern astrophysics. In the study of GC stellar populations, precise astrometry is required to measure proper motions and obtaining precious information on the contamination by field stars and on the internal kinematics (see for example Richer et al. 2013; Watkins et al. 2015; Bellini et al. 2015). To measure stellar proper motions one needs to derive position displacements between two (or more) epochs. However in virtually all available instruments, star displacements are not only due to "real" star motions, but they are also the result of instrumental effects (distortions) that alter artificially the position of stars and that need to be modeled to obtain highly accurate astrometric

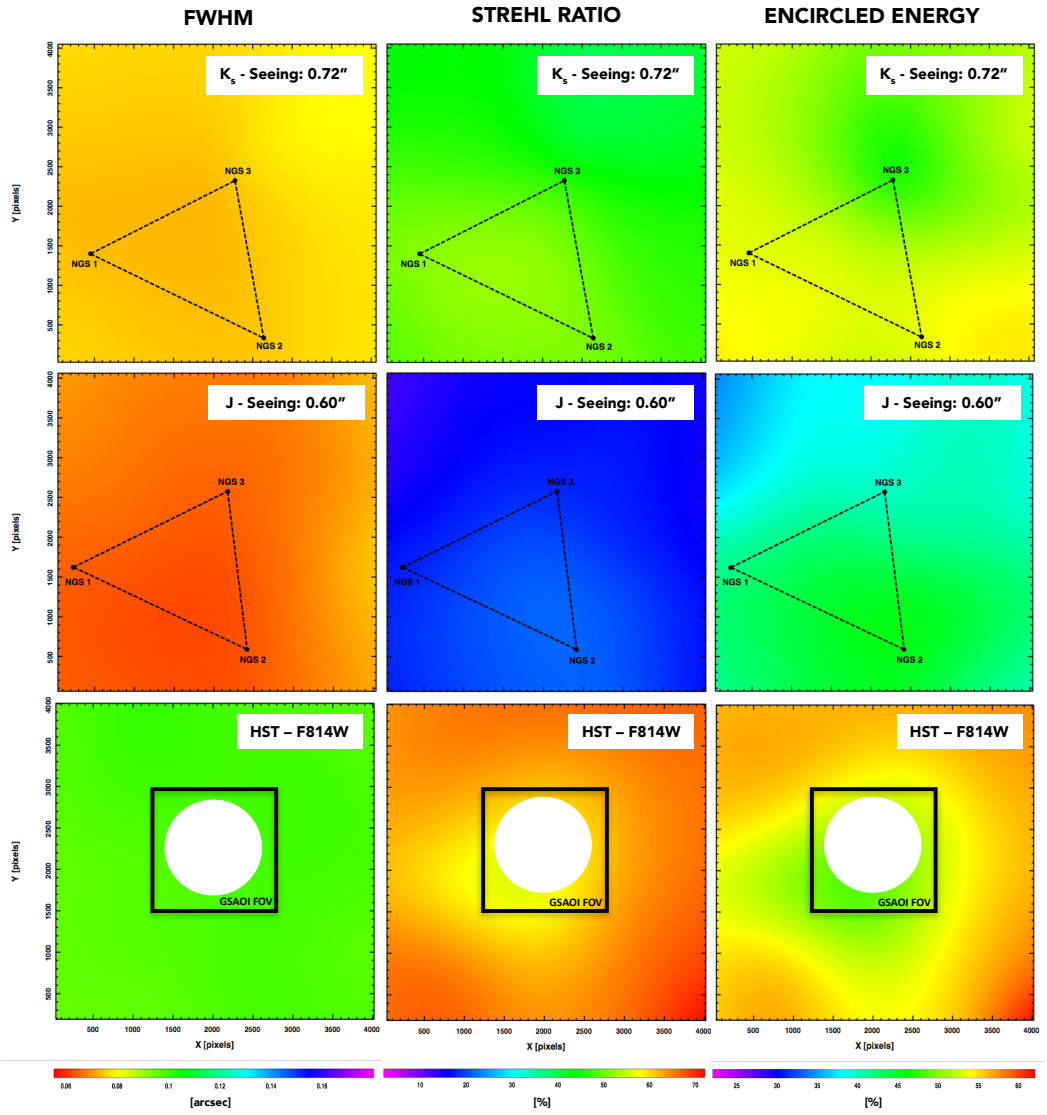

Figure 3.9: FWHM (left panels), SR (middle panels) and EE (right panels) maps for three NGC 6624 images in the K_s (top panels), J (middle panels) and F814W (bottom panels) filters, respectively. The triangle indicates the guide star asterism for the GSAOI ground-based images. The central, white area in the HST maps was excluded due to the prohibitive crowding, while the black square indicates the GeMS/GSAOI FOV.

solutions. In AO-assisted imagers, these distortions are not only of geometric nature, but they can depend also on other factors (like for example anisoplanatism), although in the following we will always refer to them as "geometric distortions" (GDs). A successful approach to model GDs has been proposed for the first time by Anderson and King (2003), who found a distortion solution for the HST Wide Field Planetary Camera 2. In recent years, other similar works aimed at measuring the GD of the ACS and the Wide Field Camera 3 (Bellini and Bedin, 2009; Bellini et al., 2011)

onboard HST or of ground-based imagers such as LBT/LBC, ESO/WFI, VLT/HAWK-I, VISTA/VIRCAM (Anderson et al., 2006; Yadav et al., 2008; Bellini et al., 2009; Bellini and Bedin, 2010; Libralato et al., 2014, 2015), have been published.

An analysis of the internal astrometric performance of GeMS/GSAOI system has been recently presented by Neichel et al. (2014a). They find that for single-epoch, well populated undithered images, an internal astrometric error of ~ 0.2 mas can be achieved for well exposed images ($t_{\rm exp} > 1$ min). On the contrary, for multi-epoch observations, an additional systematic error of $\sim$ 0.4 mas should be considered. According to the authors this is likely due to time-variable distortion induced by gravity instrument flexure.

In this work, we attempt to obtain the first formal analytic solution to the GDs of GeMS/GSAOI for the J and K_s filters and an analysis of the absolute astrometric performance of the system. To this aim, we closely followed the approach described in Anderson and King (2003) and Bellini and Bedin (2009). We used the single epoch dithered (by $\sim 3''$) images (14 in K_s and 13 in J, see Table 3.1) available for NGC 6624. Indeed this is an ideal dataset for this goal for several reasons: *i*) during the observing night, the atmospheric conditions were good and quite stable (average seeing $\approx 0.65''$, airmass close to one); *ii*) dithering allows to analyze both *dynamic* and *static* distortions of the camera (Neichel et al., 2014a); *iii*) a distortion-free catalog of the cluster stars to be used as reference is available.

3.4.1 A geometric distortion solution

The most straightforward way to solve for the GD for a given instrument is to compare the instrumental positions of stars in that instrument with the corresponding ones in a distortion-free reference catalog, so that information about distortions can be directly derived from the stellar positional residuals. For NGC 6624 we used as reference system the ACS catalog published by Sarajedini et al. (2007). In this catalog the positions are corrected for GD effects using the solutions by Anderson and King (2003) and Meurer et al. (2003). It covers a large enough FOV to entirely include the GeMS/GSAOI dataset and it samples the entire magnitude range probed by the GeMS / GSAOI images for NGC 6624.

We combined the ACS catalog with data obtained with the WFC3 UVIS channel within the *HST UV Legacy survey of globular clusters* (Prop: 13297, PI: Piotto; see Piotto et al. 2015 for a description of the dataset) and derived relative proper motions by using the approach described in Massari et al. (2013) and Dalessandro et al. (2013). Only stars in common between the ACS and the WFC3 catalogs and with proper motions $(dx, dy) < 0.1$ mas/yr (corresponding to 0.002 pixel/yr) have been selected to build the *master catalog* and derive the GD solution. Such a selection guarantees that the stars in the *master catalog* are cluster members and are virtually stationary within the proper motion uncertainties, which correspond to $\Delta v \sim 3 - 4$ Km/s with respect to the cluster systemic velocity at the distance of NGC 6624. It is important to stress here that the adopted selection corresponds to the typical proper motion

error for well measured stars obtained with similar datasets. Hence more restrictive criteria have no significant impact on the "quality" of the *master catalog*, but their main effect is on the sample size.

We then matched it with the GeMS/GSAOI catalog of NGC 6624 described in Saracino et al. (2016) and found $\sim$ 7500 stars in common covering the magnitude range $13 < K_s < 19$. The average crowding in this FOV is $\sim$ 13 stars/arcsec^2 at $K_s < 20.3$ mag. The $(V, V-I)$ and $(K_s, J-K_s)$ color-magnitude diagrams of the *master catalog* stars in common with the GeMS/GSAOI catalog of NGC 6624 presented in Saracino et al. (2016) are plotted in Figure 3.10.

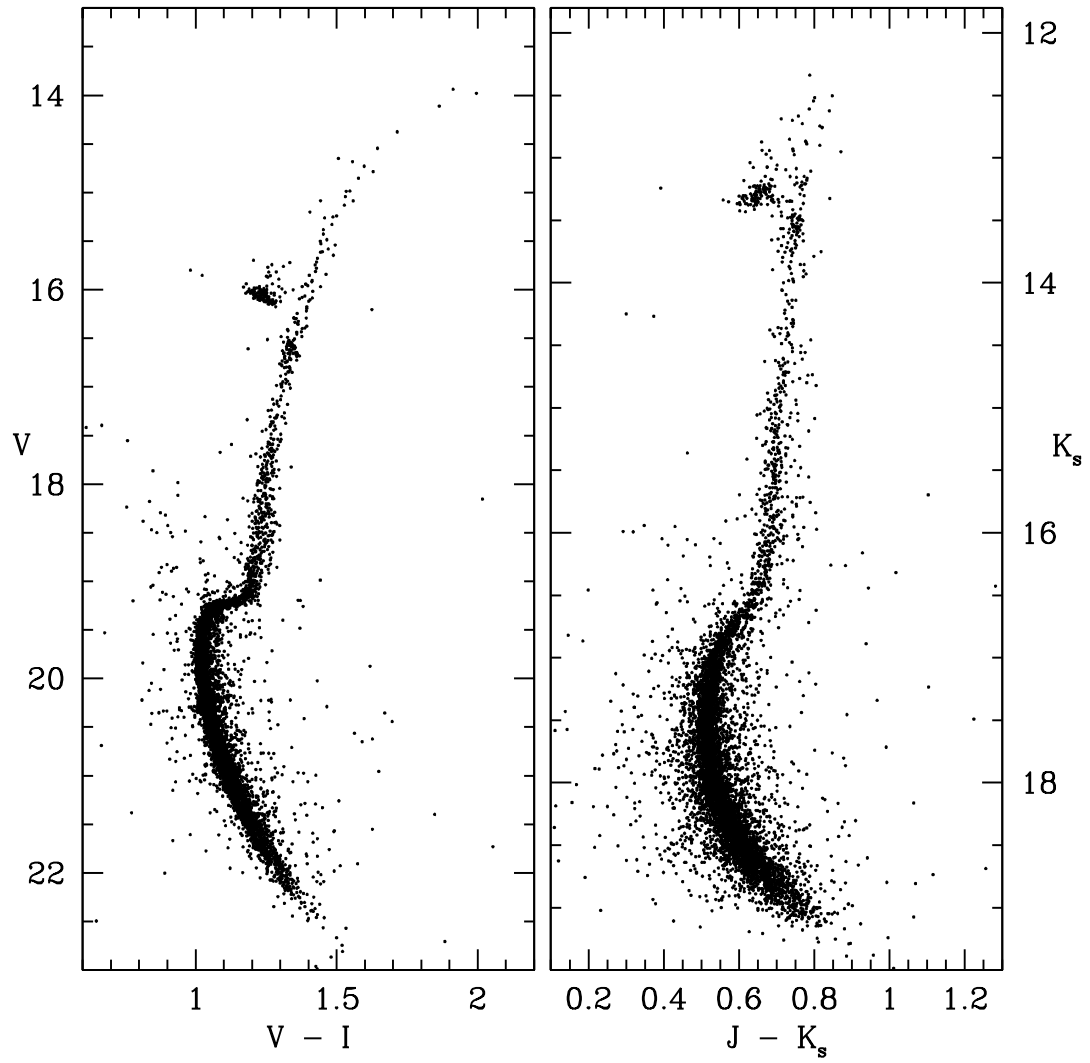

Figure 3.10: $V, V-I$ (left panel) and $K_s, J-K_s$ (right panel) CMDs of the stars in common between the *master catalog* and the GeMS/GSAOI catalog of NGC 6624 by Saracino et al. (2016).

GDs have been computed for each chip, independently, taking as reference center in each chip the position $(x_0, y_0)_k$ = (1024, 1024) in raw pixel coordinates, where the

index k = 1, 2, 3, 4 indicates the considered chip. In fact, obtaining a separate solution for each chip, rather than one that uses a common center of the distortion in the FOV, allows a better handle of potential individual detector effects.

The main steps of the procedure can be summarized as follows (see also Bellini and Bedin, 2009, for more details).

- We conformally transformed[3] each i – star coordinates in the *master catalog* $(X_i^{master}, Y_i^{master})$ into pixel coordinates of each dithered GeMS/GSAOI j–image. We then cross-correlated these nominal positions with those actually measured in each GeMS/GSAOI j–image, thus generating pairs of positional residuals:

$$\begin{cases} \Delta x_{i,j,k} = x_{i,j,k} - (X_i^{master})^{T_{j,k}} \\ \Delta y_{i,j,k} = y_{i,j,k} - (Y_i^{master})^{T_{j,k}} \end{cases} \tag{3.1}$$

  The set of positional residuals $(\Delta x_{i,j,k}, \Delta y_{i,j,k})$ of the stars in the raw images as a function of the $x_{i,j,k}$ and $y_{i,j,k}$ coordinates, determines the amount of GD and its spatial distribution in each chip.

- To create a GD map, we divided each chip (2048 $\times$ 2048 pixels) into grids of (16 $\times$ 16) cells of (128 $\times$ 128) pixels each, in order to have sufficient statistics but also spatial resolution. In each cell we estimated the following parameters[4]: $\overline{x}_{m,k}$, $\overline{y}_{m,k}$, $\overline{\Delta x}_{m,k}$, $\overline{\Delta y}_{m,k}$ and $P_{m,k}$, where m = 1, 256 is the cell reference number in our grid. $\overline{x}_{m,k}$ and $\overline{y}_{m,k}$ are the average positions of all the stars in each grid cell, $\overline{\Delta x}_{m,k}$ and $\overline{\Delta y}_{m,k}$ the average positional residuals, while $P_{m,k}$ indicates the number of stars for each cell.

- We represented our GD solution with a third-order polynomial (we omitted i, j and k indexes for simplicity):

$$\begin{cases} \delta x = a_1\tilde{x} + a_2\tilde{y} + a_3\tilde{x}^2 + a_4\tilde{x}\tilde{y} + a_5\tilde{y}^2 + a_6\tilde{x}^3 + a_7\tilde{x}^2\tilde{y} + a_8\tilde{x}\tilde{y}^2 + a_9\tilde{y}^3 \\ \delta y = b_1\tilde{x} + b_2\tilde{y} + b_3\tilde{x}^2 + b_4\tilde{x}\tilde{y} + b_5\tilde{y}^2 + b_6\tilde{x}^3 + b_7\tilde{x}^2\tilde{y} + b_8\tilde{x}\tilde{y}^2 + b_9\tilde{y}^3 \end{cases} \tag{3.2}$$

  We verified that a larger number of degrees of freedom did not significantly improve our solution. In this system, $\tilde{x}$ and $\tilde{y}$ indicate the positions of individual stars relative to the central pixel $(x_0, y_0)_k$ = (1024, 1024) of each chip, and $a_{0,k}..a_{9,k}$ and $b_{0,k}..b_{9,k}$ are the 18 coefficients that we need to determine.

  To do this, we performed a linear least-square fit of the 256 data points in each grid cell, which actually means solving a matrix system.

[3] A conformal transformation, also called Helmert transformation, allows to switch from one reference system to another, through a change of scale, a rotation and two rigid shifts along x and y axes, respectively.

[4] The average values of these quantities have been obtained by applying a 3σ-rejection.

- After the first GD solution, we determined the distortion corrected positions ($x^{corr}_{i,j,k}$, $y^{corr}_{i,j,k}$) as the observed positions ($x_{i,j,k}$, $y_{i,j,k}$) plus the distortion corrections ($\delta x_{i,j,k}$, $\delta y_{i,j,k}$):

$$\begin{cases} y^{corr}_{i,j,k} = x_{i,j,k} + \delta x(\tilde{x}_{i,j,k}, \tilde{y}_{i,j,k}) \\ y^{corr}_{i,j,k} = y_{i,j,k} + \delta y(\tilde{x}_{i,j,k}, \tilde{y}_{i,j,k}) \end{cases} \tag{3.3}$$

- The procedure was iterated more than 30 times for chip by applying at each iteration, only half of the correction in order to avoid convergence problems, until the difference in the positional residuals ($\Delta x_{i,j,k}$, $\Delta y_{i,j,k}$ vs $x_{i,j,k}$, $y_{i,j,k}$) from one iteration to the following one became negligible (in other words, when the $\chi^2_{iterN} \approx \chi^2_{iterN+1}$).

The coefficients $a_{q,k}$ and $b_{q,k}$ ($q = 1...9$) of the final GD solution for the four chips are given in Table 3.3 for the K_s filter, and in Table 3.4 for the J one.

Table 3.3: Coefficients of the third-order polynomial for each chip, representing the final GD solution for the K_s filter.

Term(q)	Polyn.	$a_{q,[1]}$	$b_{q,[1]}$	$a_{q,[2]}$	$b_{q,[2]}$	$a_{q,[3]}$	$b_{q,[3]}$	$a_{q,[4]}$	$b_{q,[4]}$
1	$\tilde{x}$	7.2959	-8.1224	-8.2342	-8.0700	-8.6718	5.5598	7.7150	5.3724
2	$\tilde{y}$	-8.6592	-6.9948	-9.5140	7.0969	5.8746	7.4350	6.7219	-5.4231
3	$\tilde{x}^2$	6.7348	0.0217	7.0562	0.0903	6.9963	0.0301	6.8232	0.1139
4	$\tilde{x}\tilde{y}$	0.1646	-0.0045	0.1435	-0.0719	0.1301	-0.0197	0.2890	0.1021
5	$\tilde{y}^2$	6.6305	0.1600	6.7711	0.2774	6.7787	0.2803	6.7095	0.4254
6	$\tilde{x}^3$	0.0688	0.0089	-0.0635	0.0066	-0.0855	0.0042	0.1567	0.0100
7	$\tilde{x}^2\tilde{y}$	0.0251	0.0770	0.0941	0.0112	-0.0543	-0.0347	0.0113	-0.0045
8	$\tilde{x}\tilde{y}^2$	-0.0922	-0.0215	0.0010	0.0774	-0.0600	0.0543	-0.0449	0.0378
9	$\tilde{y}^3$	0.0300	0.0824	-0.0325	-0.0003	0.0305	0.0243	-0.0151	0.0544

Figures 3.11 and 3.12 show the GD map and the residual trends of uncorrected star positions for the four chips of the GSAOI camera, in the K_s and J filters, respectively. In both cases, the size of the residual vectors is magnified by a factor of 10. Residual vectors connect the uncorrected average positions within each grid cell to the corrected ones. We also show the overall trend of the positional residuals ($\Delta x_{i,j,k}$ vs $x_{i,j,k}$; $y_{i,j,k}$) and ($\Delta y_{i,j,k}$ vs $x_{i,j,k}$; $y_{i,j,k}$). These trends are quite similar/symmetric in the four chips, with a maximum amplitude of $\sim$ 30 pixels both along the x and y axis. In Figures 3.13 and 3.14 we show the final residuals of the star positions in K_s and J filters, respectively, after applying our GD solution (residuals vectors are magnified by a factor 5000). Our GD solution allowed to linearize the residual trends in each chip and to reach an astrometric accuracy of about 0.07 pixels corresponding to $\sim$ 1.5 mas. In this respect it is worth recalling that, given the proper motion selection (0.1

Table 3.4: Coefficients of the third-order polynomial for each chip, representing the final GD solution for the *J* filter.

Term(q)	Polyn.	$a_{q,[1]}$	$b_{q,[1]}$	$a_{q,[2]}$	$b_{q,[2]}$	$a_{q,[3]}$	$b_{q,[3]}$	$a_{q,[4]}$	$b_{q,[4]}$
1	$\tilde{x}$	7.3378	-8.0391	-8.2090	-8.1578	-8.5896	5.6014	7.3445	5.3859
2	$\tilde{y}$	-8.5374	-6.8857	-9.5506	7.1074	5.9348	7.4968	6.6005	-5.4962
3	$\tilde{x}^2$	6.6703	0.0347	7.0411	0.0730	6.9823	0.0685	6.7324	-0.0230
4	$\tilde{x}\tilde{y}$	0.1721	0.0946	0.1203	-0.1116	0.1075	-0.0342	0.3678	0.1387
5	$\tilde{y}^2$	6.6176	0.1077	6.7432	0.2616	6.7769	0.2681	6.6951	0.2807
6	$\tilde{x}^3$	0.0220	-0.0157	-0.0464	0.0125	-0.1522	-0.0251	0.2020	-0.0321
7	$\tilde{x}^2\tilde{y}$	-0.0288	0.0233	0.1379	0.0417	-0.1129	-0.0846	0.0102	-0.0558
8	$\tilde{x}\tilde{y}^2$	-0.2149	-0.2188	0.0099	0.1537	-0.1227	0.0069	-0.0205	0.0358
9	$\tilde{y}^3$	0.0112	0.0140	0.0088	-0.0184	0.0092	-0.0102	-0.0273	0.0575

mas/yr) adopted to build the *master catalog* and that the GeMS/GSAOI images have been acquired about 7 yr after the first HST epoch, the total contribution to the final GD error budget due to proper motions can be as large as ~ 0.7 mas in this case.

As shown by Neichel et al. (2014a), the astrometric accuracy of ground-based instruments in general, and assisted by AO-systems in particular (e.g. GeMS/GSAOI), depends on a few major factors, namely: *i*) the PSF shape and variability in the FOV; *ii*) the atmospheric conditions (i.e. the seeing at the observing airmass); *iii*) the brightness of the three NGSs and their asterism; *iv*) the crowding of the observed field; *v*) the exposure time.

Because of these important factors, our GD solution based on the observations of NGC 6624 should be further tested on other stellar fields with different crowding and acquired with different atmospheric conditions, asterisms and exposure times and with available high resolution astrometric reference catalogs (likely from HST imaging). While the general formal solution would likely be still valid at a first order approximation, datasets obtained under different observing conditions may yield different coefficients. Unfortunately, our observations of Liller 1 cannot be used for such a test since for this very reddened cluster an astrometric reference catalog based on high resolution data is not available.

However, we have verified that the GD residuals (after correction) obtained for NGC 6624, are quantitatively compatible with those obtained for NGC 6681 (Massari et al., 2016a) observed under different seeing conditions and NGS asterism. Our results are also qualitatively consistent with those obtained by Ammons et al. (2016) for the globular cluster NGC 1851, although a more quantitative comparison is not possible because the authors do not provide enough details.

It is also important to stress that the analysis described in this Section has a general relevance, since it provides the mathematical formalism to correct for GDs and it can be thus effectively applied to any photometric dataset.

3.5 Conclusions

The PSF tests performed on the GeMS/GSAOI J and K_s images of the central region of two high-density globular clusters have provided very interesting results.

The ground-based MCAO-assisted imager GeMS/GSAOI instrument at Gemini South observatory provides a unique and powerful facility to derive accurate stellar photometry at nearly the diffraction limit spatial resolution, at least in the K_s band where AO correction is more efficient. Uniform (at a level of $\sim$10%) PSF over $1' - 2'$ FOV with up to $50 - 60$% EE within 2 FWHM can be obtained in good seeing conditions. These performance are comparable with those delivered by HST imagers at optical wavelengths.

Following the same strategy adopted for other imagers onboard HST and for wide-field ground-based cameras, we were also able to compute GDs for GeMS/GSAOI and provide corrected images with an astrometric accuracy of ~ 1.5 mas in a stellar field with a crowding of $\sim$13 stars/arcsec^2 at $K_s \leq 20.3$ mag, thus demonstrating that a ground-based MCAO-assisted imager at an 8m-class telescope can provide accurate NIR photometry and absolute astrometry for proper motion studies in very dense stellar fields, in some cases outperforming HST's capability, due to the higher spatial resolution. HST with its ACS and WFC3 imagers remains somewhat unique in providing photometry of the faintest stars in less crowded regions.

Looking at the future facilities, complementarity can be foreseen also with JWST, that will provide the deepest photometry in the NIR over a few arcmin FOV at about the same spatial resolution of HST, and ground-based MCAO-assisted imagers at 20-40m class telescopes, which will provide significantly higher spatial resolution at the same wavelengths of JWST but over a smaller FOV.

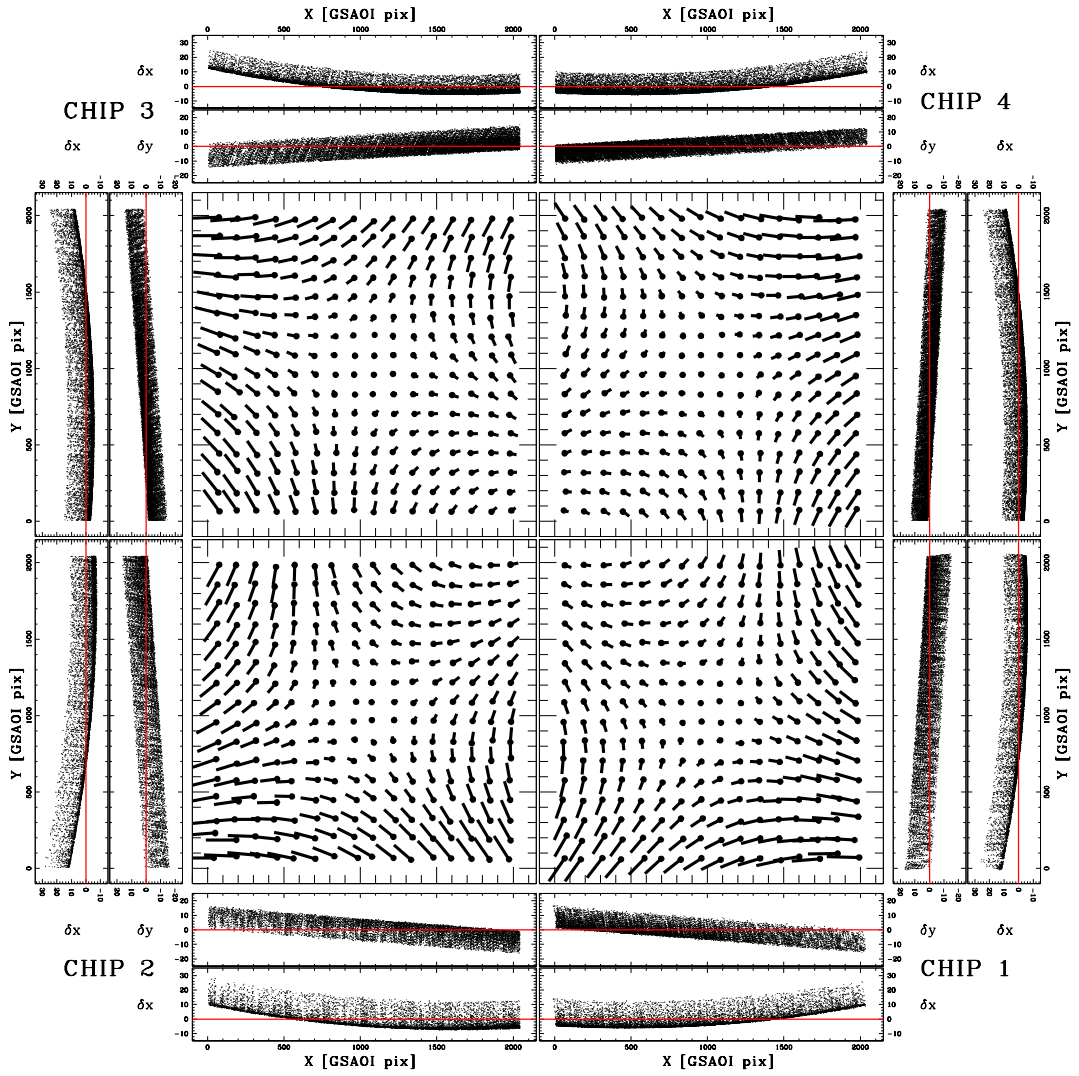

Figure 3.11: Geometric distortion map of the four chips of GSAOI camera, in the K_s filter. Residual vectors are magnified by a factor of 10. For each chip, we also show individual residuals as function of x and y axes. Units are in GSAOI pixels.

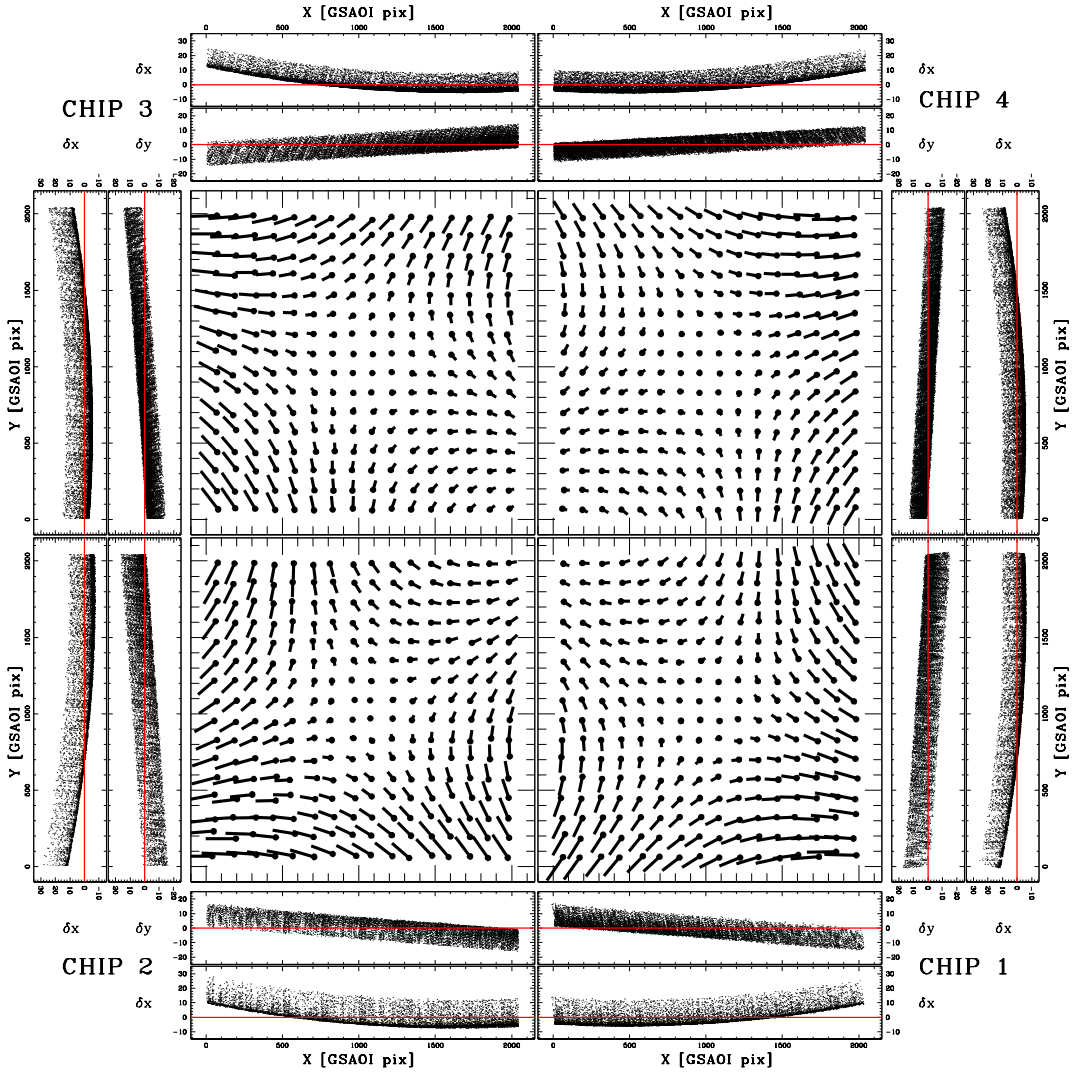

Figure 3.12: As in Figure 3.11, but for the *J* band.

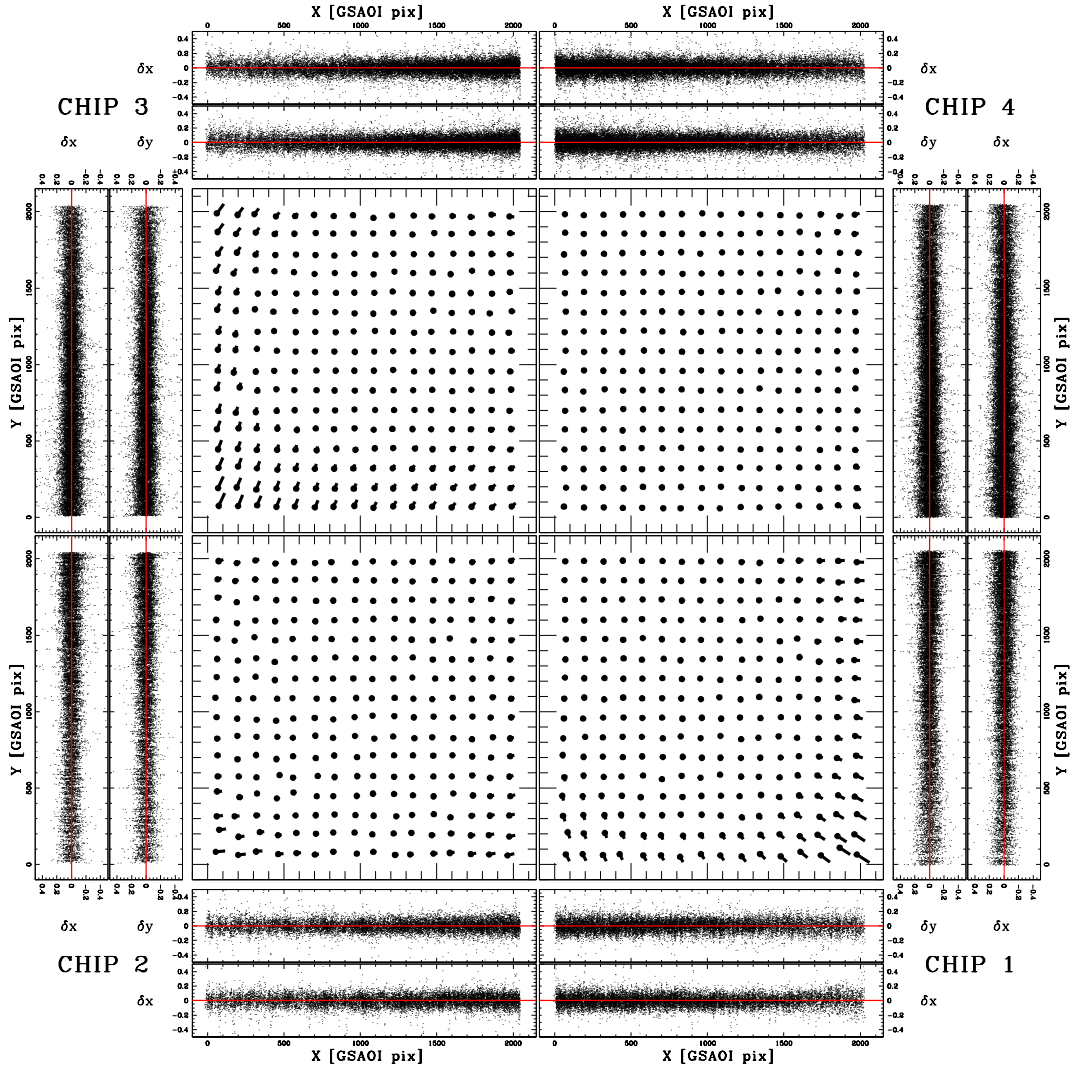

Figure 3.13: Residual map of the four chips of GSAOI camera, in the K_s filter, after the GD correction. Residual vectors are magnified by a factor of 5000.

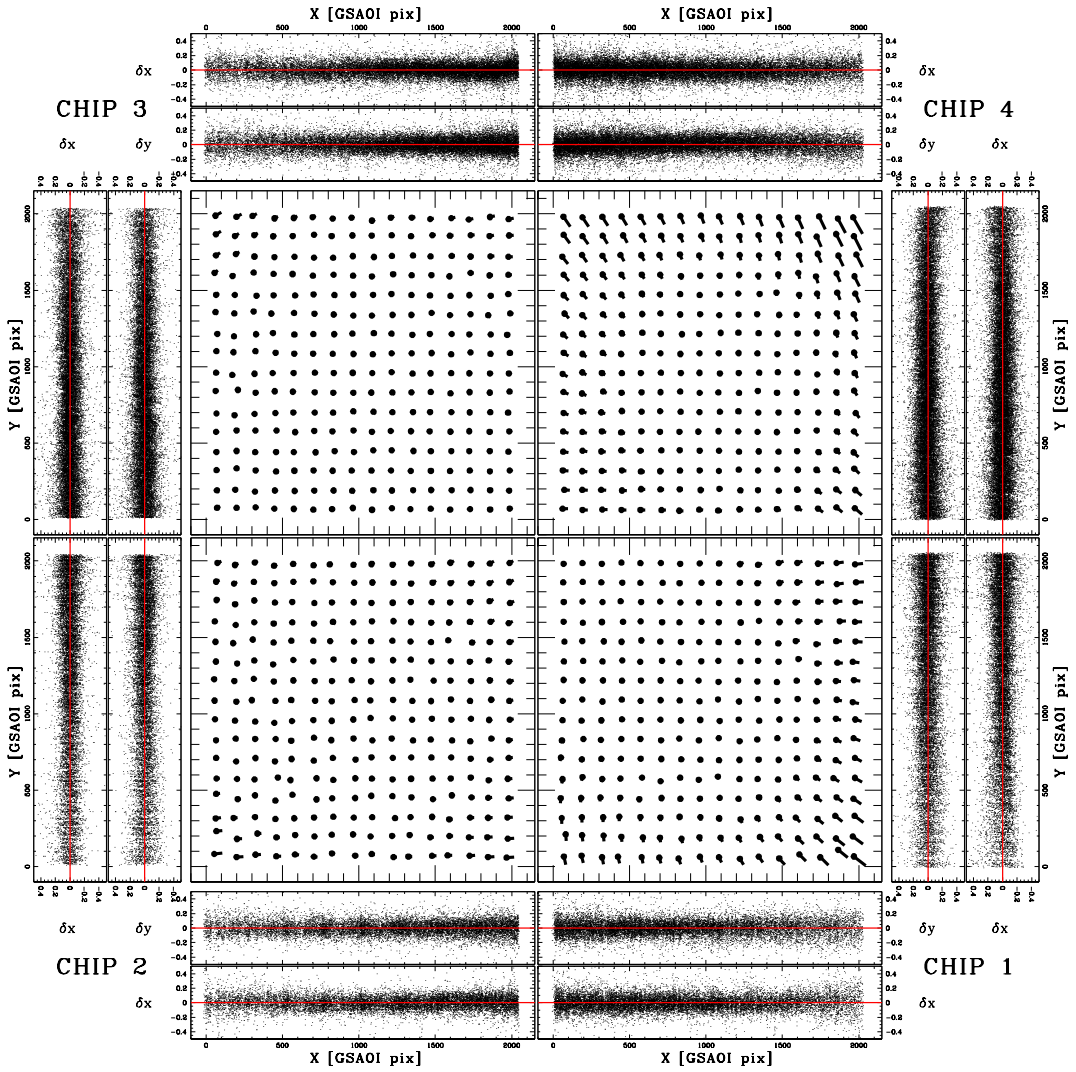

Figure 3.14: As in Figure 3.13, but for the *J* band.

CHAPTER 4

GEMINI/GeMS observations unveil the structure of the heavily obscured globular cluster Liller 1

Based on the results published in:
Saracino S., Dalessandro E., Ferraro F. R., Lanzoni B., Geisler D., Mauro F., Villanova S., Moni-Bidin C., Miocchi P., Massari D.
2015, *The Astrophysical Journal*, **806, 152S**

Subject of a GEMINI-INAF Press Release, June 15 2015:
Seeing where stars collide

Abstract

By exploiting the exceptional high resolution capabilities of the NIR camera GSAOI combined with the MCAO system GeMS at the Gemini South Telescope, we investigated the structural and physical properties of the heavily obscured GC Liller 1 in the Galactic bulge. We have obtained the deepest and most accurate CMD published so far for this cluster, reaching $K_s \sim 19$ (below the MS-TO level). We used these data to re-determine the center of gravity of the system, finding that it is located about 2.2″ south-east from the literature value. We also built new star density and surface brightness profiles for the cluster, and re-derived its main structural and physical parameters (scale radii, concentration parameter, central mass density, total mass). We find that Liller 1 is significantly less concentrated (concentration parameter $c = 1.74$) and less extended (tidal radius $r_t = 298''$ and core radius $r_c = 5.39''$) than previously thought. By using these newly determined structural parameters we estimated the mass of Liller 1 $M_{\rm tot} = 2.3\,^{-0.1}_{+0.3} \times 10^6 M_\odot$ ($M_{\rm tot} = 1.5\,^{-0.1}_{+0.2} \times 10^6 M_\odot$ for a Kroupa IMF), which is comparable to that of the most massive clusters in the Galaxy (ω Centauri and Terzan 5). Also Liller 1 has the second highest collision rate (after Terzan 5)

among all star clusters in the Galaxy, thus confirming that it is an ideal environment for the formation of collisional objects (such as MSPs).

4.1 Introduction

Liller 1 is one of the 7 GCs located within 1 kpc from the Galactic centre, at a Galactocentric distance of only 0.8 kpc, and very close to the Galactic plane ($l = 354.84$, $b = -0.16$; Harris 1996, 2010 edition, hereafter H96). This region of the Galaxy is strongly affected by a large foreground extinction: the average color excess $E(B-V)$ estimated by different authors in the direction of the cluster ranges from about 3.00 to 3.09 (Frogel et al., 1995; Ortolani et al., 1996, 2001; Valenti et al., 2010) with significant evidence of differential reddening (Ortolani et al., 2001). Such a large value of the extinction has severely hampered the observations of Liller 1 in the optical bands. Indeed very few papers about this cluster can be found in the literature: the only available optical CMD of Liller 1 is the one published by Ortolani et al. (1996) by using ESO-NTT data. More in general, the first CMD ever obtained for Liller 1 is the (K,J-K) CMD published by Frogel et al. (1995). However in both cases data are very shallow and the authors were able to sample only the brightest part of the RGB. The deepest photometry of Liller 1 published so far, was obtained by Davidge (2000) and Ortolani et al. (2001) using the Canada-France-Hawaii Telescope and the HST, respectively. However, these samples are not deep enough to properly characterize the MS-TO region of the cluster. A more recent photometric analysis of Liller 1 was performed by Valenti et al. (2010) by using the large NIR wide FOV imager SOFI mounted at the ESO-NTT. The obtained CMD samples the brightest portion of the RGB reaching the cluster RC level ($K_s \sim 14$).

Liller 1 is one of the most metal-rich GC in the Galactic bulge. In fact by using high resolution IR spectroscopy (Origlia et al., 1997), both Origlia et al. (2002) and Stephens and Frogel (2004) measured a metallicity of about one half solar ([Fe/H]$= -0.3$ dex). A similar value ([Fe/H]$= -0.36$ dex) was also estimated by Valenti et al. (2010) from a set of photometric indices (see Ferraro et al. 2000) characterizing the location and the morphology of the RGB in the (K_s, $J-K_s$) CMD, and calibrated as a function of the metallicity (Valenti et al., 2004a,b).

One of the most astonishing characteristics of Liller 1 is the extremely large value of the collision rate parameter. Verbunt and Hut (1987) showed that Liller 1 has the second highest value of stellar encounter rate (after Terzan 5; see also Lanzoni et al. 2010) among all star clusters in the Galaxy, thus suggesting that it represents an ideal environment where exotic objects, generated by collisions, can form. In fact, it is commonly believed that dynamical interactions in GCs facilitate the formation of close binary systems and exotic objects like Cataclysmic Variables (CVs), Low Mass X-ray Binaries (LMXBs), MSPs and Blue Straggler Stars (BSSs) (Bailyn, 1992; Paresce et al., 1992; Ferraro et al., 2001, 2009b, 2012; Ransom et al., 2005; Pooley and Hut, 2006, e.g.). Moreover, Hui et al. (2010) found that clusters with large collisional parameters

and high metallicity (see also Bellazzini et al., 1995) usually host more MSPs. Indeed Terzan 5[1] hosts the largest population of MSPs among all Galactic GCs (Ransom et al., 2005). A strong γ-ray emission has been recently detected in the direction of Liller 1 by the Large Area Telescope (LAT) on board the Fermi Telescope (Tam et al., 2011). This is the most intense emission detected so far from a Galactic GC, again suggesting the presence of a large number of MSPs. However, no direct radio detection of these objects has been obtained so far in this system (Ransom et al., 2005). The only exotic object identified in the cluster is the rapid burster MXB 1730-335, an LMXB observed to emit radio waves and type I and type II X-ray bursts (Hoffman et al., 1978). It seems to be located in the central region of Liller 1, but no optical/IR counterpart of this object has been found so far (Homer et al., 2001).

In this chapter we present the deepest NIR photometry of Liller 1 yet obtained and new determinations of its main structural and physical parameters. In Section 4.2 we discuss the observations and data analysis. Section 4.3 presents the results obtained, including new determinations of: the distance modulus and reddening (Sect. 4.3.1), the center of gravity (Sect. 4.3.3), the star density profile, the structural parameters and the surface brightness (SB) profile (Sect. 4.3.4), the total luminosity, total mass and central mass density of the cluster (Sect. 4.3.5). The summary and conclusions are presented in Section 4.4.

4.2 Observations and data analysis

The main photometric data used in the present study consist of a set of high resolution images obtained with the IR camera Gemini South Adaptive Optics Imager (GSAOI) assisted by the Gemini Multi-Conjugate Adaptive Optics System (GeMS) mounted at the 8 m Gemini South Telescope (Chile), in April 2013 (Program ID: GS-2013-Q-23; PI: D. Geisler). GSAOI is equipped with a 2×2 mosaic of Rockwell HAWAII-2RG 2048×2048 pixels arrays. It covers a global FOV of $85'' \times 85''$ on the sky, with a resolution of $0.02''$/pixel (Neichel et al., 2014b). We sampled the central region of Liller 1 with a mosaic of multiple exposures acquired with a dithering pattern of a few arcseconds. Seven and ten exposures have been acquired in the J and K_s bands, respectively, with an exposure time $t_{\rm exp} = 30$ s each. The entire data set was acquired in an interval of time of $\sim$ 90 mins. A constellation of five LGSs combined with three NGSs has been adopted to compensate the distortions due to the turbulence of Earth's atmosphere. We have verified that the FWHM is quite stable allover the FOV with a maximum variation of about $10 - 15\%$, in agreement with what found by Neichel et al. (2014b). The average FWHM (i.e. estimated on the entire FOV) varies from $0.09''$ to $0.13''$ for the images acquired in the J band and from $0.08''$ to $0.12''$ for the K_s ones. These values are only slightly larger than the diffraction limit of the

[1]Note that this stellar system is suspected to not be a genuine GC, because it harbors at least three stellar populations with different iron abundances (Ferraro et al., 2009a; Origlia et al., 2011, 2013; Massari et al., 2014b).

telescope. In Figure 4.1 we show a two-color image of Liller 1, obtained by combining GEMINI J and K_s band observations.

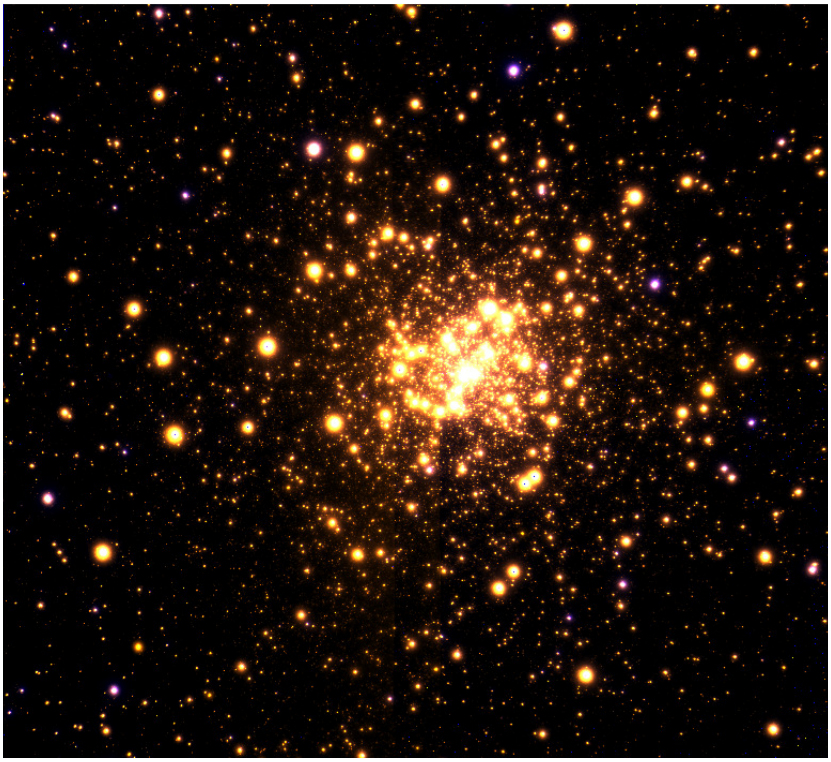

Figure 4.1: False-color image of Liller 1 obtained by combining GEMINI observations in the NIR J and K_s bands. North is up, east is on the right. The FOV is 85″ × 85″. The bluish stars are hot field objects.

As discussed in Section 4.3 below, in order to derive the radial star density and SB profiles of Liller 1, we complemented this data set with a near-IR catalog from the VVV survey (Minniti et al. 2010; Catelan et al. 2011) complemented with the photometric survey (Cutri et al., 2003).

For the GEMINI data set, a standard pre-reduction procedure, using IRAF[2] tools, was applied to the raw images to correct for flat fields and bias, and to perform the sky-subtraction. The photometric reduction was then carried out via PSF fitting technique in each chip of each image independently, using DAOPHOT (Stetson, 1987), a package developed to perform accurate photometry in crowded fields. The PSF has been modeled by selecting about one hundred bright and isolated stars uniformly distributed in each chip, and by using the DAOPHOT/PSF routine. We allowed the PSF to vary within each chip following a cubic polynomial spatial variation. The best-fit PSF analytic models obtained for the J and K_s images, selected on the basis of a χ^2 test, are a Penny function (Penny, 1976) and a Moffat function with $\beta = 1.5$ (Moffat, 1969), respectively. The PSF models thus obtained were then applied to

[2]IRAF is distributed by the National Optical Astronomy Observatory, which is operated by the Association of Universities for Research in Astronomy, Inc., under cooperative agreement with the National Science Foundation.

all the star-like sources detected at a 3σ level from the local background by using ALLSTAR. We have derived in this way the stellar instrumental magnitudes. Then, starting from the star lists thus obtained and to fill the gaps among the GSAOI chips, we created a master star list containing all the stars measured in at least one J and K_s image.

As done in other works (see, e.g., Dalessandro et al. 2014, and reference therein), the master-lists thus created have been used as input for ALLFRAME (Stetson, 1994). The files obtained as output have been combined to have a complete catalog with the J and K_s magnitudes and the positions of all detected stars. For every stellar source, different magnitude estimates have been homogenized and their mean values and standard deviations have been finally adopted as the star magnitudes and photometric errors in the final catalog (see Ferraro et al. 1991, 1992).

The distribution of the photometric errors as a function of the J and K_s magnitudes are shown in Figure 4.2. Errors vary from 0.01 - 0.02 for bright RGB stars, and they reach values $\sigma_{rmK} \sim 0.1$ and $\sigma_{rmJ} \sim 0.3$. As expected, given the overall stability of the PSF, we do not observe any significant radial trend.

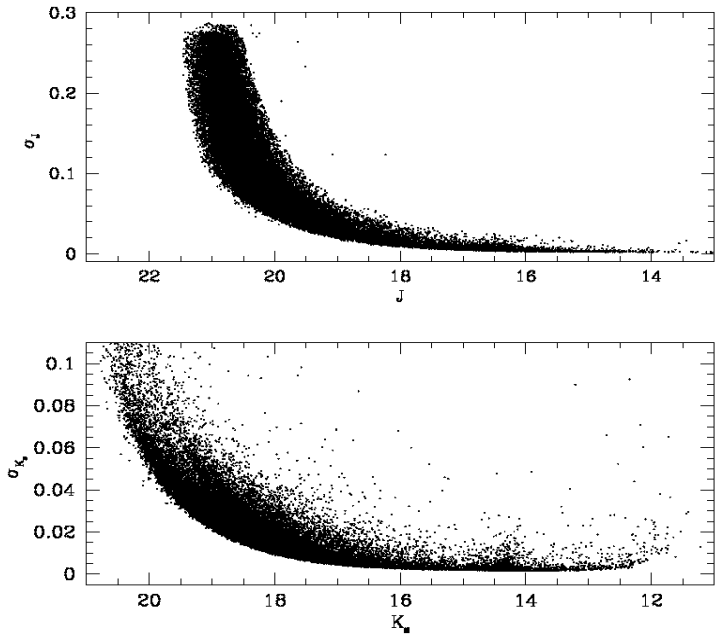

Figure 4.2: Distribution of the photometric errors of the GEMINI data set as a function of J and K_s magnitudes (upper and lower panel, respectively).

The instrumental magnitudes have been converted into the 2MASS photometric system by using the stars in common with the publicly available catalog obtained with SOFI (Valenti et al., 2010). To minimize the effect of blending, photometric errors and saturation, we used only stars at a distance larger than 30" from the cluster center and with 2.8 $<$ (SOFI K_s - GeMS K_s) $<$ 3.6 and 2.6 $<$ (SOFI J - GeMS J) $<$ 3.6, respectively. The J and K_s calibration curves are shown in Figure 4.3. As can be seen,

we used an iterative sigma-clipping procedure to estimate the median of the (SOFI K_s - GeMS K_s) and (SOFI J - GeMS J) distributions for the stars satisfying the criteria listed above. The r.m.s of the best-fit relation is 0.1 and 0.08 in K_s and J, respectively. The values thus obtained (Figure 4.3) have been applied to the instrumental GeMS magnitudes. The same stars have been used also to put the instrumental positions onto the absolute astrometric system.

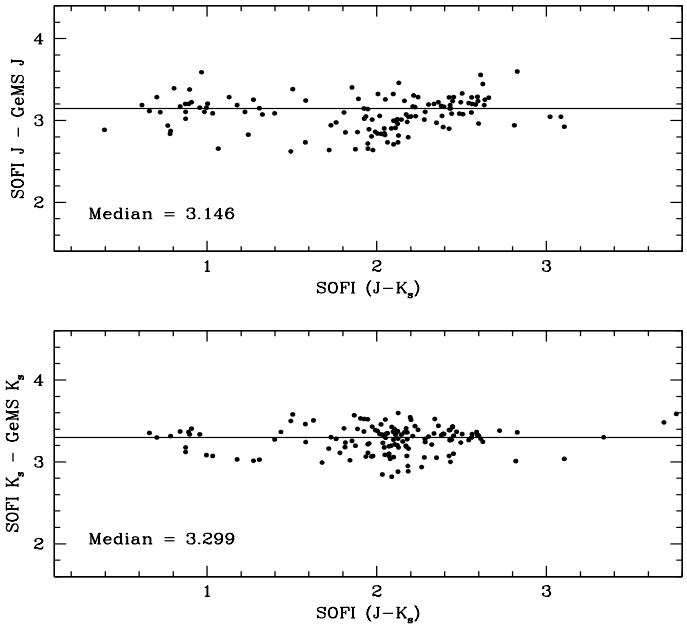

Figure 4.3: Distributions of the (SOFI - GeMS) magnitudes as a function of the SOFI color $(J - K_s)$. Stars at a distance larger than 30″ from the cluster center and with 2.8 $<$ (SOFI K_s - GeMS K_s) $<$ 3.6 and 2.6 $<$ (SOFI J - GeMS J) $<$ 3.6 respectively, are shown in figure. The solid lines instead represent the median values obtained by applying an iterative σ-clipping procedure. Finally we obtain (SOFI K_s - GeMS K_s) = 3.299 and (SOFI J - GeMS J) = 3.146.

We retrieved VVV images obtained in the direction of Liller 1 from the Vista Science Archive website[3]. The data set is composed of one exposure per filter and it covers a total FOV of 33.5′ × 33.5′. Data were prereduced at the Cambridge Astronomical Survey Unit (CASU)[4] with the VIRCAM pipeline (Irwin et al., 2004). We then performed PSF-fitting photometry by using the DAOPHOT based VVV-SkZ_pipeline (Mauro et al., 2013) on the single 2048 × 2048 pixels chip extracted from the stacked VVV pawprints (Saito et al., 2012). A quadratically variable Moffat function with $\beta = 3.5$ has been adopted. The VVV magnitudes and instrumental coordinates were then reported to the 2MASS photometric and astrometric system (see details in Chené et al., 2012; Moni Bidin et al., 2011; Mauro et al., 2013).

[3] http://horus.roe.ac.uk/vsa/
[4] http://casu.ast.cam.ac.uk/

We estimated the differential reddening in the direction of Liller 1 by adopting a procedure similar to that discussed in Massari et al. (2012), with the only difference that here we used the RGB instead of the MS stars as reference sequence. In particular, we divided the GSAOI FOV in a grid of 6×6 cells, each 18"-wide. We considered RGB stars approximately in the magnitude range $14.5 < K_s < 16.5$: the upper and the lower thresholds of the selection box have been set running parallel to the reddening vector. Considering the RGB stars within each cell, we estimated the median color. The cell with the bluest color (nominally corresponding to the lowest extinction value) has been adopted as reference. The relative color shift $\delta[(J-K_s)]_i$ of each ith cell, is then defined as the shift needed to make the median color of the ith cell match the reference cell color. Then, from the value of $\delta[(J-K_s)]_i$ we derived the corresponding $\delta[E(B-V)]_i$ by adopting the extinction coefficients $R_J = 0.87$ and $R_{K_s} = 0.35$ (Cardelli et al., 1989). Extinction variations as large as $\delta[E(B-V)] = 0.34$ mag have been measured in the direction of the cluster.

Figure 4.4 shows the differential reddening corrected $(K_s, J-K_s)$ CMD of Liller 1. This is the deepest and most accurate CMD ever obtained for this stellar system, reaching $K_s \sim 19$ and thus sampling the MS-TO region. Its well defined RC, clearly visible at $K_s \sim 14.2$, is a typical feature of a metal rich GC. Unfortunately, stars lying along the brightest portion of the RGB ($K_s < 12$) are saturated in all the available images.

As apparent from Figure 4.5, Liller 1 suffers from significant field contamination mainly from the Galactic bulge and disk stars, which define a blue plume clearly visible in the bluest portion of the CMD for $(J-K_s) < 1.5$.

In the following we focus on the derivation of the star density profile of Liller 1 and the estimate of its main structural and physical parameters.

4.3 Results

4.3.1 Distance and reddening of Liller 1

The most recent determinations of the distance and reddening of Liller 1 (Valenti et al., 2010) have been obtained on the basis of a relatively shallow $(K_s, J-K_s)$-CMD, reaching only the RC level. Since the GEMINI photometry presented here is significantly deeper, we used our new data to re-determine both these quantities. Following Valenti et al. (2007) [see also Dalessandro et al., 2008b], we used a differential method, consisting in the comparison between the CMD and the luminosity function of Liller 1 with those of a reference cluster, NGC 6553, a bulge GC with similar metallicity (Origlia et al., 2002; Meléndez et al., 2003; Alves-Brito et al., 2006; Valenti et al., 2007). The data set used for NGC 6553 is from Valenti et al. (2007) [see also Ferraro et al., 2000]. We found that, in order to align the RGB mean ridge line and the magnitude level of the RC of the two clusters, a color shift $\delta(J-K_s) = 1.2$ and a magnitude shift $\delta K_s = 1.9$ must be applied to the sequences of NGC 6553 (see Figure 4.6). Thus, by adopting $(m-M)_0 = 13.46$ and $E(B-V) = 0.84$ for NGC 6553 (Valenti et al., 2010),

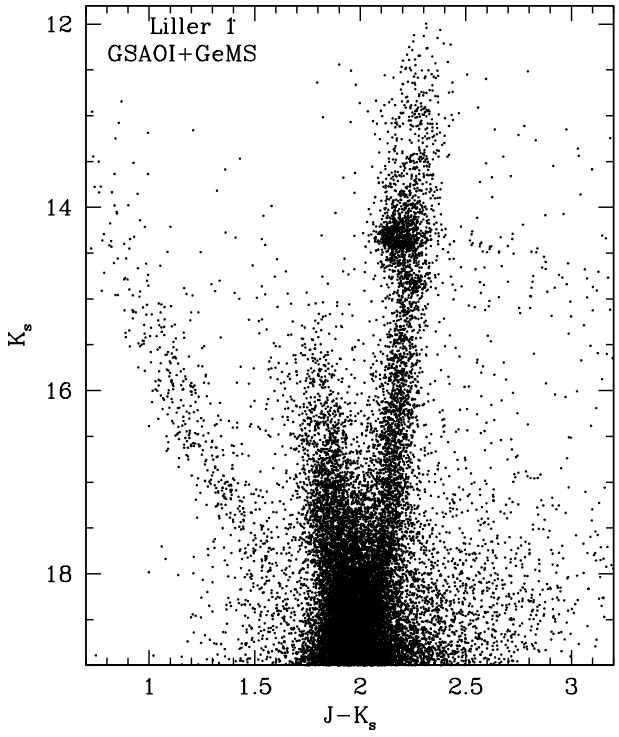

Figure 4.4: NIR differential reddening-corrected CMD of Liller 1 obtained from the GEMINI observations discussed in the chapter. The main evolutionary sequences of the cluster are well visible down to the MS-TO point. On the blue side of the CMD, for $(J - K_s) < 1.5$, the blue plume defined by the Galactic field MS is also distinguishable. The photometric errors for each bin of K_s magnitudes are shown on the right side of the panel.

we obtain $(m - M)_K = 15.65 \pm 0.15$ and $E(B - V) = 3.14 \pm 0.20$ for Liller 1. The relative uncertanties on $(m - M)_K$ and $E(B - V)$ are obtained by taking into account the photometric errors at the magnitude level of the RCs and RGB bumps of Liller 1 and NGC 6553, the errors due to the photometric calibration (Section 4.2) and the histogram bin size.

It is important to note that the adopted reddening value has been obtained by using the differential reddening-corrected CMD of Liller 1, hence it corresponds to the least extincted region in the GEMINI FOV (see Section 4.2). By averaging the values of E(B-V) of each cell considered in Section 4.2 weighted by the number of reference stars sampled, we obtain a mean extinction of $E(B - V) = 3.30 \pm 0.20$ in the direction of Liller 1. This yields a true (unreddened) distance modulus of $(m - M)_0 = 14.55 \pm 0.25$, which corresponds to a distance of 8.1 ± 1.0 kpc, in agreement with previous determinations (Harris, 1996; Valenti et al., 2010; Ortolani et al., 2007).

Interestingly, Figure 4.6 also shows that the relative positions of the red clump and of the RGB bump (Fusi Pecci et al., 1990; Ferraro et al., 1999a) are quite similar

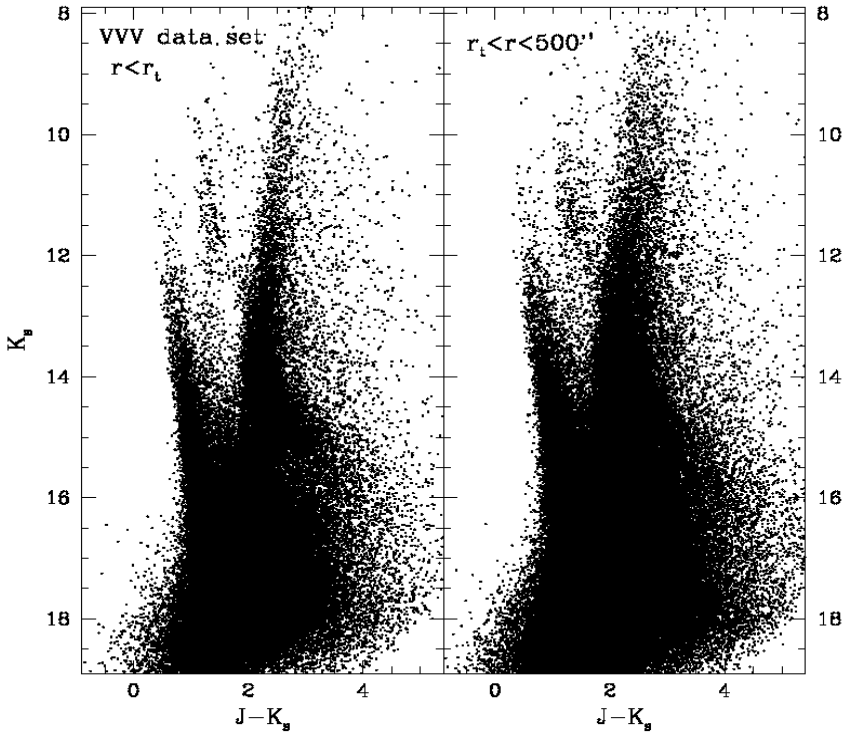

Figure 4.5: NIR CMDs of Liller 1 as obtained from the VVV data. In the *left panel* only stars external to the GEMINI FOV and located at distances smaller than r_t from $C_{\rm grav}$ are shown. In the *right panel* only stars located at $r_t < r < 500''$.

in the two clusters. Hence, since the location in magnitude of the RGB bump is quite sensitive to metal abundance, such a nice correspondence further supports the evidence that Liller 1 and NGC 6553 share the same chemistry.

4.3.2 Age

Because of its huge extinction, Liller 1 has been systematically excluded from large photometric studies aimed at determining the absolute age of Milky Way GCs. In this respect, GEMINI offers a unique opportunity to infer its age.
To estimate the age of Liller 1 we tested the isochrone fitting method. It consists in finding the best match between theoretical models and the observed CMD at the SGB/MS-TO level, a region strongly sensitive to age variations. In particular, we adopted a set of α-enhanced isochrones from the `BaSTI` (A Bag of Stellar Tracks and Isochrones) models of Pietrinferni et al. (2004). Using the distance and reddening values derived in Section 4.3.1 and a metallicity of [Fe/H] = -0.3 (Origlia et al., 2002; Stephens and Frogel, 2004; Valenti et al., 2010), we derived for Liller 1 an absolute age of 12 Gyr, with an accuracy of 1 Gyr. This match can easily see in Figure 4.7 where the best-fit isochrone is superimposed in orange on the reddening-corrected $(K_s, J - K_s)$ CMD of the cluster. This age is quite in agreement with what found for most of bulge

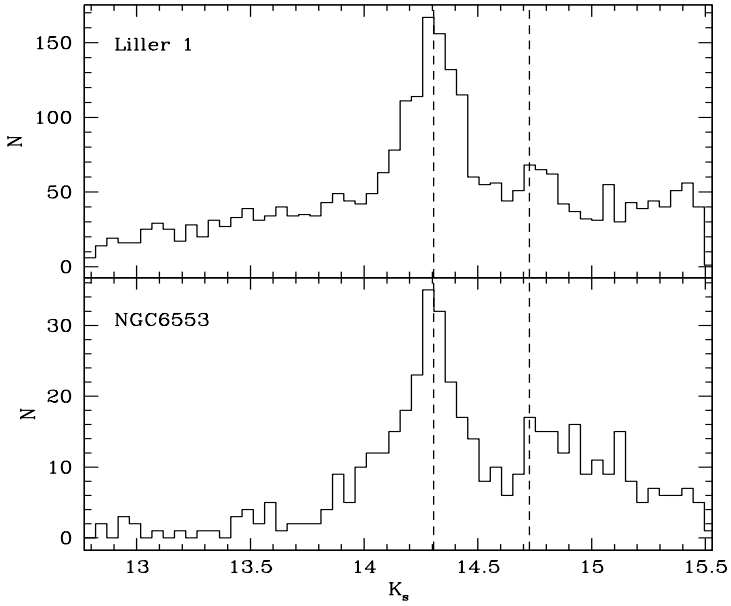

Figure 4.6: Luminosity function of the RC and the brightest portion of the RGB in Liller 1 (upper panel) and in the reference cluster NGC 6553 shifted by $\delta K = 1.9$ (lower panel). The two dashed vertical lines mark the location of the RC and the RGB bump.

GCs (Kerber et al., 2018). If the bulk of the stars in Liller 1 are predominantly old, an interesting sequence comes out at $(J - K_s) \sim 0.75$. This sequence extends up to $K_s \sim 15.5$, excluding the possibility to be populated only by blends or field stars. In order to investigate its nature, an important step is to analyze the cumulative distribution of its stars, with respect to the cluster distribution. To do this, we selected a bunch of stars along the sequence, shown in red in Figure 4.8 and we adopted both the RGB of Liller 1 and the disk MS as reference. The selected stars are shown in Figure 4.8 as black and blue dots, respectively. The cumulative radial distributions of Figure 4.9 suggest that the stars in the intermediate sequence (red line) follow the same distribution of the cluster RGB (black line). Field stars (blue line) instead seem to follow a different behavior. We performed a Kolmogorov-Smirnov (KS) test between the red and black lines, finding that there is a high probability that they came from the same parent population. As a further confirmation, in Figure 4.10 we present a map ($\alpha - \alpha_c$ vs $\delta - \delta_c$) of Liller 1. Red stars are uniformly distributed throughout the GEMINI FOV, but with a higher concentration in the central regions. In order to definitively resolve this question, Liller 1 will be observed soon with ACS and WFC3 on board HST (Program ID: GO15231; PI: F.R. Ferraro). Additionally, spectra for a dozen stars in the region will be acquired by using OSIRIS at Keck (Program ID: U0730L; PI: M. Rich). If this intermediate sequence will turn out to be part of the cluster then it should be a younger component. In this context Liller 1 might look similar to Terzan 5, the GC-like stellar system which experienced at least two bursts

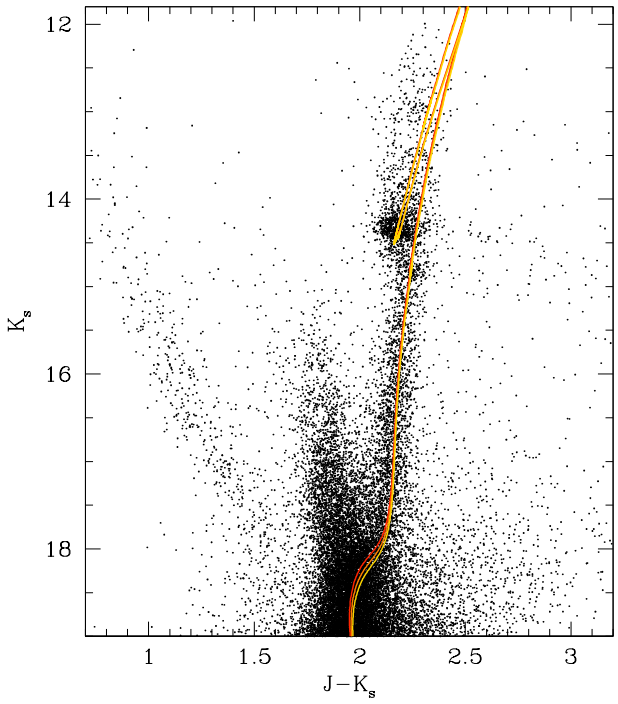

Figure 4.7: Differential reddening-corrected (K_s, $J - K_s$) CMD of Liller 1 with the best-fit BaSTI isochrone of 12 Gyr superimposed (orange line). Isochrones of 11 and 13 Gyrs are overplotted as red and yellow lines, respectively. They represent the 1 Gyr uncertainty on the absolute age estimate.

of star formation (Ferraro et al., 2009a, 2016).

4.3.3 Center of gravity

Using the absolute positions of individual stars in the GEMINI sample, we determined the center of gravity (C_{grav}) of Liller 1, by following the iterative procedure described in Montegriffo et al. (1995) [see also Ferraro et al. 2003; Lanzoni et al. 2007], averaging the right ascension (α) and declination (δ) values of properly selected stars. As discussed in Ferraro et al. (2003) [see also Lugger et al. 1995; Miocchi et al. 2013], the use of individual stars to measure the center of gravity and the star density profile provides the most robust approach to derive cluster structural parameters, since the counting of individual stars is not affected by the presence of a few bright objects (which can, instead, generate spurious luminosity clumping in the measurements based on the observed SB). However star counts can be affected by incompleteness. We estimated the effect of completeness by means of artificial stars experiments. We followed the approach and prescriptions extensively described in Dalessandro et al. (2011) [see also Bellazzini et al. 2012]. We obtained that only stars with $12.5 < K_s < 15.5$ have a completeness $C \sim 100\%$ at any distance from the cluster

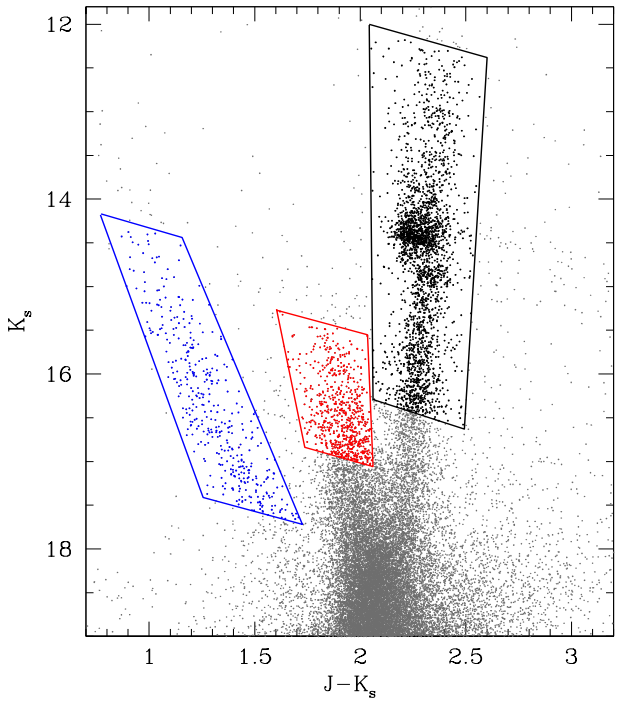

Figure 4.8: The NIR CMD of Liller 1 has been divided in three different components: *i)* the RGB of the cluster (black box); *ii)* the MS of the disk (blue box) and *iii)* the intermediate sequence (red box).

center. We used only these stars to study both the center of gravity and the density profile (Section 4.3.4).

We estimated the gravity center by considering different sub-samples of stars: we used stars lying within different distances (10″, 20″ and 30″) from a first guess center, and with three different cuts in magnitudes (K_s =15.5, 15.0 and 14.5). The final value of $C_{\rm grav}$ is the average of the different estimates. It turns out to be located at $\alpha_{\rm J2000} = 17^{\rm h}33^{\rm m}24.56^{\rm s}$, $\delta_{\rm J2000} = -33°23''22.4''$, with an uncertainty of $\pm 0.3''$ and $\pm 0.2''$ in α and δ, respectively. Our center is $\simeq 2.2''$ south-east from that reported by H96 and estimated by using the SB distribution.

4.3.4 Star density profile and structural parameters

By adopting the derived value of $C_{\rm grav}$ and the data sets described in Section 4.2, we constructed the projected density profile of the cluster over its entire radial extension (out to 900″). Following the procedure described in Ferraro et al. (1999b) [see also Lanzoni et al. 2007; Dalessandro et al. 2008a], we divided the GEMINI and the VVV samples in several concentric annuli centered on $C_{\rm grav}$, each one split into a variable number of sub-sectors. The number of stars lying within each sub-sector was counted, and the star density was obtained by dividing these values by the corresponding sub-sector areas. The stellar density in each annulus was then computed as the average of

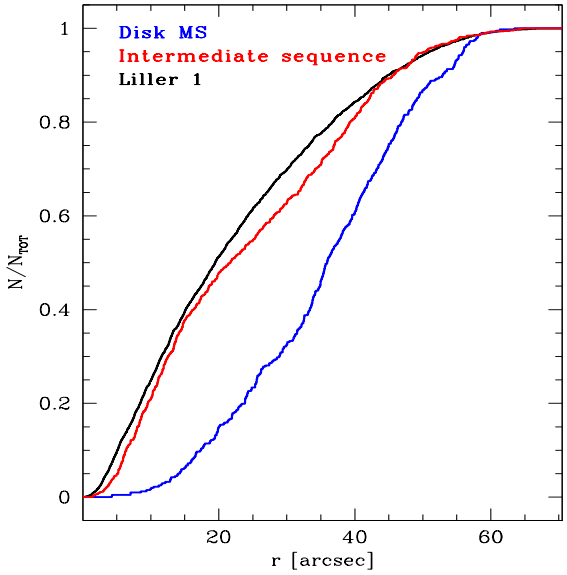

Figure 4.9: Cumulative radial distributions of the stars selected in the three boxes of Figure 4.8. The radial extension of the intermediate sequence (red line) seems to be compatible with the radial extension of the cluster itself (black line).

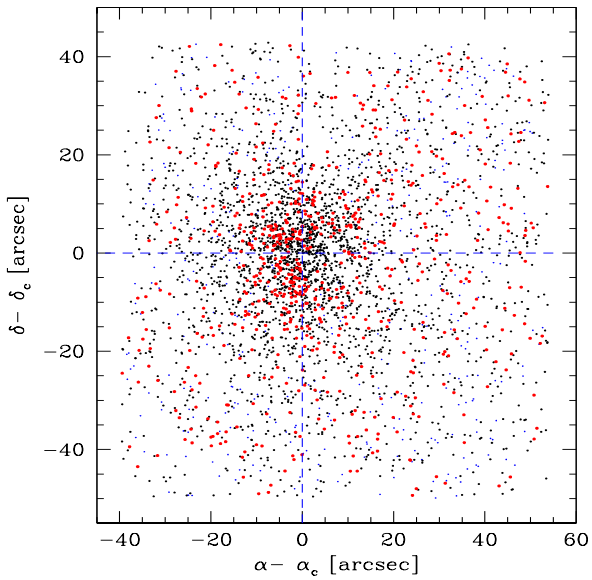

Figure 4.10: The radial distribution ($\alpha - \alpha_c$ vs $\delta - \delta_c$) of the stars in Liller 1 (back dots). The stars in the intermediate sequence are plotted in red. They are uniformly distributed, with a higher concentration around the cluster center. Blue dots instead represent field stars, which randomly populate the FOV.

the sub-sector densities and the standard deviation was adopted as the uncertainty. In order to avoid incompleteness and saturation biases, different limiting magnitudes have been adopted for the two data sets: $12.5 < K_s < 15.5$ for the GEMINI sample and $12 < K_s < 15.5$ for the VVV data set. By guaranteeing an adequate radial overlap ($\Delta r = 30 - 50''$) among the two samples, the annuli in common between the adjacent data sets have been used to join the two portions of the profile. At the end of the procedure, the inner portion ($r < 50''$) is sampled by the high resolution GEMINI data, while the outermost portion is obtained from the VVV data set.

The projected density profile thus obtained is shown in Figure 4.11 (empty circles). The distance from the center associated with each point corresponds to the mid-value of each adopted radial bin. The projected density at $r > 100''$ is approximately constant, consistent with being due to the Galactic field population alone. To estimate the background and foreground Galaxy contamination we therefore used the 1σ-clipped average of the five outermost points (dotted line in Figure 4.11). The field-decontaminated star density profile of Liller 1 is marked by the solid circles in the figure. The observed density distributions of GCs are traditionally described by means of King models (King, 1966), even if deviations from this kind of profile have been found in some cases (see, e.g., McLaughlin and van der Marel, 2005; Moni Bidin et al., 2011; Miocchi et al., 2013, and references therein). To reproduce the observed star density profile of Liller 1 and derive its structural parameters we used an isotropic, single-mass King model (King, 1966), and we followed the procedure fully described in Miocchi et al. (2013). According to a χ^2 test, the density profile of Liller 1 can be excellently reproduced by a King model with core radius $r_c = 5.39''^{-0.53}_{+0.61}$, concentration parameter $c = 1.74^{-0.15}_{+0.15}$, half-mass radius $r_h = 30.5''^{-4.7}_{+7.9}$ and tidal (or limiting) radius $r_t = 298''^{-63}_{+82}$.

The structural parameters we obtained are significantly different from those quoted by H96 based on the SB profiles in I and R bands ($r_c = 3.6''$, $c = 2.3$ and thus $r_t = 720''$). In particular, the newly derived parameters show that Liller 1 is significantly less concentrated and less extended than previously thought. A reasonably good agreement is found with the r_c values estimated from the analysis of JHK_s images by Cohen et al. (2007, $r_c = 5.2'' \pm 0.5''$)[5] and by Malkan et al. (1980, $r_c = 7'' \pm 2''$). A plausible explanation for the disagreement between the structural parameters derived from optical and NIR observations could be a differential reddening effect, that may produce a spurious distortion of the optical SB profile, as well as low S/N in the optical due to the heavy extinction.

We derived also the SB profiles of Liller 1 directly from the images. To this aim, we used the wide-field images of the 2MASS data-set, since the VVV images heavily suffer from saturation. We produced J and K_s SB profiles by following the procedure described in Dalessandro et al. (2012) [see also Cohen et al. 2007] and by adopting

[5]It is worth noticing, however, that the approach used in Cohen et al. (2007) to fit the SB profile is quite different from ours, since the authors derived the central SB and the core radius of the cluster after adopting r_t and $C_{\rm grav}$ from the online database of H96. Hence, the results obtained are not directly comparable.

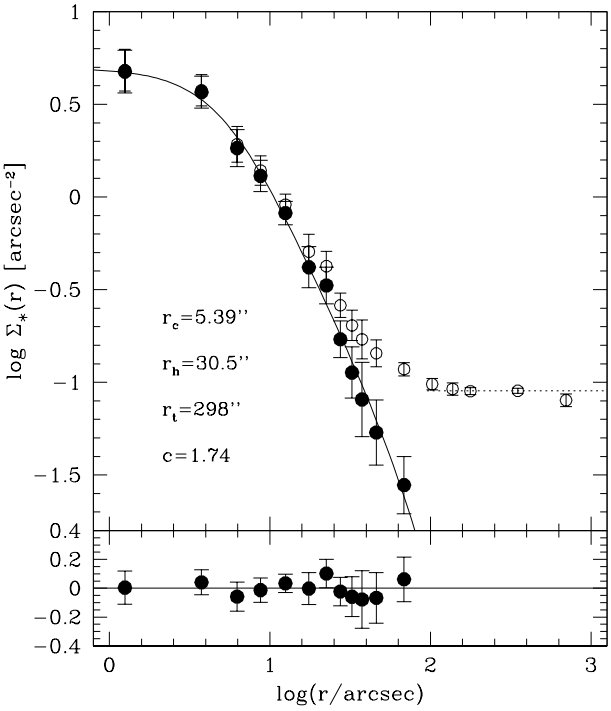

Figure 4.11: Star density profile of Liller 1, obtained from resolved star counts in the combined data set. Empty circles represent the observed profile, while solid ones are obtained after subtraction of the Galactic field density (marked with the dotted line). The best-fit single-mass King model is shown as a solid line and the corresponding structural parameters are labeled in the figure. The lower panel shows the residuals between the observations and the fitted profile at each radial coordinate.

the same center, and a setup of annuli and sub-sectors similar to the one used to obtain the density profile. Basically, for each annulus we summed the photon counts sampled in each sub-sector and we assumed as final SB the average value of the different sub-sectors. In order to reduce statistical fluctuations due to the presence of a few bright giants randomly distributed in the FOV of the J and K 2MASS images, a threshold of 8000 photon counts was adopted for each pixel. The counts have been converted into instrumental magnitudes and then calibrated by using appropriate zero-points. The contribution of the Galactic background was finally estimated for $r > 130''$, obtaining $\mu_{K_s}^{\rm back} = 12.3$ mag/arcsec^2 and $\mu_J^{\rm back} = 14.5$ mag/arcsec^2. The SB profiles thus obtained are shown in Figure 4.12. These profiles are well fit by the same King model derived from the projected density distribution, thus confirming the accuracy of the structural parameters derived in the present work. The values of the central SB measured in the J and K_s bands, $\mu_J(0)$ and $\mu_K(0)$, are listed in Table 4.1, together with all the relevant parameters derived for the cluster.

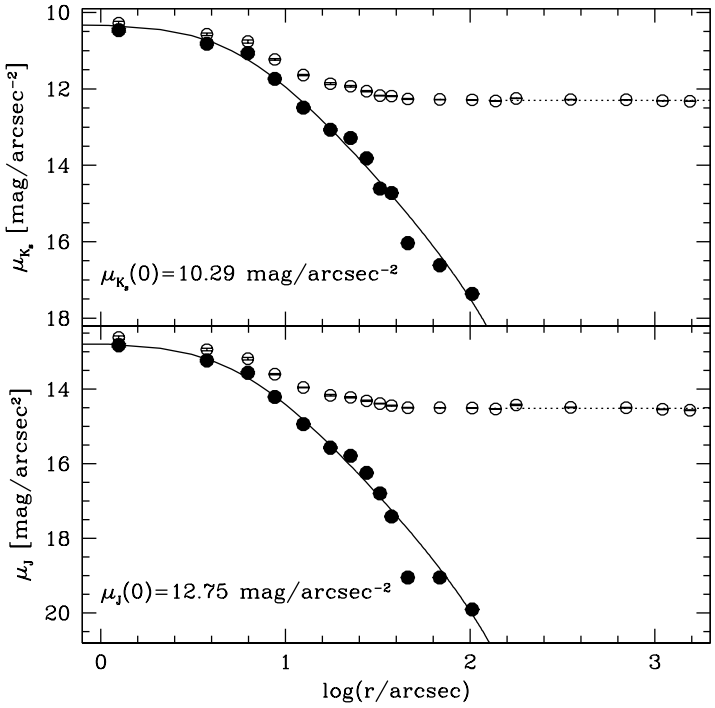

Figure 4.12: SB profiles of Liller 1 in the K_s and J bands (top and bottom panels, respectively), obtained from the 2MASS data set. Empty circles represent the observed profile, while solid ones are obtained after background subtraction (marked with a dotted line). In both panels, the solid line corresponds to the best-fit King model shown in Figure 4.11.

4.3.5 Cluster physical parameters

Given the value of the effective radius estimated from the best-fit King model discussed in the previous Section ($r_e = 22.4''^{-3.3}_{+5.6}$), we derived the integrated K_s luminosity of the cluster within r_e. By using aperture photometry on the 2MASS images and after subtracting the background contribution determined as described in Section 4.3.4, we obtained $K_s(< r_e) = 4.30^{-0.19}_{+0.12}$. Hence, by definition of r_e (i.e., the projected radius including half the total integrated light), the total integrated magnitude of the cluster is $K_s = 3.55^{-0.19}_{+0.12}$. This value is significantly brighter than previous estimates. In fact Cohen et al. (2007) found $K_s(< 50'') = 4.5$, while our estimate over the same cluster region is 0.6 mag brighter, $K_s(< 50'') = 3.9$. We emphasize, however, that our estimate is a direct measure of the integrated K_s magnitude over the 2MASS image, while that of Cohen et al. (2007) depends on the assumed cluster parameters (which are different from those derived here, as discussed in Section 4.3.4).

By adopting a color excess $E(B-V) = 3.30 \pm 0.20$, a distance modulus $(m - M)_0 = 14.55 \pm 0.25$ (see Section 4.3.1), and a bolometric correction $BC_K = 2.3$ appropriate for a population of intrinsic color $(J - K_s)_0 = 0.75$ (Montegriffo et al., 1998), we estimated a bolometric luminosity of about $L_{\rm bol}(< r_e) = 3.45^{-0.10}_{+0.45} \times 10^5 L_\odot$, corresponding to a total luminosity $L_{\rm bol} = 6.9^{-0.2}_{+0.9} \times 10^5 L_\odot$. From this value, the total

Table 4.1: New parameters for Liller 1.

Parameter	Derived Value
Center of gravity	$\alpha_{J2000} = 17^h33^m24.56^s$
	$\delta_{J2000} = -33°23'22.4'$
Reddening	$E(B-V) = 3.30 \pm 0.20$
Distance Modulus	$(m-M)_0 = 14.55 \pm 0.15$
Distance	d = 8.1 ± 1.0 Kpc
Core radius	$r_c = 5.39'' \, ^{-0.53}_{+0.61} = 0.21$ pc
Effective radius	$r_e = 22.4'' \, ^{-3.3}_{+5.6} = 0.88$ pc
Half-mass radius	$r_h = 30.5'' \, ^{-4.7}_{+7.9} = 1.20$ pc
Tidal radius	$r_t = 298'' \, ^{-63}_{+82} = 11.74$ pc
Concentration	$c = 1.74 \, ^{-0.15}_{+0.15}$
Total luminosity	$L_{bol} = 6.9 \, ^{-0.2}_{+0.9} \times 10^5 L_\odot$
Total mass	$M_{tot} = 2.3 \, ^{-0.1}_{+0.3} \times 10^6 M_\odot$ (Salpeter IMF)
	$M_{tot} = 1.5 \, ^{-0.1}_{+0.2} \times 10^6 M_\odot$ (Kroupa IMF)
Central mass density	$\rho_0 \simeq 7.2 \, ^{-1.0}_{+1.2} \times 10^6 M_\odot$ (Salpeter IMF)
	$\rho_0 \simeq 4.8 \, ^{-1.0}_{+1.2} \times 10^6 M_\odot$ (Kroupa IMF)
Central K_s-band SB	$\mu_{K_s}(0) = 10.29 \pm 0.17$ mag arcsec^{-2}
Central J-band SB	$\mu_J(0) = 12.75 \pm 0.17$ mag arcsec^{-2}

mass of Liller 1 can be estimated by assuming a mass-to-light ratio $M/L_{bol} = 3.35$ (Maraston and Thomas, 2000; Maraston et al., 2003) appropriate for a Salpeter Initial Mass Function (IMF), thus obtaining $M_{tot} = 2.3^{-0.1}_{+0.3} \times 10^6 M_\odot$. We also estimated the mass of Liller 1 assuming $M/L_{bol} = 2.19$ as obtained by Maraston et al. (2003) for a Kroupa IMF. We obtain in this case $M_{tot} = 1.5^{-0.1}_{+0.2} \times 10^6 M_\odot$.

Note that such a large value of the mass is similar to that extimated for ω Cen (Merritt et al., 1997) and Terzan 5 (Ferraro et al., 2009a; Lanzoni et al., 2010), and rankes Liller 1 in the high-mass tail of the distribution observed for GC-like stellar systems in the Milky Way.

Same values of the total mass are obtained from the total integrated K-band magnitude (see above) and adopting mass-to-light ratios $M/L_K = 1.56$ and $M/L_K = 1.03$ (Maraston and Thomas, 2000; Maraston et al., 2003) for a Salpeter and a Kroupa IMF, respectively.

We also used the available data to get a new estimate of the central mass density of the cluster. To do so, we followed the same procedure described for V-band data in Djorgovski and Meylan (1993). However, in order to minimize the effects due to the strong and differential reddening affecting the system, we re-derived eq. (5) of Djorgovski and Meylan (1993) in the appropriate form for K_s-band photometry. By adopting 3.28 as the K_s-band magnitude of the Sun, we obtain:

$$\log I_{0,K_s} = 0.4[24.852 - \mu_K(0)], \tag{4.1}$$

where I_{0,K_s} is the central projected luminosity density in units of $L_\odot$ pc^{-2}. From eq. (4) of Djorgovski and Meylan (1993) and the structural parameters quoted in Section 4.3.4, we then derived the central luminosity density of the system in the K-band. By assuming $M/L_K = 1.56$ appropriate for a Salpeter IMF, we finally converted it into

the central mass density, $\rho_0 \simeq 7.2^{-1.0}_{+1.2} \times 10^6 M_\odot$ pc^{-3}. Using instead a Kroupa IMF which gives $M/L_K = 1.03$, we obtain $\rho_0 \simeq 4.8^{-1.0}_{+1.2} \times 10^6 M_\odot$ pc^{-3}. These values are between 5 and 7 times larger than those obtained from the V-band central luminosity density quoted in H96, by assuming $M/L_V = 5.3$ (Maraston and Thomas, 2000; Maraston et al., 2003, from).

4.4 Summary and conclusions

By using GeMS+GSAOI at the Gemini South Telescope, we have obtained the deepest CMD of the Galactic GC Liller 1 published so far, properly sampling even the innermost regions of the system (except for some saturated stars). This allowed us to obtain new estimates of the cluster distance and reddening, which essentially confirm previous determinations. Liller 1 is predominantly old, with an absolute age of 12 ± 0.5 Gyr (in good agreement with what found for most of the bulge GCs), although there are some hints about the possible presence of a younger population. Significant differences with respect to the literature values, instead, have been found for the cluster center and structural parameters: with respect to the values quoted in the H96 catalog, Liller 1 turns out to be located $\sim 2.2''$ south-east, to be significantly less concentrated ($c = 1.74$, instead of $c = 2.3$), to have a larger core radius ($r_c = 5.39''$, instead of $r_c = 3.6''$), and thus to be less extended overall ($r_t = 298''$, instead of $r_t = 720''$). Also its total mass $M_{\rm tot} = 2.3 \times 10^6 M_\odot$ and central mass density $\rho_0 = 7.2 \times 10^6 M_\odot$ pc^{-3} ($M_{\rm tot} = 1.5 \times 10^6 M_\odot$ and $\rho_0 = 4.8 \times 10^6 M_\odot$ pc^{-3} for a Kroupa IMF) appear to be a factor of a few larger that those derivable from the V-band parameters listed in the H96 catalog.

From these new estimates, we also re-determined the collisional parameter of the system, which can be expressed as $\Gamma \propto \rho_0^{1.5} \times r_c^2$ for virialized and King model systems. We find that Γ is ~ 20 - 40 times larger than the one obtained by using the H96 parameters. It corresponds to about half the collisional parameter of Terzan 5 estimated in Lanzoni et al. (2010), and is much larger than the values derived for other massive GCs for which the structural parameters have been re-determined consistently with what is done here (NGC 6388, NGC 6266, 47 Tucanae; see Dalessandro et al., 2008b; Beccari et al., 2006; Marchetti et al., 2006, respectively).

Hence, our analysis confirms the previous suggestion (Verbunt and Hut, 1987) that the collisional parameter of Liller 1 is the second highest (after that of Terzan 5) among all Galactic GCs. In stellar systems with high values of Γ, large populations of "collisional" objects (like LMXBs, MSPs, BSS and CVs), whose formation is promoted by single/binary encounters, should not be unusual (also depending on the availability of the progenitors). In this respect, it is interesting to note that, while Terzan 5 hosts the largest population of MSPs ever observed in a GC (Ransom et al., 2005), no MSPs have been detected so far in Liller 1, the only exotic object being in fact a LMXB (Homer et al., 2001)[see also the Introduction]. The lack of detection of large populations of MSPs, LMXBs and CVs might be due to observational biases.

In fact Liller 1 is located in a region of the Galactic plane where diffuse emission is very strong. In this respect, deeper MSP searches, perhaps with the Square Kilometer Array, could help understanding the real MSP content of the system. On the other hand, the strong γ-ray emission (the most intense among all Galactic GCs) detected in the direction of the cluster (Tam et al., 2011) may suggest the possible presence of numerous, but still hidden, MSPs. Another possibility, emerging from the results presented in this work, is that the γ-ray emission is not associated with Liller 1. In fact Tam et al. (2011) localized the position of the intense γ-ray source at $\sim 7.5'$ from the cluster center. While this distance is smaller than the tidal radius quoted in H96 ($r_t = 720'' = 12'$), it is larger than the cluster tidal radius obtained in this work ($r_t \sim 300'' = 5'$). Even by taking into account the γ-ray position error ($\sim 2'$ for the Fermi-LAT observations), the location of the γ-ray source is only marginally compatible with the newly determined radial extension of Liller 1, thus opening the possibility that such a strong emission is not coming from this stellar system.

CHAPTER 5

Ultra-deep GEMINI near-infrared observations of the bulge globular cluster NGC 6624

Based on the results published in:
Saracino S., Dalessandro E., Ferraro F. R., Geisler D., Mauro F., Lanzoni B., Origlia L., Miocchi P., Cohen R. E., Villanova S., Moni-Bidin C.
2016, *The Astrophysical Journal*, **832, 48S**

Subject of a GEMINI-INAF Press Release, October 12 2016:
Cluster's Advanced Age in Razor-sharp Focus

Abstract

We used ultra-deep J and K_s images secured with the NIR GSAOI camera assisted by the MCAO system GeMS at the GEMINI South Telescope in Chile, to obtain a (K_s, $J - K_s$) CMD for the bulge GC NGC 6624. We obtained the deepest and most accurate NIR CMD from the ground for this cluster, by reaching $K_s \sim 21.5$, approximately 8 magnitudes below the horizontal branch (HB) level. The entire extension of the MS is nicely sampled and at $K_s \sim 20$ we detected the so-called MS "knee" in a purely NIR CMD. By taking advantage of the exquisite quality of the data, we estimated the absolute age of NGC 6624 (t_{age} = 12.0 $\pm$ 0.5 Gyr), which turns out to be in good agreement with previous studies in the literature. We also analyzed the luminosity and mass functions of MS stars down to M $\sim$ 0.45 $M_\odot$ finding evidence of a significant increase of low-mass stars at increasing distances from the cluster center. This is a clear signature of mass segregation, confirming that NGC 6624 is in an advanced stage of dynamical evolution.

5.1 Introduction

After the encouraging results obtained for Liller 1 (Saracino et al., 2015, see Chapter 4), a heavily obscured cluster located very close to the Galactic plane and center, here we present the results for NGC 6624. This GC is located just at the edge of the inner bulge, at a distance of 7.9 Kpc from Earth (Harris, 1996, 2010 edition) and it is characterized by only a moderate foreground extinction for a bulge GC, $E(B-V) = 0.28$ (Valenti et al., 2004a; Harris, 1996, 2010 edition). These features also make NGC 6624 an ideal target to investigate the sky performance of the GeMS+GSAOI system.

NGC 6624 is a well-studied cluster, but mainly in the optical bands (see Sarajedini et al., 2007; Dalessandro et al., 2014). In the NIR it was observed with the following instruments:

(i) IRCAM, mounted at the 2.5 m Du Pont telescope. These observations provided the first (K_s, $J-K_s$) CMD of the cluster sampling the brightest portion of the RGB (see Kuchinski and Frogel, 1995) down to the HB level.

(ii) IRAC-2 mounted at the ESO 2.2 m telescope MPI. The NIR CMD derived from these observations was deeper than the previous one, reaching the cluster sub-giant branch ($K_s \sim 17$), and thus allowing to study the RGB features (RGB bump and tip; see Valenti et al., 2004a,b, 2007; Ferraro et al., 2006).

(iii) Within the VVV survey. The NIR CMD obtained from the VVV catalog was deep enough ($K_s \sim 19$) to sample the MS-TO only in the external regions of the cluster (Minniti et al., 2010; Catelan et al., 2011).

NGC 6624 is quite compact and it has been catalogued as a dynamically evolved cluster, which already experienced core collapse (Trager et al., 1995). It has been found to harbour six MSPs (Lynch et al., 2012; Tam et al., 2011; Freire et al., 2011) and at least an ultra-compact LMXB (Dib et al., 2005), thus confirming that its dense environment efficiently boosts the formation of exotic objects.

In this chapter we present ultra-deep NIR observations of NGC 6624 obtained by using the powerful combination of the GeMS+GSAOI devices mounted at the Gemini South Telescope. The chapter is organized as follows: in Section 5.2 we discuss the observations and the data analysis. In Section 5.3 we present the CMD of the cluster. Section 5.4 is focused on the determination of the age of the cluster and in Section 5.5 we discuss the Luminosity (LF) and Mass Functions (MF) of the cluster MS. In Section 5.6 we present our conclusions.

5.2 Observations and data analysis

The data set analyzed in this work consists of a sample of high-quality J and K_s images obtained with GeMS and the NIR camera GSAOI. GSAOI has a resolution of about 0.02"/pixels and consists of four 2048 x 2048 pixels chips, divided by gaps of about 2", providing a total FOV of almost 85" $\times$ 85". NGC 6624 was observed

on May 24, 2013 as part of the proposal GS-2013-Q-23 (PI: D. Geisler). A total of 28 images (14 in the J and 14 in the K_s bands), with an exposure time $t_{\rm exp} = 30$ s each, was acquired during the run. To fully cover the gaps between the GSAOI chips, we adopted a dither pattern with a maximum offset of about 5″ between two consecutive images. During the observing night the DIMM monitor on Cerro Pachón recorded excellent seeing conditions, with a Full Width at Half Maximum (FWHM) of ~ 0.7″. An average stellar FWHM smaller than 4 pixels (0.08", close to the diffraction limit of the telescope) has been measured in all J and K_s images. Unfortunately, one J-band exposure was characterized by a significantly worse FWHM, so it was excluded from the subsequent analysis. In Figure 5.1 we present a two-color mosaic of K_s and J images of NGC 6624. Figure 5.2 shows the comparison between a central region (10" $\times$ 10") of NGC 6624 obtained with HST in the F435W filter (*left panel*) and with GeMS/GSAOI system in the K_s band (*right panel*): the spatial resolution of the AO corrected image is indeed impressive.

Figure 5.1: Two-color image of NGC 6624 obtained by combining GEMINI observations in the NIR J and K_s bands. North is up, east is on the left. The FOV is 93″ $\times$ 93″.

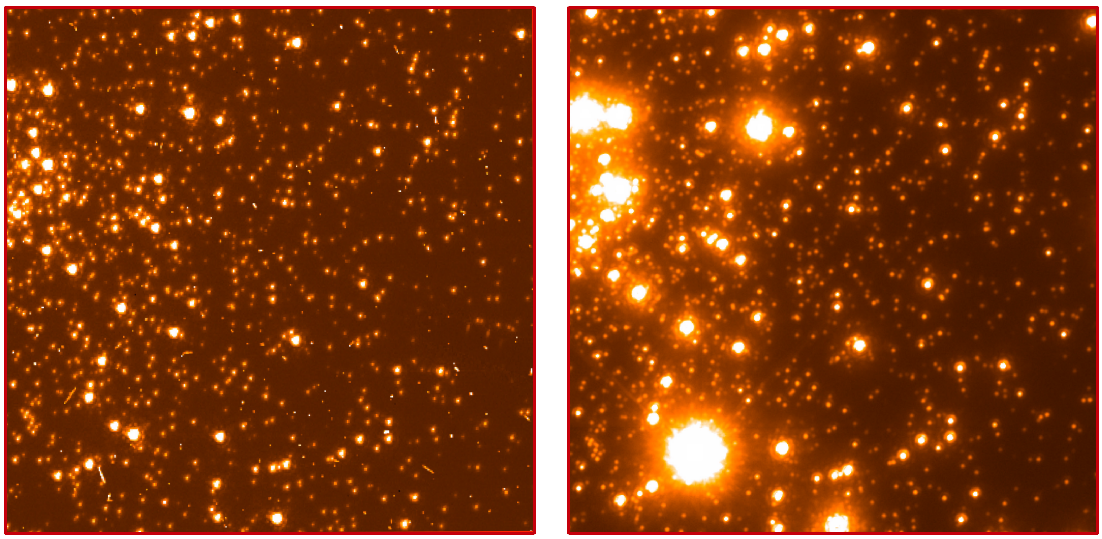

Figure 5.2: A zoom-in of a central region (10″ × 10″) of the cluster as seen by ACS/HRC (F435W filter) on board HST (Dalessandro et al., 2014, *left*) and by GSAOI+GeMS in the K_s band (this work, *right*). The spatial resolution of GEMINI in the NIR turns out to be comparable to that of HST in the optical.

The data analysis was performed following the same procedure described in Saracino et al. (2015). Briefly, each individual chip[1] was analyzed independently, by using standard pre-reduction procedure, within the `IRAF`[2] environment, in order to correct for flat-field and bias and subtract the background. For this purpose, a Master Sky was obtained by combining 5 sky images per filter of a relatively empty field. In order to get accurate photometry, even in the innermost region of the cluster, we performed PSF fitting by using `DAOPHOT` (Stetson, 1987) of all the detected stellar sources. For each chip, we selected $\sim$ 100 bright, isolated and unsaturated stars (using `FIND` and `PHOTO`), that were used to derive the best-fit PSF model. Based on a χ^2 test, the best-fit PSF analytic models were found to be a MOFFAT function (with β=1.5; Moffat, 1969) for the K_s images and a PENNY function (Penny, 1976) for the J ones. We also noted that photometry significantly improves by adopting PSF models varying within the FOV. In particular we adopted a linear dependence on the position within the frame in chip 1, and a cubic one for chips 2, 3 and 4. The selected models were then applied, using the `ALLSTAR` and `ALLFRAME` tasks (Stetson, 1994), to all the sources having peak counts larger than 3σ above the local background level, thus determining the instrumental magnitudes for each star candidate in each chip. In the catalog we included only stars present in at least two images for each filter. This criterion removed most of the cosmic rays and other spurious detections

[1]To distinguish between chips, we assigned an identification (ID) number from 1 to 4, starting from the bottom-right corner (chip 1) and proceeding clockwise.

[2]IRAF is distributed by the National Optical Astronomy Observatory, which is operated by the Association of Universities for Research in Astronomy, Inc., under cooperative agreement with the National Science Foundation.

and allowed to fill the gaps between the different chips of GSAOI. For each star, we homogenized the magnitudes estimated in different images, and their weighted mean and standard deviation have been finally adopted as the star mean magnitude and its related photometric error (see Ferraro et al., 1991, 1992). The instrumental positions have been reported onto the absolute coordinate system by adopting the star catalog by Dalessandro et al. (2014) as astrometric reference and by using the cross-correlation software `CataXcorr` (Montegriffo et al., 1995). The instrumental magnitudes of the final catalog have been finally calibrated by using a sample of stars in common with the VVV catalog. The latter has been realized by using the `DAOPHOT` based VVV-SkZ pipeline (Mauro et al., 2013) and reported into the 2MASS photometric and astrometric system (see details in Chené et al., 2012; Moni Bidin et al., 2011; Mauro et al., 2013). We adopted an iterative 2σ - clipping procedure to estimate the calibration equations transforming the instrumental GeMS K_s and J magnitudes into the VVV photometric system. In order to avoid bias, only the brightest stars (with $K_s < 16$ and $J < 16.5$) were used (see Figure 5.3), yielding a total of about 300 calibration stars in each filter. The r.m.s. of the calibration is ~ 0.02 mag both in J and in K_s.

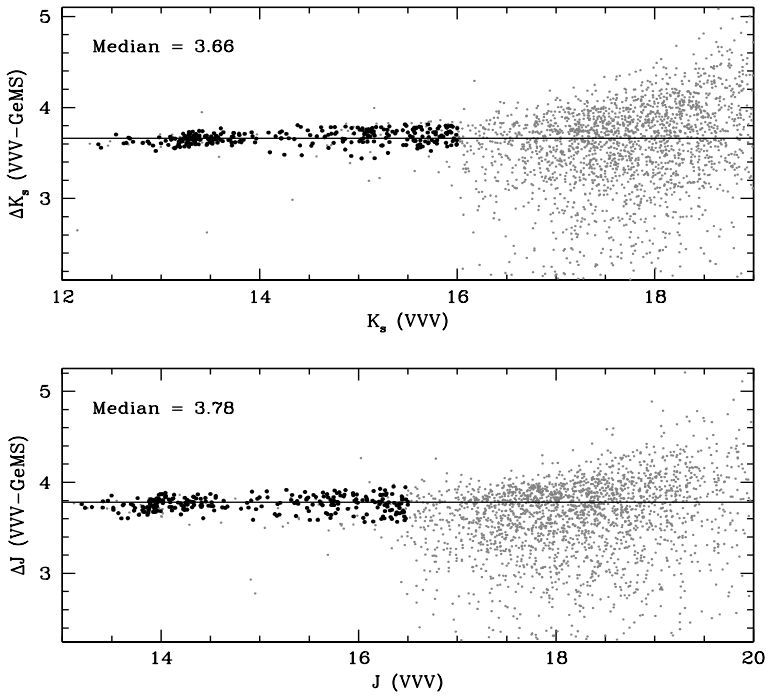

Figure 5.3: Photometric calibration plots for the GEMINI catalog of NGC 6624 in the K_s and J bands. Only bright stars (black points) have been used to determine the calibration zero points. The median values, estimated by using a $2\sigma-$rejection, are shown in the figure.

5.3 Near-Infrared Color-Magnitude diagrams of NGC 6624

In order to obtain a clear definition of the evolutionary sequences in the CMD, we selected only very well measured stars by imposing a selection in the sharpness parameter. In particular, we divided our sample in 0.5 magnitude-wide bins and for each bin we derived the median value of the sharpness by applying an iterative $2\sigma-$rejection (an example is shown in Figure 5.4). All the stars satisfying this selection criterion and lying within 6σ from the median are shown in the (K_s, $J-K_s$) and (J, $J-K_s$) CMDs plotted in Figure 5.5. These are the deepest and highest-quality CMDs in the NIR ever obtained from the ground for this cluster, but quite comparable with those obtained for NGC 6121 with HAWK-I@VLT (Libralato et al., 2014) and for M15 with PISCES@LBT (Large Binocular Telescope; Monelli et al., 2015).

The NIR GEMINI CMDs presented in this study are fully comparable, both in depth and resolution, to the optical ones obtained by using different instruments on board HST, such as the WFPC2 (Heasley et al., 2000; Dalessandro et al., 2014) and the ACS/HRC (Siegel et al., 2011; Dalessandro et al., 2014). In Figure 5.5 the red HB at K_s $\sim$ 13.3 and a well defined RGB bump at about $K_s \sim$ 13.55 are clearly distinguishable. Unfortunately, the stars lying along the brightest portion of the RGB ($K_s < 14.0$) are saturated in all the available images. The MS-TO region is well defined at $K_s \sim 17.5$ and the MS nicely extends for more than 4 magnitudes down to $K_s \sim 21.5$. At odds with Siegel et al. (2011), we find no evidence of a broad sequence located below the cluster MS at bluer colors, which has been interpreted as a background feature, due to a tidal stream of the Sagittarius dwarf galaxy, located behind the cluster along its line of sight. The reason for such a discrepancy is likely ascribable to the relatively small FOV of GSAOI compared to that of the ACS. At $K_s \sim 20$ we clearly identify the so-called MS "knee" (MS-knee), a particular feature commonly defined as the reddest MS point in NIR CMDs. This feature is due to the absorption of molecular hydrogen induced by collisions (Bono et al., 2010) and flags the portion of the MS populated by very low-mass stars (with $M < 0.55 M_{\odot}$). Until now, the MS-knee has been observed only by using HST optical+NIR images (Milone et al., 2012, 2014) and a proper combination of HST and MCAO data (MAD@VLT - Moretti et al., 2009; PISCES@LBT - Monelli et al., 2015 and GeMS - Massari et al., 2016b; Turri et al., 2015). The detection shown in Figure 5.5 is the first determination of the MS-knee feature in a purely NIR CMD obtained from the ground. The detailed study of this feature and its use as a possible age indicator (Massari et al., 2016b; Di Cecco et al., 2015; Bono et al., 2010) will be discussed in chapter 6.

5.4 Absolute age determination

In this Section we take advantage of the exquisite quality of the CMDs shown in Figure 5.5 to estimate the age of NGC 6624 by using the luminosity of the MS-TO as an age indicator.

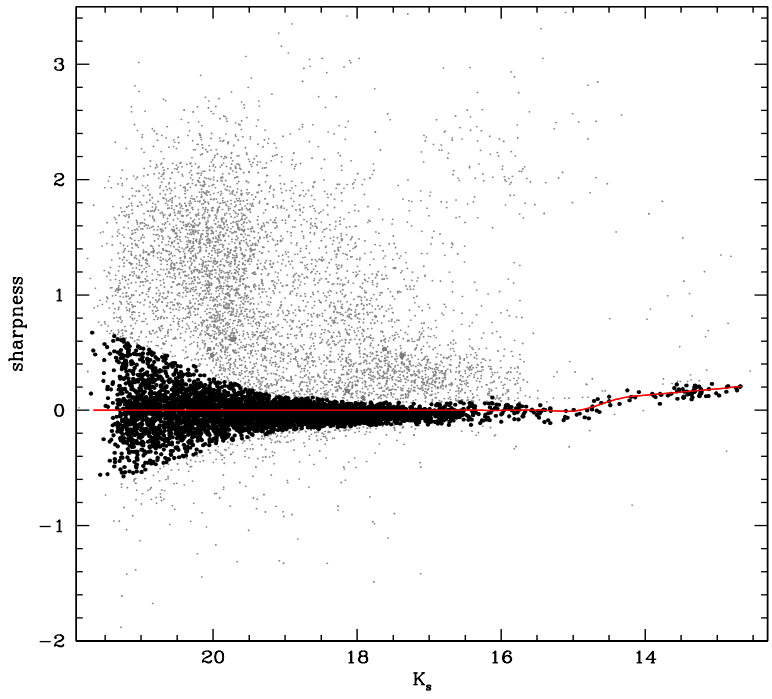

Figure 5.4: Plot of the sharpness as a function of the K_s magnitude. The black points are the stars lying within 6σ from the red line, which represents the 2σ-clipped median value in sharpness. This selection criterion is applied to all the detected stars in order to remove spurious objects and stars with large photometric errors.

5.4.1 Isochrone fitting method

In order to derive the age of the cluster via the isochrone fitting method, three main cluster parameters are needed, namely the metallicity, the distance and the reddening.
Metallicity - The most recent metallicity estimate of NGC 6624 is [Fe/H]$= -0.42 \pm 0.07$. This value has been derived indirectly from the new metallicity scale of Carretta et al. (2009, 2010), based on optical high resolution spectra of about 20 GCs. Other estimates in the literature provide slightly lower metallicities: [Fe/H]$= -0.63$ (Carretta and Gratton, 1997, hereafter CG97; Heasley et al., 2000). Recent high resolution NIR spectroscopy by Valenti et al. (2011) provides [Fe/H]$= -0.69 \pm 0.02$ and [α/Fe]$\sim +0.39$.
Reddening - $E(B-V)$ color excess estimates in the cluster direction range from 0.25 to 0.33 (Armandroff, 1989; Heasley et al., 2000) with a fair agreement on $E(B-V)$ = 0.28 (Valenti et al., 2004a; Harris, 1996, 2010 edition).
Distance modulus - Different estimates of the distance modulus of NGC 6624 have been obtained: $(m-M)_0$ = 14.49 (Harris, 1996, 2010 edition), $(m-M)_0$ =14.40 (Heasley et al., 2000), and $(m-M)_0$ =14.63 (Valenti et al., 2004a).

Both the reddening and the distance modulus were mainly derived in a differential way, by comparing the CMD of NGC 6624 with those of other clusters having the

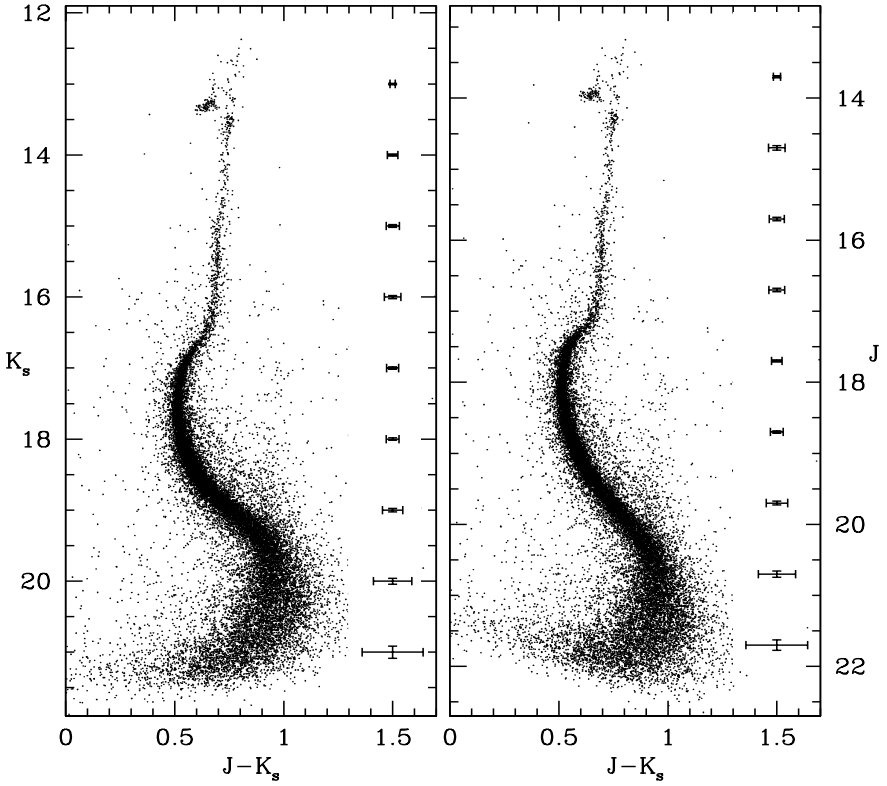

Figure 5.5: (K_s, $J - K_s$) and (J, $J - K_s$) CMDs of NGC 6624 obtained from the GEMINI observations discussed in the section 5.2. All the main evolutionary sequences of the cluster are well visible, from the RGB, HB, MS-TO down to the MS-knee. These NIR diagrams turn out to be comparable to the HST optical ones, both in depth and in photometric accuracy. The photometric errors for each bin of K_s and J magnitudes are shown on the right side of the panels.

same metallicity and known values of $E(B - V)$ and $(m - M)_0$.

In order to compare theoretical models with the NIR photometry of the cluster, we selected three different sets of α-enhanced isochrones:

1. A Bag of Stellar Tracks and Isochrones (`BaSTI`; Pietrinferni et al., 2004) isochrones with [α/Fe]=+0.4, Y = 0.259 and a mass-loss parameter η = 0.4 (Reimers, 1975).

2. Dartmouth Stellar Evolutionary Database (`DSED`; Dotter et al., 2007) isochrones with [α/Fe]=+0.4 and Y = 0.2583.

3. Victoria-Regina (`VR`; VandenBerg et al., 2014) isochrones with [α/Fe]=+0.4 and Y = 0.2583.

For each model we adopted [Fe/H] = -0.60, a distance modulus of $(m - M)_0 = 14.49$ ($d = 7.9$ Kpc) and a color excess $E(B - V) = 0.28$[3]. These parameters well reproduce

[3]The color excess in the NIR filters $E(J - K_s)$ has been derived by adopting the extinction coefficients $A_J/E(B - V) = 0.899$ and $A_{K_s}/E(B - V) = 0.366$ from Casagrande and VandenBerg (2014)

the main evolutionary features in the high-quality optical HST CMD by Dalessandro et al. (2014). However, the impact of adopting different values for these parameters will be discussed at the end of this Section.

BaSTI *isochrones* - Figure 5.6 shows a set of seven isochrones with appropriate different ages ranging from 10.5 to 13.5 Gyr, stepped by 0.5 Gyr, overplotted to the data of NGC 6624 in the $(K_s, J-K_s)$ and $(J, J-K_s)$ CMDs, by assuming the quoted distance and reddening. The BaSTI NIR colors and magnitudes are on the Johnson-Cousins-Glass photometric system, so they were converted first on the Beckers (1988) system and then, by using the transformations of Carpenter (2001), into the 2MASS photometric system (Cutri et al., 2003).
As can be seen, the agreement between BaSTI models and our data is quite good in the extended MS and in the TO region, while it is not completely satisfactory in terms of color at the level of the MS-knee (at $K_s > 19.5$)[4] and in the lower part of the RGB. A mismatch between models and data appears also at the brightest portion of the RGB, at $K_s < 14$ but in this case it is likely due to non-linearity and saturation problems that mainly affect the K_s band photometry. In spite of this, both the luminosity of the RGB bump and the ZAHB level are well reproduced (see Figure 5.6).

Focussing on the TO region, in order to identify the isochrone that best reproduces the observations, we performed a χ^2 analysis. The χ^2 parameter has been computed by selecting a subsample of stars in the MS-TO region, in the magnitude range $16.4 < K_s < 17.8$, where the isochrone shape is particularly sensitive to age variations. It has been defined as: $\chi^2 = \sum[(O_K - E_K)^2 + (O_{colJK} - E_{colJK})^2]$. We computed, iteratively, the minimum distance both in magnitude (O_K) and in color (O_{colJK}) between each star in our sample and the corresponding values E_K and E_{colJK} read along the isochrone. The result is shown in the right panel of Figure 5.7. As can be seen, a well defined minimum is visible, indicating a best-fit isochrone with an absolute age of $t_{age} = 12.0 \pm 0.5$ Gyr.

DSED *isochrones* - Following the same approach adopted for the BaSTI isochrones, Figure 5.8 shows the comparison between the observed cluster photometry and the DSED isochrones (Dotter et al., 2007). A color offset $\delta(J-K_s) = +0.003$ (corresponding to $\delta K_s = -0.003$) was needed to reconcile these evolutionary models to the data, in agreement with what found by Cohen et al. (2015). DSED isochrones do a good job of reproducing the observed CMD morphology of NGC 6624, from the SGB level down to the MS-K. The RGB instead shows the same discrepancies already seen for the BaSTI isochrones, with the only difference that in this case, even the magnitude of the RGB bump is not well reproduced. This is likely due to the fact that different models treat overshooting from convective cores in different ways. A χ^2 test has been performed also for DSED models and the minimum value has been obtained for an

[4]However, it should be noted that the BaSTI models do not sample the entire extension of the MS since they are truncated at $M = 0.5 M_{\odot}$.

absolute age of $t_{age} = 12.0 \pm 0.5$ Gyr. This result is shown in Figure 5.9, together with a zoom into the MS-TO/SGB regions of NGC 6624.

VR *isochrones* - Finally, the $(K_s, J - K_s)$ and $(J, J - K_s)$ CMDs of NGC 6624 have been compared to the new VR isochrones (VandenBerg et al., 2014) (see Figure 5.10). According to the results of VandenBerg et al. (2013) and Cohen et al. (2015) we needed to apply a color shift of -0.008 in order to have a good match between models and data. The MS-TO and the SGB level are well reproduced, as well as the shape of the MS-knee. At the base of the RGB instead, VR models are systematically too red compared with the observed photometry. By performing a χ^2 test on the VR isochrones, we obtained a slightly older absolute age of $t_{age} = 12.5 \pm 0.5$ Gyr, however in agreement, within the uncertainties of the method, with the ages derived from BaSTI and DSED models.

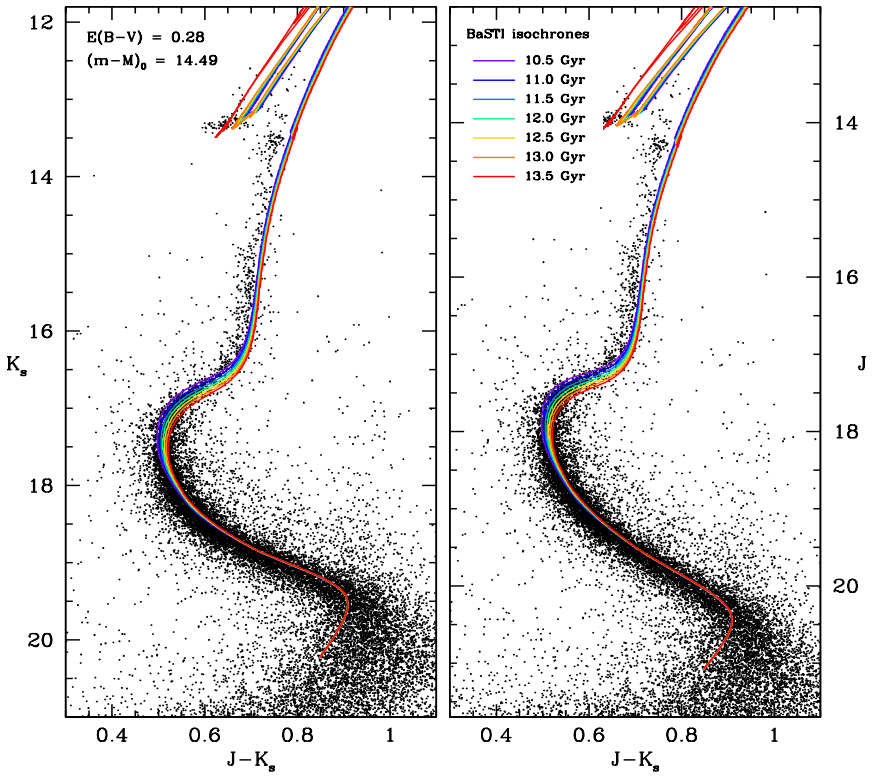

Figure 5.6: $(K_s, J - K_s)$ and $(J, J - K_s)$ CMDs of NGC 6624 CMDs with overplotted a set of BaSTI (Pietrinferni et al., 2004) isochrones with ages ranging from 10.5 Gyr up to 13.5 Gyr, in steps of 0.5 Gyr (see labels).

Figures 5.6, 5.8 and 5.10 show that there is a mismatch between all models and observation starting from the RGB base. As discussed in detail by Salaris et al. (2007), Brasseur et al. (2010) and Cohen et al. (2015), this is a well known and long-standing

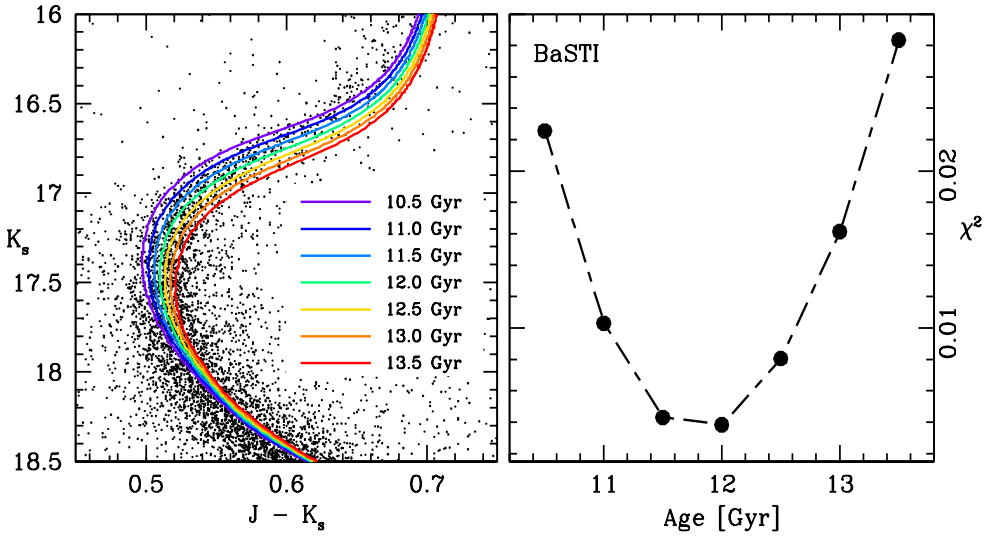

Figure 5.7: *Left panel:* zoomed MS-TO region of the $(K_s, J-K_s)$ CMD, with the selected set of BaSTI isochrones (with different ages) overplotted. *Right panel:* χ^2 parameter as a function of isochrone ages considered in the *Left Panel*. A well defined minimum identifies the best-fit isochrone (with t_{age} = 12.0 Gyr).

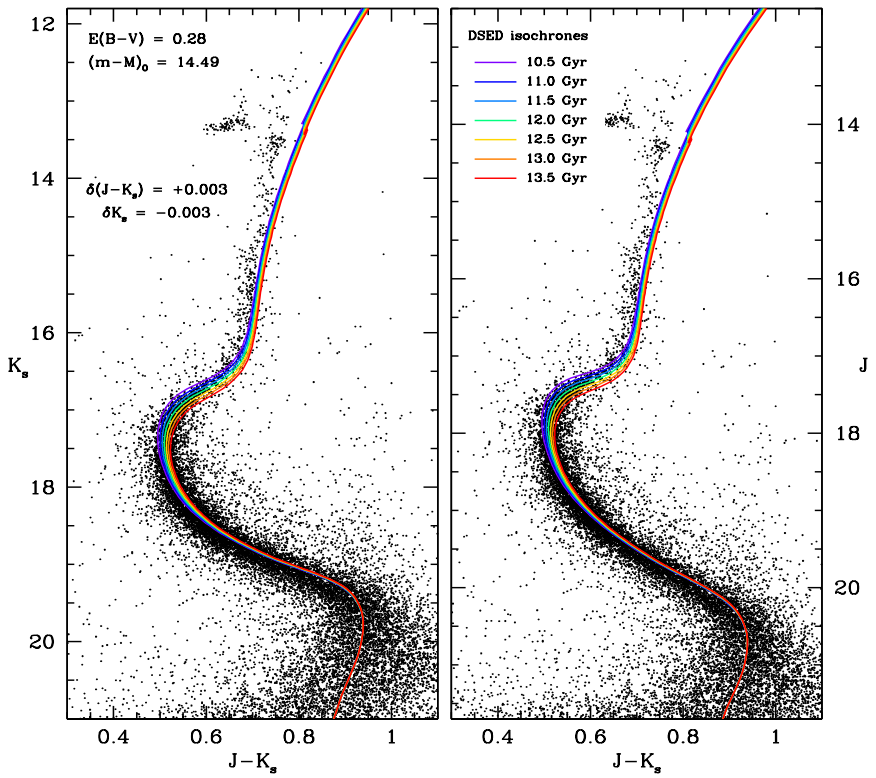

Figure 5.8: The same as in Figure 5.6 but for DSED isochrones (Dotter et al., 2007).

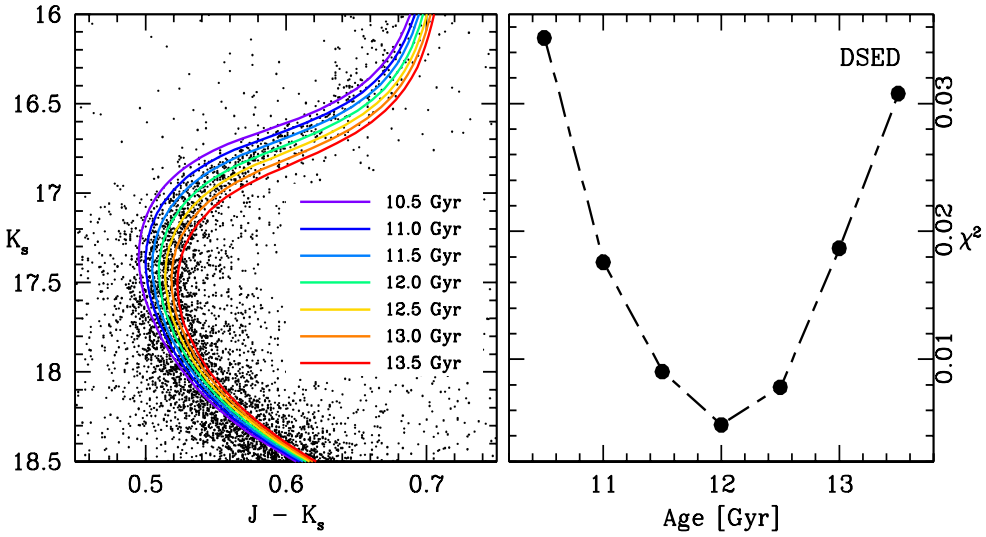

Figure 5.9: The same as in Figure 5.7 but for DSED isochrones.

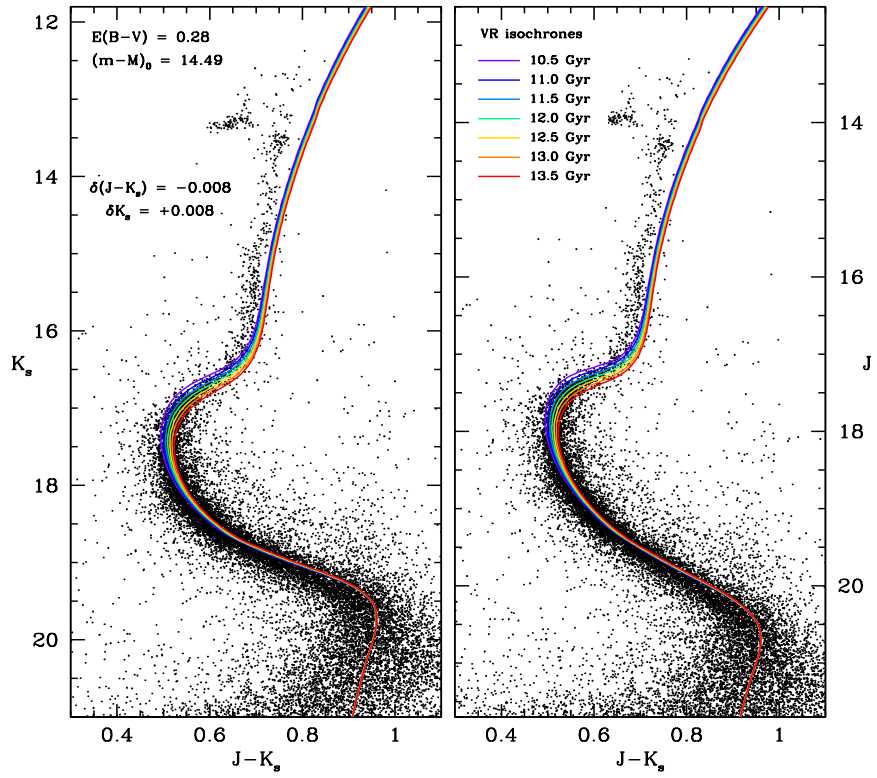

Figure 5.10: The same as in Figure 5.6 but for VR isochrones (VandenBerg et al., 2014).

problem. It may be related to some issues depending on the T_{eff} - color transformations in the IR, and possibly caused by uncertainties in the model atmospheres, like treatment of absorption lines as a function of gravity and to the abundance of some specific elements.

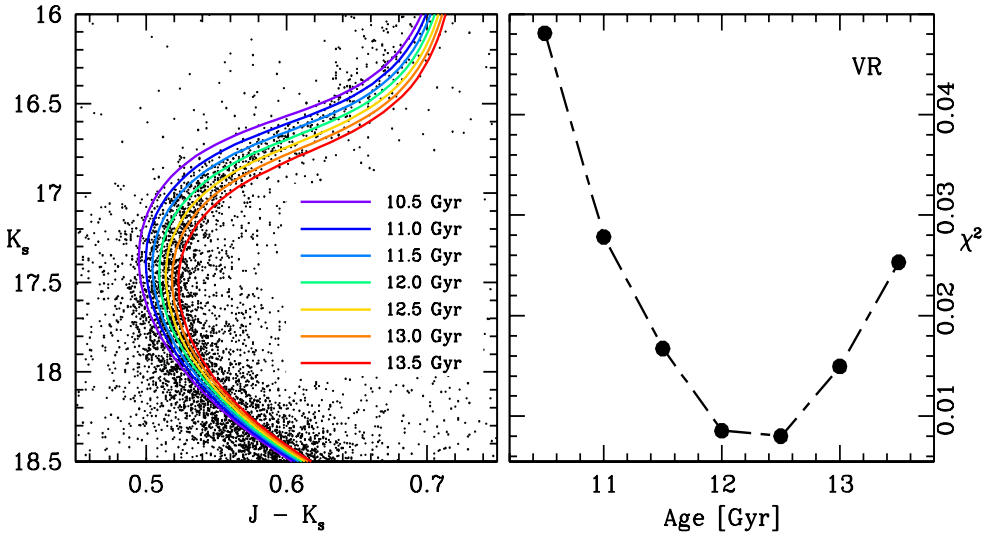

Figure 5.11: The same as in Figure 5.7 but for VR isochrones.

The impact of the adopted chemical composition on the overall quality of the fit has been tested. In particular, we compared isochrones with [Fe/H] = -0.42 and [α/Fe] = +0.2 adopted by VandenBerg et al. (2013) for their age derivation of NGC 6624 and [Fe/H] = -0.60 & [α/Fe] = +0.4 that we have used for our age derivation. For a fixed age, the two isochrones ([Fe/H] = -0.60 & [α/Fe] = +0.4 and [Fe/H] = -0.42 & [α/Fe] = +0.2) exactly match, showing only a slight difference at the MS-Knee level. We have also considered the effect of the abundance variations. Cohen et al. (2015) showed that a modest helium enhancement of Y=0.04 is not able to solve the observed disagreement between models and data at the SGB/RGB level. We verified that the overall match still remains unsatisfactory even adopting isochrones with an helium content as large as Y=0.35. In particular, while the increase of helium results in a better fit at the RGB base, it does not allow to properly reproduce the MS. Finally, we tried to test the impact of adopting different values of reddening and distance on the determination of the age of the cluster. With this aim we performed the same χ^2 analysis as before by assuming the values of Heasley et al. (2000) and Valenti et al. (2004a). This analysis gives age values of 11.0 ± 0.5 Gyr and 10.5 ± 0.5 Gyr respectively. However a visual check reveals that isochrones having such extreme values of E(B-V) and/or $(m - M)_0$ do not reproduce properly the main evolutionary sequences (MS-TO/SGB level, HB level and RGB bump) of the cluster. Hereafter, for our analysis we will adopt the absolute age of 12 Gyr derived from BaSTI, the model which better reproduce the overall shape of the CMD of NGC 6624.

5.4.2 Comparison with previous results

The age of NGC 6624 has been widely debated in recent years. As shown in Figure 5.12, the value determined in this work is in good agreement, within the errors, with most of the previous estimates quoted in the literature. The largest discrepancy is

found with respect to the value determined by Heasley et al. (2000). By comparing the CMD of NGC 6624 with those of NGC 6637 and 47 Tucanae (having a similar metallicity), the authors established that these clusters have the same age (14 ± 1 Gyr) by using the Yale isochrones. A relatively old age (13.00 ± 0.75 Gyr) was also found by Dotter et al. (2010), analyzing DSED models with the following chemical composition: [Fe/H]$= -0.50$ (by assuming the scale by Zinn and West, 1984, hereafter ZW84) and [α/Fe]$= 0$. An absolute age of 10.6 ± 1.4 Gyr, in quite good agreement with the one estimated in this work (within their large error bars), was instead obtained by Salaris and Weiss (2002), both for a metallicity of [Fe/H]$= -0.50$ (ZW84 scale) and for [Fe/H]$= -0.70$ (CG97 scale). Meissner and Weiss (2006) derived for NGC 6624 two different ages: 12 Gyr from the model best reproducing the MS-TO region (as in our case), and a lower limit of 10.5 Gyr, from the isochrone providing an acceptable fit to all the investigated age indicators. From the isochrone fitting and the ZAHB loci, VandenBerg et al. (2013) derived the ages of 55 GCs for which the optical HST/ACS photometry was publicly available. In the case of NGC 6624 the absolute age resulted to be 11.25 ± 0.5 Gyr, in good agreement with our value. Finally the most recent study of the cluster was performed by Roediger et al. (2014), within a detailed review on the state-of-the-art about age and metallicity determinations for a sample of 41 Galactic GCs. The authors quote an age of 12.5 ± 0.9 Gyr, which is again consistent with the value obtained in this work.

5.5 The Luminosity and Mass Function of NGC 6624

We have studied the LF and the MF of MS stars in NGC 6624 and their radial variations within the FOV of GSAOI. This kind of studies has been proven to be an efficient tool to study the effect of cluster internal dynamics on stars in a wide range of masses, including the faint-end of the MS where most of the cluster mass lies. In relaxed systems, the slopes of the MF and LF are expected to vary as a function of the distance from the cluster center, with indexes decreasing as distance increases, because of the different effect of mass segregation. Moreover, the radial variation in the stellar MF of star clusters allow to derive crucial information about the dynamical history of the system (including the amount of mass loss suffered by the clusters, e.g. De Marchi et al., 2007, Vesperini and Heggie, 1997) and variation in the stellar IMF as recently shown by Webb and Vesperini (2016). In this context, NGC 6624 is a quite interesting case because it has been classified as a post-core collapse cluster (Trager et al., 1995), hence it has already experienced some of the most energetic and advanced phenomena known to occur during the dynamical evolution of dense stellar systems (Meylan and Heggie, 1997).

5.5.1 Artificial Star Experiment

In order to derive a meaningful MS-LF, it is important to take into account a number of effects (such as blends, photometric errors and stellar crowding) that can limit the

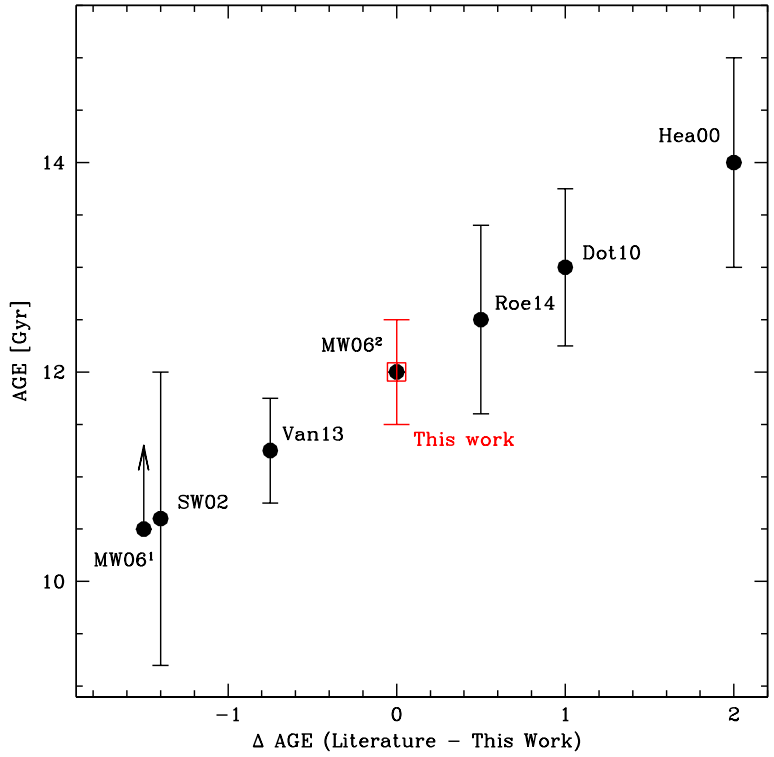

Figure 5.12: Age estimates of NGC 6624 determined in previous studies, compared to that obtained in this work (red point). The acronyms shown in the figure are so defined: **MW06**[1] & **MW06**[2] (Meissner and Weiss, 2006), **SW02** (Salaris and Weiss, 2002), **Van13** (VandenBerg et al., 2013), **Roe14** (Roediger et al., 2014), **Dot10** (Dotter et al., 2010) and **Hea00** (Heasley et al., 2000).

photometric accuracy, especially when deriving complete samples of faint stars. In order to assess the impact of these effects, we performed a set of artificial star experiments following the prescriptions reported in Bellazzini et al. (2002) and Dalessandro et al. (2011, 2015). The main steps of this procedure are briefly summarized below. We initially defined a mean ridge-line (MRL) in the (K_s, $J - K_s$) plane by considering 0.5 mag-wide bins in K_s and by selecting the corresponding median value in color after a $2\sigma-$clipping rejection (see Table 1 and the red line in Figure 5.13, left panel).

Then, we generated a catalog of simulated stars with a K_s-input magnitude ($K_{s,\mathrm{in}}$) extracted from a LF modeled to reproduce the observed LF. To each star extracted from the LF, we finally assigned a J_{in} magnitude by means of an interpolation along the MRL of the cluster. In order to avoid artificially increasing the crowding conditions, only one artificial star was simulated in each run within a 20×20 pixels cell (more than 5 times the typical FWHM of stars on the images). In addition, we imposed each simulated star to have a minimum distance of about 50 pixels from the edges of each chip. By imposing these criteria and adopting the coordinate transformations discussed in Section 5.2, artificial stars were added to the 13 J and 14 K_s images by

Table 5.1: MRL of NGC 6624 in the $(K_s, J-K_s)$ CMD.

K_s (mag)	$J-K_s$ (mag)
12.413	0.742
12.913	0.737
13.413	0.727
13.913	0.723
14.413	0.714
14.913	0.706
15.413	0.696
15.913	0.680
16.413	0.644
16.913	0.547
17.413	0.519
17.913	0.528
18.413	0.588
18.913	0.709
19.413	0.897
19.913	0.947
20.413	0.937
20.913	0.877
21.413	0.817

using the `DAOPHOT II/ADDSTAR` software. This procedure was performed individually on each chip and the artificial stars thus obtained were analyzed by using the same PSF models and the same reduction process (including the same selection criteria) adopted for the real images, as fully described in Section 5.2. A total of $\sim$ 48000 artificial stars per chip have been simulated. Figure 5.13 shows a comparison between the simulated (*left panel*) and the observed CMD (*right panel*). It is quite evident that the two CMDs are fully compatible over the entire magnitude range covered by the observations, in particular the simulated MS (for $K_s > 16$) shows the same spread in color as the observed one, thus confirming that the procedure is fully appropriate.

The artificial star catalog thus obtained was used to derive the completeness curves as the ratio ($\Gamma = N_{\rm out}/N_{\rm in}$) between the number of stars recovered after the photometric reduction ($N_{\rm out}$) and the number of simulated stars ($N_{\rm in}$) in each magnitude bin. The completeness curves as a function of the K_s magnitudes for three different radial bins ($0'' \leq r < 15''$, $15'' \leq r < 30''$ and $r \geq 30''$, where r is the distance from the cluster center[5]) are shown in Figure 5.14. This clearly testify to a high (90-100%) photometric completeness of the GEMINI catalog down to $K_s \sim 19-20$, depending on the distance from the center.

[5]We recomputed the cluster center $C_{\rm grav}$ of NGC 6624 by applying the algorithm of Casertano and Hut (1985) to evaluate, through an iterative procedure, the "density center" of the stellar positions, i.e. their average position weighted by the local number density (for more details, see Lanzoni et al. 2007, 2010). Using various initial searching radii, ranging from 5" to 20", and applying a cut in magnitude K_s = 18 to avoid incompleteness, we finally found $\alpha_{J2000} = 18^h23^m40^s.52$, $\delta_{J2000} = -30°21'40''.25$ with an uncertainty of about 0.2".

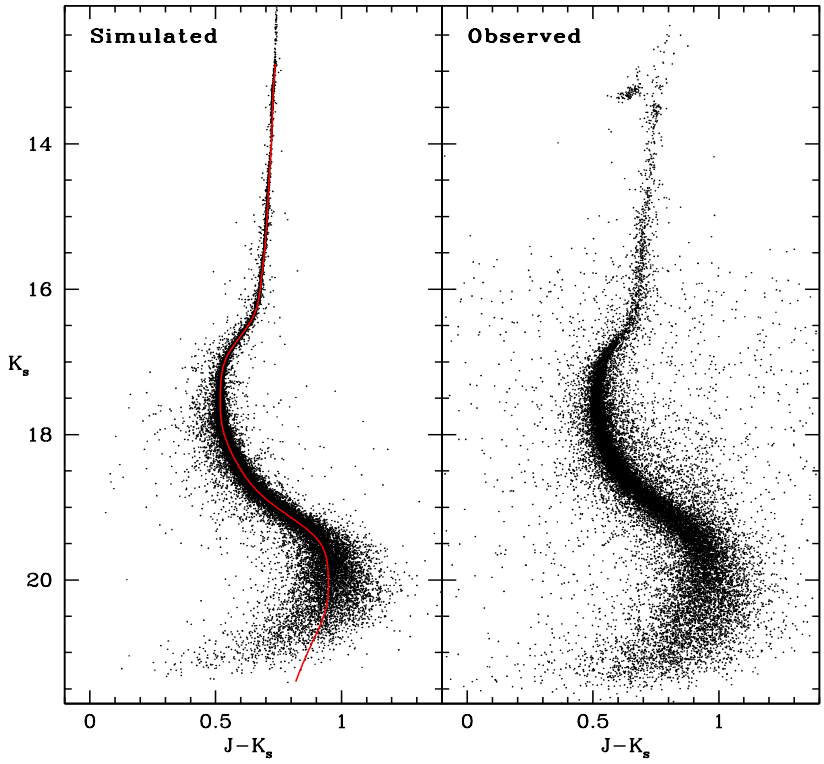

Figure 5.13: Simulated (*left* panel) and observed (*right* panel) $(K_s, J-K_s)$ CMD of NGC 6624, for all the stars that survived the selection: -0.2 $\leq$ sharpness $\leq$ 0.2. As clearly visible, the two CMDs turn out to be fully comparable, especially in the MS region (at $K_s > 16$). The red line in the left panel represents the MRL of NGC 6624 in the $(K_s, J-K_s)$ CMD.

5.5.2 Luminosity and Mass functions

In order to derive the MS-LF of NGC 6624 we adopted the radial bins defined for the determination of the completeness curves (see Section 5.5.1). Starting from the $(K_s, J-K_s)$ CMD, we selected a sample of bona-fide MS stars defined as those stars located within 2.5σ from the MRL, where σ is the combined photometric uncertainty in the K_s and J bands. For each radial interval, we considered only the stars with K_s magnitude ranging between 16 and the value corresponding to a completeness factor $\Gamma \sim 0.5$, namely K_s = 20.35 for $0'' \leq r < 15''$, $K_s = 20.45$ for $15'' \leq r < 30''$ and $K_s = 20.55$ for $r \geq 30''$. The observed LF obtained in each radial interval was thus corrected for incompleteness by adopting the appropriate value of Γ in each bin of magnitude. The completeness-corrected LF was then decontaminated from the effect of field stars by using the Besançon simulation of our Galaxy (Robin et al., 2003) for a region of about 2.5′ squared centered on NGC 6624, rescaled on the GSAOI FOV. For each magnitude bin, the density of field stars has been estimated and then subtracted (see for example Bellazzini et al. 1999). In Figure 5.15 the completeness-corrected and background-subtracted LFs of NGC 6624 in different radial bins are shown. In order

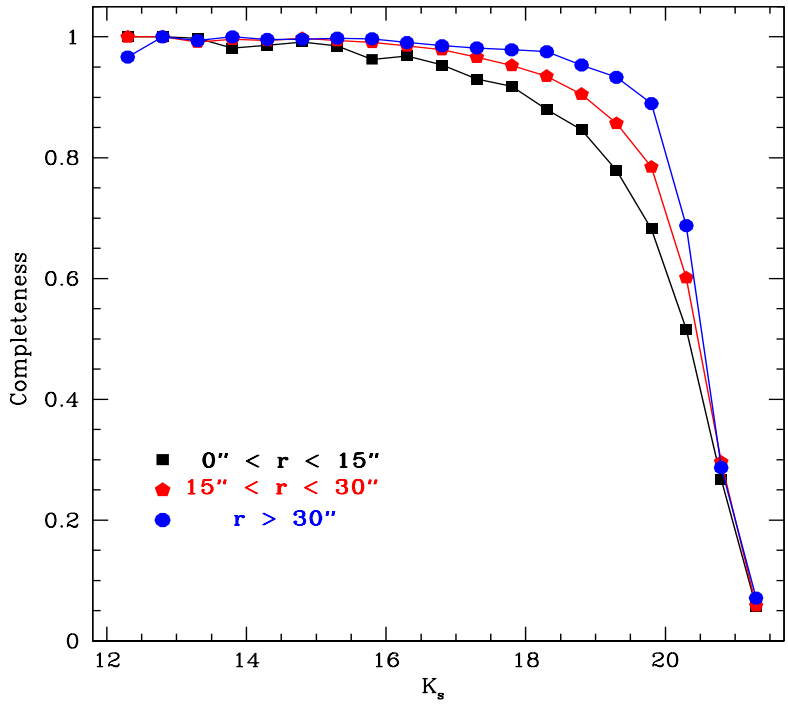

Figure 5.14: Photometric completeness (Γ) as a function of the K_s magnitude for the GEMINI catalog of NGC 6624 in three different radial bins (see labels).

to compare the LFs obtained at different distance from the cluster center, the LFs have been normalized to the one obtained for the innermost region in the magnitude range $16.0 < K_s < 17.5$. The comparison shows that the LFs are clearly different, with the LF in the outer regions of the cluster showing an overabundance of low-luminosity stars with respect to those in the innermost radial bin, consistent with the effect of mass segregation. This is in agreement with results by Goldsbury et al. (2013).

Following a similar approach, we have also derived the MF of NGC 6624. Masses have been estimated from the BaSTI isochrone that best-fits the CMD, as discussed in Section 5.4.1. This provides a MS-TO mass of $0.88M_{\odot}$. The MF covers a range in mass from $0.9M_{\odot}$ down to lower limits corresponding to $\Gamma \approx 0.5$: $M = 0.49M_{\odot}$ for $0'' \leq r < 15''$, $0.47M_{\odot}$ for $15'' \leq r < 30''$ and $0.45M_{\odot}$ for $r \geq 30''$. The MFs are shown in Figure 5.16, with the same color code as in Figure 5.15 to indicate different distances from the cluster center. We used the MF of the innermost radial bin as a reference and we normalized the more external ones by using the number counts in the mass range $0.8 \leq M/M_{\odot} < 0.9$. As appear in Figure 5.16 and in agreement with what we obtained from the analysis of the LFs, the MFs show a clear variation of their slopes, flattening moving outwards. Such a trend clearly demonstrates that this cluster has already experienced a significant degree of mass segregation. In general, all GCs are expected to show evidence of mass segregation, because of their short relaxation timescales (e.g. Paust et al., 2010). However, recent results have shown that

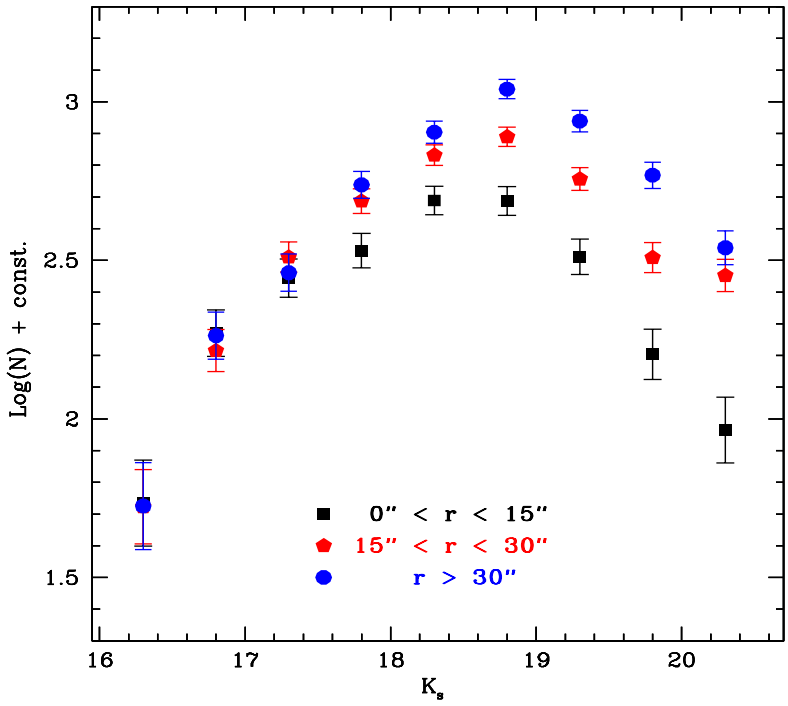

Figure 5.15: NGC 6624 completeness-corrected and field-decontaminated MS-LFs in the K_s band obtained from the GEMINI catalog in three different radial bins. The LF corresponding to the innermost radial bin is used as reference to normalize those at larger radii at the brightest bin.

there are some exceptions: see the case of ω-Centauri (Ferraro et al., 2006), NGC 2419 (Dalessandro et al., 2008b, Bellazzini et al., 2012), Terzan 8 and Arp 2 (Salinas et al., 2012), Palomar 14 (Beccari et al., 2011) and NGC 6101 (Dalessandro et al., 2015). These examples suggest that either some mechanisms able to suppress mass segregation may occur in some GCs or that theoretical relaxation times may suffer of significant uncertainties. In this context, the study of the dynamical state of a cluster becomes quite interesting.

5.6 Summary & Conclusions

This work is focused on NGC 6624, a metal-rich globular cluster located in the Galactic bulge. By combining the exceptional capabilities of the adaptive optics system GeMS with the high resolution camera GSAOI on the GEMINI South telescope, we obtained the deepest and most accurate NIR (K_s, $J-K_s$) and (J, $J-K_s$) CMDs ever obtained from the ground for NGC 6624. The quality of the photometry turns out to be fully competitive with the optical photometry from the HST. The derived CMDs span a range of more than 8 magnitudes, allowing to identify all the well known evolutionary sequences, from the HB level to the MS-TO point down to below the MS-K (detected at $K_s \sim 20$), a feature observed so far only rarely in the optical band and identified

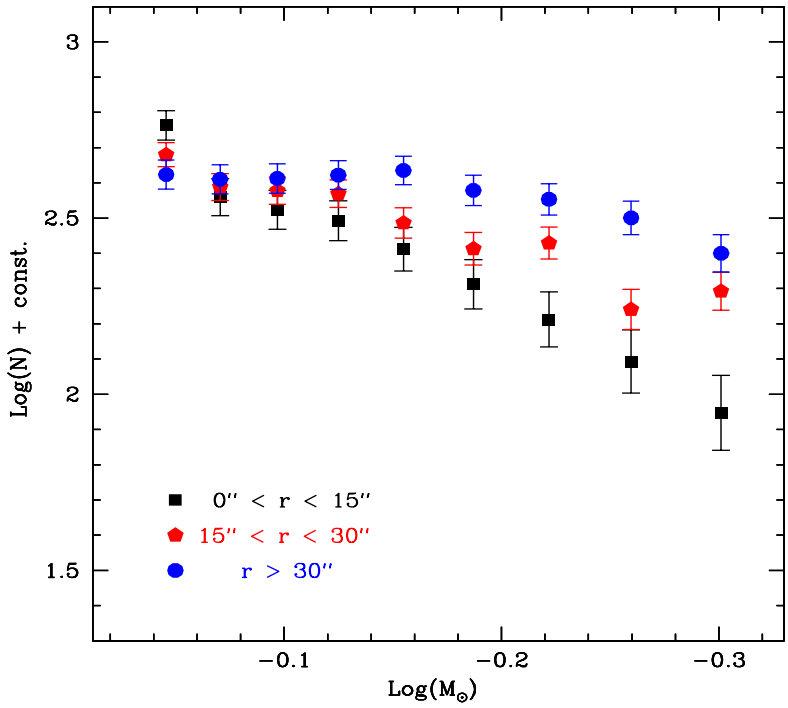

Figure 5.16: MFs derived by using a BaSTI isochrone with [Fe/H] = -0.60 and t_{age} = 12.0 Gyr (see Section 4.1). Radial bins, symbols and colors are the same as in Figure 5.15.

for the first time here in a purely infrared CMD. We took advantage of our high resolution photometry to get an accurate estimate of the absolute age of NGC 6624, which is still quite debated in the literature. By adopting the MS-TO fitting method, we determined an absolute age of about 12.0 $\pm$ 0.5 Gyr for the cluster.

Taking advantage of this high-quality sample, we studied the MS-LF and MF at different distances from the cluster center. The level of completeness of the MS sample has been evaluated from artificial star experiments and turns out to be larger than 50% down to $K_s \sim 20.3$ at any distance from the cluster center. The completeness-corrected and field-decontaminated LFs and MFs show significant signatures of mass segregation. In fact, moving from the innermost region of the cluster to the outskirts, the number of low-mass stars gradually increases compared to high-mass stars. This result confirms that NGC 6624 is a dynamically old cluster, already relaxed.

The data obtained for NGC 6624 clearly show that, under favorable conditions (for example the seeing of the observing night or the NGSs magnitude), the GeMS/GSAOI system is able to provide images with similar spatial resolution and photometric quality as HST in the optical bands.

5.7 Appendix

5.7.1 Testing stellar variability with the GeMS + GSAOI system

We could also test the stability and accuracy of the GeMS + GSAOI system in performing stellar variability studies. To do this, we focused on the core of NGC 6624. In this region Deutsch et al. (1999) discovered an exotic object (Star1) which has been classified as a quiescent CV or a LMXB. The optical counterpart to this object, named COM_Star1, has been identified by Dalessandro et al. (2014) to be a star showing a clear sinusoidal light modulation and an orbital period of $P_{orb} \approx 98$ minutes. We identified COM_Star1 in our GEMINI J and K_s images (see Figure 5.17) by using the coordinates reported by Dalessandro et al. (2014). It appears as a relatively bright star at $K_s \sim 17.76$ and $(J - K_s) \sim 0.69$ outside the MS on the red side (it is marked with a red circle in the top panel of Figure 5.19). Since the object is visible in all GEMINI images (13 in J and 14 in K_s), we could investigate its variability in the infrared bands. Its light curve (red dots in the *bottom panel* of Figure 5.19) shows a luminosity variation with an amplitude of ~ 0.2 mag and is well folded with the same period ($P_{orb} = 98$ min) found by Dalessandro et al. (2014). For sake of comparison, the light curve of a genuine MS star (StarB) with comparable luminosity (blue circle in Figure 5.18) is shown in Figure 5.19, *bottom panel*. As expected, this star is a "normal" non-variable MS, in fact its light curve does not show any evidence of flux modulation ($\sigma_K = 0.017$ mag).

The constancy of the StarB magnitude despite variation of seeing, airmass and PSF shape in the images, implies that the system is largely stable and it can be used to successfully reveal also very small flux variations (of the order of a few 0.01 mag). This test allow us to conclude that the GeMS/GSAOI system indeed has such a high performance and can be successfully used also for stellar variability studies.

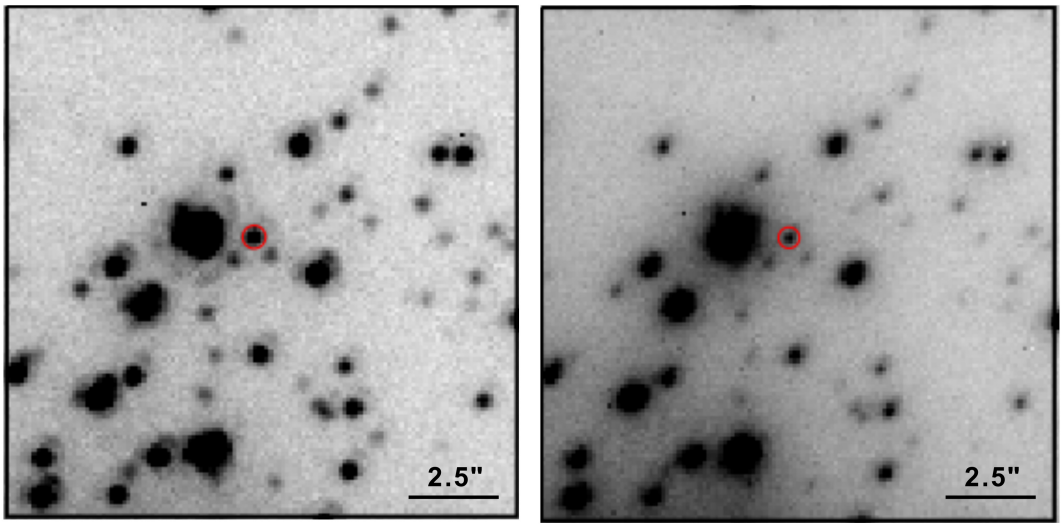

Figure 5.17: *Left panel*: K_s image of a region of (2.5″ × 2.5″) of NGC 6624, centered on the position of ComStar1, marked with a red circle, as observed by the GeMS/GSAOI system. *Right panel*: The same, but for the *J* band.

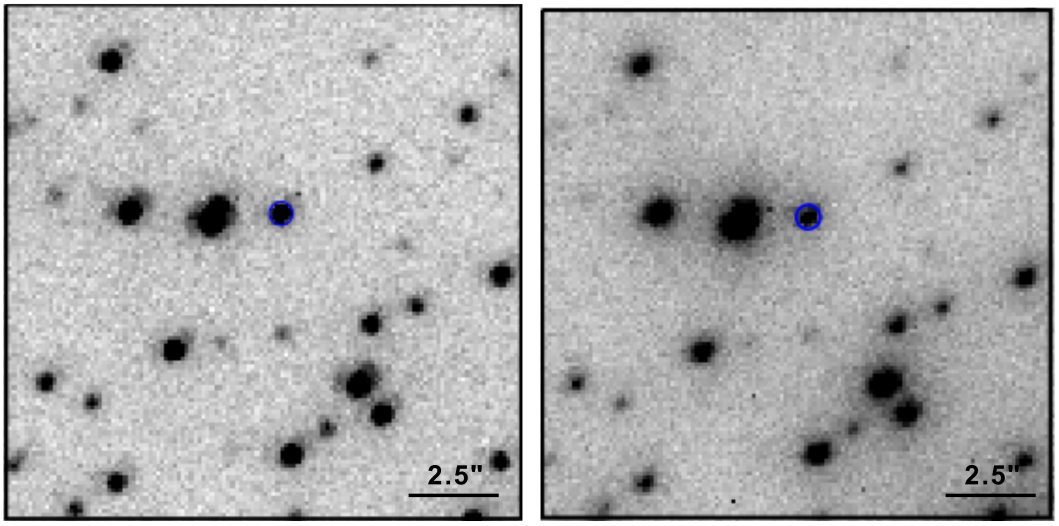

Figure 5.18: *Left panel*: K_s image of a region of (2.5″ × 2.5″) of NGC 6624, centered on the position of StarB, marked with a blue circle, as observed by the GeMS/GSAOI system. This star has the same magnitude as ComStar1 and is adopted for a comparison. *Right panel*: The same, but in the *J* band.

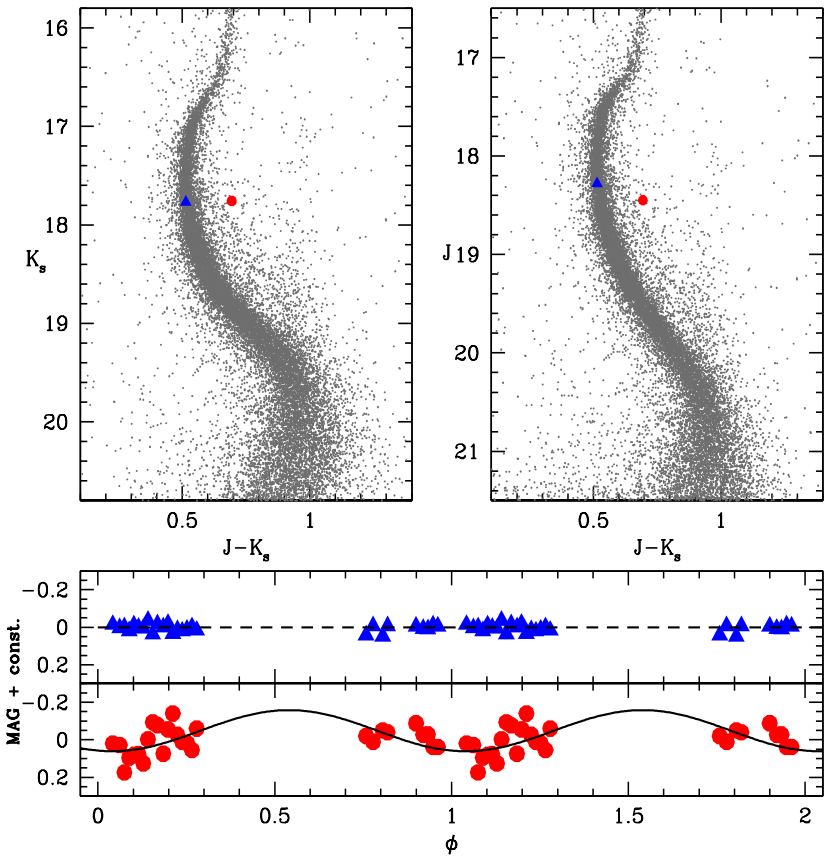

Figure 5.19: *Top panels*: Positions in the $(K_s, J-K_s)$ and $(J, J-K_s)$ CMDs of ComStar1 and StarB are highlighted with a red circle and a blue triangle, respectively. *Bottom panels*: The red circles represent the light curve of ComStar1 folded with the estimated orbital period $P_{orb} \approx 98$ min (Dalessandro et al., 2014). The black line is a sinusoidal function of amplitude ≈ 0.2. For comparison the blue triangles show the light curve of StarB, that has the same average K_s magnitude of ComStar1 but does not show any evidence of flux modulation (dashed black line).

CHAPTER 6

On the use of the main sequence knee to measure absolute globular cluster ages

Based on the results submitted in:
Saracino S., Dalessandro E., Ferraro F. R., Lanzoni B., Origlia L., Salaris M., Pietrinferni A., Geisler D., Kalirai J. S., Correnti M., Mauro F., Cohen R. E., Villanova S., Moni-Bidin C.
2017, *The Astrophysical Journal*

Abstract

In this chapter we review the operational definition of the so-called MS-knee, feature in the CMD occurring at the low-mass end of the MS. The magnitude of this feature is predicted to be independent of age at fixed chemical composition. For this reason, its difference in magnitude with respect to the MS-TO point has been suggested as a possible diagnostic to estimate absolute GC ages. We demonstrate first that the operational definition of the MS-knee currently adopted in the literature refers to the *inflection point* of the MS (that we here more appropriately named MS-saddle), a feature that is well distinct from the knee and that cannot be used as its proxy. By using different sets of isochrones we also demonstrate that the absolute magnitude of the MS-knee varies by 0.2-0.3 mag from one model to another. Hence, at the moment, the MS-knee cannot be used as reference magnitude to derive accurate absolute ages. However, the location of the MS-saddle is almost coincident in the different models, favoring its use as an age diagnostic. By means of ultra-deep multi-band photometry of two metal-rich GCs (namely 47 Tucanae and NGC 6624) we explore the location of the MS-saddle in different CMDs, finding that its magnitude depends on the color adopted in the CMD. From the detailed comparison of the difference in magnitude between the MS-TO and the MS-saddle with theoretical expectations, we attempt to determine the absolute age of the two clusters and its uncertainty. Our conclusion is

that, accounting for statistic and systematic uncertainties, the total error on absolute age achievable from this method cannot be smaller than $\sim$ 1.5-2.0 Gyr, even if high-quality datasets are available. In the next future, third-generation telescopes, such as JWST and E-ELT, will provide accurate photometric studies in the NIR for a much larger sample of clusters. At that time, a better constraint on the structure of extreme low-mass stars and the input physics of their modeling will be really appreciated.

6.1 Introduction

GCs are among the oldest stellar aggregates in the Universe and are therefore pristine fossils of the very early epoch of galaxy formation. A detailed study of their ages is useful for several reasons: *relative* ages help us to understand the formation and the assembly chronology of the different components (halo, disk, bulge) of our Galaxy (Rosenberg et al., 1999; Zoccali et al., 2003); *absolute* ages set a lower limit to the age of the Universe (Buonanno et al., 1998, Stetson et al., 1999, Gratton et al., 2003) and provide robust constraints to the physics adopted in stellar evolutionary models (Salaris and Weiss, 1998; Cassisi et al., 1999; VandenBerg et al., 2008; Dotter et al., 2008). Several methods have been used so far to estimate the relative and absolute ages of these systems, mainly based on the analysis of their optical CMDs. Relative ages can be derived by using "differential" parameters, built from the magnitude or the color of the MS-TO, (which systematically varies with time) and the magnitude or the color of a "reference" feature in the CMD that is independent of the cluster age. Examples are: (1) the *horizontal* parameter, defined as the difference in color between the MS-TO and the RGB at 2.5 magnitudes above the MS-TO level (see Sarajedini and Demarque, 1990; Sandage and Cacciari, 1990; Vandenberg et al., 1990); (2) the *vertical* parameter, based on the difference in magnitude between the HB, typically measured at the RR Lyrae instability strip, and the MS-TO (Iben and Renzini, 1984; Buonanno et al., 1998; Rosenberg et al., 1999; Stetson et al., 1999; De Angeli et al., 2005; Marín-Franch et al., 2009). Of course differential parameters have the advantage of being independent of distance and reddening. Cluster absolute ages are generally estimated by measuring the luminosity of the MS-TO point in the CMD, or by applying the isochrone fitting method. The latter has been recently used by Saracino et al. (2016) and Correnti et al. (2016), to determine sub-Gyr absolute ages using a chi-squared maximization and a maximum-likelihood technique, respectively. Absolute ages can also be derived from the direct comparison of the differential parameters with the corresponding theoretical predictions. In these cases, various sets of theoretical models (e.g., Pietrinferni et al. (2004); Salaris and Weiss, 2002; Dotter et al., 2010; VandenBerg et al., 2013) need to be considered in order to investigate the effects of different assumptions in the models.

In the recent years, advanced instruments and techniques, such as adaptive optics systems mounted on 8-10 m class telescopes, and high resolution cameras on board the HST, make also NIR observations very promising in the estimate of GC ages.

In fact, deep NIR photometry revealed the existence of a well-defined knee at the lower end of the MS, approximately three magnitudes below the MS-TO (see, e.g., the cases of ω Centauri, Pulone et al., 1998; M4, Pulone et al., 1998; Milone et al., 2014; NGC 3201, Bono et al., 2010; NGC 2808, Milone et al., 2012; Massari et al., 2016b; 47 Tucanae, Kalirai et al., 2012; M71, Di Cecco et al., 2015; M15, Monelli et al., 2015). The MS-knee arises from a redistribution of the emerging stellar flux due to an opacity change, mainly caused by the collision-induced absorptions of molecular hydrogen in the surface of cool dwarfs (Linsky, 1969; Saumon et al., 1994 and references therein), which moves low-mass MS stars towards bluer colors.[1] Since its magnitude is predicted to be independent of cluster age at fixed chemical composition, the MS-knee provides a potential anchor (alternative to the HB luminosity) at which the MS-TO magnitude can be referred to define a new *vertical* method for the age determination. As are all the other differential parameters, this approach is formally independent of GC distance and reddening. With respect to the traditional *vertical* method referred to the HB level, it has the drawback of requiring the detection of a much fainter feature in the CMD (fainter by ~ 7 magnitudes), but *i)* it is much more populated because the stellar luminosity function increases towards lower masses and *ii)* it should be less affected by model uncertainties, such as the treatment of convection (Saumon and Marley, 2008). For these reasons Bono et al. (2010) proposed a new parameter (hereafter Δ_{TO}^{knee}) to measure relative and absolute GC ages from the magnitude difference between the MS-TO and the MS-knee levels. The approach has been already tested on a few clusters (as NGC 2808, Massari et al., 2016b; M71, Di Cecco et al., 2015 and M15, Monelli et al., 2015), with the conclusion that it can provide absolute age estimates at sub-Gyr accuracy, a factor of two better than what can be obtained with classical methods. Relative age studies using the Δ_{TO}^{knee} method have not been performed yet.

This work is devoted to an in-depth analysis of both the operational definition of the MS-knee and the potential use of this parameter to estimate absolute GC ages. In Section 6.2 we review the operational definition of the MS-knee adopted in the literature, suggesting a more appropriate nomenclature: we name MS-knee the point in a NIR CMD where the MS bends to the blue, while we name MS-saddle the point where the MS changes curvature. We then use three different sets of stellar models to investigate the position of these features in CMDs with various color baselines. Sections 6.3 and 6.4 are devoted to the determination of the parameter Δ_{TO}^{saddle}, measuring the magnitude difference between the MS-saddle and the MS-TO, for estimating the age of 47 Tucanae and NGC 6624, two Galactic GCs having similar metallicity for which deep NIR data are available. We explore the effects of varying the method to define the MS mean-ridge line, the approach to determine the MS-saddle, the color baseline of the CMD, and the stellar model used to interpret the

[1] Figure 16 of Casagrande and VandenBerg (2014) shows that the shape of the low-mass end of the MS sensibly depends on the α-element abundance, suggesting that for [α/Fe]=-0.4 a MS-knee is not present. However, in the α-element abundance regime of Galactic GCs, a MS bending can be identified at all metallicities.

observations. Section 6.5 summarizes our conclusion.

6.2 A knee or a saddle?

As shown in Figure 6.1, in a pure NIR (K_s, $J-K_s$) CMD, the lowest portion of the MS bends to the blue and creates a well defined knee. Consistently, the MS-knee corresponds to the reddest point of the MS at magnitudes fainter than the MS-TO (marked with a red circle in the figure). In spite of this and probably for observational issues, the MS-knee has been originally defined as the point of minimum curvature along the low-mass end of the MS ridge line (see Bono et al., 2010). This is an inflection point (that we name *MS-saddle*), where the MS ridge line changes its curvature from convex to concave. While it is related to the presence of the knee, it is certainly not coincident with it. This is clearly illustrated in Figure 6.1, where the location of the two features is marked along a 12 Gyr old isochrone (VandenBerg et al., 2014): the MS-saddle is more than 0.7 mag brighter than the MS-knee (note that this difference is visible also in Figure 2 of Bono et al., 2010, where the MS-knee was first defined). At odds with the MS-knee, the MS-saddle is a morphological feature indicating a change in the curvature of the MS ridge line. However this feature could still be interesting. In fact, as shown in Figure 6.2, the MS-knee, as defined above, only occurs in NIR CMDs (red circle in the left panel) and is not defined in hybrid optical-NIR CMDs (right panels). Instead, the MS-saddle (blue squares) can be measured in all the diagrams. Hence, a detailed comparison between the two features is worth investigating, in particular to assess whether the MS-saddle can be considered as a proxy of the MS-knee, useful for measuring cluster ages.

To this end, we compare the location of these features in the CMD using three different sets of stellar models. We considered the BaSTI models[2] (Pietrinferni et al., 2004), the Dartmouth Stellar Evolutionary Database (DSED; Dotter et al., 2007) and the Victoria-Regina isochrones (VR; VandenBerg et al., 2014). For a coherent comparison, we adopted the 2MASS photometric system in the (K_s, $J-K_s$) filter combination and we assumed the same values of age ($t = 12$ Gyr) and chemical composition ([Fe/H]=-0.60[3] and [α/Fe]=+0.4) for all the models. The isochrones are shown in Figure 6.3 (left panel), where different colors correspond to different models according to the color code reported in the labels. Triangles, squares and circles mark the MS-TO, the MS-saddle and the MS-knee, respectively, along each isochrone. As can be seen, the three models predict the same location in the CMD for the MS-TO, but significantly different positions of the MS-knee. As reported in Figure 6.4, even in the theoretical ($L - T_{eff}$) plane, the three isochrones slightly differ at the MS-knee level. In particular, the MS-knee is located at typical masses of 0.55-0.60 $M_{\odot}$.

[2]The BaSTI NIR colors and magnitudes are on the Johnson-Cousins-Glass photometric system, thus they were converted first on the (Bessell and Brett, 1988) system and then, by using the transformations of Carpenter (2001), into the 2MASS photometric system (Cutri et al., 2003).

[3]Note that different models require slightly different [Fe/H] in order to get the same value for [M/H]. It is due to differences in the input parameter values. We adopted [Fe/H] = -0.60 for BaSTI isochrones and -0.67 for DSED and VR isochrones.

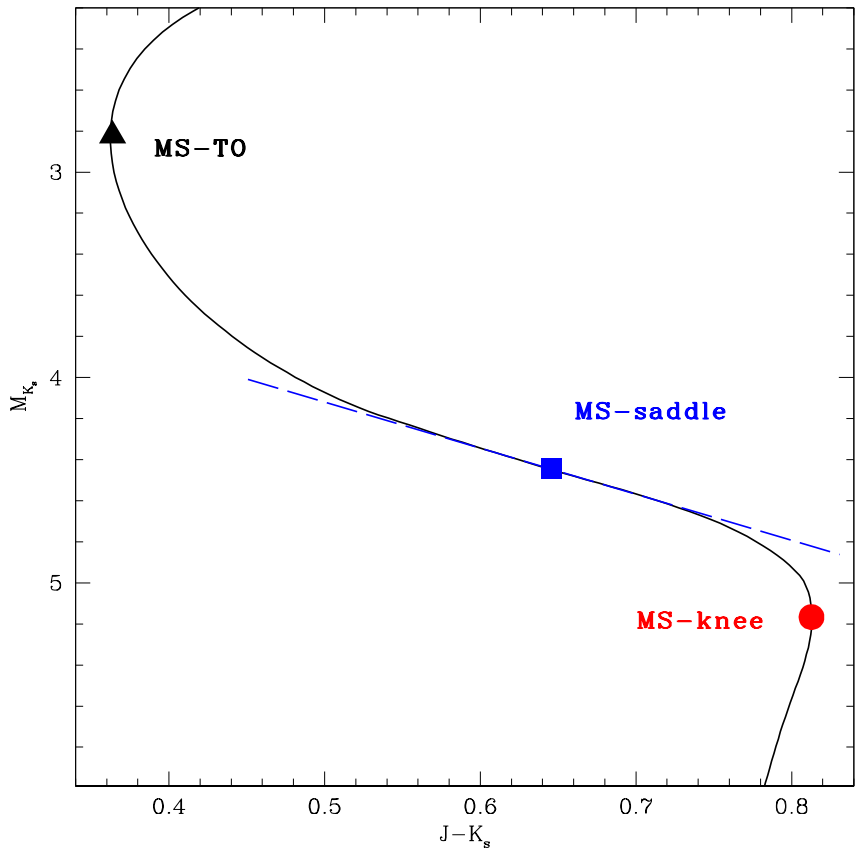

Figure 6.1: Location of the MS-TO (black triangle), MS-knee (red circle) and MS-saddle (blue square) along a 12 Gyr old isochrone extracted from the family of VandenBerg et al. (2014). The MS-knee is here defined as the reddest point along the MS MRL. The MS-saddle is the point where the MS MRL changes shape, from convex to concave, and thus shows the minimum curvature. A dashed line tangential to the isochrone is shown at the MS-saddle point to better illustrate the morphological meaning of this point.

The corresponding location of the MS-knee in the theoretical ($L - T_{eff}$) diagram is definitely affected by the uncertain choice of the stellar model boundary conditions, as discussed e.g. by Chen et al., 2014. One can clearly see in their Figs. 5, 6, 9 and 10, that changing just the choice of the boundary conditions affects the position of theoretical GCs isochrones in the ($L - T_{eff}$) diagram, at the typical bolometric luminosities of the MS-knee. Other choices of the physics inputs may also play a role, but the boundary conditions are probably the main source of uncertainty for this section of the isochrones. Bolometric corrections are also a major source of uncertainty for the determination of the position of the knee in NIR CMDs, as shown also in Chen et al., 2014. Major progress in model atmosphere calculations for low-mass and very low-mass stellar models (that provide both bolometric corrections and model

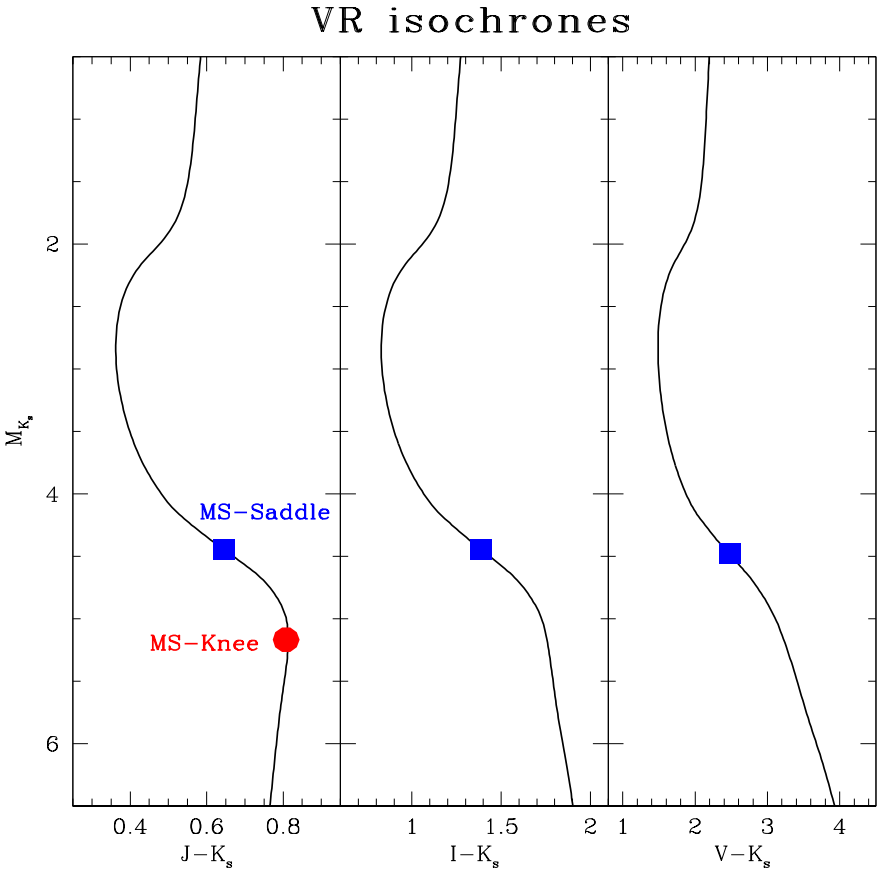

Figure 6.2: Location of the MS-knee (red circle) and MS-saddle (blue square) marked along the same isochrone plotted in Figure 6.1, but here shown in CMDs with three different color baselines: from left to right, $(K_s, J-K_s)$, $(K_s, I-K_s)$, and $(K_s, V-K_s)$. The MS-knee only occurs in the pure NIR-CMD. The MS-saddle, instead, can be defined in all the considered diagrams.

boundary conditions) is needed for firmer theoretical predictions about the MS-knee.

Obviously, this finding sets severe limits on the age estimates that can be obtained by using the MS-knee. In fact, for the same age and metallicity, the three isochrones predict values of Δ_{TO}^{knee} differing by 0.3 magnitudes, ranging from 2.08 to 2.37. In order to avoid filter-dependence, we tested also the NIR $(F110W, F110W-F160W)$ filter combination (Figure 6.3, right panel). By comparing isochrones of t = 11.5 Gyr, [Fe/H] = -0.77 and $[\alpha/Fe]$ = +0.4, we found the same discrepancy as before. Consequently, any use of this parameter, even with a formal measurement error of zero, would yield uncertainties of several Gyrs in the derived age ($\delta t \sim 5 Gyr$) just because of the different model predictions. The discrepancy shown in Figures 6.3 and 6.4 demonstrates that stellar evolutionary models still present strong limitations in reproducing the properties of low-mass MS stars and it calls for a new theoretical effort in order to understand its origin. In particular the ingredients affecting both the

stellar color (such as bolometric corrections and color-temperature transformations; see Salaris et al., 2007; Brasseur et al., 2010; Cohen et al., 2015) and the star luminosity (hence, different input physics used to describe stellar evolution in the low-mass regime) may play a role in generating such differences. Unfortunately, because of the large uncertainties currently affecting the theoretical models, the MS-knee cannot be used to estimate reliable absolute ages of stellar systems, even if accurate and high quality NIR photometry is available. It could be still useful for relative age studies where a comparison between different stellar models is not necessary.

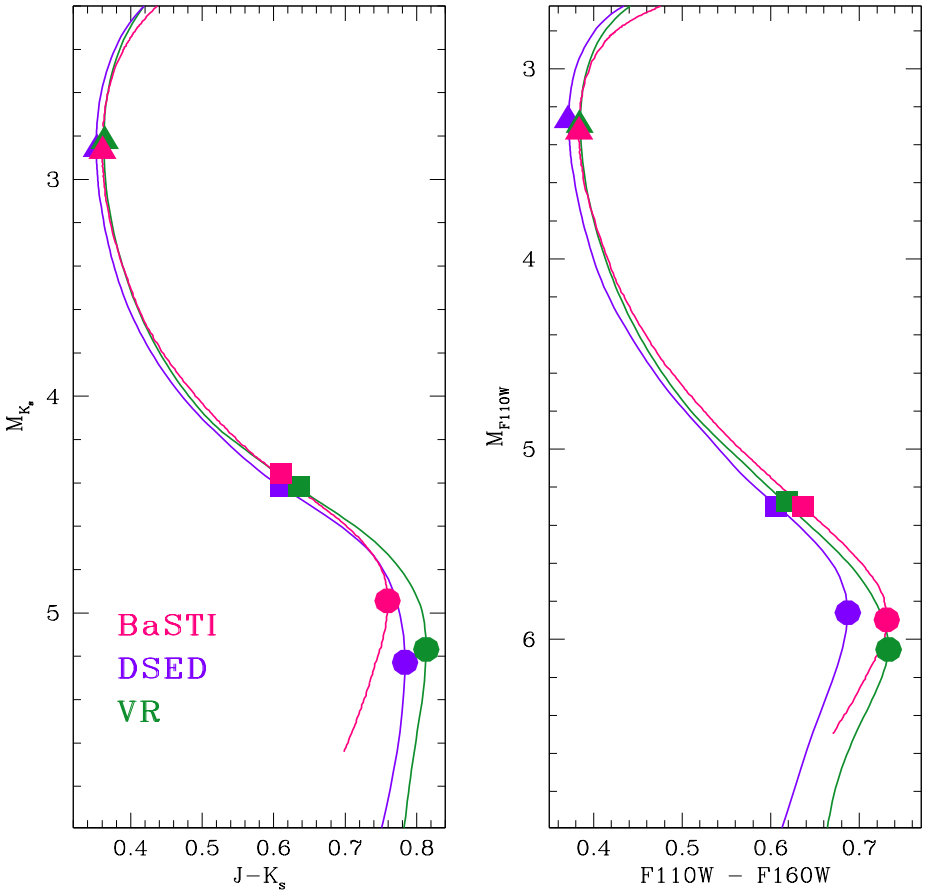

Figure 6.3: Location of the MS-TO (triangles), MS-knee (circles) and MS-saddle (squares) marked along 12 Gyr old isochrones from three different sets of theoretical models: BaSTI (red), DSED (purple) and VR (green) in the (K_s, $J-K_s$, *left panel*) and ($F110W$, $F110W-F160W$, *right panel*) filter combinations. The three models predict different locations of the MS-knee, while they agree on the color-magnitude position of the MS-saddle. This clearly illustrates that the two features are different.

In spite of the large differences in the predicted shape and CMD position of the MS-knee, the location of the MS-saddle appears to be much more stable (with magnitude variations smaller than 0.1 in K_s). The three isochrones exactly overlap in the ($L-T_{eff}$) plane, demonstrating that the MS-saddle, which corresponds to stars having masses

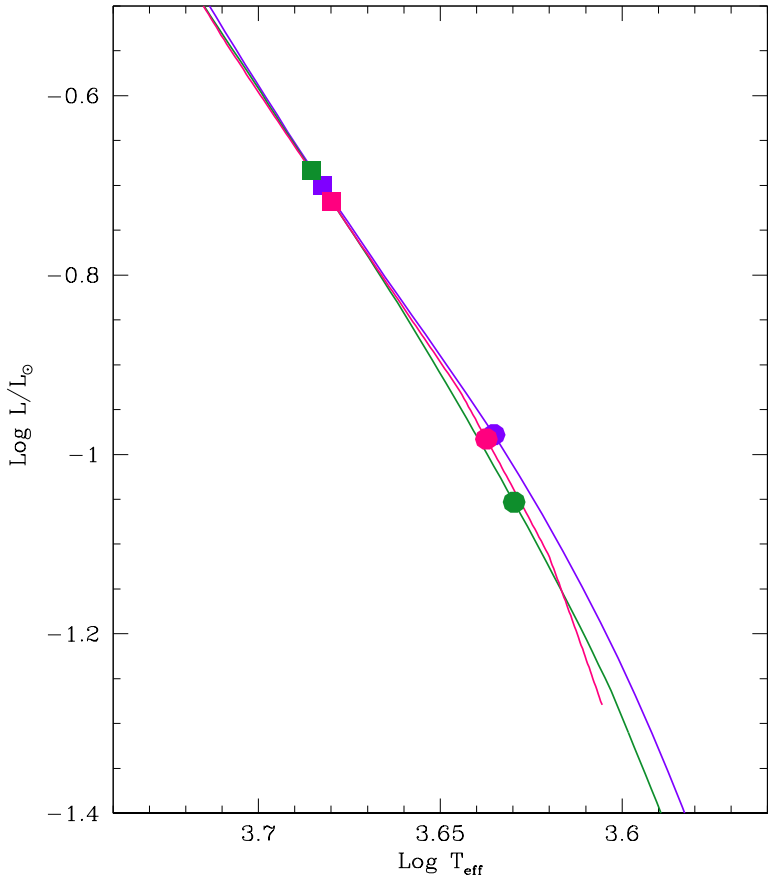

Figure 6.4: The same as in Figure 6.3 but in the $(L - T_{eff})$ plane. At the MS-knee level, the three models start to be different even in the theoretical plane, suggesting that not only bolometric corrections but also input physics for low-mass stars can be responsible of the mismatch among the models.

of 0.65-0.70 $M_{\odot}$, is not very sensitive to the morphology and the location of the knee. Hence the first result of this investigation is that the MS-saddle cannot be used as a proxy for the MS-knee. However its reduced model-dependence (in the $(K_s, J - K_s)$ and $(F110W, F110W - F160W)$ diagrams) and its potential measurability also in combined optical-NIR CMDs call for a thorough investigation of its reliability and stability as "reference" feature to estimate cluster ages. Of course, the first requisite is that, for fixed chemical composition, the magnitude of the MS-saddle is independent of cluster age. This is indeed confirmed by all the stellar models considered above. The predicted K_s-band magnitude of the MS-saddle (and, for comparison, of the MS-knee) for stellar populations with ages ranging from 9.5 Gyr to 13.5 Gyr is shown in Figure 6.5 for the three families of adopted stellar models. The constancy of the MS-saddle magnitude with varying isochrone age indicates that, in principle, it can be used as an anchor to which the MS-TO can be referred and used to measure both

relative and absolute ages[4]. However, since it is just a geometrical point dependent on the morphology of the MS ridge line, the MS-saddle is expected to be a "not-so-robust" feature from an observational point of view. Hence, an adequate analysis of the age accuracy and/or precision attainable by using this parameter determined from observational data is examined here.

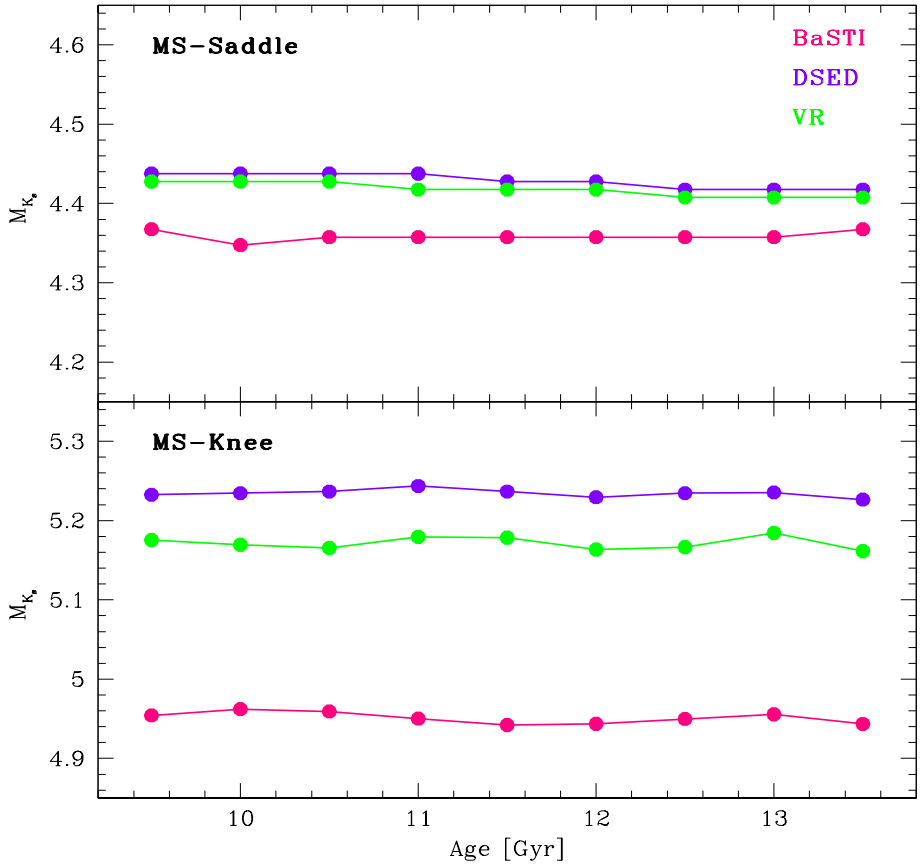

Figure 6.5: *Upper panel*– Dependence of the MS-saddle K_s-band magnitude on cluster age for the three different sets of adopted isochrones (BaSTI, DSED and VR in red, purple and green, respectively). Ages vary from 9.5 to 13.5 Gyr in steps of 0.5 Gyr. At fixed chemical composition, the MS-saddle *K*-band magnitude is independent of age and shows small difference in all the considered models. *Lower panel* – The same as in the upper panel, but for the MS-knee. In this case, different models predict significantly different values of the *K*-band magnitude of the MS-saddle.

[4]The bottom panel of Figure 6.5 shows that also the MS-knee magnitude is constant for varying cluster ages. However its value (and thus the parameter Δ_{TO}^{knee}) significantly depends on the adopted family of isochrones, thus making unacceptably model-dependent any age estimate, as discussed above.

6.3 Observational data - 47 Tucanae and NGC 6624

In order to test whether the magnitude difference between the MS-TO and the MS-saddle can be a reliable age indicator, we have analyzed 47 Tucanae and NGC 6624, two GCs having similar chemical composition, as first science cases. For 47 Tucanae we used the catalog presented in Kalirai et al. (2012) where a detailed description of the observations can be found. The images were acquired using the infrared channel of the WFC3 on board the HST in the F110W and F160W filters (GO-11677 PI: Richer). The resulting ($F110W$, $F110W - F160W$) CMD is shown in the left panel of Figure 6.6. It exhibits very well defined evolutionary sequences, from the base of the RGB to the low-mass end of the MS, reaching ~ 3 magnitudes below the MS-knee. The photometric precision is of the order of a few thousandths of a magnitude over the luminosity range sampled: ≈ 0.002 mag at the MS-TO level, ≈ 0.005 at the MS-knee.

In the case of NGC 6624, we have used the catalog described in Saracino et al. (2016). It has been obtained by using J and K_s data acquired with the MCAO GeMS at the Gemini South Telescope in Chile, as part of the proposal GS-2013-Q-23 (PI: D. Geisler). A detailed description of the observations and the data-reduction procedure is reported in Section 2 of Saracino et al. (2016). The (K_s, $J - K_s$) CMD of NGC 6624 is presented in the right panel of Figure 6.6. It spans a range of more than 8 magnitudes, from the HB level down to $K_s \approx 21.5$. In this case, the photometric errors are of ≈ 0.005 mag at the MS-TO level and ≈ 0.035 mag at the MS-knee. For 47 Tucanae only the NIR CMD shown in Figure 6.6 is available, since the Kalirai et al. (2012) catalog samples external regions of the cluster where no optical data of comparable depth have been acquired. Instead, for NGC 6624 we have combined the GEMINI catalog of Saracino et al. (2016) with the optical HST/ACS catalog of Sarajedini et al. (2007), providing V and I data for the stars in common. Hence this cluster provides us with the opportunity of studying the MS morphology and empirically evaluate the stability of the MS-saddle in three CMDs having same magnitude but different color baselines, namely the (K_s, $J - K_s$), (K_s, $I - K_s$) and (K_s, $V - K_s$) planes. Note that the hybrid optical-NIR CMDs are the most used in the literature to detect the MS-saddle (see Massari et al., 2016b, Monelli et al., 2015, Di Cecco et al., 2015 and Bono et al., 2010).

6.3.1 Measuring the MS-saddle

The first step to locate the MS-saddle is to determine the cluster MRL. The catalog adopted for 47 Tucanae was already cleaned for spurious objects (Kalirai et al., 2012). In the case of NGC 6624 CMDs, however, a selection in the stellar sharpness parameter (defined as in Stetson, 1987) was applied. We divided the sample of stars in our catalog in 0.5 magnitude-wide bins and for each bin we computed the median sharpness value and its standard deviation (σ). Only stars with sharpness parameter lying within 6σ from the median were flagged as "well-measured" and were used to determine the MRL independently in all the three CMDs defined above. This

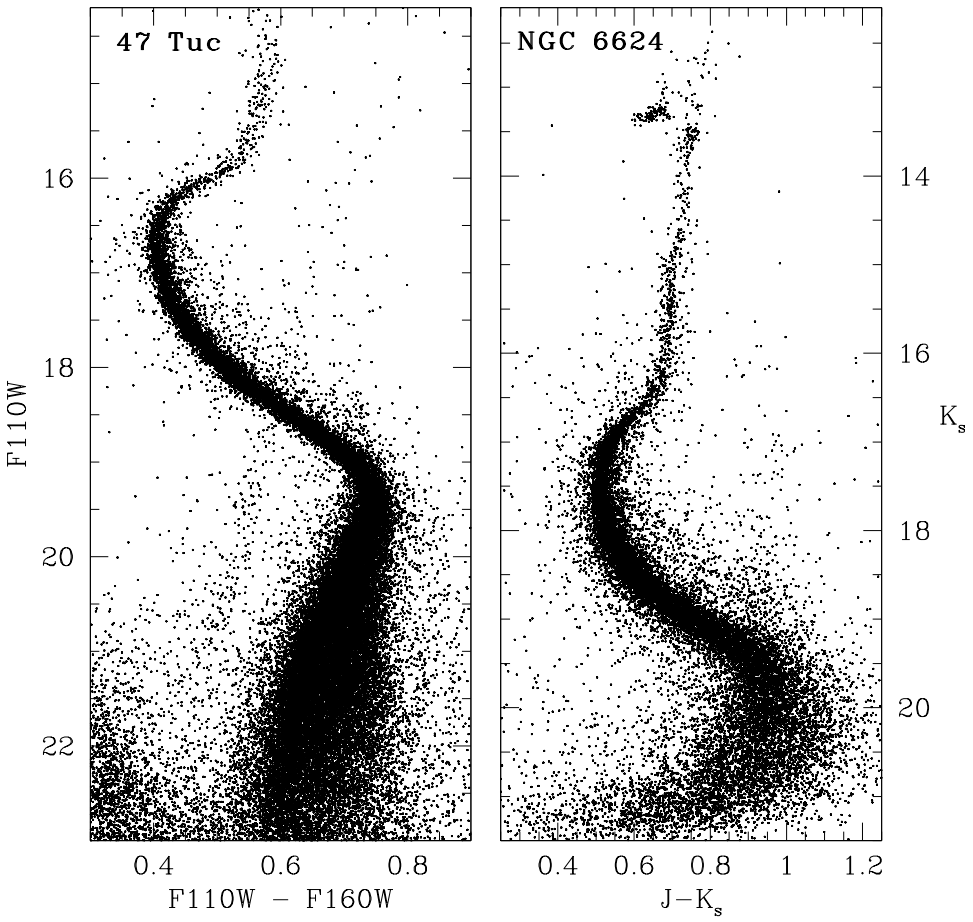

Figure 6.6: *Left panel* – ($F110W, F110W - F160W$) CMD of 47 Tucanae from HST observations. *Right panel* – ($K_s, J - K_s$) CMD of NGC 6624 from deep observations acquired with a ground-based adaptive optics system.

was done by adopting three different approaches in order to evaluate the impact of slightly different MRLs on the location of the MS-saddle and to derive the precision achievable in determining this feature.

Method 1: Static bins - we considered different magnitude bins (in $F110W$ for 47 Tucanae and K_s for NGC 6624) and we computed the mean color[5] of all the stars falling in each bin, by applying an iterative 2σ-rejection procedure. We allowed the bin size to vary from 0.10 mag (lower limit, necessary to have a reasonable number of stars per bin) to 0.50 mag (upper limit, imposed to keep an accurate sampling of the fiducial line), in steps of 0.01 mag. At the end of the procedure, for each of the four filter combinations, we had 41 (differently sampled) MRLs, which have been re-sampled with a 0.01 mag-stepped cubic spline.

[5]In order to be less sensitive to outliers (e.g. binaries, field stars), the median color was also derived. Negligible differences have been found with respect to the mean color due to the very well cleaned catalogs.

Method 2: Dynamic bins - This approach is similar to the previous one, with the substantial difference that each bin, of constant size in magnitude, is no longer separated from the others but it partially overlaps (e.g. even if the bin size is 0.20 mag, the starting point of each bin is only 0.05 mag fainter than the previous one). This means that, at any fixed bin size, the MRLs derived from dynamic bins are more densely sampled (at higher resolution) than those obtained from static bins. In this case we modified the bin size from 0.10 mag to 0.50 mag in steps of 0.05 mag, obtaining a sampling of 0.05 mag for each MRL. The resulting 9 MRLs per each filter combination have also been re-sampled with a cubic spline of 0.01 mag steps.

Method 3: Polynomial fit - This approach directly performs a polynomial fit to the observed sequences in the CMD. The degree of the polynomial has been chosen as a compromise between having an adequate ability to reproduce the shape of the MS in the CMD and the need of limiting the number of coefficients. We thus produced 11 different MRLs per CMD by varying the degree of the polynomial from 5 to 15, in step of 1.

The visual inspection of the MRLs derived with the three methods for each cluster in each color combination shows that they are all similar and they provide equivalently good representations of the cluster MS. However, in order to test the effect of adopting slightly different MRLs we determined the MS-TO and the MS-saddle in all the obtained MRLs, separately. In doing this we adopted the following prescriptions. The MS-TO has been defined as the bluest point of the MS. This is one of the classical and most used definitions and it allows an easy estimate of the error on its determination. The MS-saddle is defined as the point of minimum curvature along the MS. To measure it we used both an analytical and a geometric approach. *Analytical approach:* we defined the MS-saddle as the point where the second derivative of the MRL is equal to zero. *Geometric approach:* we adopted the "circumference method" described in Massari et al. (2016b). It consists in determining the circumference that connects each point of the MRL with the two adjacent/contiguous points located at $\pm$ 0.5 mag, and then adopt as MS-saddle the point corresponding to the circumference with the largest radius (minimum curvature). Following the suggestion in Massari et al., 2016b, we tested the robustness of such a procedure by changing the distance in magnitude among the three points on the MRL from 0.1 mag to 0.8 mag, in steps of 0.1 mag. This provided us with 8 different estimates of the MS-saddle point for each MRL. In all cases the 8 measures nicely agree (typically within $\pm$0.03 mag). Hence, their average value has been adopted as final "geometrical" measure of the MS-saddle.

The application of different methods for determining the cluster MRL and the use of CMDs with different color baselines affect the estimate of the MS-saddle magnitude as illustrated in Figure 6.7 for NGC 6624. The results are shown for the "geometrical" measure of the MS-saddle; those obtained from the analytical approach are fully consistent. According to the description above, we have derived 41, 9 and 11 MLRs from methods 1, 2 and 3, respectively, for each color baseline. Hence, the three panels

in the upper row of Figure 6.7 show the distribution of the 41, 9 and 11 values of the MS-saddle K_s-band magnitude determined in the $(K_s, J - K_s)$ CMD from the three methods. The middle and bottom rows show the analogous results obtained from the $(K_s, I - K_s)$ and $(K_s, V - K_s)$ diagrams. As apparent, for fixed CMD (along each row in the figure) the estimated magnitude of the MS-saddle is essentially independent of the method adopted to determine the MRL (all the measures agree within ± 0.04 mag). However, for any fixed method to determine the MRL, the magnitude of the MS-saddle varies by 0.2-0.25 mag when different CMDs are considered (i.e., along each column in Figure 6.7). In particular, the MS-saddle K_s-band magnitude shows a systematic trend with the color baseline, becoming increasingly fainter for color combinations that involve filters at shorter wavelengths. This is also illustrated in Figure 6.8, where the MS-saddle point (determined as the average of the 41 measures resulting from the "static bins" and the "geometric" approaches) is marked with a blue square in each of the three available CMDs. This trend might be an indirect morphological effect induced by the presence and the relevance of the MS-knee on the shape of the MS MRL. In fact the presence of a clear knee in the $(K_s, J - K_s)$ CMD (see the left panel of Figure 6.2) might impose an "early change" in the curvature of the MRL (i.e. the inflection point must occur at relative bright luminosity). Instead, as soon as the knee disappears becoming a "light bend" in the MRL (middle and right panels of Figure 6.2), the change in the MRL curvature becomes "less pronounced" (i.e. the inflection point tends to slide to fainter and fainter luminosities). At odds with the systematic drift of the MS-saddle magnitude with the color baselines, the measures of the MS-TO stay nicely stable (within 0.02 mag) independently of the considered CMD. This is also apparent in Figure 6.8 (black triangles). If the CMD location of the MS-saddle significantly depends on the details of the MS MRL morphology, this might suggest an intrinsic fragility in measuring the point.

Since the magnitude of the MS-saddle does not depend on the method used to determine the MRL, in the following we will consider only the values obtained from Method 1 (*static bins*), which also provides the largest statistics (41 data points). The magnitudes of the MS-TO and MS-saddle (and their uncertainties) obtained as the average (and the standard deviation) of the 41 measurements in each of the available color combinations are listed in Table 6.1. For 47 Tucanae the listed magnitudes are in the $F110W$ band, while for NGC 6624 they are in the K_s band. The last two columns of the table list the values obtained from the two methods (analytic and geometric) used to identify the MS-saddle point along the MRL. As can be seen, the results are fully consistent and in the following we will thus adopt the values obtained from the *geometric approach*, which has been already used in the literature.

We finally estimated the parameter $\Delta_{\rm TO}^{\rm saddle}$ from the difference between the adopted MS-saddle and MS-TO magnitudes and by taking into account: *(1)* the error associated to the MS-TO determination; *(2)* the uncertainty related to the MS-saddle point and *(3)* the photometric error affecting both parameters. In fact, photometric errors are an additional source of uncertainty in the derivation of the MS-saddle and the

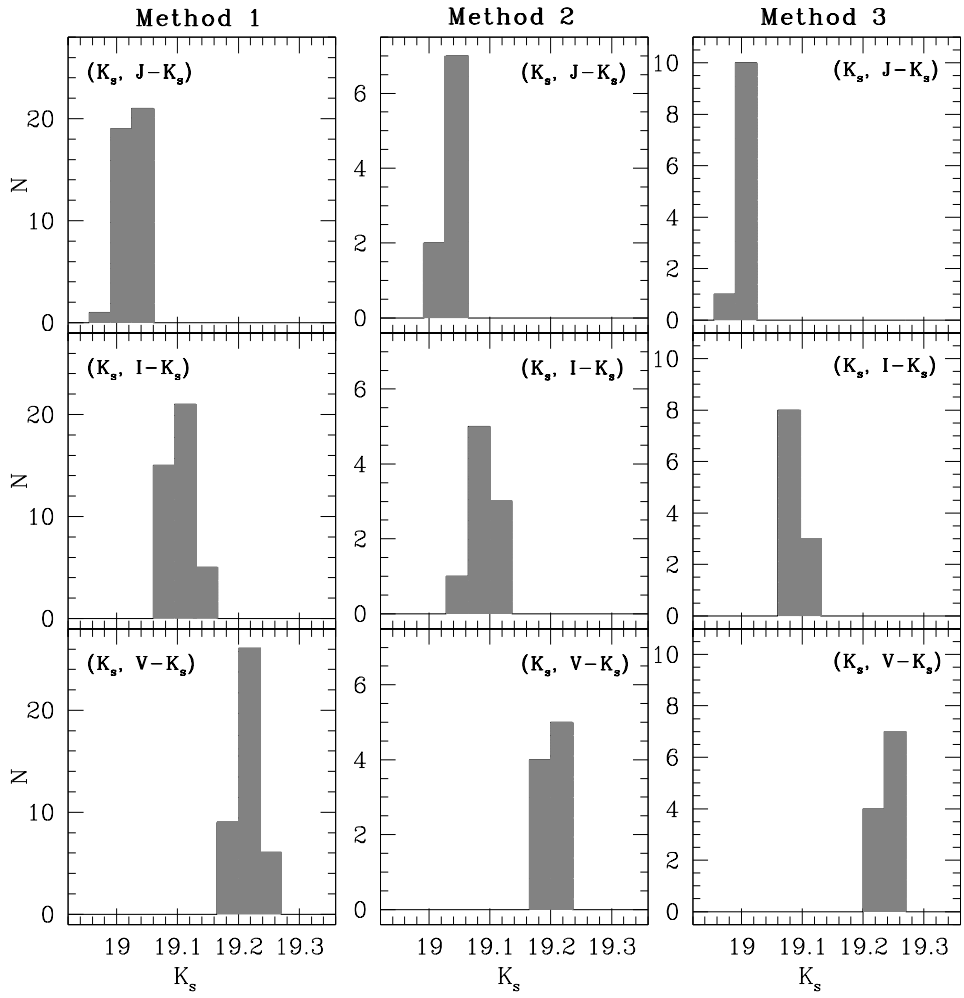

Figure 6.7: Histograms of the MS-saddle K-band magnitude measured in the $(K_s, J-K_s)$, $(K_s, I-K_s)$, and $(K_s, V-K_s)$ CMDs (upper, central and bottom rows, respectively), for NGC 6624. Multiple measures of this value have been obtained in each case because the MS MRL has been determined with different methods (see Section 6.3.1): Method 1 or static bins (left column, providing 41 MRLs and 41 measures of the MS-saddle magnitude), Method 2 or dynamic bins (central column, 9 measures) and Method 3 or Polynomial fit (right column, 11 measures).

MS-TO positions, so they have to be taken into account. They have been computed as the average of the photometric errors (in $F110W$ and in K for 47 Tucanae and NGC 6624, respectively) of all the stars falling within $\pm$ 0.1 magnitudes from the MS-TO and the MS-saddle points. In the case of 47 Tucanae, we obtained $\sigma_{F110W,\mathrm{MSTO}} = 0.002$ mag and $\sigma_{F110W,\mathrm{saddle}} = 0.005$ mag. For NGC 6624 we found $\sigma_{K,\mathrm{MSTO}} = 0.005$ mag and $\sigma_{K,\mathrm{saddle}} = 0.035$ mag for all the color combinations. Photometric errors don't actually have any impact on the final uncertainties of $\Delta_{\mathrm{TO}}^{\mathrm{saddle}}$, because they are relatively small with respect to other uncertainties. However, it is worth mentioning that when we measure the MRL, their contribution is intrinsically taken into account. The broadening of the MS in fact is only a function of photometric errors. The final values

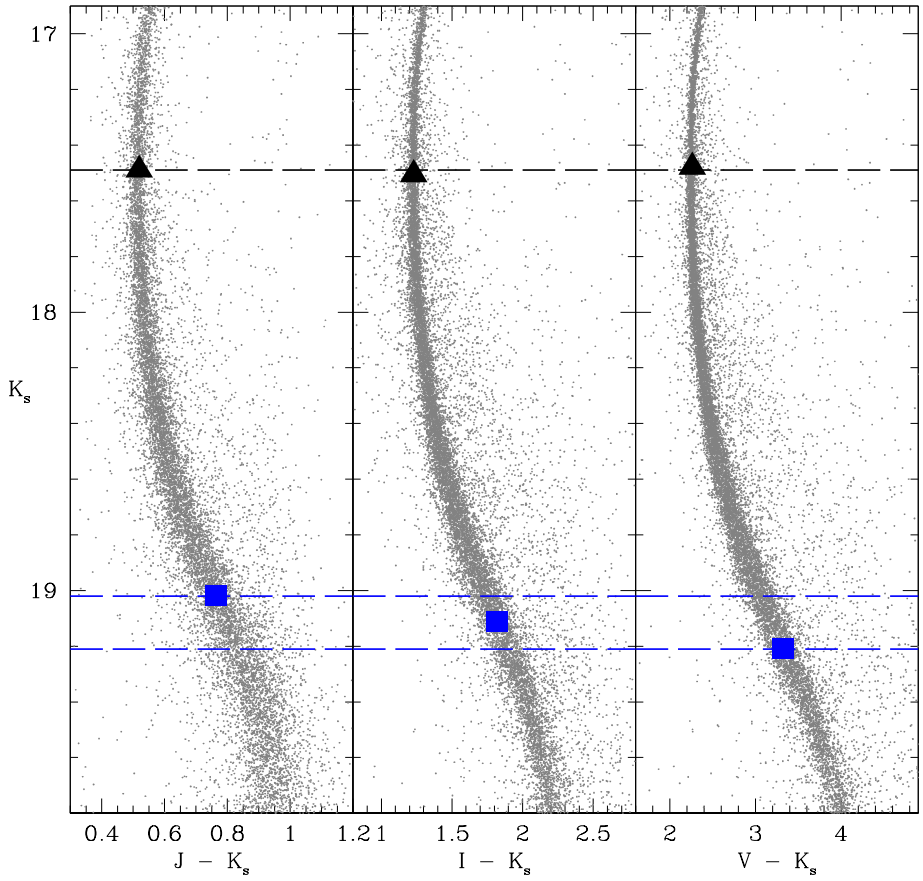

Figure 6.8: Location of the MS-TO (black triangle) and MS-saddle (blue square) in the three CMDs available for NGC 6624. The horizontal black dashed line marks the MS-TO level, the horizontal dashed blue lines flag the two extreme values of the MS-saddle, which vary by 0.2 mag.

and uncertainties of $\Delta_{\rm TO}^{\rm saddle}$ are listed in the last column of Table 6.1. As can be seen, this parameter changes by 0.2 mag because of the sensitivity of the MS-saddle point to the color baseline.

Table 6.1: MS-TO and MS-saddle magnitudes, and their difference $\Delta_{\rm TO}^{\rm saddle}$ in the $F110W$ (for 47 Tucanae) and in the K_s band (for NGC 6624). The listed values are the average of the 41 measures determined by adopting the *static bin* and the *geometric* approaches (see Sect. 3.1).

cluster	CMD	MS-TO	MS-saddle (analytic)	MS-saddle (geometric)	$\Delta_{\rm TO}^{\rm saddle}$
47 Tucanae	$(F110W, F110W - F160W)$	16.64 ± 0.03	18.53 ± 0.03	18.51 ± 0.04	1.87 ± 0.05
NGC 6624	$(K_s, J - K_s)$	17.49 ± 0.03	19.08 ± 0.05	19.02 ± 0.05	1.53 ± 0.07
...	$(K_s, I - K_s)$	17.51 ± 0.03	19.15 ± 0.05	19.11 ± 0.04	1.61 ± 0.05
...	$(K_s, V - K_s)$	17.48 ± 0.02	19.22 ± 0.03	19.21 ± 0.03	1.73 ± 0.06

6.4 Absolute GC ages derived from the MS-saddle

The fact that the position in magnitude of the MS-saddle in the CMD is color dependent weakens a bit its use as reference anchor for absolute age estimates. Nevertheless, for sake of completeness here we estimate the absolute age of the two program clusters from the observed difference in magnitude between the MS-saddle and the MS-TO (Δ_{TO}^{saddle}) and its comparison with the predictions of the stellar evolution models presented in Section 6.2.

In order to provide a set of analytical relations linking the cluster age and the (Δ_{TO}^{saddle}) parameter, we considered models covering a meaningful range of ages and metallicities. In particular, the cluster age was sampled in steps of 0.5 Gyr, from 9.5 Gyr to 13.5 Gyr (this is a reasonable age range for both clusters, according to previous literature estimates; see Correnti et al., 2016 for 47 Tucanae, and Saracino et al., 2016 and references therein for NGC 6624). As for the age, the two considered clusters roughly share the same metallicity ([Fe/H] = -0.77 and -0.60 for 47 Tucanae and NGC 6624, respectively; see Correnti et al., 2016 and reference therein and Saracino et al., 2016 and reference therein). However slightly different values (covering approximately 0.2 dex) can be found in the literature for both clusters (see, e.g., Carretta et al., 2009, 2010; Valenti et al., 2004a,b). For this reason, we decided to allow the models to sample a range of $\pm$0.1 dex centered on the metallicity quoted above for each cluster, in steps of 0.05 dex. Thus a grid of isochrones with the adopted ages and metallicities has been produced. To estimate the theoretical values of Δ_{TO}^{saddle} in all filter combinations, we re-sampled the BaSTI, DSED and VR models adopting the same magnitude steps used for the determination of the MRLs with the "static bins" method. Then, the magnitudes of the MS-TO and the MS-saddle points have been derived by adopting the same geometric approach used for the observed CMDs.

At the end of the procedure we thus have a grid of points corresponding to one value of Δ_{TO}^{saddle} for each of the considered isochrones of different ages and metallicities. To determine the absolute cluster age (in Gyr) as a function of Δ_{TO}^{saddle} and metallicity we use a linear bi-parametric fit. The resulting analytic relations are listed in Table 6.2 for the three adopted families of stellar models and for each of the color combinations available in our observational datasets. The results confirm that metallicity has a non-negligible impact on the age determination. In particular, the DSED isochrones appear to be the most sensitive to the metallicity: an uncertainty of $\pm$0.1 dex in metallicity produces an uncertainty of $\pm$ 0.8-0.9 Gyr in age. Instead, the BASTI isochrones appear to be the most sensitive to the parameter Δ_{TO}^{saddle}: an uncertainty of $\pm$0.1 dex in Δ_{TO}^{saddle} produces uncertainties up to 2 Gyr in age. The results of this analysis are also shown in Figure 6.9 for 47 Tucanae and Figure 6.9 for NGC 6624, with the three panels referring to the three adopted stellar models. The dashed line in each panel corresponds to the analytical relation obtained for the adopted cluster metallicities (from Correnti et al., 2016 and Saracino et al., 2016 for 47 Tucanae and NGC 6624, respectively). The dark gray region surrounding each dashed line

represents the variation due to the change of ± 0.1 dex in metallicity.

Table 6.2: Analytic relations between age (t, in Gyr), Δ_{TO}^{saddle} and metallicity derived from the three adopted families of stellar models and the color combinations available in our observational datasets of 47 Tucanae and NGC 6624.

BASTI models	
$(F110W, F110W-F160W)$	$t\,[\mathrm{Gyr}] = 40.66(\pm0.82) - 16.99(\pm0.46) \times \Delta_{TO}^{saddle} - 6.02(\pm0.41) \times [Fe/H]$
$(K_s, J-K_s)$	$t\,[\mathrm{Gyr}] = 38.34(\pm0.63) - 20.56(\pm0.47) \times \Delta_{TO}^{saddle} - 7.05(\pm0.36) \times [Fe/H]$
$(K_s, I-K_s)$	$t\,[\mathrm{Gyr}] = 39.74(\pm0.68) - 20.63(\pm0.48) \times \Delta_{TO}^{saddle} - 5.81(\pm0.36) \times [Fe/H]$
$(K_s, V-K_s)$	$t\,[\mathrm{Gyr}] = 41.70(\pm0.34) - 20.54(\pm0.23) \times \Delta_{TO}^{saddle} - 4.92(\pm0.17) \times [Fe/H]$
DSED models	
$(F110W, F110W-F160W)$	$t\,[\mathrm{Gyr}] = 33.51(\pm0.68) - 14.94(\pm0.45) \times \Delta_{TO}^{saddle} - 7.11(\pm0.44) \times [Fe/H]$
$(K_s, J-K_s)$	$t\,[\mathrm{Gyr}] = 32.13(\pm0.87) - 16.62(\pm0.65) \times \Delta_{TO}^{saddle} - 9.03(\pm0.65) \times [Fe/H]$
$(K_s, I-K_s)$	$t\,[\mathrm{Gyr}] = 33.60(\pm0.59) - 16.95(\pm0.42) \times \Delta_{TO}^{saddle} - 8.01(\pm0.40) \times [Fe/H]$
$(K_s, V-K_s)$	$t\,[\mathrm{Gyr}] = 37.16(\pm0.45) - 18.13(\pm0.30) \times \Delta_{TO}^{saddle} - 7.83(\pm0.27) \times [Fe/H]$
VR models	
$(F110W, F110W-F160W)$	$t\,[\mathrm{Gyr}] = 38.11(\pm0.85) - 14.94(\pm0.45) \times \Delta_{TO}^{saddle} - 4.20(\pm0.44) \times [Fe/H]$
$(K_s, J-K_s)$	$t\,[\mathrm{Gyr}] = 37.02(\pm0.72) - 17.53(\pm0.47) \times \Delta_{TO}^{saddle} - 4.02(\pm0.39) \times [Fe/H]$
$(K_s, I-K_s)$	$t\,[\mathrm{Gyr}] = 38.70(\pm0.45) - 18.29(\pm0.29) \times \Delta_{TO}^{saddle} - 3.48(\pm0.23) \times [Fe/H]$
$(K_s, V-K_s)$	$t\,[\mathrm{Gyr}] = 40.17(\pm0.48) - 18.58(\pm0.30) \times \Delta_{TO}^{saddle} - 3.99(\pm0.24) \times [Fe/H]$

In Figures 6.9 and 6.10 we also plot the observed values of Δ_{TO}^{saddle} (horizontal solid lines) and their uncertainty (light gray region) as obtained in Section 6.3.1. From the intersection of the lines and regions in these diagrams we can finally derive the absolute age of the program clusters and their uncertainties. The results are listed in Table 6.3.

For 47 Tucanae we obtain an absolute age of $\sim$ 13 Gyr with uncertainties of 1.2-1.5 Gyr, depending on the stellar model. This value is larger (even if marginally consistent) than the age of 11.6 Gyr recently obtained by Correnti et al. (2016) by using the same CMD. For NGC 6624 we obtain age values that are formally consistent with the recent determination ($t = 12$ Gyr) of Saracino et al. (2016). For both clusters the error associated to the age values ranges between 1 and 2 Gyr, i.e., it is significantly larger than the typical uncertainty estimated by Massari et al. (2016b) and Di Cecco et al. (2015) from similar analysis based on the MS-saddle method. Moreover in the case of NGC 6624, where the comparison of results from different color combinations is possible, the age values obtained clearly demonstrate the limit of this approach. In fact, differences in age as large as 1.5-2 Gyr are found by just changing the CMD where the analysis is performed, independently of the stellar model adopted. Moreover, with all the adopted isochrone sets, a systematic effect is found: the derived absolute age always decreases when optical filters (at shorter wavelengths) are used in the CMD color baseline.

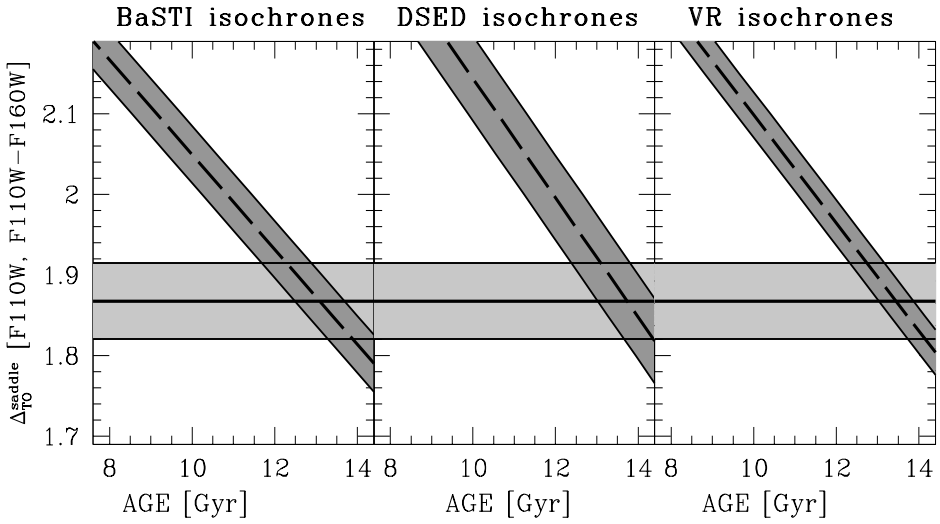

Figure 6.9: Predicted relation between age (in Gyr) and the parameter Δ_{TO}^{saddle} obtained from BaSTI, DSED and VR isochrones of varying metallicity (see also Table 6.2): the dashed lines are the theoretical relations computed at the metallicity of 47 Tucanae ([Fe/H] = −0.77, from Correnti et al. (2016) and references therein); the dark gray regions surrounding each dashed line mark the variation induced by changes of ±0.1 dex in the adopted metallicity. The solid line and gray region in each panel mark the observed value and uncertainty of the Δ_{TO}^{saddle} parameter measured in the $(F110W, F110W - F160W)$ CMD of 47 Tucanae.

Table 6.3: Absolute ages of 47 Tucanae and NGC 6624 estimated from the measured values of Δ_{TO}^{saddle} and for the three adopted families of stellar models (BsSTI, DSED, VR; see text).

cluster	CMD	t_{BaSTI} (Gyr)	t_{DSED} (Gyr)	t_{VR} (Gyr)
47 Tucanae	$(F110W, F110W - F160W)$	13.1 ± 1.4	13.5 ± 1.5	13.7 ± 1.2
NGC 6624	$(K_s, J - K_s)$	11.1 ± 2.1	12.7 ± 2.0	13.0 ± 1.7
...	$(K_s, I - K_s)$	10.1 ± 1.6	11.8 ± 1.7	11.7 ± 1.3
...	$(K_s, V - K_s)$	9.9 ± 1.8	11.0 ± 1.9	10.7 ± 1.6

6.5 Summary and Conclusions

In this chapter we presented a detailed analysis of the MS-knee and the MS-saddle parameters for absolute GC age determinations. To this end we used three different families of stellar models and deep observations of two metal-rich Galactic GCs (47 Tucanae and NGC 6624). In particular, both NIR and optical data were available for NGC 6624, and they offered us the possibility to explore the behavior of the two parameters in CMDs characterized by different color baselines. The main conclusions of this work are summarized in the following points:

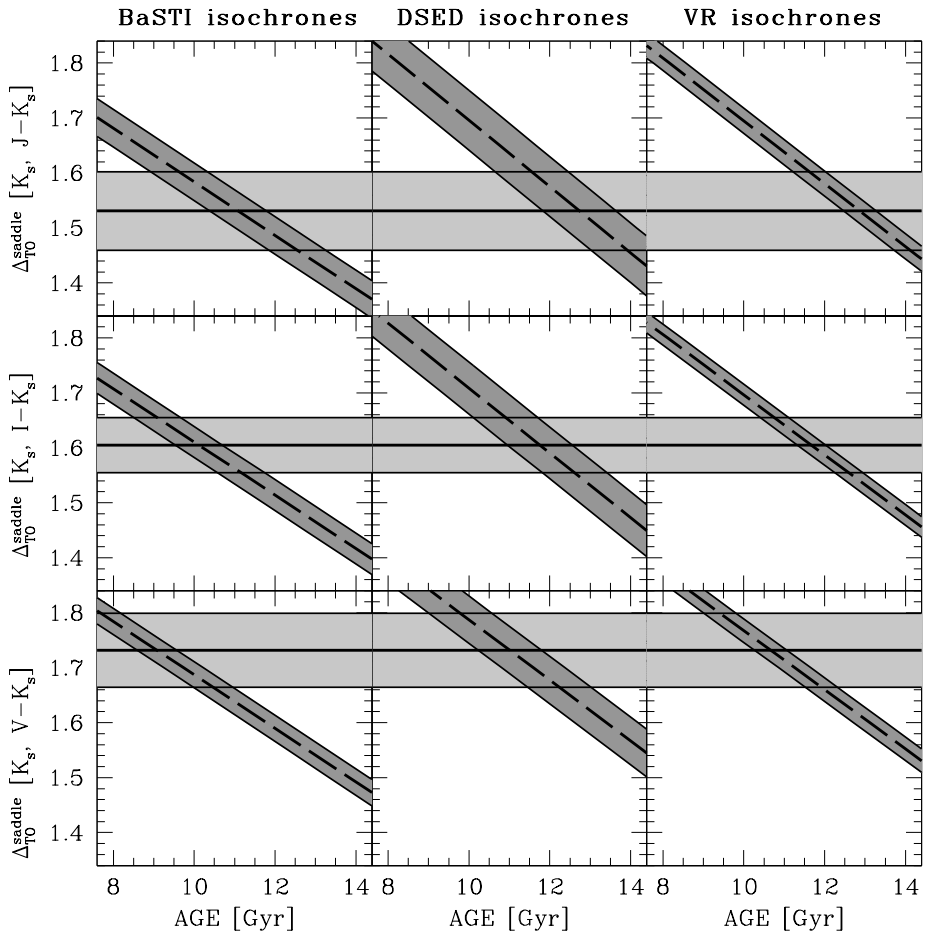

Figure 6.10: The same as in Figure 6.8 but for NGC 6624. In this case the theoretical relations and the observed values have been determined in the three available CMDs (see labels): $(K_s, J-K_s)$, $(K_s, I-K_s)$, and $(K_s, V-K_s)$.

1. *A more-suitable definition of the MS-knee* - Because in NIR CMDs the low-mass end of the MS bends to the blue and forms a "knee" (see Figure 6.6), this feature needs to be defined consistently as the reddest point along the MS. Unfortunately, however, this definition strictly holds only for pure NIR CMDs (see Figure 6.2). Moreover, the predicted magnitude and color of the MS-knee are still significantly model-dependent (see Figures 6.3 and 6.4), thus making largely uncertain any age determination based on this feature. In fact the predicted value of $\Delta K_{\rm TO}^{\rm knee}$ ranges from 2.08 to 2.37 among the three families of stellar models considered here, and a variation of 0.3 mag in this parameter implies a several Gyrs uncertainty in the absolute age estimate ($\delta t \sim 5$ Gyr), just due to the different model predictions. Hence, beside the observational difficulties of properly detecting such a faint feature (~ 7 mag fainter than the HB) in the CMD, with a not straightforward definition in hybrid NIR-optical diagrams, also a theoretical effort is required so that the MS-knee can be used

to really improve absolute cluster age estimates. In fact, it is first necessary to remove the large discrepancies in the location of the MS-knee from different isochrones, by identifying the input physics and/or the color transformations that can be responsible for them.

2. *A MS-saddle, not a knee* - In spite of its real appearance (that well corresponds to the meaning of "knee"), the MS-knee was originally defined as the point of minimum curvature along the MS MRL (Bono et al., 2010). Figure 6.1 shows that the point where the MS bends to the blue (the so-called "knee") does not coincide with the *inflection point*, where the MS MRL has its minimum curvature because it changes its curvature from convex to concave. Hence, here we more appropriately named this latter point *"MS-saddle"*. The MS-saddle is 0.7 mag brighter than the MS-knee and typically samples a mass $\sim$0.1 $M_{\odot}$ higher with respect to the MS-knee. The analysis summarized in Figure 6.3 demonstrates that the MS-saddle is insensitive to the morphology and the location of the MS-knee, since different bends of the MS (hence different CMD locations of the MS-knee) correspond to very similar MS-saddle points, with consistent luminosities and colors. Hence the MS-saddle cannot be considered a proxy of the MS-knee.

3. *The MS-saddle: a not-so-robust feature* - At odds with the MS-knee which has a physical nature, the MS-saddle is just a morphological feature indicating a change in the curvature of the MS MRL. We performed a detailed analysis of its properties by making use of deep NIR and optical data of the GCs 47 Tucanae and NGC 6624. Interestingly, the measure of the MS-saddle seems to be insensitive to the method adopted to build the MS MRL and the approach used to operationally identify the feature along the MS (all the measures of the MS-saddle magnitude obtained from the different approaches turned out agree within $\pm$0.04 mag).

   The analysis of NGC 6624 offered the possibility to study the location of the MS-saddle in CMDs with different color baselines, namely the (K_s, $J-K_s$), (K_s, $I-K_s$) and (K_s, $V-K_s$) diagrams. We found that the K_s band magnitude of the MS-saddle changes by 0.2-0.25 mag when different color baselines are considered (see Figure 6.7). Moreover, a systematic trend has been detected, with the MS-saddle becoming brighter with color combinations involving filters at shorter and shorter wavelengths (see Figures 6.7 and 6.8, and Table 6.1). On the other hand, we note that in the same CMDs the luminosity of the MS-TO stays nicely constant (within 0.02 mag) independently of the adopted MRL or the considered CMDs (see Figure 6.8 and Table 6.1). Such different trend suggests that the MS-saddle might be a not-so-robust feature for absolute GC age estimates.

4. *The* $\Delta_{\rm TO}^{\rm saddle}$ *parameter: up to now, not an improvement* - The age values derived from $\Delta_{\rm TO}^{\rm saddle}$ are not inconsistent with those found in the literature, but this is

mainly because of their large error bars. In fact by changing the color of the adopted CMD, the absolute ages vary by 1.5-2.0 Gyr, because stellar models do not predict the observed trend. For this reason, to date the overall uncertainty associated to ages derived from the Δ_{TO}^{saddle} parameter cannot be smaller than these values. Such an error is significantly larger than what previously claimed using other techniques (Di Cecco et al., 2015; Massari et al., 2016b).

In conclusion, at the state-of-the-art of theoretical predictions for the low-mass MS, adopting the MS-saddle as reference level where to anchor the TO magnitude seems to offer no significant advantages with respect to using the HB or the classical isochrone fitting method: not only it is a very faint feature (thus requiring very deep observations), but also the involved uncertainties are not smaller that those obtained from other approaches.

The next generation of space and ground-based telescopes, like the James Webb Space Telescope (JWST) and the European Extremely Large Telescope (E-ELT), is expected to give a significant impulse to NIR observations. In particular, the low-mass MS could be studied in great detail in many more GCs. This will allow a more precise observational characterization of the MS-knee to better constrain the structure of extreme low-mass stars and the input physics of their modeling, in order to finally solve the current discrepancies among stellar models. The main improvement in terms of absolute GC ages is expected from the significant refinement of the distance determinations that the final release of the Gaia mission will make possible in the next future (Gaia Collaboration et al., 2016). This perspective definitively suggests that the absolute GC age dating methods will live very soon a renewed youth.

Conclusions and Future Perspectives

This Thesis is part of a project devoted at the exploration and characterization of the stellar content of the Galactic bulge by means of a sample of GCs. In fact, bulge GCs are important tools to trace the formation and evolution of this Milky Way component, as they are among the oldest stellar structures in the Universe formed at the same epoch of the Galaxy assembly. However, they have been widely excluded from large surveys and have remained only poorly investigated for decades because of critical observational limitations, like severe foreground extinction and crowding, which make them almost inaccessible at optical wavelengths and to seeing-limited instruments. For these reasons, the majority of bulge GCs studies have focused on the characterization of only the brightest evolutionary sequences in the CMDs (Minniti et al., 1995; Davidge, 2000; Ortolani et al., 2001, 2007; Valenti et al., 2007, 2010), with very few exceptions (see Kim et al., 2006; Ortolani et al., 2011; Cohen et al., 2017).

In this Thesis we took advantage of the exquisite capabilities offered by the MCAO system GeMS combined with the high resolution NIR camera GSAOI at the Gemini South Telescope, in Chile. Indeed, the advent of NIR MCAO systems, which are able to sample and correct in real time the wavefront deformation due to atmospheric turbulence, opened a new line of investigation for bulge GCs, that can be finally studied at the same level of detail as halo clusters.

This Thesis is mainly focused on the results obtained for two GCs, namely Liller 1 and NGC 6624. They are massive (M_V>-7) and metal-rich ([Fe/H]>-0.6), located close to the Galactic plane. These two systems represent two ideal test-cases. Liller 1 is the prototype of a very obscured and dense cluster for which it is necessary to push the GeMS+GSAOI system capabilities to its limits. In this case we have been able, for the first time, to resolve the MS-TO and directly derive the cluster structural parameters. NGC 6624 has been extensively studied in the past with HST, thus it provides a very useful opportunity to test the GeMS performance. For the first time in bulge GC studies, we reached the low-mass MS of the system.

A detailed summary of the main results of this Thesis is reported in the following:

1. Liller 1 is the first cluster analyzed in our sample (see Chapter 4). In spite of the strong obscuration, larger than 10 magnitudes in the visual band (E(B-V)=3.09, Valenti et al., 2010), we were able to resolve individual stars even in the innermost regions of the cluster, down to its MS-TO at $K_s \approx 18.5$ mag. From direct star counts, we derived first the center of gravity, then the star density

profile of Liller 1 from the center to the outskirts by combining GeMS data with wide-field images from the VVV survey (Minniti et al., 2010; Catelan et al., 2011). Based on this analysis, Liller 1 turned out to be significantly less concentrated (concentration parameter c=1.74) and less extended (tidal radius $r_t = 298''$ and core radius $r_c = 5.39''$) than previously thought (c=2.3, $r_t = 720''$ and $r_c = 3.6''$). This cluster has a mass of about 1.5×10^6 $M_\odot$, which classifies it as the second most massive GC in the Galaxy after Terzan 5. Finally, we confirmed that Liller 1 has also the second-highest collision rate among the Milky Way clusters. Again, the record is held by Terzan 5 (Lanzoni et al., 2010). It is interesting to note, however, that at odds with Terzan 5, no MSPs have been detected so far in this system.

The detailed view of the stellar content of Liller 1 triggered new questions that we plan to answer in the near future. The most interesting one is related to its stellar population and, as a consequence, to its age. In fact, Liller 1 seems to be predominantly old with an absolute age of 12 ± 1 Gyr, but the NIR CMD of Liller 1 shows the presence of an evolutionary sequence at $(J - K_s) \sim 0.75$, exactly located between the cluster RGB and the disk MS (see Figure 4.4). Its extension at bright magnitudes would exclude the possibility that it is populated only by blends or field stars. Moreover, the radial extension of the sequence seems to be compatible with the radial extension of the cluster itself. In order to investigate the nature of this sequence, Liller 1 will be observed soon with the ACS and WFC3 on board HST (Program ID: GO15231; PI: F.R. Ferraro). Additionally, spectra for a dozen stars in the region will be acquired by using OSIRIS at Keck (Program ID: U0730L; PI: M. Rich).

2. NGC 6624 can be considered the best target to assess the real performance achievable with the GeMS+GSAOI system (see Chapter 5). A high-quality NIR CMD has been obtained for the cluster. Its depth and photometric quality are fully comparable to those reached with ground-based observations in the same wavelength range for no-obscured GCs in the Milky Way halo. The MS-knee has been sampled at $K_s \sim 20$ mag and the limiting magnitude of $K_s = 21.5$ mag has been reached with a typical photometric error smaller than 4 cents of a magnitude. The absolute age of NGC 6624 has been found to be 12.0 ± 0.5 Gyr, in good agreement with previous studies in the literature. In particular we adopted the MS fitting technique with a chi-squared minimization and a comparison among different stellar evolutionary models. The completeness-corrected and background-subtracted luminosity and mass functions of NGC 6624 have been derived down to stars of about 0.45 $M_\odot$, in three different radial bins. The strong radial variation we found in both functions is the first clear evidence of mass segregation in the cluster.

3. The problem of GC absolute age estimates has been extensively discussed in this Thesis, triggered by the introduction of a new possible age indicator in

the low-mass end of the MS in NIR CMDs: the MS-knee (see Chapter 6). We made use of the highest-quality ground-based and HST CMDs available at the moment for NGC 6624 and 47 Tucanae to test the MS-knee method suggested by Bono et al. (2010), based on the magnitude difference between the MS-TO and the MS-knee. We demonstrated that to date it is very difficult to determine GC absolute ages with errors smaller than 1.5-2 Gyr, at odds with what proposed in the literature. We show that the main limitation is related to theoretical model uncertainties. This represents a key result for the upcoming JWST and E-ELT projects and a new challenge for stellar evolution models.

4. To support all the scientific results presented in this Thesis, an in-depth characterization of the astrometric and photometric performance of the GeMS+GSAOI system has been carried out (see Chapter 3). In particular, we used data of Liller 1 and NGC 6624, taken in different observational conditions (in terms of seeing, airmass and brightness of guide stars) and we estimated median values of the FWHM, SR and EE both in K_s and in J. We found that only K_s-band images reach the telescope's diffraction limit and we obtained SR $\sim$ 40% and EE $\geq$ 50% in the K_s-band and SR > 10% and EE > 40% in the J one. A PSF variation has been found in the FOV in both filters, with an improvement of the AO correction closer to the NGS asterism. An analytic solution to sample and correct the GD of the GSAOI imager has been also obtained, by comparing GeMS data of NGC 6624 with a flat reference catalog from HST (Sarajedini et al., 2007). Our approach unveiled spatial displacements larger than 30 pixels (>0.5") in both axes at the edges of the camera. At the end of this iterative process we were able to finally reach an astrometric accuracy better than 1 mas.

The results presented in this Thesis clearly demonstrate the power of the GeMS + GSAOI system to investigate the stellar population properties of bulge GCs. In this sense, the future perspectives of this work are mainfold.

Our plan for the next future is to provide the scientific community with the first homogeneous census of bulge GCs based on high resolution diffraction-limited MCAO observations in the NIR, with significant improvements with respect to previous works in terms of both completeness and accuracy. To this aim, a sample of $\sim$ 15 bulge GCs already observed with GEMINI has been collected over the last years (PI: R.E. Cohen). This sample has been selected to span nearly 1 dex in metallicity, from metal-poor to metal-rich clusters, with the idea to finally derive the age-metallicity relation for bulge GCs.

The next goal is also to determine star density profiles and structural parameters for all the clusters in our sample, by means of direct star counts, rather than of surface brightness, which is often biased towards bright sources. We will take advantage of the ESO public VVV survey (as already done in the case of Liller 1; see Figure 4.11) and/or wide-field ground-based instruments like HAWK-I at the VLT to sample the outskirts of the clusters. The combination of GeMS data and wide-field observations

will allow to cover the clusters' entire radial extension, thus to derive the full star density profile, to constrain the structural parameters and to search for extra-tidal tails due to possible interactions with the bulge field.

The final goal of our project is the determination of the internal and global kinematics of the surveyed bulge GCs. To date radial velocities and proper motions are available only for small samples of stars in just a fraction of these systems. However this information is crucial to derive their orbits (thus constraining the mass distribution and potential well of the bulge), and to determine their internal kinematics (which is a mandatory ingredient for any meaningful modeling of these systems). GeMS data represent first-epoch imagery for proper motion studies, but second-epoch data, covering a time baseline of more than 5 years, will be acquired with new dedicated observations, either with GeMS and/or with JWST. Radial velocities will be instead derived for hundreds of individual stars taking advantage of a multi-instrument approach: ESO/SINFONI to sample the cluster centers and ESO/MUSE for the external regions. The 3D velocity dispersion profile and rotation curve will be determined, thus unveiling the internal kinematic structure (including possible rotation and pressure anisotropy) and the present-day total (dynamical) mass of each cluster.

Bibliography

Abadi, M. G. et al. (2003). "Simulations of Galaxy Formation in a Λ Cold Dark Matter Universe. I. Dynamical and Photometric Properties of a Simulated Disk Galaxy". In: ApJ 591, pp. 499–514. DOI: 10.1086/375512. eprint: astro-ph/0211331.

Alves-Brito, A. et al. (2006). "VLT-UVES abundance analysis of four giants in NGC 6553". In: A&A 460, pp. 269–276. DOI: 10.1051/0004-6361:20065488. eprint: astro-ph/0609128.

Alves-Brito, A., J. Meléndez, and M. Asplund (2010). "Chemical similarities between the Galactic bulge and local thick disk red giant stars: analysis from optical data". In: *Chemical Abundances in the Universe: Connecting First Stars to Planets*. Ed. by K. Cunha, M. Spite, and B. Barbuy. Vol. 265. IAU Symposium, pp. 342–343. DOI: 10.1017/S1743921310000839.

Ammons, S. M. et al. (2016). "Precision astrometry with adaptive optics: constraints on the mutual orbit of Luhman 16AB from GeMS". In: *Adaptive Optics Systems V*. Vol. 9909. Proc. SPIE, 99095T. DOI: 10.1117/12.2233775.

Anderson, J. and I. R. King (2003). "An Improved Distortion Solution for the Hubble Space Telescope's WFPC2". In: *PASP* 115, pp. 113–131. DOI: 10.1086/345491.

Anderson, J. et al. (2006). "Ground-based CCD astrometry with wide field imagers. I. Observations just a few years apart allow decontamination of field objects from members in two globular clusters". In: *A&A* 454, pp. 1029–1045. DOI: 10.1051/0004-6361:20065004. eprint: astro-ph/0604541.

Armandroff, T. E. (1989). "Erratum - the Properties of the Disk System of Globular Clusters". In: AJ 97, p. 1532. DOI: 10.1086/115092.

Arp, H. (1965). "Properties of the Galactic Nucleus in the Direction of NGC 6522." In: ApJ 141, p. 43. DOI: 10.1086/148089.

Athanassoula, E. (2005). "On the nature of bulges in general and of box/peanut bulges in particular: input from N-body simulations". In: MNRAS 358, pp. 1477–1488. DOI: 10.1111/j.1365-2966.2005.08872.x. eprint: astro-ph/0502316.

Athanassoula, E. (2012). "Manifold-driven spirals in N-body barred galaxy simulations".

In: MNRAS 426, pp. L46–L50. DOI: 10.1111/j.1745-3933.2012.01320.x. arXiv: 1207.4590.

Baade, W. (1951). "Galaxies - Present Day Problems". In: *Publications of Michigan Observatory* 10, p. 7.

Babcock, H. W. (1953). "The Possibility of Compensating Astronomical Seeing". In: PASP 65, p. 229. DOI: 10.1086/126606.

Babusiaux, C. et al. (2010). "Insights on the Milky Way bulge formation from the correlations between kinematics and metallicity". In: A&A 519, A77, A77. DOI: 10.1051/0004-6361/201014353. arXiv: 1005.3919.

Bailyn, C. D. (1992). "Are there two kinds of blue stragglers in globular clusters?" In: ApJ 392, pp. 519–521. DOI: 10.1086/171452.

Barbuy, B., E. Bica, and S. Ortolani (1998). "Globular clusters within 5(deg) of the Galactic center". In: A&A 333, pp. 117–124.

Barbuy, B. et al. (2015). "Zinc abundances in Galactic bulge field red giants: Implications for damped Lyman-α systems". In: A&A 580, A40, A40. DOI: 10.1051/0004-6361/201525694. arXiv: 1506.01612.

Beccari, G. et al. (2006). "The Dynamical State and Blue Straggler Population of the Globular Cluster NGC 6266 (M62)". In: AJ 131, pp. 2551–2560. DOI: 10.1086/500643. eprint: astro-ph/0601187.

Beccari, G. et al. (2011). "The Non-segregated Population of Blue Straggler Stars in the Remote Globular Cluster Palomar 14". In: ApJ 737, L3, p. L3. DOI: 10.1088/2041-8205/737/1/L3. arXiv: 1107.0576 [astro-ph.SR].

Beckers, J. M. (1988). "Increasing the Size of the Isoplanatic Patch with Multiconjugate Adaptive Optics". In: *European Southern Observatory Conference and Workshop Proceedings*. Ed. by M.-H. Ulrich. Vol. 30. European Southern Observatory Conference and Workshop Proceedings, p. 693.

Behrendt, M., A. Burkert, and M. Schartmann (2016). "Clusters of Small Clumps Can Explain the Peculiar Properties of Giant Clumps in High-redshift Galaxies". In: ApJ 819, L2, p. L2. DOI: 10.3847/2041-8205/819/1/L2. arXiv: 1512.03430.

Bekki, K. and K. C. Freeman (2003). "Formation of ω Centauri from an ancient nucleated dwarf galaxy in the young Galactic disc". In: MNRAS 346, pp. L11–L15. DOI: 10.1046/j.1365-2966.2003.07275.x. eprint: astro-ph/0310348.

Bekki, K. and J. E. Norris (2006). "The Origin of the Double Main Sequence in ω Centauri: Helium Enrichment due to Gas Fueling from Its Ancient Host Galaxy?" In: ApJ 637, pp. L109–L112. DOI: 10.1086/500413. eprint: astro-ph/0512385.

Bellazzini, M. et al. (1995). "Low-mass X-ray binaries in globular clusters: A new metallicity effect". In: ApJ 439, pp. 687–694. DOI: 10.1086/175208. eprint: astro-ph/9407086.

Bellazzini, M., F. R. Ferraro, and R. Buonanno (1999). "The Sagittarius Dwarf Galaxy Survey (SDGS) - II. The stellar content and

constraints on the star formation history". In: MNRAS 307, pp. 619–636. DOI: 10.1046/j.1365-8711.1999.02673.x. eprint: astro-ph/9903371.

Bellazzini, M. et al. (2002). "Deep Hubble Space Telescope WFPC2 Photometry of NGC 288. II. The Main-Sequence Luminosity Function". In: AJ 123, pp. 2541–2551. DOI: 10.1086/340082. eprint: astro-ph/0202176.

Bellazzini, M. et al. (2012). "The luminosity function and stellar mass-to-light ratio of the massive globular cluster NGC 2419". In: MNRAS 423, pp. 844–855. DOI: 10.1111/j.1365-2966.2012.20922.x. arXiv: 1203.3024.

Bellini, A. and L. R. Bedin (2009). "Astrometry and Photometry with HST WFC3. I. Geometric Distortion Corrections of F225W, F275W, F336W Bands of the UVIS Channel". In: *PASP* 121, p. 1419. DOI: 10.1086/649061. arXiv: 0910.3250 [astro-ph.IM].

— (2010). "Ground-based CCD astrometry with wide field imagers. IV. An improved geometric-distortion correction for the blue prime-focus camera at the LBT". In: *A&A* 517, A34, A34. DOI: 10.1051/0004-6361/200913783. arXiv: 1005.0848 [astro-ph.IM].

Bellini, A. et al. (2009). "Ground-based CCD astrometry with wide field imagers. III. WFI@2.2m proper-motion catalog of the globular cluster ω Centauri". In: *A&A* 493, pp. 959–978. DOI: 10.1051/0004-6361:200810880. arXiv: 0810.1914.

Bellini, A., J. Anderson, and L. R. Bedin (2011). "Astrometry and Photometry with HST WFC3. II. Improved Geometric-Distortion Corrections for 10 Filters of the UVIS Channel". In: *PASP* 123, p. 622. DOI: 10.1086/659878. arXiv: 1102.5218 [astro-ph.IM].

Bellini, A. et al. (2013). "The Intriguing Stellar Populations in the Globular Clusters NGC 6388 and NGC 6441". In: *ApJ* 765, 32, p. 32. DOI: 10.1088/0004-637X/765/1/32. arXiv: 1301.2822 [astro-ph.SR].

Bellini, A. et al. (2015). "The Hubble Space Telescope UV Legacy Survey of Galactic Globular Clusters: The Internal Kinematics of the Multiple Stellar Populations in NGC 2808". In: *ApJl* 810, L13, p. L13. DOI: 10.1088/2041-8205/810/1/L13. arXiv: 1508.01804.

Bensby, ed. (2015). *Galactocentric variation of the abundance structure in the Milky Way stellar disk - results from the Gaia-ESO survey*.

Bensby, T. et al. (2013). "Chemical evolution of the Galactic bulge as traced by microlensed dwarf and subgiant stars. V. Evidence for a wide age distribution and a complex MDF". In: A&A 549, A147, A147. DOI: 10.1051/0004-6361/201220678. arXiv: 1211.6848.

Bensby, T. et al. (2017). "Chemical evolution of the Galactic bulge as traced by microlensed dwarf and subgiant stars. VI. Age and abundance structure of the

stellar populations in the central sub-kpc of the Milky Way".
In: A&A 605, A89, A89. DOI: 10.1051/0004-6361/201730560.
arXiv: 1702.02971.

Bessell, M. S. and J. M. Brett (1988).
"JHKLM photometry - Standard systems, passbands, and intrinsic colors".
In: PASP 100, pp. 1134–1151. DOI: 10.1086/132281.

Bica, E., S. Ortolani, and B. Barbuy (2016). "Globular Clusters in the Galactic Bulge".
In: PASA 33, e028, e028. DOI: 10.1017/pasa.2015.47.
arXiv: 1510.07834 [astro-ph.SR].

Binney, J. (1978). "On the rotation of elliptical galaxies". In: MNRAS 183, pp. 501–514.
DOI: 10.1093/mnras/183.3.501.

Blanco, V. M., M. F. McCarthy, and B. M. Blanco (1984).
"Giant M stars in Baade's Window". In: AJ 89, pp. 636–647. DOI: 10.1086/113560.

Boggess, N. W. (1992). "The Cosmic Background Explorer (COBE)."
In: JRASC 86, pp. 282–283.

Bono, G. et al. (2010). "On a New Near-Infrared Method to Estimate the Absolute Ages of Star Clusters: NGC 3201 as a First Test Case". In: *ApJl* 708, pp. L74–L79.
DOI: 10.1088/2041-8205/708/2/L74. arXiv: 0912.0824 [astro-ph.SR].

Borissova, J. et al. (2011). "New Galactic star cluster candidates discovered in the VVV Survey within 10 degrees around the Galactic center". In: *Boletin de la Asociacion Argentina de Astronomia La Plata Argentina* 54, pp. 277–280.

Borissova, J. et al. (2014). "New galactic star clusters discovered in the VVV survey. Candidates projected on the inner disk and bulge". In: A&A 569, A24, A24.
DOI: 10.1051/0004-6361/201322483. arXiv: 1406.7051.

Brasseur, C. M. et al. (2010).
"Fiducial Stellar Population Sequences for the VJK$_S$ Photometric System".
In: AJ 140, pp. 1672–1686. DOI: 10.1088/0004-6256/140/6/1672.
arXiv: 1010.0247 [astro-ph.SR].

Brown, T. M. et al. (2009). "The WFC3 Galactic Bulge Treasury Program: A First Look at Resolved Stellar Population Tools". In: *AJ* 137, pp. 3172–3180.
DOI: 10.1088/0004-6256/137/2/3172. arXiv: 0812.0023.

Buonanno, R. et al. (1998).
"On the relative ages of galactic globular clusters. A new observable, a semi-empirical calibration and problems with the theoretical isochrones".
In: A&A 333, pp. 505–523.

Burstein, D. and C. Heiles (1982).
"Reddenings derived from H I and galaxy counts - Accuracy and maps".
In: AJ 87, pp. 1165–1189. DOI: 10.1086/113199.

Calamida, A. et al. (2009).
"A new method to estimate the ages of globular clusters: the case of NGC 3201".
In: *The Ages of Stars*. Ed. by E. E. Mamajek, D. R. Soderblom, and R. F. G. Wyse.
Vol. 258. IAU Symposium, pp. 189–196. DOI: 10.1017/S1743921309031846.

Cardelli, J. A., G. C. Clayton, and J. S. Mathis (1989). "The relationship between infrared, optical, and ultraviolet extinction". In: ApJ 345, pp. 245–256. DOI: 10.1086/167900.

Carollo, C. M. et al. (2007). "Old and Young Bulges in Late-Type Disk Galaxies". In: ApJ 658, pp. 960–979. DOI: 10.1086/511125. eprint: astro-ph/0610638.

Carpenter, J. M. (2001). "Color Transformations for the 2MASS Second Incremental Data Release". In: AJ 121, pp. 2851–2871. DOI: 10.1086/320383. eprint: astro-ph/0101463.

Carretta, E. and R. G. Gratton (1997). "Abundances for globular cluster giants. I. Homogeneous metallicities for 24 clusters". In: A&AS 121, pp. 95–112. DOI: 10.1051/aas:1997116. eprint: astro-ph/9607078.

Carretta, E. et al. (2009). "Intrinsic iron spread and a new metallicity scale for globular clusters". In: A&A 508, pp. 695–706. DOI: 10.1051/0004-6361/200913003. arXiv: 0910.0675.

Carretta, E. et al. (2010). "Properties of stellar generations in globular clusters and relations with global parameters". In: A&A 516, A55, A55. DOI: 10.1051/0004-6361/200913451. arXiv: 1003.1723.

Casagrande, L. and D. A. VandenBerg (2014). "Synthetic stellar photometry - I. General considerations and new transformations for broad-band systems". In: MNRAS 444, pp. 392–419. DOI: 10.1093/mnras/stu1476. arXiv: 1407.6095 [astro-ph.SR].

Casertano, S. and P. Hut (1985). "Core radius and density measurements in N-body experiments Connections with theoretical and observational definitions". In: ApJ 298, pp. 80–94. DOI: 10.1086/163589.

Casetti-Dinescu, D. I. et al. (2007). "Space Velocities of Southern Globular Clusters. V. A Low Galactic Latitude Sample". In: AJ 134, pp. 195–204. DOI: 10.1086/518507. arXiv: 0705.3438.

Casetti-Dinescu, D. I. et al. (2010). "Space Velocities of Southern Globular Clusters. VI. Nine Clusters in the Inner Milky Way". In: AJ 140, pp. 1282–1293. DOI: 10.1088/0004-6256/140/5/1282. arXiv: 1008.4545.

Casetti-Dinescu, D. I. et al. (2013). "Space Velocities of Southern Globular Clusters. VII. NGC 6397, NGC 6626 (M28), and NGC 6656 (M22)". In: AJ 146, 33, p. 33. DOI: 10.1088/0004-6256/146/2/33. arXiv: 1305.7431 [astro-ph.SR].

Cassisi, S. et al. (1999). "Galactic globular cluster stars: From theory to observation". In: A&AS 134, pp. 103–113. DOI: 10.1051/aas:1999126. eprint: astro-ph/9811329.

Catelan, M. et al. (2011). "The Vista Variables in the Vía Láctea (VVV) ESO Public Survey: Current Status and First Results". In: *RR Lyrae Stars, Metal-Poor Stars, and the Galaxy*. Ed. by A. McWilliam. Vol. 5, p. 145. arXiv: 1105.1119 [astro-ph.GA].

Chen, Y. et al. (2014). "Improving PARSEC models for very low mass stars". In: MNRAS 444, pp. 2525–2543. DOI: 10.1093/mnras/stu1605. arXiv: 1409.0322 [astro-ph.SR].

Chené, A.-N. et al. (2012). "Massive open star clusters using the VVV survey. I. Presentation of the data and description of the approach". In: A&A 545, A54, A54. DOI: 10.1051/0004-6361/201219064. arXiv: 1206.6104 [astro-ph.SR].

Clarkson, W. et al. (2008). "Stellar Proper Motions in the Galactic Bulge from Deep Hubble Space Telescope ACS WFC Photometry". In: ApJ 684, 1110-1142, pp. 1110–1142. DOI: 10.1086/590378. arXiv: 0809.1682.

Clarkson, W. I. et al. (2011). "The First Detection of Blue Straggler Stars in the Milky Way Bulge". In: ApJ 735, 37, p. 37. DOI: 10.1088/0004-637X/735/1/37. arXiv: 1105.4176.

Cohen, J. G. et al. (2007). "Integrated-Light Two Micron All Sky Survey Infrared Photometry of Galactic Globular Clusters". In: AJ 133, pp. 99–121. DOI: 10.1086/509127. eprint: astro-ph/0609353.

Cohen, R. E. et al. (2015). "Wide Field Near-infrared Photometry of 12 Galactic Globular Clusters: Observations Versus Models on the Red Giant Branch". In: AJ 150, 176, p. 176. DOI: 10.1088/0004-6256/150/6/176. arXiv: 1509.01470 [astro-ph.SR].

Cohen, R. E. et al. (2017). "Near-infrared photometry of globular clusters towards the Galactic bulge: observations and photometric metallicity indicators". In: MNRAS 464, pp. 1874–1902. DOI: 10.1093/mnras/stw2435. arXiv: 1609.07824 [astro-ph.SR].

Combes, F. and R. H. Sanders (1981). "Formation and properties of persisting stellar bars". In: A&A 96, pp. 164–173.

Correnti, M. et al. (2016). "Constraining Globular Cluster Age Uncertainties using the IR Color-Magnitude Diagram". In: ApJ 823, 18, p. 18. DOI: 10.3847/0004-637X/823/1/18. arXiv: 1603.05254 [astro-ph.SR].

Cutri, R. M. et al. (2003). *2MASS All Sky Catalog of point sources.*

Dalessandro, E. et al. (2008a). "Another Nonsegregated Blue Straggler Population in a Globular Cluster: the Case of NGC 2419". In: ApJ 681, 311-319, pp. 311–319. DOI: 10.1086/588462. arXiv: 0803.2149.

Dalessandro, E. et al. (2008b). "Blue Straggler Stars in the Unusual Globular Cluster NGC 6388". In: ApJ 677, 1069-1079, pp. 1069–1079. DOI: 10.1086/529028. arXiv: 0712.4272.

Dalessandro, E. et al. (2011). "The Binary Fraction in the Globular Cluster M10 (NGC 6254): Comparing Core and Outer Regions". In: ApJ 743, 11, p. 11. DOI: 10.1088/0004-637X/743/1/11. arXiv: 1108.5675 [astro-ph.SR].

Dalessandro, E. et al. (2012). "Ultraviolet Properties of Galactic Globular Clusters with Galex. II. Integrated Colors". In: AJ 144, 126, p. 126. DOI: 10.1088/0004-6256/144/5/126. arXiv: 1208.5698.

Dalessandro, E. et al. (2013).
"Double Blue Straggler Sequences in Globular Clusters: The Case of NGC 362".
In: *ApJ* 778, 135, p. 135. DOI: 10.1088/0004-637X/778/2/135.
arXiv: 1310.2389 [astro-ph.SR].

Dalessandro, E. et al. (2014).
"Constraining the True Nature of an Exotic Binary in the Core of NGC 6624".
In: ApJ 784, L29, p. L29. DOI: 10.1088/2041-8205/784/2/L29.
arXiv: 1401.7779 [astro-ph.SR].

Dalessandro, E. et al. (2015). "No Evidence of Mass Segregation in the Low-mass Galactic Globular Cluster NGC 6101". In: ApJ 810, 40, p. 40.
DOI: 10.1088/0004-637X/810/1/40. arXiv: 1507.04776.

Dalessandro, E. et al. (2016). "GeMS/GSAOI Photometric and Astrometric Performance in Dense Stellar Fields". In: *ApJ* 833, 111, p. 111.
DOI: 10.3847/1538-4357/833/1/111. arXiv: 1610.03489 [astro-ph.IM].

Davidge, T. J. (2000). "A Near-Infrared Photometric Study of the Low-Latitude Globular Clusters Liller 1, Djorgovski 1, HP 1, and NGC 6528".
In: ApJS 126, pp. 105–126. DOI: 10.1086/313292. eprint: astro-ph/9909408.

De Angeli, F. et al. (2005). "Galactic Globular Cluster Relative Ages".
In: AJ 130, pp. 116–125. DOI: 10.1086/430723. eprint: astro-ph/0503594.

De Marchi, G., F. Paresce, and L. Pulone (2007).
"Why Haven't Loose Globular Clusters Collapsed Yet?" In: ApJ 656, pp. L65–L68.
DOI: 10.1086/512856. eprint: astro-ph/0701613.

Dékány, I. et al. (2013). "VVV Survey Near-infrared Photometry of Known Bulge RR Lyrae Stars: The Distance to the Galactic Center and Absence of a Barred Distribution of the Metal-poor Population". In: ApJ 776, L19, p. L19.
DOI: 10.1088/2041-8205/776/2/L19. arXiv: 1309.5933.

Deutsch, E. W. et al. (1999). "Serendipitous Discovery of a Cataclysmic Variable in the Globular Cluster NGC 6624". In: AJ 118, pp. 2888–2893. DOI: 10.1086/301150.
eprint: astro-ph/9909344.

Di Cecco, A. et al. (2015). "On the Absolute Age of the Metal-rich Globular M71 (NGC 6838). I. Optical Photometry". In: AJ 150, 51, p. 51.
DOI: 10.1088/0004-6256/150/2/51. arXiv: 1506.01180 [astro-ph.SR].

Di Matteo, P. (2016). "The Disc Origin of the Milky Way Bulge".
In: PASA 33, e027, e027. DOI: 10.1017/pasa.2016.11. arXiv: 1603.05485.

Dib, R. et al. (2005). "An RXTE Archival Search for Coherent X-Ray Pulsations in the Low-Mass X-Ray Binary 4U 1820-30". In: ApJ 626, pp. 333–342.
DOI: 10.1086/429814. eprint: astro-ph/0407629.

Dicke, R. H. (1975). "Real-time correction of telescope "seeing"."
In: *Journal of the Optical Society of America (1917-1983)* 65, p. 1206.

Dinescu, D. I. et al. (1997). "Space velocities of southern globular clusters. I. Astrometric techniques and first results." In: AJ 114, pp. 1014–1029.
DOI: 10.1086/118532.

Dinescu, D. I., T. M. Girard, and W. F. van Altena (1999a). "Space Velocities of Globular Clusters. III. Cluster Orbits and Halo Substructure". In: AJ 117, pp. 1792–1815. DOI: 10.1086/300807.

Dinescu, D. I. et al. (1999b). "Space Velocities of Southern Globular Clusters. II. New Results for 10 Clusters". In: AJ 117, pp. 277–285. DOI: 10.1086/300699.

Dinescu, D. I. et al. (2003). "Space Velocities of Southern Globular Clusters. IV. First Results for Inner Galaxy Clusters". In: AJ 125, pp. 1373–1382. DOI: 10.1086/367801. eprint: astro-ph/0212279.

Diolaiti, E., R. Ragazzoni, and M. Tordi (2001). "Closed loop performance of a layer-oriented multi-conjugate adaptive optics system". In: *A&A* 372, pp. 710–718. DOI: 10.1051/0004-6361:20010514.

Diolaiti, E. et al. (2010). "Conceptual design and performance of the multiconjugate adaptive optics module for the European Extremely Large Telescope". In: *Adaptive Optics Systems II*. Vol. 7736. Proc. SPIE, 77360R. DOI: 10.1117/12.857634.

Djorgovski, S. G. and G. Meylan, eds. (1993). *Structure and dynamics of globular clusters*. Vol. 50. Astronomical Society of the Pacific Conference Series.

D'Orgeville, C. et al. (2002). "Gemini north and south laser guide star systems requirements and preliminary designs". In: *Adaptive Optics Systems and Technology II*. Ed. by R. K. Tyson, D. Bonaccini, and M. C. Roggemann. Vol. 4494. Proc. SPIE, pp. 302–316. DOI: 10.1117/12.454804.

d'Orgeville, C. et al. (2003). "Preliminary results of the 2001-2002 Gemini sodium monitoring campaign at Cerro Tololo, Chile". In: *Adaptive Optical System Technologies II*. Ed. by P. L. Wizinowich and D. Bonaccini. Vol. 4839. Proc. SPIE, pp. 492–503. DOI: 10.1117/12.457005.

d'Orgeville, C. et al. (2008). "The Gemini South MCAO laser guide star facility: getting ready for first light". In: *Adaptive Optics Systems*. Vol. 7015. Proc. SPIE, 70152P. DOI: 10.1117/12.788970.

Dotter, A. et al. (2007). "The ACS Survey of Galactic Globular Clusters. II. Stellar Evolution Tracks, Isochrones, Luminosity Functions, and Synthetic Horizontal-Branch Models". In: AJ 134, pp. 376–390. DOI: 10.1086/517915. arXiv: 0706.0847.

Dotter, A. et al. (2008). "The Dartmouth Stellar Evolution Database". In: ApJS 178, 89-101, pp. 89–101. DOI: 10.1086/589654. arXiv: 0804.4473.

Dotter, A. et al. (2010). "The ACS Survey of Galactic Globular Clusters. IX. Horizontal Branch Morphology and the Second Parameter Phenomenon". In: ApJ 708, pp. 698–716. DOI: 10.1088/0004-637X/708/1/698. arXiv: 0911.2469 [astro-ph.SR].

Dwek, E. et al. (1995). "Morphology, near-infrared luminosity, and mass of the Galactic bulge from COBE DIRBE observations". In: ApJ 445, pp. 716–730. DOI: 10.1086/175734.

Ellerbroek, B. L. and G. Cochran (2002). "Wave optics propagation code for multiconjugate adaptive optics". In: *Adaptive Optics Systems and Technology II*. Ed. by R. K. Tyson, D. Bonaccini, and M. C. Roggemann. Vol. 4494. Proc. SPIE, pp. 104–120. DOI: 10.1117/12.454784.

Ellerbroek, B. L. and D. W. Tyler (1998). "Adaptive Optics Sky Coverage Calculations for the Gemini-North Telescope". In: *PASP* 110, pp. 165–185. DOI: 10.1086/316120.

Elmegreen, B. G. (1999). "Galactic Bulge Formation as a Maximum Intensity Starburst". In: ApJ 517, pp. 103–107. DOI: 10.1086/307200. eprint: astro-ph/9901025.

— (2009). "Bulge Formation by the Coalescence of Giant Clumps in Primordial Disk Galaxies". In: *Galaxy Evolution: Emerging Insights and Future Challenges*. Ed. by S. Jogee et al. Vol. 419. Astronomical Society of the Pacific Conference Series, p. 23. arXiv: 0903.1937 [astro-ph.CO].

Elmegreen, B. G., F. Bournaud, and D. M. Elmegreen (2008). "Bulge Formation by the Coalescence of Giant Clumps in Primordial Disk Galaxies". In: ApJ 688, 67-77, pp. 67–77. DOI: 10.1086/592190. arXiv: 0808.0716.

Feltzing, S. and G. Gilmore (2000). "Age and metallicity gradients in the Galactic Bulge. A differential study using HST/WFPC2". In: A&A 355, pp. 949–965.

Ferraro, F. R. et al. (1991). "CCD-photometry of galactic globular clusters. III - NGC 6171". In: MNRAS 252, pp. 357–377. DOI: 10.1093/mnras/252.3.357.

Ferraro, F. R. et al. (1992). "On the giant, horizontal and asymptotic branches of Galactic globular clusters. IV - CCD photometry of NGC 1904". In: MNRAS 256, pp. 391–403. DOI: 10.1093/mnras/256.3.391.

Ferraro, F. R. et al. (1999a). "Blue Straggler Stars: The Spectacular Population in M80". In: ApJ 522, pp. 983–990. DOI: 10.1086/307700. eprint: astro-ph/9904196.

Ferraro, F. R. et al. (1999b). "The Giant, Horizontal, and Asymptotic Branches of Galactic Globular Clusters. I. The Catalog, Photometric Observables, and Features". In: AJ 118, pp. 1738–1758. DOI: 10.1086/301029. eprint: astro-ph/9906248.

Ferraro, F. R. et al. (2000). "A New Infrared Array Photometric Survey of Galactic Globular Clusters: A Detailed Study of the Red Giant Branch Sequence as a Step toward the Global Testing of Stellar Models". In: AJ 119, pp. 1282–1295. DOI: 10.1086/301269. eprint: astro-ph/9912265.

Ferraro, F. R. et al. (2001). "Blue Stragglers, Young White Dwarfs, and UV-Excess Stars in the Core of 47 Tucanae". In: ApJ 561, pp. 337–345. DOI: 10.1086/322773. eprint: astro-ph/0107056.

Ferraro, F. R. et al. (2003). "The Puzzling Dynamical Status of the Core of the Globular Cluster NGC 6752". In: ApJ 595, pp. 179–186. DOI: 10.1086/377352. eprint: astro-ph/0306138.

Ferraro, F. R. et al. (2006). "The Pure Noncollisional Blue Straggler Population in the Giant Stellar System ω Centauri". In: ApJ 638, pp. 433–439. DOI: 10.1086/498735. eprint: astro-ph/0510280.

Ferraro, F. R. et al. (2009a). "The cluster Terzan 5 as a remnant of a primordial building block of the Galactic bulge". In: *Nature* 462, pp. 483–486. DOI: 10.1038/nature08581. arXiv: 0912.0192.

Ferraro, F. R. et al. (2009b). "Two distinct sequences of blue straggler stars in the globular cluster M 30". In: Nature 462, pp. 1028–1031. DOI: 10.1038/nature08607. arXiv: 1001.1096.

Ferraro, F. R. et al. (2012). "Dynamical age differences among coeval star clusters as revealed by blue stragglers". In: Nature 492, pp. 393–395. DOI: 10.1038/nature11686. arXiv: 1212.5071 [astro-ph.SR].

Ferraro, F. R. et al. (2016). "The Age of the Young Bulge-like Population in the Stellar System Terzan 5: Linking the Galactic Bulge to the High-z Universe". In: ApJ 828, 75, p. 75. DOI: 10.3847/0004-637X/828/2/75. arXiv: 1609.01515.

Foy, R. and A. Labeyrie (1985). "Feasibility of adaptive telescope with laser probe". In: *A&A* 152, pp. L29–L31.

Fragkoudi, F. et al. (2018). "The disc origin of the Milky Way bulge: II. Dissecting the chemo-morphological relations using N-body simulations and APOGEE". In: *ArXiv e-prints*. arXiv: 1802.00453.

Freeman, K. et al. (2013). "ARGOS - II. The Galactic bulge survey". In: MNRAS 428, pp. 3660–3670. DOI: 10.1093/mnras/sts305. arXiv: 1212.1541 [astro-ph.GA].

Freire, P. C. C. et al. (2011). "Fermi Detection of a Luminous γ-Ray Pulsar in a Globular Cluster". In: *Science* 334, p. 1107. DOI: 10.1126/science.1207141. arXiv: 1111.3754.

Frogel, J. A. and A. E. Whitford (1987). "M giants in Baade's window - Infrared colors, luminosities, and implications for the stellar content of E and S0 galaxies". In: ApJ 320, pp. 199–237. DOI: 10.1086/165535.

Frogel, J. A., L. E. Kuchinski, and G. P. Tiede (1995). "Infrared array photometry of metal rich globular clusters. 2: Liller 1–the most metal rich cluster?" In: AJ 109, pp. 1154–1168. DOI: 10.1086/117348.

Fulbright, J. P., A. McWilliam, and R. M. Rich (2006). "Abundances of Baade's Window Giants from Keck HIRES Spectra. I. Stellar Parameters and [Fe/H] Values". In: ApJ 636, pp. 821–841. DOI: 10.1086/498205. eprint: astro-ph/0510408.

— (2007). "Abundances of Baade's Window Giants from Keck HIRES Spectra. II. The Alpha and Light Odd Elements". In: ApJ 661, pp. 1152–1179. DOI: 10.1086/513710. eprint: astro-ph/0609087.

Fusco, T. et al. (1999). "Myopic deconvolution method for adaptive optics images of stellar fields". In: *A&A Supplements* 134, pp. 193–200. DOI: 10.1051/aas:1999133.

Fusco, T. et al. (2010). "ATLAS: the E-ELT laser tomographic adaptive optics system". In: *Adaptive Optics Systems II*. Vol. 7736. Proc. SPIE, p. 77360D. DOI: 10.1117/12.857468.

Fusi Pecci, F. et al. (1990). "The variation of the red giant luminosity function 'Bump' with metallicity and the age of the globular clusters". In: A&A 238, pp. 95–110.

Gaia Collaboration et al. (2016). "The Gaia mission". In: A&A 595, A1, A1. DOI: 10.1051/0004-6361/201629272. arXiv: 1609.04153 [astro-ph.IM].

Garzón, F. and M. López-Corredoira (2014). "Dynamical evolution of two associated galactic bars". In: *Astronomische Nachrichten* 335, p. 865. DOI: 10.1002/asna.201412120. arXiv: 1409.1916.

Genzel, R. et al. (2011). "The Sins Survey of z ˜ 2 Galaxy Kinematics: Properties of the Giant Star-forming Clumps". In: ApJ 733, 101, p. 101. DOI: 10.1088/0004-637X/733/2/101. arXiv: 1011.5360.

Goldsbury, R., J. Heyl, and H. Richer (2013). "Quantifying Mass Segregation and New Core Radii for 54 Milky Way Globular Clusters". In: ApJ 778, 57, p. 57. DOI: 10.1088/0004-637X/778/1/57. arXiv: 1308.3706.

Gonzalez, O. A. et al. (2011). "Alpha element abundances and gradients in the Milky Way bulge from FLAMES-GIRAFFE spectra of 650 K giants". In: A&A 530, A54, A54. DOI: 10.1051/0004-6361/201116548. arXiv: 1103.6104.

Gonzalez, O. A. et al. (2012). "Reddening and metallicity maps of the Milky Way bulge from VVV and 2MASS. II. The complete high resolution extinction map and implications for Galactic bulge studies". In: A&A 543, A13, A13. DOI: 10.1051/0004-6361/201219222. arXiv: 1204.4004.

Gonzalez, O. A. et al. (2013). "Reddening and metallicity maps of the Milky Way bulge from VVV and 2MASS. III. The first global photometric metallicity map of the Galactic bulge". In: A&A 552, A110, A110. DOI: 10.1051/0004-6361/201220842. arXiv: 1302.0243.

Gonzalez, O. A. et al. (2015). "The GIRAFFE Inner Bulge Survey (GIBS). II. Metallicity distributions and alpha element abundances at fixed Galactic latitude". In: A&A 584, A46, A46. DOI: 10.1051/0004-6361/201526737. arXiv: 1508.02576.

Gratton, R. et al. (2003). "New Determination of the Distances to NGC 6397, NGC 6752 and 47 Tuc Based on Main Sequence Fitting".

In: *New Horizons in Globular Cluster Astronomy*. Ed. by G. Piotto et al. Vol. 296. Astronomical Society of the Pacific Conference Series, p. 381.

Gullieuszik, M. et al. (2008). "Resolving stellar populations outside the Local Group: MAD observations of UKS 2323-326". In: *A&A* 483, pp. L5–L8. DOI: 10.1051/0004-6361:200809631. arXiv: 0803.3728.

Hankla, A. K. et al. (2006). "20 W and 50 W solid-state sodium beacon guidestar laser systems for the Keck I and Gemini South Telescopes". In: *Society of Photo-Optical Instrumentation Engineers (SPIE) Conference Series*. Vol. 6272. Proc. SPIE, 62721G. DOI: 10.1117/12.670054.

Harris, W. E. (1996). "A Catalog of Parameters for Globular Clusters in the Milky Way". In: AJ 112, p. 1487. DOI: 10.1086/118116.

Hauser, M. G. et al. (1998). "The COBE Diffuse Infrared Background Experiment Search for the Cosmic Infrared Background. I. Limits and Detections". In: ApJ 508, pp. 25–43. DOI: 10.1086/306379. eprint: astro-ph/9806167.

Haywood, M. et al. (2016). "Hiding its age: the case for a younger bulge". In: A&A 593, A82, A82. DOI: 10.1051/0004-6361/201628816. arXiv: 1606.04092.

Heasley, J. N. et al. (2000). "Hubble Space Telescope Photometry of the Metal-rich Globular Clusters NGC 6624 and NGC 6637". In: AJ 120, pp. 879–893. DOI: 10.1086/301461.

Herriot, G. et al. (2010). "NFIRAOS: TMT's facility adaptive optics system". In: *Adaptive Optics Systems II*. Vol. 7736. Proc. SPIE, 77360B. DOI: 10.1117/12.857662.

Hill, V. et al. (2011). "The metallicity distribution of bulge clump giants in Baade's window". In: A&A 534, A80, A80. DOI: 10.1051/0004-6361/200913757. arXiv: 1107.5199.

Hoffman, J. A., H. L. Marshall, and W. H. G. Lewin (1978). "Dual character of the rapid burster and a classification of X-ray bursts". In: Nature 271, pp. 630–633. DOI: 10.1038/271630a0.

Holtzman, J. A. et al. (1993). "Wide field camera observations of Baade's Window". In: AJ 106, pp. 1826–1838. DOI: 10.1086/116768.

Homer, L. et al. (2001). "The Rapid Burster in Liller 1: The Chandra X-Ray Position and a Search for an Infrared Counterpart". In: AJ 122, pp. 2627–2633. DOI: 10.1086/323545. eprint: astro-ph/0106140.

Howard, C. D. et al. (2008). "The Bulge Radial Velocity Assay (BRAVA). I. Sample Selection and a Rotation Curve". In: ApJ 688, 1060-1077, pp. 1060–1077. DOI: 10.1086/592106. arXiv: 0807.3967.

Howard, C. D. et al. (2009). "Kinematics at the Edge of the Galactic Bulge: Evidence for Cylindrical Rotation". In: ApJ 702, pp. L153–L157. DOI: 10.1088/0004-637X/702/2/L153. arXiv: 0908.1109 [astro-ph.GA].

Hui, C. Y., K. S. Cheng, and R. E. Taam (2010).
"Dynamical Formation of Millisecond Pulsars in Globular Clusters".
In: ApJ 714, pp. 1149–1154. DOI: 10.1088/0004-637X/714/2/1149.
arXiv: 1003.4332 [astro-ph.HE].

Iben, I. and A. Renzini (1984). "Single star evolution I. Massive stars and early evolution of low and intermediate mass stars". In: Phys. Rep. 105, pp. 329–406.
DOI: 10.1016/0370-1573(84)90142-X.

Immeli, A. et al. (2004).
"Gas physics, disk fragmentation, and bulge formation in young galaxies".
In: A&A 413, pp. 547–561. DOI: 10.1051/0004-6361:20034282.
eprint: astro-ph/0312139.

Irwin, M. J. et al. (2004).
"VISTA data flow system: pipeline processing for WFCAM and VISTA".
In: *Optimizing Scientific Return for Astronomy through Information Technologies*.
Ed. by P. J. Quinn and A. Bridger. Vol. 5493. Proc. SPIE, pp. 411–422.
DOI: 10.1117/12.551449.

Johnson, C. I. et al. (2014).
"Light, Alpha, and Fe-peak Element Abundances in the Galactic Bulge".
In: AJ 148, 67, p. 67. DOI: 10.1088/0004-6256/148/4/67.
arXiv: 1407.2282 [astro-ph.SR].

Kalirai, J. S. et al. (2012). "A Deep, Wide-field, and Panchromatic View of 47 Tuc and the SMC with HST: Observations and Data Analysis Methods".
In: AJ 143, 11, p. 11. DOI: 10.1088/0004-6256/143/1/11.
arXiv: 1112.1426 [astro-ph.SR].

Kerber, L. O. et al. (2018). "Ages of the Bulge Globular Clusters NGC 6522 and NGC 6626 (M28) from HST Proper-motion-cleaned ColorMagnitude Diagrams".
In: ApJ 853, 15, p. 15. DOI: 10.3847/1538-4357/aaa3fc.
arXiv: 1801.03876 [astro-ph.SR].

Kim, J.-W. et al. (2006). "Deep near-IR photometry of eight metal-poor globular clusters in the Galactic bulge and halo". In: A&A 459, pp. 499–509.
DOI: 10.1051/0004-6361:20065007.

King, I. R. (1966). "The structure of star clusters. III. Some simple dynamical models".
In: AJ 71, p. 64. DOI: 10.1086/109857.

Kormendy, J. and R. C. Kennicutt Jr. (2004).
"Secular Evolution and the Formation of Pseudobulges in Disk Galaxies".
In: ARA&A 42, pp. 603–683. DOI: 10.1146/annurev.astro.42.053102.134024.
eprint: astro-ph/0407343.

Kuchinski, L. E. and J. A. Frogel (1995). "Infrared Array Photometry of Metal-Rich Globular Clusters.III.Two More Clusters and an Analysis of V-K Colors".
In: AJ 110, p. 2844. DOI: 10.1086/117733.

Kuijken, K. and R. M. Rich (2002). "Hubble Space Telescope WFPC2 Proper Motions in Two Bulge Fields: Kinematics and Stellar Population of the Galactic Bulge". In: AJ 124, pp. 2054–2066. DOI: 10.1086/342540. eprint: astro-ph/0207116.

Kunder, A. et al. (2012). "The Bulge Radial Velocity Assay (BRAVA). II. Complete Sample and Data Release". In: AJ 143, 57, p. 57. DOI: 10.1088/0004-6256/143/3/57. arXiv: 1112.1955 [astro-ph.SR].

Lanzoni, B. et al. (2007). "The Surface Density Profile of NGC 6388: A Good Candidate for Harboring an Intermediate-Mass Black Hole". In: ApJ 668, pp. L139–L142. DOI: 10.1086/522927. arXiv: 0709.0119.

Lanzoni, B. et al. (2010). "New Density Profile and Structural Parameters of the Complex Stellar System Terzan 5". In: ApJ 717, pp. 653–657. DOI: 10.1088/0004-637X/717/2/653. arXiv: 1005.2847.

Lecureur, A. et al. (2007). "Oxygen, sodium, magnesium, and aluminium as tracers of the galactic bulge formation". In: A&A 465, pp. 799–814. DOI: 10.1051/0004-6361:20066036. eprint: astro-ph/0610346.

Libralato, M. et al. (2014). "Ground-based astrometry with wide field imagers. V. Application to near-infrared detectors: HAWK-I@VLT/ESO". In: *A&A* 563, A80, A80. DOI: 10.1051/0004-6361/201322059. arXiv: 1401.3344 [astro-ph.IM].

Libralato, M. et al. (2015). "High-precision astrometry with VVV - I. An independent reduction pipeline for VIRCAM@VISTA". In: *MNRAS* 450, pp. 1664–1673. DOI: 10.1093/mnras/stv674. arXiv: 1503.07519 [astro-ph.IM].

Linsky, J. L. (1969). "On the Pressure-Induced Opacity of Molecular Hydrogen in Late-Type Stars". In: ApJ 156, p. 989. DOI: 10.1086/150030.

Liuzzo, E. et al. (2016). "MAD Adaptive Optics Imaging of High-luminosity Quasars: A Pilot Project". In: *AJ* 152, 38, p. 38. DOI: 10.3847/0004-6256/152/2/38. arXiv: 1605.08406.

Lugger, P. M., H. N. Cohn, and J. E. Grindlay (1995). "CCD photometry of globular cluster core structure. 2: U-band profiles for 15 candidate collapsed-core clusters". In: ApJ 439, pp. 191–201. DOI: 10.1086/175164.

Lynch, R. S. et al. (2012). "The Timing of Nine Globular Cluster Pulsars". In: ApJ 745, 109, p. 109. DOI: 10.1088/0004-637X/745/2/109. arXiv: 1112.2612 [astro-ph.HE].

Malkan, M., D. E. Kleinmann, and J. Apt (1980). "Infrared studies of globular clusters near the galactic center". In: ApJ 237, pp. 432–437. DOI: 10.1086/157886.

Maraston, C. and D. Thomas (2000). "Strong Balmer Lines in Old Stellar Populations: No Need for Young Ages in Ellipticals?" In: ApJ 541, pp. 126–133. DOI: 10.1086/309433. eprint: astro-ph/0004145.

Maraston, C. et al. (2003). "Integrated spectroscopy of bulge globular clusters and fields. II. Implications for population synthesis models and elliptical galaxies".

In: A&A 400, pp. 823–840. DOI: 10.1051/0004-6361:20021723.
eprint: astro-ph/0209220.

Marchetti, E. et al. (2006). "MAD star oriented: laboratory results for ground layer and multi-conjugate adaptive optics".
In: *Society of Photo-Optical Instrumentation Engineers (SPIE) Conference Series*. Vol. 6272. Proc. SPIE, 62720O. DOI: 10.1117/12.671088.

Marchetti, E. et al. (2007).
"On-sky Testing of the Multi-Conjugate Adaptive Optics Demonstrator".
In: *The Messenger* 129, pp. 8–13.

Marchetti, E. et al. (2008). "MAD on sky results in star oriented mode".
In: *Adaptive Optics Systems*. Vol. 7015. Proc. SPIE, 70150F.
DOI: 10.1117/12.787240.

Marín-Franch, A. et al. (2009).
"The ACS Survey of Galactic Globular Clusters. VII. Relative Ages".
In: ApJ 694, pp. 1498–1516. DOI: 10.1088/0004-637X/694/2/1498.
arXiv: 0812.4541.

Marshall, D. J. et al. (2006).
"Modelling the Galactic interstellar extinction distribution in three dimensions".
In: A&A 453, pp. 635–651. DOI: 10.1051/0004-6361:20053842.
eprint: astro-ph/0604427.

Martinez-Valpuesta, I. and O. Gerhard (2011).
"Unifying A Boxy Bulge and Planar Long Bar in the Milky Way".
In: ApJ 734, L20, p. L20. DOI: 10.1088/2041-8205/734/1/L20. arXiv: 1105.0928.

Massari, D. et al. (2012).
"High-resolution Reddening Map in the Direction of the Stellar System Terzan 5".
In: ApJ 755, L32, p. L32. DOI: 10.1088/2041-8205/755/2/L32.
arXiv: 1209.0990 [astro-ph.GA].

Massari, D. et al. (2013). "Hubble Space Telescope Absolute Proper Motions Of NGC 6681 (M70) and the Sagittarius Dwarf Spheroidal Galaxy". In: *ApJ* 779, 81, p. 81.
DOI: 10.1088/0004-637X/779/1/81. arXiv: 1310.2096.

Massari, D. et al. (2014a). "Ceci N'est Pas a Globular Cluster: The Metallicity Distribution of the Stellar System Terzan 5". In: ApJ 795, 22, p. 22.
DOI: 10.1088/0004-637X/795/1/22. arXiv: 1409.1682 [astro-ph.SR].

Massari, D. et al. (2014b). "Chemical and Kinematical Properties of Galactic Bulge Stars Surrounding the Stellar System Terzan 5". In: ApJ 791, 101, p. 101.
DOI: 10.1088/0004-637X/791/2/101. arXiv: 1407.0047.

Massari, D. et al. (2015). "Proper Motions in Terzan 5: Membership of the Multi-iron Subpopulations and First Constraint on the Orbit". In: ApJ 810, 69, p. 69.
DOI: 10.1088/0004-637X/810/1/69. arXiv: 1507.03020.

Massari, D. et al. (2016a). "Astrometry with MCAO: HST-GeMS proper motions in the globular cluster NGC 6681". In: *ArXiv e-prints*.
arXiv: 1609.05923 [astro-ph.SR].

Massari, D. et al. (2016b). "GeMS MCAO observations of the Galactic globular cluster NGC 2808: the absolute age". In: A&A 586, A51, A51. DOI: 10.1051/0004-6361/201527686. arXiv: 1512.03194.

Mauro, F. et al. (2013). "The VVV-SkZ_pipeline: an automatic PSF-fitting photometric pipeline for the VVV survey". In: Rev. Mexicana Astron. Astrofis. 49, pp. 189–207. arXiv: 1303.1824 [astro-ph.IM].

McGregor, P. et al. (2004). "Gemini South Adaptive Optics Imager (GSAOI)". In: *Ground-based Instrumentation for Astronomy*. Ed. by A. F. M. Moorwood and M. Iye. Vol. 5492. Proc. SPIE, pp. 1033–1044. DOI: 10.1117/12.550288.

McLaughlin, D. E. and R. P. van der Marel (2005). "Resolved Massive Star Clusters in the Milky Way and Its Satellites: Brightness Profiles and a Catalog of Fundamental Parameters". In: ApJS 161, pp. 304–360. DOI: 10.1086/497429. eprint: astro-ph/0605132.

McWilliam, A. and R. M. Rich (1994). "The first detailed abundance analysis of Galactic bulge K giants in Baade's window". In: ApJS 91, pp. 749–791. DOI: 10.1086/191954.

McWilliam, A. and M. Zoccali (2010). "Two Red Clumps and the X-shaped Milky Way Bulge". In: ApJ 724, pp. 1491–1502. DOI: 10.1088/0004-637X/724/2/1491. arXiv: 1008.0519.

Meissner, F. and A. Weiss (2006). "Global fitting of globular cluster age indicators". In: A&A 456, pp. 1085–1096. DOI: 10.1051/0004-6361:20065133.

Meléndez, J. et al. (2003). "Gemini-Phoenix infrared high-resolution abundance analysis of five giants in the bulge globular cluster NGC 6553". In: A&A 411, pp. 417–426. DOI: 10.1051/0004-6361:20031357. eprint: astro-ph/0309552.

Merkle, F. et al. (1989). "Successful tests of adaptive optics." In: *The Messenger* 58, pp. 1–4.

Merritt, D., G. Meylan, and M. Mayor (1997). "The stellar dynamics of omega centauri." In: AJ 114, pp. 1074–1086. DOI: 10.1086/118538. eprint: astro-ph/9612184.

Meurer, G. R. et al. (2003). "Calibration of geometric distortion in the ACS detectors". In: *Future EUV/UV and Visible Space Astrophysics Missions and Instrumentation*. Ed. by J. C. Blades and O. H. W. Siegmund. Vol. 4854. Proc. SPIE, pp. 507–514. DOI: 10.1117/12.460259.

Meylan, G. and D. C. Heggie (1997). "Internal dynamics of globular clusters". In: A&A Rev. 8, pp. 1–143. DOI: 10.1007/s001590050008. eprint: astro-ph/9610076.

Mignani, R. P. et al. (2008). "Near infrared VLT/MAD observations of the isolated neutron stars RX J0420.0-5022 and RX J1856.5-3754". In: *A&A* 488, pp. 267–270. DOI: 10.1051/0004-6361:200809926. arXiv: 0806.4136.

Milone, A. P. et al. (2012).
"The Infrared Eye of the Wide-Field Camera 3 on the Hubble Space Telescope Reveals Multiple Main Sequences of Very Low Mass Stars in NGC 2808".
In: ApJ 754, L34, p. L34. DOI: 10.1088/2041-8205/754/2/L34.
arXiv: 1206.5529 [astro-ph.SR].

Milone, A. P. et al. (2014). "The M 4 Core Project with HST - II. Multiple stellar populations at the bottom of the main sequence". In: MNRAS 439, pp. 1588–1595.
DOI: 10.1093/mnras/stu030. arXiv: 1401.1091 [astro-ph.SR].

Minniti, D. (1996). "Kinematics of Bulge Giants in F588". In: ApJ 459, p. 579.
DOI: 10.1086/176923.

Minniti, D. and M. Zoccali (2008). "The Galactic bulge: a review".
In: *Formation and Evolution of Galaxy Bulges*.
Ed. by M. Bureau, E. Athanassoula, and B. Barbuy. Vol. 245. IAU Symposium, pp. 323–332. DOI: 10.1017/S1743921308018048. arXiv: 0710.3104.

Minniti, D., E. W. Olszewski, and M. Rieke (1995). "IR Color-Magnitude Diagrams of 20 Galactic Globular Clusters and Bulge Fields". In: AJ 110, p. 1686.
DOI: 10.1086/117641.

Minniti, D. et al. (2010). "VISTA Variables in the Via Lactea (VVV): The public ESO near-IR variability survey of the Milky Way". In: New A 15, pp. 433–443.
DOI: 10.1016/j.newast.2009.12.002. arXiv: 0912.1056.

Minniti, D. et al. (2011). "Discovery of VVV CL001. A low-mass globular cluster next to UKS 1 in the direction of the Galactic bulge". In: A&A 527, A81, A81.
DOI: 10.1051/0004-6361/201015795. arXiv: 1012.2450.

Minniti, D. et al. (2017a). "New Metal-poor Globular Clusters in the Galactic Bulge: The Elephant Graveyard".
In: *Research Notes of the American Astronomical Society* 1, 16, p. 16.
DOI: 10.3847/2515-5172/aa9ab7.

Minniti, D. et al. (2017b).
"New VVV Survey Globular Cluster Candidates in the Milky Way Bulge".
In: ApJ 849, L24, p. L24. DOI: 10.3847/2041-8213/aa95b8.

Miocchi, P. et al. (2013). "Star Count Density Profiles and Structural Parameters of 26 Galactic Globular Clusters". In: ApJ 774, 151, p. 151.
DOI: 10.1088/0004-637X/774/2/151. arXiv: 1307.6035 [astro-ph.GA].

Moffat, A. F. J. (1969). "A Theoretical Investigation of Focal Stellar Images in the Photographic Emulsion and Application to Photographic Photometry".
In: A&A 3, p. 455.

Momany, Y. et al. (2008). "Multi-Conjugate Adaptive Optics VLT imaging of the distant old open cluster FSR1415". In: *MNRAS* 391, pp. 1650–1658.
DOI: 10.1111/j.1365-2966.2008.14019.x. arXiv: 0810.0341.

Monelli, M. et al. (2015). "The Absolute Age of the Globular Cluster M15 Using Near-infrared Adaptive Optics Images from PISCES/LBT." In: ApJ 812, 25, p. 25.
DOI: 10.1088/0004-637X/812/1/25. arXiv: 1507.08845 [astro-ph.SR].

Moni Bidin, C. et al. (2011). "Three Galactic globular cluster candidates". In: A&A 535, A33, A33. DOI: 10.1051/0004-6361/201117488. arXiv: 1109.1854.

Montegriffo, P. et al. (1995). "IR-array photometry of Galactic globular clusters - II. JK photometry of 47 TUC". In: MNRAS 276, pp. 739–752. DOI: 10.1093/mnras/276.3.739.

Montegriffo, P. et al. (1998). "Towards the absolute planes: a new calibration of the bolometric corrections and temperature scales for Population II giants". In: MNRAS 297, pp. 872–884. DOI: 10.1046/j.1365-8711.1998.01553.x. eprint: astro-ph/9804297.

Moretti, A. et al. (2009). "MCAO near-IR photometry of the globular cluster NGC 6388: MAD observations in crowded fields". In: *A&A* 493, pp. 539–546. DOI: 10.1051/0004-6361:200810718. arXiv: 0810.2248.

Nataf, D. M. et al. (2010). "The Split Red Clump of the Galactic Bulge from OGLE-III". In: ApJ 721, pp. L28–L32. DOI: 10.1088/2041-8205/721/1/L28. arXiv: 1007.5065.

Neichel, B. and F. Rigaut (2011). "Rayleigh scattering, Fratricide effect and spot elongation: first on-sky results with GeMS". In: *Second International Conference on Adaptive Optics for Extremely Large Telescopes. Online at <A href="http://ao4elt2.lesia.obspm.fr">http://ao4elt2.lesia.obspm.fr</A>, id.54*, p. 54.

Neichel, B. et al. (2014a). "Astrometric performance of the Gemini multiconjugate adaptive optics system in crowded fields". In: *MNRAS* 445, pp. 500–514. DOI: 10.1093/mnras/stu1766. arXiv: 1409.0719 [astro-ph.IM].

Neichel, B. et al. (2014b). "Gemini multiconjugate adaptive optics system review - II. Commissioning, operation and overall performance". In: *MNRAS* 440, pp. 1002–1019. DOI: 10.1093/mnras/stu403. arXiv: 1402.6906 [astro-ph.IM].

Ness, M. and K. Freeman (2012). "The formation of the Galactic bulge of the Milky Way". In: *European Physical Journal Web of Conferences*. Vol. 19. European Physical Journal Web of Conferences, p. 06003. DOI: 10.1051/epjconf/20121906003.

Ness, M. et al. (2013a). "ARGOS - III. Stellar populations in the Galactic bulge of the Milky Way". In: MNRAS 430, pp. 836–857. DOI: 10.1093/mnras/sts629. arXiv: 1212.1540.

Ness, M. et al. (2013b). "ARGOS - IV. The kinematics of the Milky Way bulge". In: MNRAS 432, pp. 2092–2103. DOI: 10.1093/mnras/stt533. arXiv: 1303.6656.

Ness, M. et al. (2016). "APOGEE Kinematics. I. Overview of the Kinematics of the Galactic Bulge as Mapped By APOGEE". In: ApJ 819, 2, p. 2. DOI: 10.3847/0004-637X/819/1/2. arXiv: 1512.04948.

Norman, C. A., J. A. Sellwood, and H. Hasan (1996). "Bar Dissolution and Bulge Formation: an Example of Secular Dynamical Evolution in Galaxies". In: ApJ 462, p. 114. DOI: 10.1086/177133.

Origlia, L. et al. (1997). "Infrared stellar absorption lines around 1.6μm: a new metallicity scale for old stellar populations." In: A&A 321, pp. 859–866.

Origlia, L., R. M. Rich, and S. Castro (2002). "High-Resolution Infrared Spectra of Bulge Globular Clusters: Liller 1 and NGC 6553". In: AJ 123, pp. 1559–1569. DOI: 10.1086/338897. eprint: astro-ph/0112104.

Origlia, L. et al. (2011). "Spectroscopy Unveils the Complex Nature of Terzan 5". In: ApJ 726, L20, p. L20. DOI: 10.1088/2041-8205/726/2/L20. arXiv: 1012.2047.

Origlia, L. et al. (2013). "The Terzan 5 Puzzle: Discovery of a Third, Metal-poor Component". In: ApJ 779, L5, p. L5. DOI: 10.1088/2041-8205/779/1/L5. arXiv: 1311.1706.

Ortolani, S. et al. (1995). "Near-coeval formation of the Galactic bulge and halo inferred from globular cluster ages". In: Nature 377, pp. 701–704. DOI: 10.1038/377701a0.

Ortolani, S., E. Bica, and B. Barbuy (1996). "NTT V, I and Gunn Z colour-magnitude diagrams of Liller 1: a globular cluster as metal-rich as the inner bulge stellar population?" In: A&A 306, p. 134.

Ortolani, S. et al. (2001). "HST NICMOS photometry of the reddened bulge globular clusters NGC 6528, Terzan 5, Liller 1, UKS 1 and Terzan 4". In: *ApJ* 376, pp. 878–884. DOI: 10.1051/0004-6361:20011045. eprint: astro-ph/0107459.

Ortolani, S. et al. (2007). "Distances of the bulge globular clusters Terzan 5, Liller 1, UKS 1, and Terzan 4 based on HST NICMOS photometry". In: *A&A* 470, pp. 1043–1049. DOI: 10.1051/0004-6361:20066628. arXiv: 0705.4030.

Ortolani, S. et al. (2011). "A Fossil Bulge Globular Cluster Revealed by very Large Telescope Multi-conjugate Adaptive Optics". In: *ApJ* 737, 31, p. 31. DOI: 10.1088/0004-637X/737/1/31. arXiv: 1106.2725.

Paresce, F., G. de Marchi, and F. R. Ferraro (1992). "Possible cataclysmic variable in the core of the globular cluster 47 Tucanae". In: Nature 360, pp. 46–48. DOI: 10.1038/360046a0.

Paust, N. E. Q. et al. (2010). "The ACS Survey of Galactic Globular Clusters. VIII. Effects of Environment on Globular Cluster Global Mass Functions". In: AJ 139, pp. 476–491. DOI: 10.1088/0004-6256/139/2/476.

Penny, A. J. (1976). *Electronographic stellar photometry*.

Pietrinferni, A. et al. (2004). "A Large Stellar Evolution Database for Population Synthesis Studies. I. Scaled Solar Models and Isochrones". In: ApJ 612, pp. 168–190. DOI: 10.1086/422498. eprint: astro-ph/0405193.

Pietrukowicz, P. et al. (2015). "Deciphering the 3D Structure of the Old Galactic Bulge from the OGLE RR Lyrae Stars". In: ApJ 811, 113, p. 113. DOI: 10.1088/0004-637X/811/2/113. arXiv: 1412.4121.

Piotto, G. et al. (2015). "The Hubble Space Telescope UV Legacy Survey of Galactic Globular Clusters. I.

Overview of the Project and Detection of Multiple Stellar Populations". In: *AJ* 149, 91, p. 91. DOI: 10.1088/0004-6256/149/3/91. arXiv: 1410.4564 [astro-ph.SR].

Pooley, D. and P. Hut (2006). "Dynamical Formation of Close Binaries in Globular Clusters: Cataclysmic Variables". In: ApJ 646, pp. L143–L146. DOI: 10.1086/507027. eprint: astro-ph/0605048.

Portail, M. et al. (2017). "Dynamical modelling of the galactic bulge and bar: the Milky Way's pattern speed, stellar and dark matter mass distribution". In: MNRAS 465, pp. 1621–1644. DOI: 10.1093/mnras/stw2819. arXiv: 1608.07954.

Pulone, L. et al. (1998). "The Lower Main Sequence of ω Centauri from Deep Hubble Space Telescope NICMOS Near-Infrared Observations". In: ApJ 492, pp. L41–L44. DOI: 10.1086/311094.

Ragazzoni, R., E. Marchetti, and F. Rigaut (1999). "Modal tomography for adaptive optics". In: *A&A* 342, pp. L53–L56.

Ragazzoni, R., E. Marchetti, and G. Valente (2000). "Adaptive-optics corrections available for the whole sky". In: *Nature* 403, pp. 54–56. DOI: 10.1038/47425.

Raha, N. et al. (1991). "A dynamical instability of bars in disk galaxies". In: Nature 352, p. 411. DOI: 10.1038/352411a0.

Ramírez, S. V. et al. (2000). "Metallicity of Red Giants in the Galactic Bulge from Near-Infrared Spectroscopy". In: AJ 120, pp. 833–844. DOI: 10.1086/301466. eprint: astro-ph/0003116.

Ransom, S. M. et al. (2005). "Twenty-One Millisecond Pulsars in Terzan 5 Using the Green Bank Telescope". In: *Science* 307, pp. 892–896. DOI: 10.1126/science.1108632. eprint: astro-ph/0501230.

Reimers, D. (1975). "Circumstellar absorption lines and mass loss from red giants". In: *Memoires of the Societe Royale des Sciences de Liege* 8, pp. 369–382.

Rich, R. M. (1988). "Spectroscopy and abundances of 88 K giants in Baade's Window". In: AJ 95, pp. 828–865. DOI: 10.1086/114681.

— (1990). "Kinematics and abundances of K giants in the nuclear bulge of the Galaxy". In: ApJ 362, pp. 604–619. DOI: 10.1086/169299.

— (2013). "The Galactic Bulge". In: *Planets, Stars and Stellar Systems. Volume 5: Galactic Structure and Stellar Populations*. Ed. by T. D. Oswalt and G. Gilmore, p. 271. DOI: 10.1007/978-94-007-5612-0_6.

Rich, R. M. and L. Origlia (2005). "The First Detailed Abundances for M Giants in Baade's Window from Infrared Spectroscopy". In: ApJ 634, pp. 1293–1299. DOI: 10.1086/432592. eprint: astro-ph/0506051.

Rich, R. M., L. Origlia, and E. Valenti (2012). "Detailed Abundances for M Giants in Two Inner Bulge Fields from Infrared Spectroscopy". In: ApJ 746, 59, p. 59. DOI: 10.1088/0004-637X/746/1/59. arXiv: 1112.0306.

Richer, H. B. et al. (2013). "A Dynamical Signature of Multiple Stellar Populations in 47 Tucanae". In: *ApJl* 771, L15, p. L15. DOI: 10.1088/2041-8205/771/1/L15. arXiv: 1306.1226 [astro-ph.SR].

Rigaut, F. et al. (2012). "GeMS: first on-sky results". In: *Adaptive Optics Systems III*. Vol. 8447. Proc. SPIE, p. 84470I. DOI: 10.1117/12.927061.

Rigaut, F. et al. (2014). "Gemini multiconjugate adaptive optics system review - I. Design, trade-offs and integration". In: *MNRAS* 437, pp. 2361–2375. DOI: 10.1093/mnras/stt2054. arXiv: 1310.6199 [astro-ph.IM].

Rigaut, F. J., B. L. Ellerbroek, and R. Flicker (2000). "Principles, limitations, and performance of multiconjugate adaptive optics". In: *Adaptive Optical Systems Technology*. Ed. by P. L. Wizinowich. Vol. 4007. Proc. SPIE, pp. 1022–1031. DOI: 10.1117/12.390311.

Robin, A. C. et al. (2003). "A synthetic view on structure and evolution of the Milky Way". In: A&A 409, pp. 523–540. DOI: 10.1051/0004-6361:20031117.

Robin, A. C. et al. (2012). "Stellar populations in the Milky Way bulge region: towards solving the Galactic bulge and bar shapes using 2MASS data". In: A&A 538, A106, A106. DOI: 10.1051/0004-6361/201116512. arXiv: 1111.5744.

Roddier, F. and C. Roddier (1988). "Curvature Sensing and Compensation: A New Concept in Adaptive Optics". In: *European Southern Observatory Conference and Workshop Proceedings*. Ed. by M.-H. Ulrich. Vol. 30. European Southern Observatory Conference and Workshop Proceedings, p. 667.

Rodriguez-Fernandez, N. J. and F. Combes (2008). "Gas flow models in the Milky Way embedded bars". In: A&A 489, pp. 115–133. DOI: 10.1051/0004-6361:200809644. arXiv: 0806.4252.

Roediger, J. C. et al. (2014). "Constraining Stellar Population Models. I. Age, Metallicity and Abundance Pattern Compilation for Galactic Globular Clusters". In: ApJS 210, 10, p. 10. DOI: 10.1088/0067-0049/210/1/10. arXiv: 1310.3275.

Rojas-Arriagada, A. et al. (2014). "The Gaia-ESO Survey: metallicity and kinematic trends in the Milky Way bulge". In: A&A 569, A103, A103. DOI: 10.1051/0004-6361/201424121. arXiv: 1408.4558.

Romero-Gómez, M. et al. (2011). "Modelling the inner disc of the Milky Way with manifolds - I. A first step". In: MNRAS 418, pp. 1176–1193. DOI: 10.1111/j.1365-2966.2011.19569.x. arXiv: 1108.0660.

Rosenberg, A. et al. (1999). "Galactic Globular Cluster Relative Ages". In: AJ 118, pp. 2306–2320. DOI: 10.1086/301089. eprint: astro-ph/9907394.

Rossi, L. J. et al. (2015). "Proper motions and kinematics of selected bulge globular clusters". In: MNRAS 450, pp. 3270–3288. DOI: 10.1093/mnras/stv748. arXiv: 1504.01743.

Rossi, L. J., K. Bekki, and J. R. Hurley (2016). "Evolution of star cluster systems in isolated galaxies: first results from direct N-body simulations". In: MNRAS 462, pp. 2861–2877. DOI: 10.1093/mnras/stw1827. arXiv: 1608.02309.

Rousset, G. et al. (1990). "Adaptive optics prototype system for infrared astronomy: I. System description". In: *Amplitude and Intensity Spatial Interferometry*. Ed. by J. B. Breckinridge. Vol. 1237. Proc. SPIE, pp. 336–344. DOI: 10.1117/12.19305.

Sadler, E. M., R. M. Rich, and D. M. Terndrup (1996). "K Giants in Baade's Window. II. The Abundance Distribution". In: AJ 112, p. 171. DOI: 10.1086/117998. eprint: astro-ph/9604045.

Saha, K., I. Martinez-Valpuesta, and O. Gerhard (2012). "Spin-up of low-mass classical bulges in barred galaxies". In: MNRAS 421, pp. 333–345. DOI: 10.1111/j.1365-2966.2011.20307.x. arXiv: 1105.5797.

Saito, R. K. et al. (2011). "Mapping the X-shaped Milky Way Bulge". In: AJ 142, 76, p. 76. DOI: 10.1088/0004-6256/142/3/76. arXiv: 1107.5360.

Saito, R. K. et al. (2012). "VVV DR1: The first data release of the Milky Way bulge and southern plane from the near-infrared ESO public survey VISTA variables in the Vía Láctea". In: A&A 537, A107, A107. DOI: 10.1051/0004-6361/201118407. arXiv: 1111.5511.

Salaris, M. and L. Girardi (2002). "Population effects on the red giant clump absolute magnitude: the K band". In: MNRAS 337, pp. 332–340. DOI: 10.1046/j.1365-8711.2002.05917.x. eprint: astro-ph/0208057.

Salaris, M. and A. Weiss (1998). "Metal-rich globular clusters in the galactic disk: new age determinations and the relation to halo clusters". In: A&A 335, pp. 943–953. eprint: astro-ph/9802075.

— (2002). "Homogeneous age dating of 55 Galactic globular clusters. Clues to the Galaxy formation mechanisms". In: A&A 388, pp. 492–503. DOI: 10.1051/0004-6361:20020554. eprint: astro-ph/0204410.

Salaris, M. et al. (2007). "Deep near-infrared photometry of the globular cluster 47 Tucanae. Reconciling theory and observations". In: A&A 476, pp. 243–253. DOI: 10.1051/0004-6361:20078445.

Salinas, R. et al. (2012). "Structural parameters and blue stragglers in Sagittarius dwarf spheroidal galaxy globular clusters". In: MNRAS 421, pp. 960–970. DOI: 10.1111/j.1365-2966.2011.20354.x. arXiv: 1112.1614 [astro-ph.GA].

Sandage, A. and C. Cacciari (1990). "The absolute magnitudes of RR Lyrae stars and the age of the galactic globular cluster system". In: ApJ 350, pp. 645–661. DOI: 10.1086/168417.

Saracino, S. et al. (2015). "GEMINI/GeMS Observations Unveil the Structure of the Heavily Obscured Globular Cluster Liller 1." In: *ApJ* 806, 152, p. 152. DOI: 10.1088/0004-637X/806/2/152. arXiv: 1505.00568 [astro-ph.SR].

Saracino, S. et al. (2016). "Ultra-deep GEMINI Near-infrared Observations of the Bulge Globular Cluster NGC 6624." In: *ApJ* 832, 48, p. 48. DOI: 10.3847/0004-637X/832/1/48. arXiv: 1609.02152 [astro-ph.SR].

Sarajedini, A. and P. Demarque (1990). "A new age diagnostic applied to the globular clusters NGC 288 and NGC 362". In: ApJ 365, pp. 219–223. DOI: 10.1086/169472.

Sarajedini, A. et al. (2007). "The ACS Survey of Galactic Globular Clusters. I. Overview and Clusters without Previous Hubble Space Telescope Photometry". In: *AJ* 133, pp. 1658–1672. DOI: 10.1086/511979. eprint: astro-ph/0612598.

Saumon, D. and M. S. Marley (2008). "The Evolution of L and T Dwarfs in Color-Magnitude Diagrams". In: ApJ 689, 1327-1344, pp. 1327–1344. DOI: 10.1086/592734. arXiv: 0808.2611.

Saumon, D. et al. (1994). "Cool zero-metallicity stellar atmospheres". In: ApJ 424, pp. 333–344. DOI: 10.1086/173892.

Schlegel, D. J., D. P. Finkbeiner, and M. Davis (1998). "Maps of Dust Infrared Emission for Use in Estimation of Reddening and Cosmic Microwave Background Radiation Foregrounds". In: ApJ 500, pp. 525–553. DOI: 10.1086/305772. eprint: astro-ph/9710327.

Schultheis, M. et al. (1999). "Interstellar extinction towards the inner Galactic Bulge". In: A&A 349, pp. L69–L72. eprint: astro-ph/9908349.

Schultheis, M. et al. (2014). "Extinction Maps toward the Milky Way Bulge: Two-dimensional and Three-dimensional Tests with APOGEE". In: AJ 148, 24, p. 24. DOI: 10.1088/0004-6256/148/1/24. arXiv: 1405.2180.

Schultheis, M. et al. (2017). "Baade's window and APOGEE. Metallicities, ages, and chemical abundances". In: A&A 600, A14, A14. DOI: 10.1051/0004-6361/201630154. arXiv: 1702.01547.

Shack, R. V. and B. Platt (1971). "Production and Use of a Lenticular Hartmann Screen". In: *JOSA* 61, p. 656.

Shen, J. et al. (2010). "Our Milky Way as a Pure-disk Galaxy - A Challenge for Galaxy Formation". In: ApJ 720, pp. L72–L76. DOI: 10.1088/2041-8205/720/1/L72. arXiv: 1005.0385.

Siegel, M. H. et al. (2011). "The ACS Survey of Galactic Globular Clusters. XI. The Three-dimensional Orientation of the Sagittarius Dwarf Spheroidal Galaxy and Its Globular Clusters". In: ApJ 743, 20, p. 20. DOI: 10.1088/0004-637X/743/1/20. arXiv: 1108.6276.

Smith, B. J., S. D. Price, and R. I. Baker (2004). "The COBE DIRBE Point Source Catalog". In: ApJS 154, pp. 673–704. DOI: 10.1086/423248. eprint: astro-ph/0406177.

Stephens, A. W. and J. A. Frogel (2004). "An Infrared Spectroscopic Study of Eight Galactic Globular Clusters". In: AJ 127, pp. 925–937. DOI: 10.1086/381294. eprint: astro-ph/0312512.

Stetson, P. B. (1987). "DAOPHOT - A computer program for crowded-field stellar photometry". In: PASP 99, pp. 191–222. DOI: 10.1086/131977.

— (1994). "The center of the core-cusp globular cluster M15: CFHT and HST Observations, ALLFRAME reductions". In: PASP 106, pp. 250–280. DOI: 10.1086/133378.

Stetson, P. B. et al. (1999). "Ages for Globular Clusters in the Outer Galactic Halo: The Second-Parameter Clusters Palomar 3, Palomar 4, and Eridanus". In: AJ 117, pp. 247–263. DOI: 10.1086/300670. eprint: astro-ph/9809176.

Tacchella, S. et al. (2015). "Evidence for mature bulges and an inside-out quenching phase 3 billion years after the Big Bang". In: *Science* 348, pp. 314–317. DOI: 10.1126/science.1261094. arXiv: 1504.04021.

Tam, P. H. T. et al. (2011). "Gamma-ray Emission from the Globular Clusters Liller 1, M80, NGC 6139, NGC 6541, NGC 6624, and NGC 6752". In: ApJ 729, 90, p. 90. DOI: 10.1088/0004-637X/729/2/90. arXiv: 1101.4106 [astro-ph.HE].

Tatarskii, V. I. (1961). *Wave Propagation in Turbulent Medium*. McGraw-Hill.

Terndrup, D. M., E. M. Sadler, and R. M. Rich (1995). "K Giants in Baade's Window. I. Velocity and Line-Strength Measurements". In: AJ 110, p. 1774. DOI: 10.1086/117649. eprint: astro-ph/9508105.

Terzan, A. (1968). "Six nouveaux amas stellaires (Terzan 3-8) dans la region du centre de la Voie lactee et les constellations du Scorpion et du Sagittaire". In: *Publications of the Observatoire Haute-Provence* 10.

Tiede, G. P. and D. M. Terndrup (1997). "A New Survey of Stellar Kinematics in the Central Milky Way". In: AJ 113, pp. 321–334. DOI: 10.1086/118255.

Trager, S. C., I. R. King, and S. Djorgovski (1995). "Catalogue of Galactic globular-cluster surface-brightness profiles". In: AJ 109, pp. 218–241. DOI: 10.1086/117268.

Turri, P. et al. (2015). "Toward Precision Photometry for the ELT Era: The Double Subgiant Branch of NGC 1851 Observed with the Gemini/GeMS MCAO System". In: ApJ 811, L15, p. L15. DOI: 10.1088/2041-8205/811/2/L15. arXiv: 1509.01764.

Valenti, E., F. R. Ferraro, and L. Origlia (2004a). "Red giant branch in near-infrared colour-magnitude diagrams - I. Calibration of photometric indices". In: MNRAS 351, pp. 1204–1214. DOI: 10.1111/j.1365-2966.2004.07861.x. eprint: astro-ph/0403563.

— (2004b). "Red giant branch in near-infrared colour-magnitude diagrams - II. The luminosity of the bump and the tip". In: MNRAS 354, pp. 815–820. DOI: 10.1111/j.1365-2966.2004.08249.x. eprint: astro-ph/0404403.

— (2007). "Near-Infrared Properties of 24 Globular Clusters in the Galactic Bulge". In: *AJ* 133, pp. 1287–1301. DOI: 10.1086/511271. eprint: astro-ph/0612280.

— (2010). "Near-infrared properties of 12 globular clusters towards the inner bulge of the Galaxy". In: *MNRAS* 402, pp. 1729–1739. DOI: 10.1111/j.1365-2966.2009.15991.x. arXiv: 0911.1264.

Valenti, E., L. Origlia, and R. M. Rich (2011). "High-resolution near-infrared spectra of NGC 6624 and 6569". In: MNRAS 414, pp. 2690–2695. DOI: 10.1111/j.1365-2966.2011.18580.x. arXiv: 1103.0233 [astro-ph.SR].

Valenti, E. et al. (2013). "Stellar ages through the corners of the boxy bulge". In: A&A 559, A98, A98. DOI: 10.1051/0004-6361/201321962. arXiv: 1309.4570.

Valenti, E. et al. (2016). "Stellar density profile and mass of the Milky Way bulge from VVV data". In: A&A 587, L6, p. L6. DOI: 10.1051/0004-6361/201527500. arXiv: 1510.07425.

Vandenberg, D. A., M. Bolte, and P. B. Stetson (1990). "A new method for estimating relative ages of star clusters." In: JRASC 84, pp. 412–413.

VandenBerg, D. A. et al. (2008). "On the Use of Blanketed Atmospheres as Boundary Conditions for Stellar Evolutionary Models". In: ApJ 675, 746-763, pp. 746–763. DOI: 10.1086/521600. arXiv: 0708.1188.

VandenBerg, D. A. et al. (2013). "The Ages of 55 Globular Clusters as Determined Using an Improved \Delta V^HB_TO Method along with Color-Magnitude Diagram Constraints, and Their Implications for Broader Issues". In: ApJ 775, 134, p. 134. DOI: 10.1088/0004-637X/775/2/134. arXiv: 1308.2257 [astro-ph.GA].

VandenBerg, D. A. et al. (2014). "Isochrones for Old (>5 Gyr) Stars and Stellar Populations. I. Models for -2.4 <= [Fe/H] <=+0.6, 0.25 <= Y <= 0.33, and -0.4 <= [α/Fe] <=+0.4". In: ApJ 794, 72, p. 72. DOI: 10.1088/0004-637X/794/1/72. arXiv: 1409.1283 [astro-ph.SR].

Vásquez, S. et al. (2013). "3D kinematics through the X-shaped Milky Way bulge". In: A&A 555, A91, A91. DOI: 10.1051/0004-6361/201220222. arXiv: 1304.6427.

Verbunt, F. and P. Hut (1987). "The Globular Cluster Population of X-Ray Binaries". In: *The Origin and Evolution of Neutron Stars*. Ed. by D. J. Helfand and J.-H. Huang. Vol. 125. IAU Symposium, p. 187.

Vesperini, E. and D. C. Heggie (1997). "On the effects of dynamical evolution on the initial mass function of globular clusters". In: MNRAS 289, pp. 898–920. DOI: 10.1093/mnras/289.4.898. eprint: astro-ph/9705073.

Vidal, F. et al. (2013). "GeMS: from the on-sky experimental system to science operation. The AO point of view". In: *Proceedings of the Third AO4ELT Conference*. Ed. by S. Esposito and L. Fini, p. 46. DOI: 10.12839/AO4ELT3.13276.

Watkins, L. L. et al. (2015). "Hubble Space Telescope Proper Motion (HSTPROMO) Catalogs of Galactic Globular Cluster. II. Kinematic Profiles and Maps". In: *ApJ* 803, 29, p. 29. DOI: 10.1088/0004-637X/803/1/29. arXiv: 1502.00005.

Webb, J. J. and E. Vesperini (2016). "Radial variation in the stellar mass functions of star clusters". In: MNRAS 463, pp. 2383–2393. DOI: 10.1093/mnras/stw2186. arXiv: 1608.07293.

Wegg, C. and O. Gerhard (2013). "Mapping the three-dimensional density of the Galactic bulge with VVV red clump stars". In: MNRAS 435, pp. 1874–1887. DOI: 10.1093/mnras/stt1376. arXiv: 1308.0593.

Wegg, C., O. Gerhard, and M. Portail (2015). "The structure of the Milky Way's bar outside the bulge". In: MNRAS 450, pp. 4050–4069. DOI: 10.1093/mnras/stv745. arXiv: 1504.01401.

Weiland, J. L. et al. (1994). "COBE diffuse infrared background experiment observations of the galactic bulge". In: ApJ 425, pp. L81–L84. DOI: 10.1086/187315.

Wizinowich, P. et al. (2010). "W. M. Keck Observatory's next-generation adaptive optics facility". In: *Adaptive Optics Systems II*. Vol. 7736. Proc. SPIE, 77360K. DOI: 10.1117/12.857628.

Yadav, R. K. S. et al. (2008). "Optical and near-infrared photometric study of the open cluster NGC 637 and 957". In: *MNRAS* 390, pp. 985–996. DOI: 10.1111/j.1365-2966.2008.13740.x. arXiv: 0810.1409.

Zinn, R. and M. J. West (1984). "The globular cluster system of the galaxy. III - Measurements of radial velocity and metallicity for 60 clusters and a compilation of metallicities for 121 clusters". In: ApJS 55, pp. 45–66. DOI: 10.1086/190947.

Zoccali, M. (2010). "The Stellar Population of the Galactic Bulge". In: *Chemical Abundances in the Universe: Connecting First Stars to Planets*. Ed. by K. Cunha, M. Spite, and B. Barbuy. Vol. 265. IAU Symposium, pp. 271–278. DOI: 10.1017/S1743921310000736. arXiv: 0910.5133.

Zoccali, M. and E. Valenti (2016). "The 3D Structure of the Galactic Bulge". In: PASA 33, e025, e025. DOI: 10.1017/pasa.2015.56. arXiv: 1601.02839.

Zoccali, M. et al. (2001). "The Proper Motion of the Globular Cluster NGC 6553 and of Bulge Stars with the Hubble Space Telescope". In: AJ 121, pp. 2638–2646. DOI: 10.1086/320411.

Zoccali, M. et al. (2003). "Age and metallicity distribution of the Galactic bulge from extensive optical and near-IR stellar photometry". In: *A&A* 399, pp. 931–956. DOI: 10.1051/0004-6361:20021604. eprint: astro-ph/0210660.

Zoccali, M. et al. (2008). "The metal content of bulge field stars from FLAMES-GIRAFFE spectra. I. Stellar parameters and iron abundances". In: A&A 486, pp. 177–189. DOI: 10.1051/0004-6361:200809394. arXiv: 0805.1218.

Zoccali, M. et al. (2014). "The GIRAFFE Inner Bulge Survey (GIBS). I. Survey description and a kinematical map of the Milky Way bulge". In: A&A 562, A66, A66. DOI: 10.1051/0004-6361/201323120. arXiv: 1401.4878.